FUNDAMENTALS OF ELECTROMAGNETIC NANONETWORKS IN THE TERAHERTZ BAND

A Dissertation
Presented to
The Academic Faculty

By

Josep Miquel Jornet Montana

In Partial Fulfillment
of the Requirements for the Degree
Doctor of Philosophy
in
Electrical and Computer Engineering

School of Electrical and Computer Engineering
Georgia Institute of Technology
December 2013

FUNDAMENTALS OF ELECTROMAGNETIC NANONETWORKS IN THE TERAHERTZ BAND

Approved by:

Dr. Ian F. Akyildiz, Advisor
Ken Byers Chair Professor in Telecommunications, School of Electrical and Computer Engineering
Georgia Institute of Technology

Dr. Geoffrey Ye Li
Professor, School of Electrical and Computer Engineering
Georgia Institute of Technology

Dr. Faramarz Fekri
Professor, School of Electrical and Computer Engineering
Georgia Institute of Technology

Dr. Bernard Kippelen
Professor, School of Electrical and Computer Engineering
Georgia Institute of Technology

Dr. Zhong Lin Wang
Hightower Chair Professor, School of Materials Science and Engineering
Georgia Institute of Technology

Date Approved: August 6, 2013

To my family, for their endless love, encouragement and support

ACKNOWLEDGMENT

I would like to express my deepest gratitude to my advisor and mentor, Dr. Ian F. Akyildiz, for giving me the life-changing opportunity to work under his guidance, and for his trust, support and encouragement throughout my entire Ph.D.. I am also thankful to him for his unbounded energy and passion, which helped me to steadily advance towards the successful completion of this thesis. I would also like to thank Dr. Akyildiz for his endless mentoring, which has and will continue helping me to pave my future career.

I would also like to extend my appreciation to all the academic members of the School of Electrical and Computer Engineering at the Georgia Institute of Technology for their helpful and critical reviews throughout the Ph.D. program. In particular, I would like to sincerely thank Dr. Geoffrey Ye Li, Dr. Faramarz Fekri, Dr. Bernard Kippelen, and Dr. Zhong Lin Wang, who kindly agreed to serve in my Ph.D. Defense Committee. Their invaluable comments have helped me to achieve a solid research path towards this thesis.

I would also like to thank all former and current members of the Broadband Wireless Networking (BWN) Lab, for their constant support and true friendship since the very beginning. I keep a vivid memory of all my days in the lab and all the fantastic people that I have met throughout these years. It would be almost impossible to mention everyone, and it would be unfair to only mention a few. To all of you, thank you for the unique atmosphere we have had in the lab.

I cannot find the words to express my gratitude to my family, and in particular my parents, my sister and my grandmother. This achievement would have not been possible without their encouragement, support and love. Last but not least, I would like to thank Elena for making the last part of this adventure even more exciting.

SUMMARY

Nanotechnology is providing a new set of tools to the engineering community to design nanoscale components with unprecedented functionalities. The integration of several nano-components into a single entity will enable the development of advanced nanomachines. Nanonetworks, *i.e.*, networks of nanomachines, will enable a plethora of applications in the biomedical, environmental, industrial and military fields. To date, it is still not clear how nanomachines will communicate. The miniaturization of a classical antenna to meet the size requirements of nanomachines would impose the use of very high radiation frequencies. The available transmission bandwidth increases with the antenna resonant frequency, but so does the propagation loss. Due to the expectedly very limited power of nanomachines, the feasibility of nanonetworks would be compromised if this approach were followed. Therefore, a new wireless technology is needed to enable this paradigm.

The objective of this thesis is to establish the foundations of graphene-enabled electromagnetic communication in nanonetworks. First, novel graphene-based plasmonic nano-antennas are proposed, modeled and analyzed. The obtained results point to the Terahertz Band (0.1-10 THz) as the frequency range of operation of novel nano-antennas. For this, the second contribution in this thesis is the development of a novel channel model for Terahertz Band communication. In addition, the channel capacity of the Terahertz Band is numerically investigated to highlight the potential of this still-unregulated frequency band. Third, a novel modulation based on the transmission of femtosecond-long pulses is proposed and its performance is analyzed.Fourth, the use of low-weight codes to prevent channel errors in nanonetworks is proposed and investigated. Fifth, a novel symbol detection scheme at the receiver is developed to support the proposed modulation scheme. Sixth, a new energy model for self-powered nanomachines with piezoelectric nano-generators is developed. Moreover, a new Medium Access Control protocol tailored to the Terahertz Band is developed. Finally, a one-to-one nano-link is emulated to validate the proposed solutions.

TABLE OF CONTENTS

LIST OF FIGURES

CHAPTER 1

INTRODUCTION

In 1959, the Nobel laureate physicist Richard Feynman, in his famous speech entitled *"There's Plenty of Room at the Bottom"*, described for the first time how the manipulation of individual atoms and molecules would give rise to more functional and powerful man-made devices. In his talk, he noted that several scaling issues would arise when reaching the nanoscale, which would require the engineering community to rethink the way in which devices are conceived. More than half century later, nanotechnology is providing a new set of tools to the engineering community to control matter at an atomic and molecular scale. At this scale, novel nanomaterials show new properties not observed at the microscopic level. By exploiting these properties, a new generation of nanoscale components with unprecedented functionalities is being developed.

Amongst many nanomaterials, graphene, *i.e.*, a one-atom-thick layer of carbon atoms in a honeycomb crystal lattice [92, 38], has recently attracted the attention of the scientific community due to its unique physical, electrical and optical properties. Indeed, despite theoretical research on graphene started back in the 19th century, the experimental discovery of graphene in 2004 by Andre Geim and Konstantin Novoselov, which earned them the Nobel Prize in Physics in 2010, drastically boosted the interest in this unique nanomaterial as well as on its derivatives, *e.g.*, graphene nanoribbons (GNRs), which are thin strips of graphene, and carbon nanotubes (CNTs), which can be analyzed as rolled graphene. Their unique properties enable the development of new types of nano-processors, nano-memories, nano-batteries, and nanosensors, amongst others.

The integration of several of these nano-components in a single entity will enable the development of novel nanomachines. More importantly, similarly to the way in which communication among computers enabled revolutionary applications such as the Internet, by means of communication, nanomachines will be able to overcome their limitations and expand their potential applications [1, 2, 3, 5, 60]. The resulting nanonetworks, *i.e.*, networks of nanomachines, will be able to cover larger areas, to reach unprecedented locations in a non-invasive way, and to perform additional in-network processing.

1.1 Applications of Nanonetworks

Nanonetworks are the enabling technology of many long-awaited applications:

- **Biomedical applications:** The nanoscale is the natural domain of molecules, proteins, DNA, organelles and the major components of living cells [89]. As a result, a very large number of applications of nanonetworks is in the biomedical field. For example, nanomaterial-based biological nanosensors [163] can be deployed over (*e.g.*, tattoo-like) or even inside the human body (*e.g.*, a pill or intramuscular injection) to monitor glucose, sodium, and cholesterol [28, 72], to detect the presence of infectious agents [136], or to identify specific types of cancer [139]. A wireless interface between these nanomachines and a micro-device, such as a cellphone or medical equipment, could be used to collect data and to forward it to a healthcare provider.

- **Environmental applications:** Trees, herbs, or bushes, release several chemical composites to the air in order to attract the natural predators of the insects that are attacking them, or to regulate their blooming among different plantations, amongst others [49, 50, 109]. Chemical nanosensors [163] could be used to detect the chemical compounds that are being released and exchanged between plants. Nanonetworks can be build around classical sensor devices which are already deployed in agriculture fields [4]. Other environmental applications include biodiversity control, biodegradation assistance, or air pollution control [114].

- **Industrial and consumer goods applications:** The applications of nanotechnology in the development of new industrial and consumer goods range from flexible and stretchable electronic devices [115] to new functionalized nanomaterials for self-cleaning anti-microbial textiles [138]. In addition, the integration of nanomachines with communication capabilities in every single object will allow the interconnection of almost everything in our daily life, from cooking utensils to every element in our working place, or also the components of every device, enabling what we define as *the Internet of Nano-Things* (see Figure 1) [3]. Moreover, as nano-cameras and nano-phones are developed, in a more futuristic approach, the *the Internet of Multimedia Nano-Things* [60] will also become a reality.

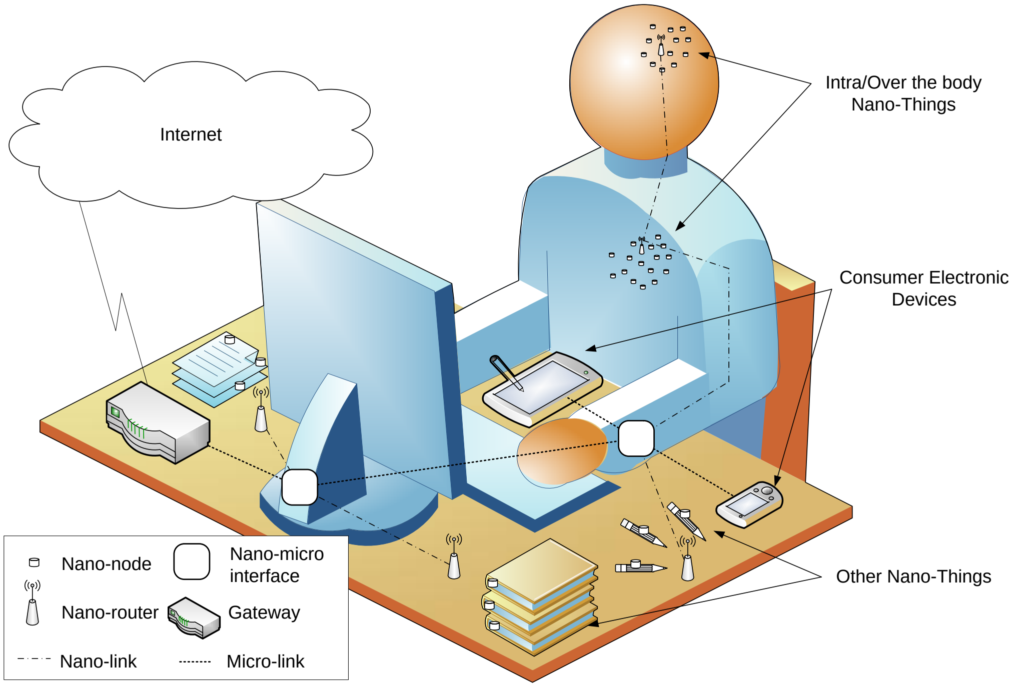

Figure 1. The Internet of Nano-Things.

- **Military and defense applications:** Advanced nuclear, biological and chemical (NBC) defenses, and sophisticated damage detection systems for civil structures, soldiers' armor and military vehicles, are two examples of the military applications enabled by nanonetworks. For example, a network of nanosensors can be used to detect harmful chemicals and biological weapons with unprecedented accuracy and timeliness, in very different scenarios, from the battle-field (*e.g.*, deployed from an unmanned vehicle and imperceptible by the human eye) to airport lobbies or a conference room (*e.g.*, contained within the wall paint).

1.2 Nanomachine Hardware Architecture

There are many challenges in the development of autonomous nanomachines. In Figure 2, a conceptual nanomachine architecture is shown. To the best of our knowledge, fully functional nanomachines have not been built to date. However, several solutions for each nano-component have been prototyped and tested:

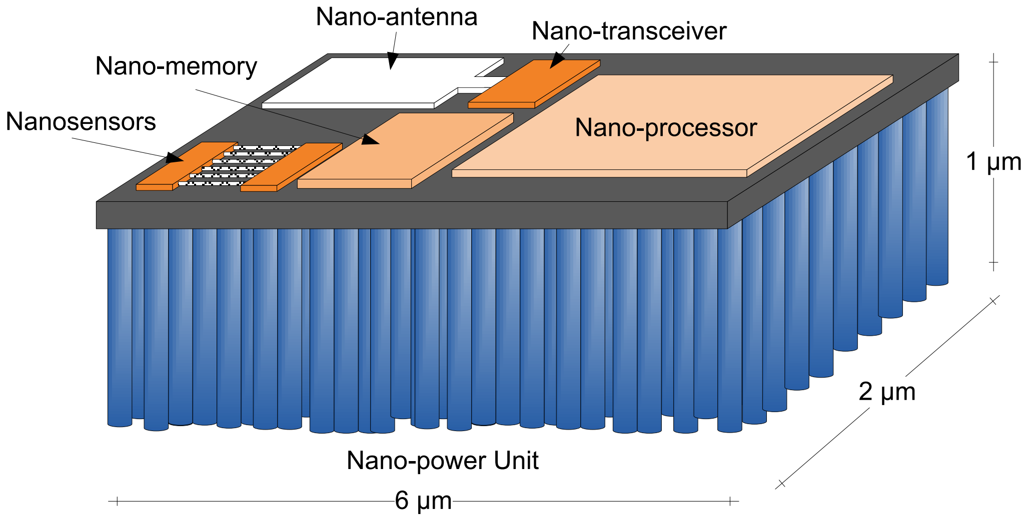

Figure 2. Nanomachine hardware architecture.

- **Processing Unit:** Nano-processors are being enabled by the development of tinier FET transistors in different forms. The smallest transistor that has been experimentally tested to date is based on a thin graphene strip made of just 10 by 1 carbon atoms [110]. These transistors are not only smaller, but also able to operate at higher frequencies. The complexity of the operations that a nano-processor will be able to handle directly depend on the number of integrated transistors in the chip, thus, on its total size.
- **Data Storage Unit:** Nanomaterials and new manufacturing processes are enabling the development of single-atom nano-memories, in which the storage of one bit of

information requires only one atom [10]. For example, in a magnetic memory [102], atoms are placed over a surface by means of magnetic forces. While these memories are not ready yet for nanomachines, they serve as a starting point. The total amount of information storable in a nano-memory will ultimately depend on its dimensions.

- **Power Unit:** Powering nanomachines requires new types of nano-batteries [59, 133] as well as nanoscale energy harvesting systems [152]. One of the most promising techniques relies on the piezoelectric effect seen in zinc oxide nanowires, which are used to convert vibrational energy into electricity. This energy can then be stored in a nano-battery and dynamically consumed by the device. The rate at which energy is harvested and the total energy that can be stored in a nano-device depends ultimately on the device size.
- **Sensing Unit:** Physical, chemical and biological nanosensors have been developed by using graphene and other nanomaterials [51, 163]. A nanosensor is not just a tiny sensor, but a device that makes use of the novel properties of nanomaterials to identify and measure new types of events in the nanoscale, such as the physical characteristics of structures just a few nanometers in size, chemical compounds in concentrations as low as one part per billion, or the presence of biological agents such as virus, bacteria or cancerous cells. Their accuracy and timeliness is much higher than those of existing sensors.
- **Communication Unit:** The miniaturization of an antenna to meet the size constraints of nanomachines would impose the use of very high frequencies. This would limit the feasibility of electromagnetic nanonetworks due to the energy limitations of nanomachines. As we will discuss in Chapter 2, nanomaterials can be used to develop new types of nano-antennas as well as nano-transceivers, which can operate at much lower frequencies than miniature metallic antennas. However, these introduce many challenges for the realization of communication in nanonetworks. This sets the starting point of this thesis.

In addition, there are many crucial challenges in the integration of the different components into a single device. New methods to position and contact different nano-components are currently being developed. Amongst others, DNA scaffolding [63] is one of the most promising techniques. In [63], a procedure to arrange DNA synthesized strands on surfaces made of materials compatible with semiconductor manufacturing equipment has been demonstrated. The positioned DNA nano-structures can serve as scaffolds, or miniature circuit boards, for the precise assembly of the nano-components.

1.3 Research Objectives and Solutions

Due to the hardware peculiarities of nanomachines and the specific applications in which they will be used, nanonetworks are not just a miniaturization of classical wireless networks. There are several challenges in the realization of this new networking paradigm that require new solutions and even to rethink some well-established concepts in communication and network theory. These challenges range from the design of novel nano-antennas, to the characterization of the electromagnetic frequency band in which nano-antennas will radiate or the development of tailored communication mechanisms for nanomachines.

The objective of this thesis is to establish the foundations of graphene-enabled electromagnetic nanonetworks in the Terahertz Band (0.1-10 THz). The starting point is the development of pioneering graphene-based nano-antennas for communication among nanomachines. The developed analytical models and the related work in graphene-based nanoelectronic for RF applications point to the Terahertz Band as the communication band for nanomachines. Motivated by this result, a novel Terahertz Band channel model is developed and the channel capacity of the Terahertz Band is investigated. For very short distances, *i.e.*, much below one meter, the Terahertz Band behaves as a single transmission window which is almost 10 THz wide. Starting from this result, a new set of communication mechanisms for nanonetworks is developed. These include a novel modulation, new channel coding techniques, a novel receiver symbol detection scheme and a medium access control protocol for nanonetworks. In addition, a complete energy model for energy-harvesting self-powered nanomachines is developed to investigate the energy limitations of perpetual nanonetworks. Moreover, an emulation platform is defined and used to validate a one-to-one nano-link between two active nanomachines.

In the following sections, the developed solutions within each topic are summarized.

1.3.1 Graphene-based Plasmonic Nano-antenna

The miniaturization of a classical metallic antenna to satisfy the size constraints of a nanomachine would result in very high radiating frequencies. The available transmission bandwidth increases with the resonant frequency, but so does the propagation loss. The expectedly very limited energy of nanomachines would drastically compromise the feasibility of nanonetworks if this approach were followed. In addition, the availability of compact nanoscale transceivers able to generate and process the signals radiated and detected with the nano-antenna remains uncertain. The properties of novel nanomaterials can be exploited to enable electromagnetic communication among nanomachines. Indeed, in the same way that nanomaterials are enabling the development of smaller and faster processors, higher density memories, or very high accuracy sensors, new types of nano-antennas and nano-transceivers can be developed, which are more suitable for nanomachines. We should find the solutions for future nanonetworking challenges by looking at future technology opportunities, and not at current technology limitations.

The first contribution of this thesis (Chapter 2) is the design, modeling and analysis of a graphene-based nano-antenna for communication among nanomachines. The proposed graphene-based nano-antenna exploits the behavior of Surface Plasmon Polariton (SPP) waves in graphene. Two different approaches are followed to analyze the performance of the proposed nano-antenna. On the one hand, we develop a transmission line model of the GNRs, by using the tight-binding approach. Then, we compute the total GNR impedance and the propagation speed of SPP waves in GNRs. We model the proposed nano-structure as a resonant plasmonic cavity and compute the resonant frequency for the fundamental resonant mode. On the other hand, in a much more complete model, we develop a conductivity model tailored to GNRs, by starting from the Kubo formalism. We then use this model to analyze the propagation properties of SPP waves in GNRs, namely, the confinement factor and the propagation length, for two types of modes. Finally, we obtain the full frequency response of the antenna by modeling the antenna as a resonant plasmonic cavity.

1.3.2 Terahertz Band Channel Modeling and Capacity Analysis

Our analysis of the resonant frequency of graphene-based plasmonic nano-antennas as well as existing related work point to the Terahertz Band as the communication frequency band for electromagnetic nanonetworks. This still unregulated spectral band spans the frequencies between 100 GHz and 10 THz. The propagation of electromagnetic waves at Terahertz Band frequencies has several peculiarities. Amongst others, one of the main factors affecting the Terahertz Band communication is the molecular absorption. Molecular absorption is the process by which part of the electromagnetic energy of a wave is converted into kinetic energy in internally vibrating molecules. Terahertz Band radiation is not ionizing, *i.e.*, it cannot permanently damage the internal structure of molecules, but it can induce internal vibrations. From the communication perspective, this results in an additional energy loss, that further increases the already high propagation loss. As a result, classical channel models for lower frequency bands (*e.g.*, for the radio frequency or microwave bands), cannot directly be used for communication in nanonetworks.

The second contribution of this thesis (Chapter 3) is the development of a Terahertz Band channel model. We use tools from radiative transfer theory as well as the HITRAN database to obtain formulations for the path loss and molecular absorption noise at Terahertz Band frequencies. In addition, we quantize the potential of the Terahertz Band for communication by conducting a capacity analysis under four different power allocation schemes. Our results show how the Terahertz Band channel is drastically impacted by the presence of water vapor molecules. For short distances or low concentrations of molecules, the Terahertz Band behaves as a single transmission window, which is almost 10 THz wide.

This enables very high speed links, *e.g.*, up to a few Tbps, for short range applications. As the transmission distance or the concentration of molecules increases, molecular absorption defines a set of transmission windows, which are several GHz wide each. These enable multi-Gbps links if windows are individually used, but motivates further research for large scale Terahertz Band communication networks.

1.3.3 Femtosecond-long Pulse-based Modulation

Our channel model and capacity analysis shows as that, for the expected communication distance in nanonetworks, the Terahertz Band behaves as an almost 10 THz wide window. This result motivates the development of ultra-broadband modulations able to exploit this very large bandwidth. However, it is extremely challenging to generate high-power carrier signals at Terahertz Band frequencies with nanoscale solid-state Terahertz Band sources at room temperature. On the contrary, very short pulses, which are just one-hundred-femtosecond long, can be generated with high electron mobility transistors (HEMTs) based on III-V semiconductor materials [66, 97, 144, 145]. Moreover, pulse detectors based on the same device technology have also been demonstrated. These pulses are currently being used in Terahertz Band imaging applications. Consistently with the trends of ultra-low power, compact-size and ultra-low complexity design in broadband communications, we look at the potential of impulse-based communication for nanonetworks.

The third contribution of this thesis (Chapter 4) is the development of a pulse-based modulation and channel access scheme for nanonetworks in the Terahertz Band. The proposed technique is based on the transmission of one-hundred-femtosecond-long pulses by following an asymmetric On-Off Keying modulation Spread in Time (TS-OOK). We study the performance of TS-OOK in terms of the achievable information rate in the single-user and the the multi-user cases. For this, we develop novel stochastic models for the molecular absorption noise in the Terahertz Band and for the multi-user interference in TS-OOK. We numerically show that nanonetworks can support a very large number of nano-devices (thousands of nanomachines) simultaneously transmitting at very high bit-rates each (up to several Terabits per second) using the proposed modulation technique.

1.3.4 Low-weight Channel Coding

Channel errors in electromagnetic nanonetworks become frequent due to i) the limited transmission power of nanomachines, ii) the peculiar behavior of molecular absorption noise at Terahertz Band frequencies, and iii) multi-user interference among uncoordinated nanomachines that operate under TS-OOK. However, classical error control mechanisms might not be suitable for nanonetworks. For example, the very limited energy of nanomachines makes the use of retransmissions not recommended. Similarly, the complexity of existing channel coding techniques render many of the existing solutions unfeasible for nanonetworks. This motivates the development of new channel error control techniques.

The fourth contribution of this thesis (Chapter 5) is the study of the performance of low-weight channel codes for error prevention in nanonetworks. Indeed, rather than ignoring the channel errors sources and just retransmitting or using classical error correction schemes, we propose to prevent channel errors from happening by minimizing the generated noise and interference power. For this, first, we analyze the impact of the coding weight, *i.e.,* the average number of logical “1”s in a coded message, on the molecular absorption noise and the multi-user interference power. Then, we quantize the overhead introduced by using constant-weight codes. Finally, we analytically and numerically study the achievable information rate after coding and codeword error rate as functions of the coding weight. We show the existence of an optimal coding weight for which the achievable information rate after coding is maximized, which depends on the several network parameters.

1.3.5 Receiver Symbol Detection Scheme

Our proposed one-hundred-femtosecond-long modulation and coding techniques enable very ultra-broadband communication in the Terahertz Band. However, the detection of these very long pulses introduce several challenges to classical symbol detection schemes.

Existing receiver architectures cannot directly be used for the detection of femtosecond-long pulses, when transmitted at several Gigabits or even Terabits per second. Amongst others, the assumptions on the shape, energy, duration and emission rate of the pulses as well as on the channel effects are different for nanonetworks in the Terahertz Band. In addition, multi-user interference that originates from uncoordinated transmission among nanomachines may further challenge the proper detection cause a major obstacle for communication in nanonetworks.

The fifth contribution of this thesis (Chapter 6) is the development of a new receiver symbol detection scheme suited for ultra-short pulse communication over the Terahertz Band. The proposed symbol detector is based on a Continuous-Time Moving Average (CTMA) scheme, and can be implemented with a single low-pass filter. This scheme bases its decision in the received signal power maximum peak after the CTMA. Afterwards, to decode the symbol, this maximum is compared with a previously defined threshold. We analyze the performance of this detection scheme in terms of symbol error rate both in interference-free as well as in interference-limited scenarios.

1.3.6 Energy Modeling for Self-powered Nanomachines

The limited energy that can be stored in nano-batteries poses a major challenge for the development of useful applications of nanonetworks. For this, novel nanoscale energy harvesting systems are being developed. One of the most promising technologies to date is based on the use of piezoelectric nano-generators based on Zinc Oxide (ZnO) nanowires [152, 158]. ZnO nanowires exhibit piezoelectric behavior, *i.e.*, a small amount of charge is generated at the tips of the nanowire each time that these are bent or released. This charge can be used to then recharge an ultra-nano-capacitor, after proper rectification. Several prototypes have already been developed. For the time being, neither an analytical model of such devices nor the impact of nanoscale energy harvesting on the performance of nanonetworks has been explored.

The next contribution of this thesis (Chapter 7) is an energy model for self-powered nanomachines, which success-fully captures the correlation between the energy harvesting and the energy consumption processes. The energy harvesting process is realized by means of a piezoelectric nano-generator, for which a new circuital model is developed which can accurately reproduce existing experimental data. The energy consumption process is due to the communication in the Terahertz Band (0.1-10 THz). The proposed energy model captures the dynamic network behavior by means of a probabilistic analysis of the total network traffic and the multi-user interference. Our results show even if the Terahertz Band enables nanomachines to communicate at very high bit-rates, their energy limitations can drastically reduce their throughput by several orders of magnitude, unless the energy consumption process and the energy harvesting process are jointly designed.

1.3.7 Medium Access Control Protocol for Nanonetworks

Medium Access Control (MAC) protocols are needed to regulate the access to the channel and to coordinate concurrent transmissions among nanomachines. Classical MAC protocols cannot directly be used in nanonetworks because they do not capture either the limitations of nano-devices or the peculiarities of the Terahertz Band. In particular, existing MAC protocols are usually designed for narrow-band systems, in which a very limited bandwidth is shared by neighboring nodes. However, the Terahertz Band provides a very large bandwidth, almost 10 THz wide window. Similarly, the use of pulse-based modulations hampers the application of the majority of MAC protocols based on carrier sensing techniques. In addition, the limited computational capabilities of nanomachines and the use of energy harvesting systems introduces new constraints for the protocol design.

The next contribution of this thesis (Chapter 8) is the development of a PHysical Layer Aware MAC protocol for nanonetworks in the Terahertz Band (PHLAME). This protocol is built on top of the Rate Division Time-Spread On Off Keying (RD TS-OOK), which is a revised version of our proposed pulse-based communication scheme, and it exploits the benefits of novel low-weight channel coding schemes. PHLAME is based on the joint selection by the transmitter and the receiver of the optimal communication parameters and channel coding scheme which minimize the interference in the nanonetwork and maximize the probability of successfully decoding the received information. Moreover, the fluctuations in the energy of the nano-devices are taken into account. We numerically investigate the performance of the proposed protocol and analyze the impact of several parameters on the achievable throughput, delay and end-to-end delivery probability.

1.3.8 One-to-one Nano-link Emulation

As mentioned before, integrated nanomachines have not been built to date. As a result, many of the developed solutions cannot be experimentally validated. However, very advanced simulation and emulation tools are available and are a great asset for the partial validation of analytical models.

In this direction, the last contribution in this thesis is the development of a simulation framework for the emulation of a one-to-one nano-link between two nanomachines. In particular, first, the proposed graphene-based nano-antennas are implemented in COMSOL Multi-physics [19]. The dynamic conductivity model developed in this thesis is used to define the graphene material in COMSOL. Second, the channel between two nano-antennas is also emulated in COMSOL. The medium properties are incorporated in the simulation platform by means of the medium absorption coefficient. Ideal antennas are considered first in order to separate the channel effects from the nano-antenna effects. Afterwards, two graphene-based nano-antennas are used to establish the Terahertz Band link. Finally, COMSOL Multi-physics is linked with Matlab by means of LiveLink. This allows us to define the signals that we want to radiate according to our proposed modulation and channel coding schemes.

1.4 Organization of the Thesis

The thesis is organized as follows. In Chapter 2, the graphene-based plasmonic nano-antenna is proposed, modeled and analyzed. First, the working principle of the antenna is presented. Then, two different methodologies are used to analyze its frequency response, namely, the transmission line model and the dynamic conductivity model.

In Chapter 3, the Terahertz Band channel model is developed, by using radiative transfer theory to obtain formulations for the total path loss and molecular absorption in the Terahertz Band. In addition, the channel capacity is investigated for four different power allocation schemes.

In Chapter 4, the femtosecond-long pulse-based modulation and channel access scheme for nanonetworks is proposed. Its performance its analyzed in terms of achievable information rate both for the single-user case and the multi-user case. Novel stochastic models of molecular absorption noise and interference are also developed.

In Chapter 5, the low-weight channel coding technique for error prevention in nanonetworks is developed. First, the impact of the coding weight on the noise and the multi-user interference power is analyzed. Then, the performance of low-weight codes is analytically and numerically investigated.

In Chapter 6, the receiver symbol detection scheme to support the proposed pulse-based modulation and coding techniques is developed. First, the functioning and potential implementation of the CTMA-based detection mechanism is presented. Afterwards, the performance of the proposed scheme is analyzed in interference-free and interference-limited scenarios.

In Chapter 7, the joint energy harvesting and energy consumption model for perpetual nanonetworks in the Terahertz Band is developed. First, an analytical model of novel piezoelectric nano-generators developed and the energy consumption due to communication is quantized. Afterwards, the two processes are jointly analyzed.

In Chapter 8, the physical layer aware MAC protocol for nanonetworks is presented. Its performance is numerically analyzed in terms of energy consumption, end-to-end delay and throughput, by making active use of the developed channel, noise and interference models for nanonetworks in the Terahertz Band.

In Chapter 9, the multi-physics emulation framework is presented. Its implementation is explained in detail. First, the validation of the nano-antenna and the Terahertz Band channel model is performed separately in COMSOL. Afterwards, the integration of COMSOL and Matlab is explained and the complete nano-link is emulated.

Finally, in Chapter 10, the research contributions are summarized and future research directions are identified.

CHAPTER 2

GRAPHENE-BASED PLASMONIC NANO-ANTENNA FOR TERAHERTZ BAND COMMUNICATION

The first step towards enabling electromagnetic communication among nanomachines is the development of antennas suited for the expected size of nanomachines, *i.e.*, from a few nanometers up to a few micrometers at most. In this chapter, we first motivate the use of graphene to develop nano-antennas and review the existing related work. Then, we propose a novel graphene-based nano-antenna design, which exploits the behavior of SPP waves in GNRs. We follow two different approaches to analyze the frequency response of the proposed nano-antenna. First, we develop a preliminary model based on the transmission line properties of GNRs and obtain the propagation speed of SPP waves in GNRs. We then use this model to obtain the fundamental resonant frequency of the proposed plasmonic nano-antenna. Second, we develop a much more complete model by starting from the dynamic complex conductivity of GNRs and obtain the propagation constant of SPP waves in GNRs. Similarly, we then use this model to obtain the antenna frequency response.

2.1 Motivation and Related Work

The miniaturization of a classical metallic antenna to meet the size requirements of nanomachines would impose the use of very high radiation frequencies. For example, a one-micrometer-long dipole antenna would resonate at approximately 150 THz. The available transmission bandwidth increases with the antenna resonant frequency, but so does the propagation loss. Due to the very limited power of nanomachines [152], the feasibility of nanonetworks would be compromised if this approach were followed. In addition, it is not clear how a miniature transceiver could be engineered to operate at these very high frequencies. Moreover, intrinsic material properties of common metals remain unknown at the nanoscale [15, 46] and, thus, common assumptions in antenna theory, such as the ideal perfect electric conductor (PEC) behavior of the antenna building components, might not hold in this realm.

Alternatively, the unique properties of nanomaterials can be exploited to develop novel miniature antennas and transceivers which are expected to operate at much lower frequencies. Amongst others, graphene has recently attracted the attention of the scientific community due to its unique electrical and optical properties. The interaction of EM radiation with graphene and its derivatives, *i.e.*, CNTs and GNRs, differs from that with conventional metals. For example, the complex dynamic surface conductivity of graphene-based nano-structures has been thoroughly investigated in many recent works for DC as well as for frequencies ranging from the Terahertz Band to the optical spectral band [30, 126, 105, 43, 44, 34, 33]. In particular, it has been shown that it drastically changes with the dimensions or the chemical potential. For example, the infrared surface conductivity of infinitely large two-dimensional graphene sheets at zero chemical potential has been found to be essentially independent of frequency and equal to $\sigma_0 = \pi e^2/2h \approx 10^{-4}$ S, where e refers to the electron charge and h refers to the Planck constant. More interestingly, it has been recently shown that the lateral confinement of electrons in semi-finite-size GNRs enhances the surface conductivity of graphene in the Terahertz Band [52, 119].

Resulting from its peculiar surface conductivity, it has been theoretically and experimentally shown that graphene nano-structures support the propagation of SPP waves at frequencies in the Terahertz Band [53, 29, 142, 84, 68, 61, 90]. SPP waves are confined EM waves coupled to the surface electric charges at the interface between a metal and a dielectric material. Many metals support the propagation of SPP waves, but usually at very high frequencies (*e.g.*, near-infrared and optical frequency bands). In addition, the propagation of SPP waves even on noble metals, which are considered the best plasmonic materials [156], exhibit large Ohmic losses and cannot be easily tuned. On the contrary, SPP waves on graphene have been observed at frequencies as low as in the Terahertz Band and, in addition, these can be easily tuned by material doping.

Starting from these properties, a few nano-antenna designs have been proposed. In [15], a mathematical framework to analyze the performance of CNTs as nano-dipole antennas was developed, by obtaining the transmission line properties of CNTs. In [46], the frequency response and radiation efficiency of CNT-based nano-dipole antennas was compared to those of classical metallic thin-wire nano-dipole antennas. The main outcome from these two analyses is that the propagation of EM waves in CNT-based nano-dipole antennas is governed by the behavior of SPP waves in CNTs and, thus, the EM-wave propagation speed in CNTs can be up to one hundred times below the EM-wave propagation speed in the free-space. As a result, the resonant frequency of CNT-based nano-dipole antennas can be up to two orders of magnitude below that of a conventional antenna.

The possibility to operate at much lower frequencies relaxes the energy and power requirements for the nanomachines. However, due to the mismatch between the EM-wave propagation on CNTs and the EM-wave propagation in the free space, the radiation efficiency of CNT-based nano-dipole antennas can be very low. Moreover, the input impedance of CNT-based nano-dipole antennas is in the order of the quantum contact resistance (*i.e.*, several kΩ), which can drastically increase the losses in the interconnection of the nano-antenna with its driving circuitry. Similar results were discussed in [127, 88]. More recently, in [100] the authors provided a time-domain analysis of CNT-based nano-dipole antennas when transmitting very short pulses. Their simulation results are consistent with the aforementioned works, which were all conducted in the frequency domain.

The propagation of EM waves on infinitely large graphene sheets has been thoroughly analyzed [85, 86, 47, 48]. However, little research has been conducted on EM propagation in finite size GNRs, which is what is mainly needed for the design of a nano-antenna. In [23], the propagation of EM waves on GNRs was measured. The main outcome of this study is that the same quantum phenomena that affect the propagation of EM waves in CNTs still hold for GNRs and, moreover, can be easily tuned by modifying the GNR edge structure and width. In addition, the planar nature of GNRs, when compared to the cylindrical structure of CNTs, simplifies their integration with other nanomachines components such as the transceiver. All these motivate the further investigation of graphene-based nano-structures as novel nano-antennas for EM communication among nanomachines.

2.2 Working Principle

The conceptual design of the proposed graphene-based plasmonic nano-antenna is shown in Figure 3. The nano-antenna is composed of a GNR (the active element), mounted over a metallic flat surface (the ground plane), with a dielectric material layer in between, which is used both to support the GNR as well as to change its chemical potential by means of material doping. In the complete model, an ohmic contact or a mechanism to feed the antenna is necessary. However, the design of adequate feeding mechanisms for nano-antennas remains an open challenge and is outside of the scope of this work.

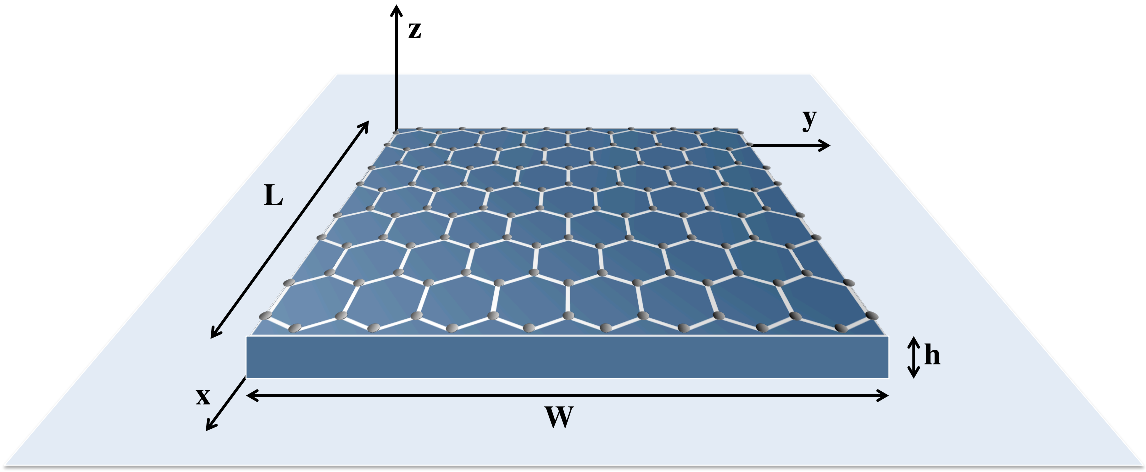

Figure 3. Proposed GNR-based nano-patch antenna.

The working principle of the proposed plasmonic nano-antenna is as follows. For simplicity, we explain first the device functioning in reception. Consider an incident EM plane wave, $\vec{E}_{inc}$, given by

$$\vec{E}_{inc}\left(z,t\right) = E_0 e^{\mathrm{i}(-k_1 z+\omega t)}\hat{\alpha}, \tag{1}$$

where E_0 is the field amplitude, k_1 is the propagation constant in medium 1 (above the GNR), $-z$ is the propagation direction (perpendicular to the GNR, see Figure 3), ω is the angular frequency, t stands for time and $\alpha = x, y$ is the wave polarization. When $\vec{E}_{inc}$ irradiates the antenna, it excites the free electrons on the graphene layer. At the interface between the graphene layer and the dielectric material layer, SPP waves are excited. The propagation properties of the SPP waves depend on the size, temperature and chemical potential of the GNR. By exploiting the high mode compression factor of SPP waves in GNRs, novel graphene-based plasmonic nano-antennas can be developed.

Similarly, according to the antenna reciprocity theorem [8], the behavior of the nano-antenna in transmission can similarly be explained as follows. Consider a time-varying electric current, $\vec{J}$,

$$\vec{J}(z, t) = J_0 e^{\mathrm{i}\omega t} \delta\,(z - h)\,\hat{\alpha} \tag{2}$$

where J_0 is the current amplitude, ω is the angular frequency, t stands for time, δ stands for the Dirac delta function, h is the z coordinate of the GNR, *i.e.*, the separation between the ground plane and the GNR itself, and corresponds to the feeding point (see Figure 3), and $\alpha = x, y$ is the current direction. When $\vec{J}$ excites the graphene layer, an SPP wave is generated at the interface with the dielectric material layer. If the length of the graphene patch corresponds to integer number of half *plasmon wavelengths*, λ_{spp}, the plasmonic antenna resonates, and the antenna radiated EM field is maximized. Ultimately, the frequency response and efficiency of nano-antennas depends on the properties of SPP waves, which on their turn depend on the electrical properties of the GNRs.

Plasmonic nano-antennas differ largely from classical metallic antennas. The main differences between plasmonic nano-antennas and metallic antennas are summarized as follows:

- **Finite Complex Conductivity:** In classical antenna theory, a common assumption is to model the material of the antenna building components as Perfect Electrical Conductor (PEC), *i.e.*, as a material with infinite conductivity, $\sigma_{PEC} \rightarrow \infty$. This assumption simplifies the analytical study of the antenna by forcing the field inside the antenna $\vec{E}^{in}$ to be zero. If the field were non-zero, the current inside the antenna would tend to infinite, $\vec{J}^{in} \rightarrow \infty$, as defined by the Ohm's law. Since infinite currents are not allowed, $\vec{E}^{in}$ is required to be zero. On the contrary, a finite complex conductivity is required for the propagation of SPP waves, as will be shown in Section 2.4. Moreover, this conductivity drastically changes with the temperature, size or chemical potential of the material.

- **Plasmonic Current Wave:** In classical antenna theory, the electrical current wave traveling along a PEC antenna propagates at the speed of light in vacuum c_0 with wave vector k_0. On the contrary, the electrical current wave traveling along a plasmonic antenna propagates at the much lower SPP wave propagation speed with wave vector k_{spp}. Moreover, it is analytically proven in [25], that a plasmonic nano-antenna cannot support an additional current which propagates with k_0. This much slower propagation of the current wave is what allows the reduction of the physical antenna size in accordance with the SPP wave compression factor, as will be shown in Section 2.4.2. The wave vector of SPP waves depends strongly on the type of SPP modes and the size and chemical potential of the plasmonic nano-structure.

As a result of these two main differences, many other implications affect the design of plasmonic nano-antennas. For example, in classical antenna theory, when considering PEC materials, the resonant frequency of the fundamental dipole antenna depends only its length. However, for a plasmonic antenna, the resonant frequency of a nanowire-based dipole antenna, depends also on the temperature, chemical potential or radius of the wire, due to the impact of these parameters in its conductivity [25]. This can be extrapolated to other types of plasmonic nano-antennas [32, 73, 79].

In this remainder of this chapter, we analytically and numerically model the proposed graphene-based plasmonic nano-antenna. We follow two different methodologies to analyze the frequency response of the proposed plasmonic nano-antenna. First, we compute the transmission line properties of GNRs and obtain the SPP wave propagation speed (Section 2.3). We then use this magnitude to obtain the fundamental resonant frequency of the antenna. Second, in a much more complete analysis, we develop a novel complex conductivity model for GNRs and use this model to investigate the propagation constant of SPP waves in GNRs (Section 2.4). Similarly, we then utilize this magnitude to obtain the frequency response of the proposed graphene-based plasmonic nano-antenna.

2.3 Transmission-line-based Analysis

In this section, we model the proposed graphene-based plasmonic nano-antenna starting from the transmission line properties of GNRs, which are obtained by means of tight-binding modeling. Two types of GNRs are considered in our analysis according to their edge structure, namely, zigzag GNRs (ZGNRs) and armchair GNRs (AGNRS) (Figure 2.3). First, the electronic band-structure of GNRs is obtained. Then, the quantum resistance, quantum capacitance, kinetic inductance and total line impedance of GNRs are computed as functions of the GNR edge, width and chemical potential. Second, starting from these, we compute the SPP-wave propagation speed in GNRs. Finally, the antenna frequency response is obtained by modeling the nano-structure as a resonant plasmonic cavity.

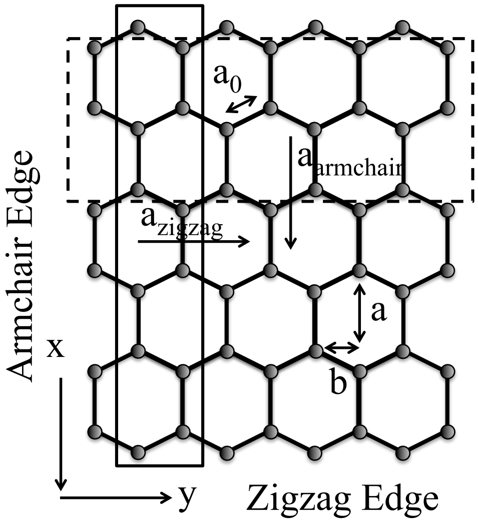

Figure 4. Lattice structure of a graphene sheet.

2.3.1 Transmission Line Properties of Graphene Nanoribbons

2.3.1.1 Electronic Band-structure of Graphene Nanoribbons

The electronic band-structure of GNRs describes the energy states that an electron is allowed to have. This is obtained by solving the Schrödinger equation, which in its time-independent form can be written as [20]:

$$\left(-\frac{\hbar^2}{2m_0}\nabla^2 + U(\vec{r})\right)\psi(\vec{r}) = E\psi(\vec{r}), \tag{3}$$

where $\hbar$ is the reduced Plank's constant, m_0 is the electron mass, U stands for the potential energy of an electron at position $\vec{r} = (x, y, z)$, ψ is the wave-function describing the energy of an electron located at position $\vec{r}$, and E refers to the total energy that an electron has. Alternatively, the Schrödinger equation can be written using matrix notation as follows:

$$[H]\{\psi\} = E\{\psi\}, \tag{4}$$

where $[H]$ stands for the Hamiltonian matrix of the system, E is the electron energy and $\{\psi\}$ is the vectorial form of the electron wave-function. Solving the Schrödinger equation stands for obtaining a set of eigenfunctions ψ and eigenenergies E that satisfy (4) for fixed boundary conditions.

In order to simplify the complexity of analyzing an atomically large structure, we use the *tight-binding model* [21] and exploit the symmetry of GNRs. By means of tight-binding modeling, the complexity of solving the Schrödinger equation for the entire system is reduced to that of solving the matrix equation for a smaller structure or *unit cell* that can generate the entire GNR. This unit cell depends on the edge structure along the main axis of the GNR. For a ZGNR, the set of atoms that compose a possible unit cell is marked in Figure 2.3 using a solid line. This unit cell can reproduce an entire ZGNR by using a vector parallel to the y axis. Similarly, a unit cell that can reproduce an entire AGNR by using a vector parallel to the x axis is shown by using a dotted line.

The Hamiltonian matrix $[H]$ in (4) for the GNR is written as

$$[h(k)] = \sum_m H_{n,m} e^{i\vec{k}\cdot\left(\vec{d}_m - \vec{d}_n\right)}, \tag{5}$$

where $H_{n,m}$ is the individual Hamiltonian matrix accounting for the interactions of a unit cell with itself ($n = m$) and its neighboring cells ($n \neq m$), $\vec{k}$ is the wavevector of the solution to the Schrödinger equation, and $\vec{d}_m - \vec{d}_n$ defines a vector in the direction in which the unit cell is moved to reproduce the structure. In our analysis, we consider a single level of electrons at each carbon atom (S-orbitals). We also consider that only the nearest neighbors to an atom, located at a distance equal to the graphene lattice constant a_0=0.142 nm, interact with it. We refer to this interaction as $t \approx 3$ eV. For a ZGNR, (5) becomes

$$[h^z(k)] = H^z_{n,n} + H^z_{n-1,n} e^{ik_y 2b} + H^z_{n+1,n} e^{-ik_y 2b}, \tag{6}$$

and, similarly, for an AGNR, (5) can be written as

$$[h^a(k)] = H^a_{n,n} + H^a_{n,n-1} e^{ik_x 2a} + H^a_{n,n+1} e^{-ik_x 2a}. \tag{7}$$

The standard procedure to obtain the individual Hamiltonian matrixes can be found in [21].

The electronic band-structure of the device under analysis can be now obtained by solving (6) or (7) in (4) for a ZGNR and an AGNR, respectively. The Brillouin zone, *i.e.*, the area of interest in the wavevector domain, is the region defined as $-\pi \leq k_y 2b \leq \pi$ for a ZGNR and $-\pi \leq k_x 2a \leq \pi$ for an AGNR [21]. The points of interest in a band-structure are those for which the energy bands are close to zero, as those are the first states to be occupied when the energy of the GNR is increased.

In Figure 5(a), the electronic band-structure of a ZGNR with a width W =2.52 nm is shown as a function of the wavevector $\vec{k}$. A ZGNR has always a metallic behavior independently of its dimensions, *i.e.*, there is always at least one conducting band even for a Fermi energy equal to zero [13]. On the contrary, an AZGNR can be either metallic or semiconducting depending on its width. In Figure 5(b) and 5(c), the band-structure of a metallic AGNR and that of a semiconducting AGNR are illustrated, respectively.

2.3.1.2 Number of Conducting Bands

The number of conducting bands in the GNR depends on the Fermi energy, the temperature of the system, and the GNR width and edge geometry. In Figure 6(a), the number of

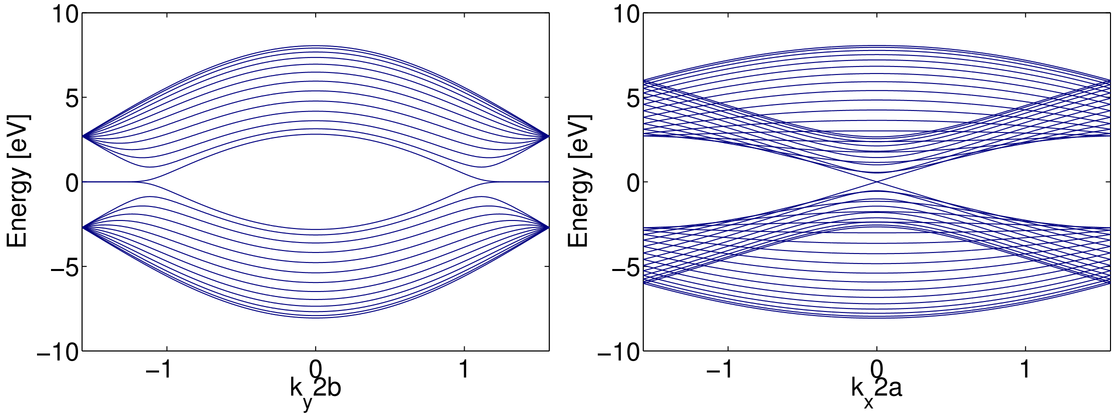

(a) ZGNR, W=2.52 nm (b) AGNR, W=2.52 nm

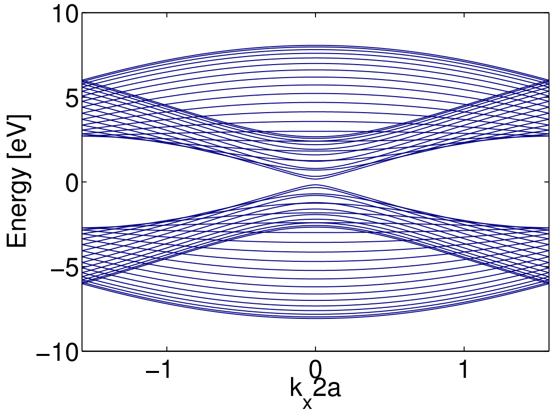

(c) AGNR, W=2.73 nm

Figure 5. Energy band-structure of different types of GNR.

conducting bands both in a ZGNR and an AGNR are shown as functions of their width for different Fermi energies. For a fixed Fermi energy and temperature, the number of conducting bands increases with the GNR width because the separation among bands is reduced. For the same size, the number of conducting bands in an AGNR is similar to that of a ZGNR, and in both cases it increases with the energy that is being considered for the system. The number of conducting bands plays an important role in the transmission line properties of GNRs, as we discuss next.

2.3.1.3 Quantum Resistance

Despite GNRs show almost ballistic transport of electrons for lengths in the order of a few micrometers [27, 141], the contact resistance of GNRs is not negligible. For a very thin

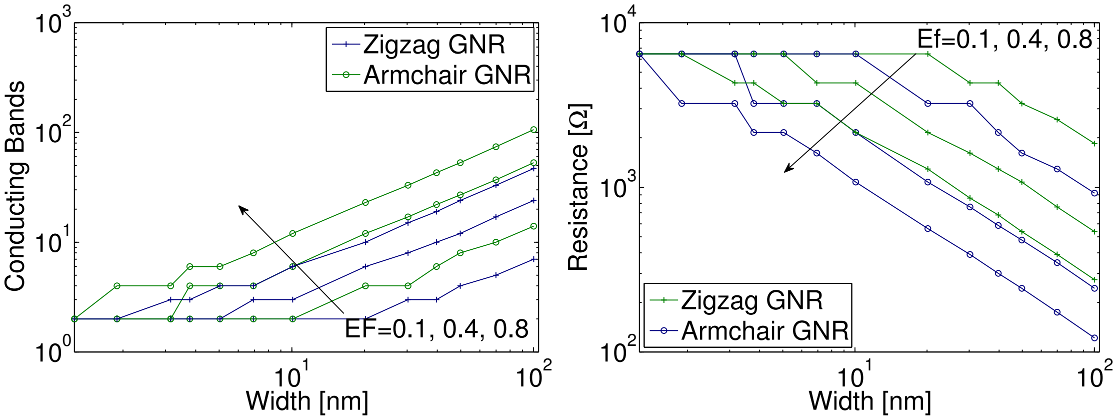

(a) (b)

Figure 6. (a) Number of conducting bands and (b) quantum resistance of a ZGNR and an AGNR as functions of their width.

GNR with only one occupied band, the quantum or contact resistance $\mathcal{R}_Q$ is given by [20]

$$\mathcal{R}_Q = \frac{h}{2e^2} \approx 12.9\ k\Omega, \tag{8}$$

where h is the Planck constant, e stands for the electron charge, and there is a factor of 2 accounting for the electron spin [1]. As the number of conducting bands increases (either because a wider GNR is considered or because the Fermi energy or GNR temperature are increased), the resistance becomes

$$\mathcal{R} \approx \frac{h}{2e^2 M}, \tag{9}$$

where M refers to the number of conducting bands. In Figure 6(b), the total resistance of a ZGNR and an AGNR are plotted as functions of the width for different Fermi energies at $T = 0$ K. The resistance rapidly decreases with the GNR width as well as with the Fermi energy, because the number of conducting bands increases with these two magnitudes.

2.3.1.4 Kinetic Inductance

GNRs show a very high inductance related to the kinetic energy of moving electrons in quantum systems. Moving electrons oppose to the changes in the direction of an alternating current. In addition, due to the Pauli Exclusion Principle [20], moving electrons can only occupy empty energy states. This additional energy is conventionally captured with the

---

[1] That property of an electron which gives rise to its angular momentum about an axis within the electron.

kinetic inductance. For a very thin GNR, with only one occupied energy band, the kinetic inductance per unit length is given by [11]

$$\mathcal{L}_{\mathcal{K}} = \frac{h}{4 v_F e^2}, \tag{10}$$

where h is the Planck constant, e stands for the electron charge and v_F is the Fermi velocity or electron group velocity, which is given by

$$v_F = \frac{1}{\hbar}\frac{dE}{dk}, \tag{11}$$

where $\hbar$ is the reduced Planck constant, E is the energy and k stands for the wavenumber. When the number of conducting band increases, the total kinetic inductance per unit length becomes

$$\mathcal{L}_{\mathcal{K}}{}^{T} = \left(\sum_{n=1}^{M} (\mathcal{L}_{\mathcal{K}}{}^{n})^{-1} \right)^{-1}, \tag{12}$$

where the contribution of the bands is accounted by considering the bands as a set of inductors in parallel. In Figure 7(a), the kinetic inductance per unit length of a ZGNR and an AGNR are shown as functions of the width for different Fermi energies. By increasing the GNR width or the Fermi energy, the total kinetic inductance decreases.

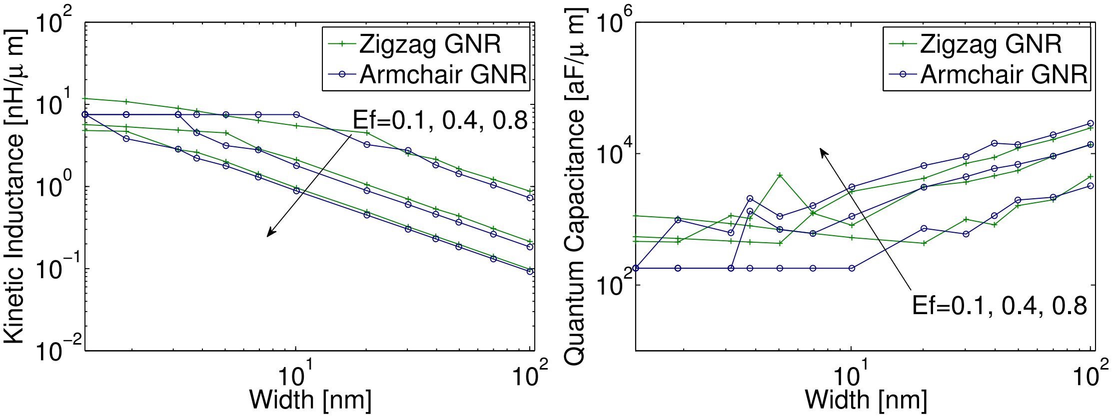

(a) (b)

Figure 7. (a) Kinetic inductance and (b) quantum capacitance of a ZGNR and an AGNR as functions of their width.

2.3.1.5 *Quantum Capacitance*

To add electric charge in a GNR, one must add electrons to the available quantized states above the Fermi level, again due to the Pauli Exclusion Principle. This extra energy is modeled by using an equivalent quantum capacitance per unit length. For a very thing GNR with only one conducting band, this is given by [11]

$$C_Q = \frac{4e^2}{hv_F}, \tag{13}$$

where h is the Planck constant, e is the electron charge and v_F is the Fermi velocity or electron group velocity (11). If there are several conducting bands, the total quantum capacitance per unit length can be obtained as

$$C_Q{}^T = \sum_{n=1}^{M} C_Q{}^n, \tag{14}$$

where the contribution from the different bands is accounted by considering the bands as a set of capacitors in parallel. Therefore, when increasing the GNR width or the system energy, the quantum capacitance increases. This is shown in Figure 7(b), where the quantum capacitance per unit length of a ZGNR and an AGNR are shown as functions of the width for different Fermi energies.

2.3.1.6 *Line Impedance*

In the proposed antenna design, the GNR is placed above a ground plane with a dielectric layer in between. Therefore, there are two additional terms to take into account: the electrostatic capacitance and the magnetic inductance. The former can be obtained by recalling the expression for the capacitance of a parallel plaques capacitor

$$C_E = \epsilon \frac{W}{d}, \tag{15}$$

where ϵ stands for permittivity of the material between the GNR and the ground plane, W is the GNR width and d refers to the separation between the GNR and the ground plane. We consider the ratio between W and d constant. The total capacitance per unit length is

$$C = \left(\frac{1}{C_E} + \frac{1}{C_Q{}^T} \right)^{-1}, \tag{16}$$

where it has been taken into account that the electrostatic and the quantum capacitances are in series. As discussed before, the quantum capacitance increases with width and energy, thus, the much smaller electrostatic capacitance dominates the parallel equivalent circuit of both capacitors. This is shown in Figure 8(a), in which the total capacitance per unit length of a ZGNR and an AGNR are shown as functions of the width for different Fermi energies.

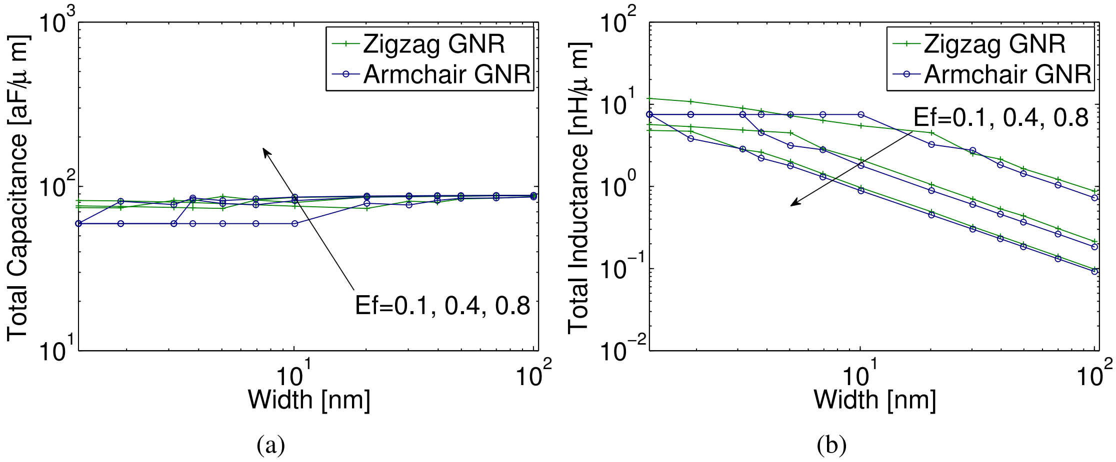

Figure 8. (a) Total capacitance per unit length and (b) total inductance per unit length of a ZGNR and an AGNR as functions of their width.

The magnetic inductance can be obtained from the following relation:

$$\frac{1}{\sqrt{\mathcal{L}_m C_E}} = \frac{c_0}{\sqrt{\epsilon_r}} = v_{p0}, \tag{17}$$

where c_0 is the speed of light in vacuum and ϵ_r stands for the relative permittivity of the material between the GNR and the ground plane. The total inductance per unit length is

$$\mathcal{L} = \mathcal{L}_m + \mathcal{L}_{\mathcal{K}}{}^T, \tag{18}$$

where we have taken into account that the magnetic and the kinetic inductances are in series. As discussed above, the kinetic inductance of a nano-structure decreases with its width and the system energy. Thus, the total inductance of the system decreases with the GNR width and the system energy. This can be seen in Figure 8(b), where the total inductance per unit length is plotted as a function of the GNR width for different Fermi energies. The resulting transmission line model of GNRs is illustrated in Figure 9(a). Note that while the different inductances and capacitances are distributed values, the quantum resistance only appear in the contacts of the GNR.

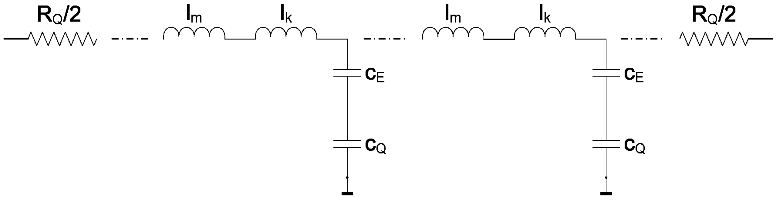

(a)

Figure 9. Equivalent transmission line model GNRs.

2.3.2 Surface Plasmon Polariton Wave Propagation Speed

The propagation speed of SPP waves in GNRs, based on the transmission line model, is given by

$$v_p = \frac{1}{\sqrt{\mathcal{L}C}}, \tag{19}$$

where C refers to the total capacitance per unit length in (16) and $\mathcal{L}$ stands for the total inductance per unit length obtained in (18).

In Figure 10, the SPP-wave propagation speed is shown as a function of the GNR width for different Fermi energies. For a very thin GNR, where only a few energy bands are conducting, the speed is 100 times below the speed of light in vacuum. As the GNR becomes wider, the speed tends to that of an EM wave propagating in a dielectric material with relative permittivity ϵ given by (17). A similar reasoning can be applied when thinking of different Fermi energies of the system. The behavior of both ZGNRs and AGNRs is almost the same, which relaxes the accuracy requirements on the fabrication process. For thin GNRs, with only one conducting band, these results agree with that of CNTs in [15].

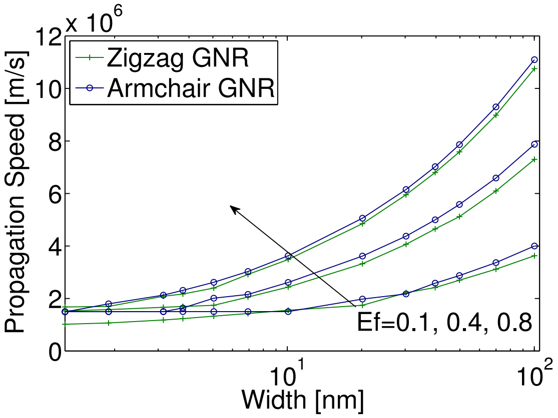

Figure 10. SPP-wave propagation speed in a ZGNR and an AGNR as a function of their width.

2.3.3 Antenna Frequency Response

We model our proposed graphene-based nano-antenna as a *plasmonic nanostrip antenna* [129, 150]. At the microscale, microstrip antennas (also known as planar antennas or printed antennas) have been widely used in many applications due to their simple manufacture, compatibility with planar circuitry, low profile, planar structure, and unidirectional radiation. For example, patch antennas, *i.e.*, rectangular microstrip antennas, are some of the most common antennas in current mobile devices for communications and radar applications.

The two dimensional nature of graphene makes it, at least intuitively, a perfect candidate to port the advantages of microstrip antennas to the nanoscale. Contrary to carbon nanotube-based antennas [15, 46] or nano-wire-based antennas [25], the planar geometry of graphene is supposed to ease the integration of nano-antennas in advanced nano-devices with diverse applications, such as, biological and chemical nanosensor networks [2] or optical interconnects in advanced multi-core computing architectures.

In order to analyze the frequency response of nano-strip antennas, we model the graphene-based heterostructure composed of the GNR, the dielectric material and the ground plane, as a *plasmonic resonant cavity*. This imposes a condition of the GNR length L for the antenna to resonate. Up to this point, we have analyzed the impact of the finite width W of the GNR on its transmission line properties and the SPP-wave propagation speed, while considering the length L of the GNR to tend to infinite or, at least, to satisfy

$$L \gg W \gg h, \tag{20}$$

where h is the dielectric high. However, for the plasmonic nano-antenna to resonate, there is an additional constraint on the AGNR length, which depends on the type of SPP modes propagating along the antenna.

Following the potential vector approach as in [8], for a nano-patch antenna with $L > W \gg h$, the first resonant frequency of the cavity for SPP-waves propagating along the GNR edge is given by

$$f_{r0} = \frac{v_p}{2L}, \tag{21}$$

where v_p is the EM-wave propagation speed along the GNR (19) and L is the GNR length. From Figure 10, for a fixed antenna length, when the GNR width is increased, the EM-wave propagation speed in the GNR tends to $c_0/\sqrt{\epsilon_r}$. As a result, the resonant frequency increases with the GNR width. For example, as shown in Figure 11, for a nano-patch antenna with a total length $L = 1\mu$ m, the resonant frequency varies between 500 GHz and 4 THz depending on the GNR width and edge geometry, when the Fermi energy of the system is 0.4 eV. These preliminary results are consistent with the analytical and experimental results related to SPP waves in graphene recently reported in [53, 29, 142, 84, 68, 61, 90], and will be further validated in the next section.

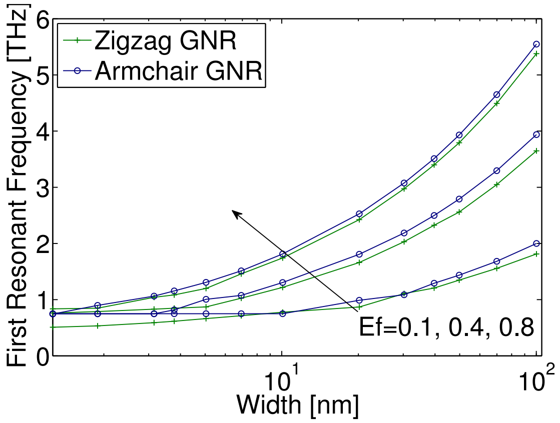

Figure 11. First resonant frequency of the proposed GNR-based nano-patch antenna.

2.4 Dynamic-conductivity-based Analysis

In this section, we develop a much more accurate model of the proposed graphene-based plasmonic nano-antennas, by starting from the dynamic conductivity of GNRs. First, we analytically and numerically investigate the conductivity of GNRs. We focus on AGNRs only, but a similar study can conducted for ZGNRs. For this, first, we recall the closed-form expression for the electronic band-structure and the electron wave functions of AGNRs, and then we use the Kubo formalism to study the conductivity of AGNRs as a function of their width and chemical potential. Afterwards, we make use of the conductivity to analyze the propagation properties of SPP waves in AGNRs. Finally, we obtain the antenna frequency response for different resonant modes.

2.4.1 Dynamic Conductivity of Graphene Nanoribbons

2.4.1.1 Electronic Band-structure and Electron Wave Functions

The electronic band-structure ε in electron-volts (eV) of an AGNR can be written in closed-form expression as [146]

$$\varepsilon^{s}(k,\theta) = st\sqrt{1 + 4\cos^{2}\theta + 4\cos\theta\cos\left(\frac{kb}{2}\right)}, \tag{22}$$

where s is the band index ($s = 1$ for the conduction band, $s = -1$ for the valence band), $t \approx 3$ eV is the nearest-neighbor atom interaction in the tight-binding model of graphene, k and θ are the wave vectors parallel and perpendicular to the AGNR edge, respectively, and $b = 3a_o$, where $a_0 = 0.142$ nm is the graphene lattice constant. The Brillouin zone, *i.e.*, the area of interest in the wave vector domain, is the region defined by the values of $kb \in [0, \pi)$ and $\theta \in (0, \pi)$. The conduction and the valence bands touch at the point $(k, \theta) = (0, 2\pi/3)$, which is referred to as the Dirac point.

Due to the finite width W of the AGNR, the values of θ are quantized. In particular, by defining the AGNR width as $W = \sqrt{3}/2a_0(N-1)$, with N being the number of single-atom columns across the AGNR width (see Figure 12(a)), the values of θ are given by

$$\theta_n = \frac{n\pi}{N+1}, \tag{23}$$

where $n = 1, 2, ..., N$ stands for the band index. By considering the GNR length L much larger than its width, the wave vector k is treated as a continuous variable. In our analysis, L is in the order of several hundreds of nanometers and up to one micrometer, and $L \gg W$.

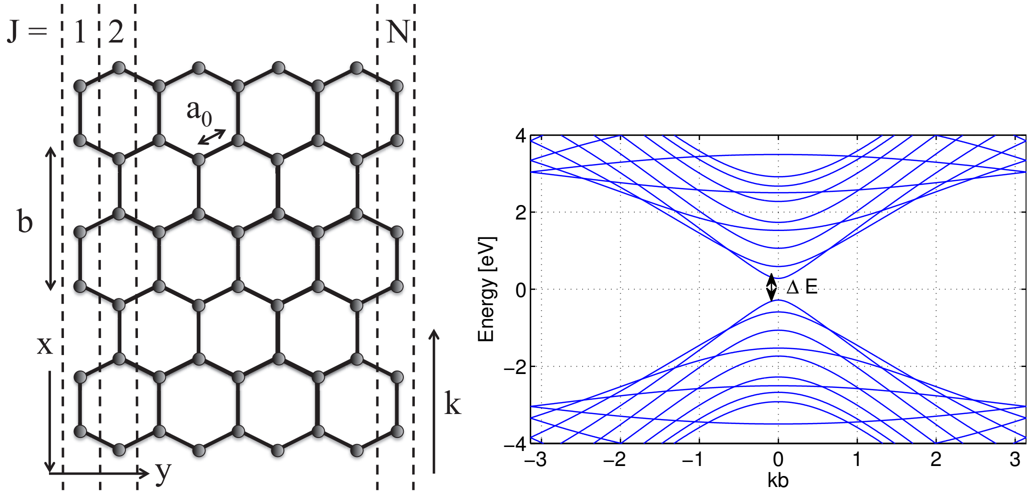

Figure 12. Lattice structure of an AGNR (left) and electronic band-structure an AGNR with $N = 18$ **(**$\Delta E = 0.56$ **eV).**

The wave functions Φ_J^s in an AGNR are given by [121]

$$\phi_J^s(k, \theta_n) = \frac{1}{\sqrt{N}} e^{-ik\frac{b}{2}(J-1)} \sin J\theta_n \begin{pmatrix} e^{-i\Theta(k,\theta_n)} \\ s \end{pmatrix}, \tag{24}$$

where $J = 1, 2, ..., N$ is the single-atom column index across the AGNR width (see Figure 12(a)) and Θ is the polar angle between k and θ_n defined with respect to the Dirac point and it is given by

$$\Theta(k, \theta_n) = \text{atan}\left(\frac{kb}{\theta_n - \frac{2\pi}{3}}\right), \tag{25}$$

where atan refers to the inverse trigonometric tangent function and θ_n is defined as in (23).

In Figure 12(b), the electronic band-structure ε of an AGNR, given by (22), with width $W \approx 2.1$ nm ($N = 18$) is shown. For this width, the AGNR has a semi-conducting behavior, *i.e.*, there is a gap between the valence and the conduction bands. This is the same behavior that we described in Section 2.3.1. The energy bandgap ΔE in AGNRs depends on N and is given in eV by

$$\Delta E = \begin{cases} 0, & N = 3m-1, \\ -2t\left[1+\cos\left(\frac{2m+1}{3m+1}\pi\right)\right], & N = 3m, \\ -2t\left[1+\cos\left(\frac{2m+1}{3m+2}\pi\right)\right], & N = 3m+1, \end{cases} \tag{26}$$

where $m = 1, 2, ...$ As we show next, the energy bandgap ΔE plays a major role in the conductivity of thin AGNRs. In the rest of this chapter, we use the following nomenclature for simplicity: $\varepsilon_n^s = \varepsilon^s(k, \theta_n)$, $\Theta^n = \Theta(k, \theta_n)$.

2.4.1.2 Analytical Study of the Dynamical Complex Conductivity

The dynamical complex conductivity of AGNRs is computed next by means of the Kubo formalism. Following the procedure described in [119, 52], and contrary to many existing conductivity analysis which are only valid for infinitely large graphene sheets [105, 43, 44, 34, 33, 132], we do not make any simplifying assumption on the electronic band-structure of AGNRs, temperature or chemical potential. Simply stated, we compute the conductivity by counting all the allowed electron transitions in the electronic band-structure.

The dynamical complex conductivity σ of AGNRs depends on the polarization of the incident electromagnetic field ($\alpha = x, y$), and it is given by

$$\sigma_{\alpha\alpha}(f) = \mathrm{i}\frac{\hbar e^2}{S} \sum_{s,s'} \sum_{n,m} \int_k \frac{\left(n_F(\varepsilon_m^{s'}) - n_F(\varepsilon_n^s)\right)}{(\varepsilon_n^s - \varepsilon_m^{s'})} \frac{\left|\langle \phi_m^{s'} | v_\alpha | \phi_n^s \rangle\right|^2}{(\varepsilon_n^s - \varepsilon_m^{s'} + hf - \mathrm{i}\nu)} dk, \tag{27}$$

where f stands for frequency in Hz, $\hbar$ is the reduced Planck constant in eV·s, e is the electron charge in C, S is the area of the reference unit structure [6], $\{s, s'\}$ stand for band indexes, $\{n, m\}$ refer to the sub-bands indexes, k is the wave vector parallel to the AGNR edge, n_F is the Fermi-Dirac distribution given by

$$n_F(\varepsilon) = \frac{1}{1 + e^{\frac{\varepsilon - \mu}{k_B T}}}, \tag{28}$$

where μ is the chemical potential in eV, k_B is the Boltzmann constant in eV/K, and T stands for the temperature in K. $\langle \phi_m^{s'} | v_\alpha | \phi_n^s \rangle$ is the matrix element of the α component of the velocity operator for the transition from the energy state $\{s, n\}$ to the energy state $\{s', m\}$. The matrix elements are classified into inter-band transitions ($s \neq s'$) and intra-band transitions ($s = s'$). The matrix elements of velocity operator for intra-band transitions in AGNRs are obtained in [119, 120], and are given by

$$\langle \phi_m^c | v_x | \phi_n^c \rangle = \begin{cases} 0, & m - n \in \text{ even}, \\ -\mathrm{i}\frac{2}{\pi}\frac{v_F}{m-n}\langle \varsigma_x \rangle_{m,n} & m - n \in \text{ odd}, \end{cases} \tag{29}$$

$$\langle \phi_m^c | v_y | \phi_n^c \rangle = \delta_{m,n} v_F \langle \varsigma_y \rangle_{m,n}, \tag{30}$$

where $v_F = tb/(2\hbar)$ is the Fermi velocity, $\delta_{m,n}$ refers to the Kronecker delta, and $\langle \varsigma_\alpha \rangle$ ($\alpha = x, y$) stands for the Pauli matrixes, whose elements are given by

$$\langle \varsigma_x \rangle_{m,n} = \frac{1}{2}\left(e^{\mathrm{i}\Theta^m} + e^{-\mathrm{i}\Theta^n}\right), \langle \varsigma_y \rangle_{m,n} = \frac{-\mathrm{i}}{2}\left(e^{\mathrm{i}\Theta^m} + e^{-\mathrm{i}\Theta^n}\right), \tag{31}$$

and the polar angle Θ^n is defined in (25). Similarly, the matrix elements of velocity operator for inter-band transitions in AGNRs are given by

$$\langle \phi_m^c | v_x | \phi_n^v \rangle = \begin{cases} 0, & m - n \in \text{ even}, \\ -\frac{2}{\pi}\frac{v_F}{m-n}\langle \varsigma_y \rangle_{m,n} & m - n \in \text{ odd}, \end{cases} \tag{32}$$

$$\langle \phi_m^c | v_y | \phi_n^v \rangle = \delta_{m,n} v_F \langle \varsigma_x \rangle_{m,n}. \tag{33}$$

The details to derive (29), (30), (32) and (33) are given in [119]. Finally, the parameter ν in (27) refers to the inverse of the relaxation time. Note that in (27), when $s = s'$ and $m = n$, both the numerator and the denominator vanish. However, by using the Taylor expansion of the Fermi-Dirac distribution function, we can rewrite (27) for this specific case as

$$\sigma_{\alpha\alpha}(f) \approx \mathrm{i}\frac{\hbar e^2}{S}\sum_{s,s'}\sum_{n,m}\int_k \frac{e^{\frac{\varepsilon_m^{s'} - \mu}{k_B T}} n_F(\varepsilon_m^{s'}) n_F(\varepsilon_n^s)}{k_B T} \frac{\left|\langle \phi_m^{s'} | v_\alpha | \phi_n^s \rangle\right|^2}{(\varepsilon_n^s - \varepsilon_m^{s'} + hf - \mathrm{i}\nu)} dk. \tag{34}$$

A semi-closed-form expression for the real part of the conductivity is given [52]. However, for the characterization of the SPP waves in AGNRs, both the real part and the imaginary part of σ are necessary. Next, we numerically study the complex conductivity of AGNRs.

2.4.1.3 Numerical Study of the Dynamical Complex Conductivity

In Figure 13, the real and imaginary parts of σ_{xx} and σ_{yy} given by (27) are plotted as functions of the frequency for three different GNR widths $W = 2.1$ nm ($N = 18$), $W = 10.1$ nm ($N = 84$) and $W = 50.0$ nm ($N = 408$), and for two different chemical potentials $\mu = 0$ eV and $\mu = 0.3$ eV, at $T = 300$ k. We use $\nu = 20$ meV, which corresponds to a relaxation time $\tau = h/\nu = 0.2$ ps, which is a conservative value.

For $W = 2.1$ nm, $\mu = 0$ eV, the conductivity, σ_{xx}, along the AGNR edge is dominated by inter-band transitions. The first peak in the real part of σ_{xx} corresponds to $f_0 = \Delta E/h$, where ΔE is the energy band gap given by (26). When the conductivity is dominated by inter-band transitions, the imaginary part of σ_{xx} is negative. The sign of the imaginary part of the conductivity plays a major role in the propagation of SPP waves, as we discuss in Section 2.4.2. When the chemical potential is $\mu = 0.3$ eV, the inter-band transitions below $f_\mu = \mu/h = 72.5$ THz disappear. This is better seen for wider GNRs. When the chemical potential is increased, a component close to 0 Hz appears due to intra-band transitions.

The conductivity, σ_{yy}, across the AGNR width, is also dominated by inter-band transitions. However, there is only one peak at a frequency above the first inter-band transition frequency f_0. This peak corresponds to an indirect inter-band transition between sub-band n in the valence band and sub-band $n-1$ in the conduction band. Note that inter-band transitions between sub-bands with $m = n$ are not allowed (32), as explained in [119]. When $\mu = 0.3$ eV, σ_{yy} is almost unaltered. Note that there is no component close to $f = 0$ Hz in this case, because the diagonal elements of the velocity operator $m = n$ are equal to 0.

The behavior of the conductivity for $W = 10.1$ nm is similar. The conductivity, σ_{xx} along the AGNR edge is dominated by inter-band transitions. The first peak appears at a much lower frequency, due to the fact that the energy band gap decreases with the AGNR width. When the chemical potential is increased, the inter-band transitions below $f_\mu = \mu/h = 72.5$ THz disappear. This turns into an increased conductivity component for $f = 0$ Hz, attributed to intra-band transitions. Note that the imaginary part of the conductivity is positive when it is mainly governed by intra-band transitions.

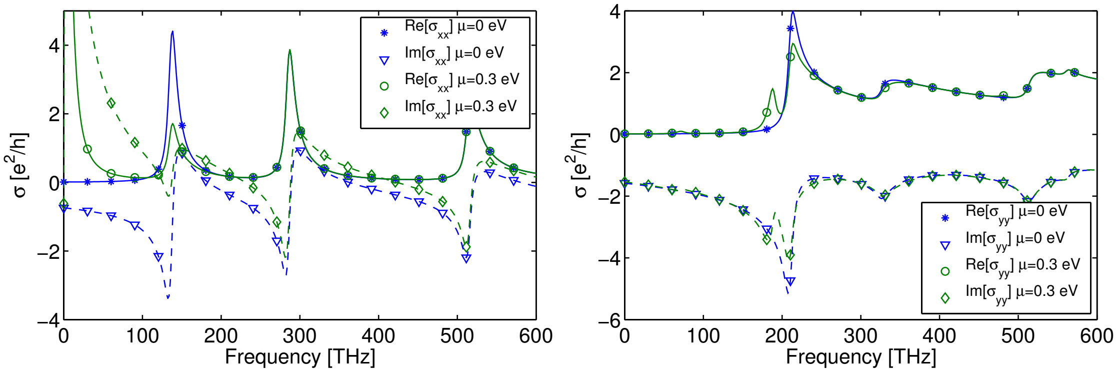

(a) σ_{xx}, W = 2.1 nm, N = 18 (b) σ_{yy}, W = 2.1 nm, N = 18

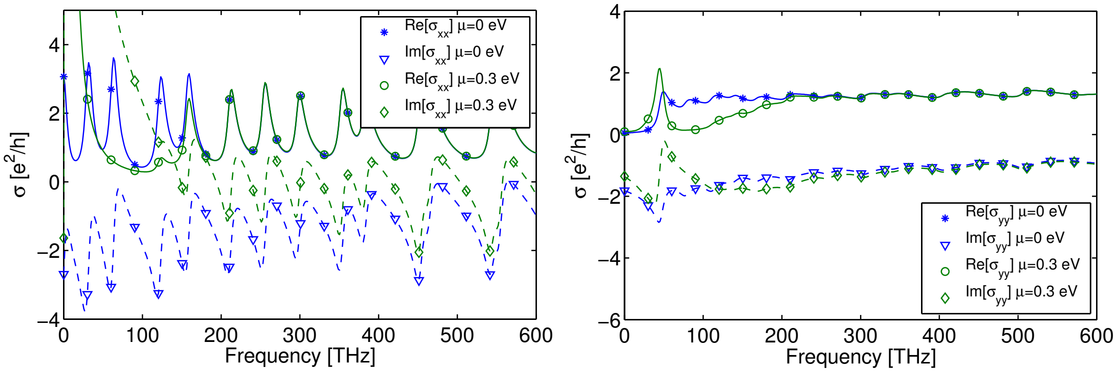

(c) σ_{xx}, W = 10.1 nm, N = 84 (d) σ_{yy}, W = 10.1 nm, N = 84

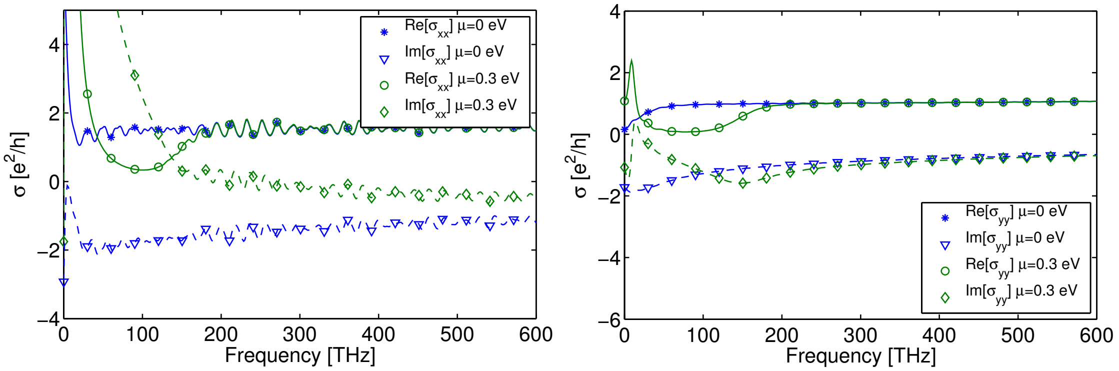

(e) σ_{xx}, W = 50.0 nm, N = 408 (f) σ_{yy}, W = 50.0 nm, N = 408

Figure 13. Conductivity of AGNRs for different polarizations and GNR widths.

Similarly, the conductivity σ_{yy} across the AGNR width is dominated by a single peak, corresponding to inter-band transitions. After that, the conductivity tends to the well-known minimum value for the optical conductivity of graphene, which further validates these numerical results. When the chemical potential is increased to μ = 0.3 eV, intra-band transitions create the peak at $f = 0$ Hz for σ_{xx}. Similarly for σ_{yy}, forward intra-band transitions create the peak at lower frequencies. Finally, a similar behavior can be observed for $W = 50.0$ nm. The conductivity σ_{xx} tends to that of infinitely large graphene sheets, and similarly occurs with σ_{yy}.

2.4.2 Surface Plasmon Polariton Wave Propagation Constant

2.4.2.1 Analytical Study

Starting from the unique conductivity of GNRs, in this section, we analytically compute the dynamic complex wave vector of SPP waves in AGNRs and numerically study their main propagation properties. The majority of existing studies [58, 68, 47, 29] are focused on infinitely large graphene sheets. Only recently in [128], the dielectric function of GNRs is utilized to investigate SPP waves in metallic AGNRs. Next, we capture the impact of the finite width of AGNRs and the chemical potential on the SPP waves.

The dynamic complex wave vector k_{spp} of SPP waves in graphene determines the propagation properties of SPP waves. k_{spp} strongly depends on the conductivity of the AGNR $\sigma_{\alpha\alpha}$ as well as the permeability μ_n and permittivity ϵ_n of the materials surrounding the AGNR. The real part of the wave vector,

$$\mathrm{Re}\{k_{spp}\} = \frac{2\pi}{\lambda_{spp}}, \tag{35}$$

determines the SPP wavelength. The imaginary part of the wave vector $\mathrm{Im}\{k_{spp}\}$ determines the SPP decay or, inversely, $1/\mathrm{Im}\{k_{spp}\}$ determines the SPP propagation length. We proceed next to compute the complex value of k_{spp}.

In reception, an α-polarized incident EM plane wave (1) excites a SPP wave mode on the AGNR, which propagates in the α direction. Two types of SPP modes can be supported by the AGNR depending on its conductivity:

- Transverse Magnetic (TM) mode: there is no magnetic field in the direction of propagation, *i.e.*, $H_\alpha = 0$.

- Transverse Electric (TE) mode: there is no electric field in the direction of propagation, *i.e.*, $E_\alpha = 0$.

TM Modes In order to determine the wave vector k_{spp} for TM modes we proceed as follows. The SPP electric field $\vec{E}$ and magnetic field $\vec{H}$ are governed by the Maxwell's equations, which can be written in their differential form as:

$$\nabla \times \vec{E} = -\mu_n \frac{\partial \vec{H}}{\partial t}, \nabla \times \vec{H} = \vec{J} + \epsilon_n \frac{\partial \vec{E}}{\partial t}, \tag{36}$$

where $\nabla \times$ is the curl operator, $\mu_n = \mu_0 \mu_n^r$ is the permeability of medium n ($n = 1$ above the AGNR, $n = 2$ below the AGNR), $\epsilon_n = \epsilon_0 \epsilon_n^r$ is the permittivity of medium n, and $\vec{J}$ is the current created by the α-component of the electric field, E_α, given by

$$\vec{J} = \sigma_{\alpha\alpha} E_\alpha \delta\left(z - h\right) \hat{\alpha}, \tag{37}$$

where $\sigma_{\alpha\alpha}$ is the AGNR conductivity given by (27) and h is the z coordinate of the AGNR.

The complex propagation index of TM modes can be found by assuming that the electric field $\vec{E}$ has the form:

$$\begin{aligned} \vec{E} &= E_1 e^{\mathrm{i}\left(k_{spp}\alpha - k_1(z-h)\right)} \hat{\alpha} + E_2 e^{\mathrm{i}\left(k_{spp}\alpha - k_1(z-h)\right)} \hat{z} \quad z \geq h, \\ \vec{E} &= E_3 e^{\mathrm{i}\left(k_{spp}\alpha + k_2(z-h)\right)} \hat{\alpha} + E_4 e^{\mathrm{i}\left(k_{spp}\alpha + k_2(z-h)\right)} \hat{z} \quad z < h, \end{aligned} \tag{38}$$

and the magnetic field $\vec{H}$ has the form:

$$\begin{aligned} \vec{H} &= H_1 e^{\mathrm{i}\left(k_{spp}\alpha - k_1(z-h)\right)} \hat{\alpha}' \quad z \geq h, \\ \vec{H} &= H_2 e^{\mathrm{i}\left(k_{spp}\alpha + k_2(z-h)\right)} \hat{\alpha}' \quad z < h, \end{aligned} \tag{39}$$

where E_1, E_2, E_3, E_4, H_1 and H_2 are constants, k_{spp} is the SPP wave vector, $\hat{\alpha}$ is the polarization direction, $\hat{\alpha}' = |\hat{\alpha} \times \hat{z}|$ and k_n is the wavector in medium n given by:

$$k_n = \frac{2\pi}{\lambda_n} = \omega \sqrt{\mu_n \epsilon_n} = \frac{2\pi f}{c_0} \sqrt{\mu_n^r \epsilon_n^r}, \tag{40}$$

where λ_n, μ_n, and ϵ_n are the wavelength, permeability and permittivity of medium n, respectively, ω stands for the angular frequency f refers to the frequency, and c_0 is the speed of light in vacuum. In the rest of the chapter, we consider $\mu_n^r = 1$ for both media ($n = 1$ is usually air, and $n = 2$ is a non-magnetic dielectric material).

By inserting (38) and (39) in (36) and solving for the boundary condition at $z = h$, which is given by,

$$H_{\alpha'}\Big|_{z=h+} - H_{\alpha'}\Big|_{z=h-} = \sigma_{\alpha\alpha} E_\alpha, \tag{41}$$

the following dispersion equation for TM SPP waves in graphene is found [58, 47, 29]:

$$\frac{\epsilon_1^r}{\sqrt{k_{spp}^2 - \frac{\epsilon_1^r \omega^2}{c_0^2}}} + \frac{\epsilon_2^r}{\sqrt{k_{spp}^2 - \frac{\epsilon_2^r \omega^2}{c_0^2}}} = -\mathrm{i}\frac{\sigma_{\alpha\alpha}}{\omega\epsilon_0}, \tag{42}$$

where all the parameters have already been defined. A closed-form solution for k_{spp} can only be obtained when considering a single isolated AGNR surrounded by air ($\epsilon_1^r = \epsilon_2^r = 1$), which is not our case. For this, we numerically study the propagation index of TM SPP waves in the next section.

TE Modes The propagation index for TE modes can be obtained by following a similar procedure to that for the TM case. In particular, first, by assuming that the magnetic field $\vec{H}$ and electric field $\vec{E}$ have a similar form to that of the electric field $\vec{E}$ in (38) and the magnetic field $\vec{H}$ in (39), second, by plugging this into the Maxwell's equations (36), and, third, by forcing the boundary condition at $z = h$, the following dispersion equation for the SPP wave vector k_{spp} can be found [47],

$$\sqrt{k_{spp}^2 - \frac{\omega^2}{c_0^2}\epsilon_1} + \sqrt{k_{spp}^2 - \frac{\omega^2}{c_0^2}\epsilon_2} + \mathrm{i}\omega\mu_0\sigma_{\alpha'\alpha'} = 0, \tag{43}$$

where ω is the angular frequency, $\epsilon_n = \epsilon_0\epsilon_n^r$ stands for the permeability of medium n, c_0 is the speed of light in vacuum, μ_0 is the permittivity of the medium n, and $\sigma_{\alpha'\alpha'}$ is the AGNR conductivity for α'-polarized waves given by (27). Moreover, a closed-form expression for k_{spp} can be found in this case,

$$k_{spp} = \frac{\omega}{c_0}\sqrt{\epsilon_1^r - \left(\frac{\left(\epsilon_1^r - \epsilon_2^r\right) + \sigma_{\alpha'\alpha'}^2\eta_0^2}{2\sigma_{\alpha'\alpha'}\eta_0}\right)^2}, \tag{44}$$

where $\eta_0 = \mu_0/\epsilon_0$. Next, we numerically investigate the propagation of SPP TE modes in AGNRs.

2.4.2.2 Numerical Study

In this section, we numerically study the propagation of SPP waves in semi-finite size graphene nanoribbons. As in Section 2.4.1.3, we consider AGNRs with different widths, *i.e.*, $W = 2.1$ nm ($N = 18$), $W = 10.1$ nm ($N = 84$), and $W = 50.0$ nm ($N = 408$), as well as different chemical potential ($\mu = 0$ eV and $\mu = 0.3$ eV), at a temperature $T = 300$ K. We consider the medium above the AGNR to be air ($\epsilon_1^r = 1$) and the medium below the AGNR to be silicon dioxide SiO_2 ($\epsilon_2^r = 4$ for the frequency range considered in our analysis).

TM Modes The propagation of TM SPP modes in graphene is governed by the dispersion equation given in (42). For a TM mode to exist, the real part of the SPP wave vector, $Re\{k_{spp}\}$, must be positive. As a result, from (42), TM modes along the α-axis only exist if the imaginary part of the conductivity, $\sigma_{\alpha\alpha}$, is positive. This is in accordance with the results obtained for infinitely large graphene sheets in [68, 47, 142, 58]. As a result, based on the conductivity analysis in Section 2.4.1.3, SPP TM modes only propagate in AGNRs with a chemical potential $\mu > 0$. In addition, TM modes are mainly supported along the x-axis or weakly along the y-axis in relatively wide ribbons (*e.g.*, $W = 50.0$ nm).

In Figure 14(a), we plot the real part of the SPP wave vector, $\mathrm{Re}\{k_{spp}\}$, of TM modes propagating along the x-axis for a $W = 2.1$ nm wide AGNR, with chemical potential $\mu = 0.3$ eV, as a function of the frequency. The values are normalized by the wave vector in the medium 1, k_1. In the same figure, we illustrate the imaginary part of the conductivity for x-polarized radiation, $\mathrm{Im}\{\sigma_{xx}\}$ from (27), as a function of the frequency. The SPP wave vector is only defined at those frequencies for which the imaginary part of the complex conductivity for x-polarized radiation is positive. This is achieved when the conductivity is governed by intra-band transitions (see Section 2.4.1.3). We can see that the real part of k_{spp} can be more than two orders of magnitude higher than that of the wave vector in medium 1, *i.e.*, in the air.

In Figure 14(b), the impact of the AGNR width on the propagation of TM SPP modes is illustrated, by plotting the real part of the SPP wave vector, $\mathrm{Re}\{k_{spp}\}$, as a function of the

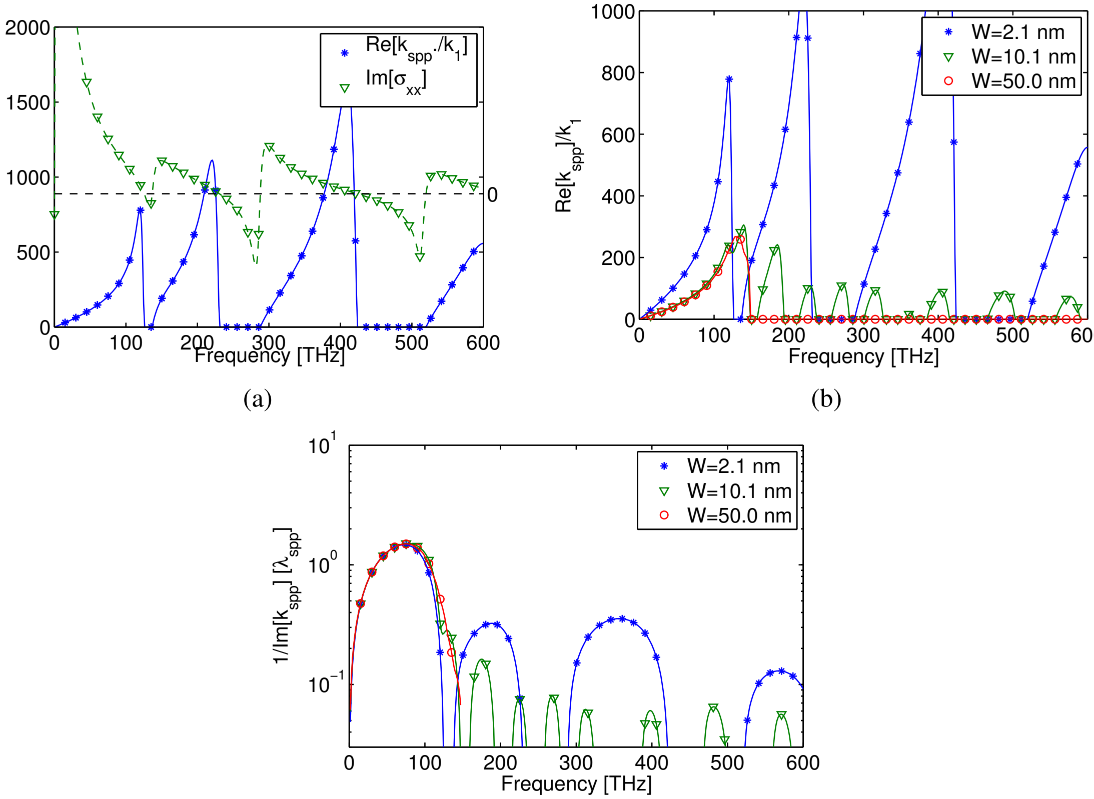

(a)

(b)

(c)

Figure 14. TM Modes Analysis: (a) Real part of k_{spp}/k_1 and imaginary part of σ_{xx} for an AGNR with $W = 2.1$ nm, (b) Real part of k_{spp}/k_1 for different AGNR width, and (c) 1/e-amplitude decay propagation distance in terms of λ_{spp} for different AGNR width ($\mu = 0.3$ eV, $T = 300$ K).

frequency for different values of W. For $W = 2.1$ nm, SPP modes appear mainly due to the forward intra-band transitions at frequencies close to 0 (the so-called Drude component) as well as right after the frequencies corresponding to inter-band transitions, due to backward intra-band transitions [119]. When the AGNR width increases, the conductivity is dominated by the forward intra-band transitions at frequencies close to 0. For relative wide AGNRs, $W = 50.0$ nm, the conductivity tends to that of infinitely large graphene sheets, and the SPP wave vector tends to that of graphene [68]. The SPP mode compression factor, $\text{Re}\{k_{spp}\}/k_1$ is lower for wider AGNRs. However, this higher compression comes at the cost of lower SPP propagation distances, as we discuss next.

In Figure 14(c), we analyze the impact of the AGNR width on the propagation length of TM SPP modes in graphene, by plotting the inverse of the imaginary part of the SPP wave vector, $1/\mathrm{Im}\{k_{spp}\}$, as a function of the frequency for different values of W. To better illustrate the propagation length of SPP waves, this is represented in terms of the SPP mode wavelength, λ_{spp} in (35). For example, the $1/e$-amplitude decay distance of TM SPP waves is on the order of a few SPP wavelengths for frequencies below 100 THz. We can see also that the width does not drastically impact the relative attenuation of the SPP waves on graphene, while, as we discussed above, narrower AGNRs allow more highly compressed SPP modes. Therefore, for thin AGNRs, $\lambda_{spp} \ll \lambda_1$ specially for narrower AGNRs, while the relative SPP propagation length remains similar.

From Figure 13, the propagation of TM SPP modes along the y-axis is possible only for $W = 50.0$ nm (and expectedly for wider AGNRs, as ultimately this converges for infinitely-large graphene sheets). For this case, however, despite the real part of the wave vector reaches values on the order of $100k_1$, the $1/e$-amplitude decay is much lower than λ_{spp}, which makes them less relevant than TM SPP waves along the x-axis.

TE Modes The propagation of TE SPP modes in graphene is governed by the dispersion equation given in (43). For a TE mode to exist, the real part of the SPP wave vector, $Re\{k_{spp}\}$, must be positive. As a result, from (43), TE modes along the α-axis only exist if the imaginary part of the conductivity, $\sigma_{\alpha'\alpha'}$, is negative. This is in accordance with the results obtained for infinitely large graphene sheets in [90, 47, 142]. As a result, based on the conductivity analysis in Section 2.4.1.3, SPP TE modes can propagate in AGNRs with a chemical potential $\mu \geq 0$.

The real part of the SPP wave vector for TE modes propagating along the x-axis, normalized by the wave vector in the medium 1, $\mathrm{Re}\{k_{spp}\}/k_1$, is shown in Figure 15(a), as a function of the frequency for a $W = 2.1$ nm wide AGNR, with chemical potential $\mu = 0.3$ eV. In the same figure, we illustrate the imaginary part of the conductivity for y-polarized radiation, $\mathrm{Im}\{\sigma_{yy}\}$ from (27). For this width W and chemical potential μ, the SPP wave vector is for all the frequencies in our analysis, given that the imaginary part of the complex conductivity for y-polarized radiation is always negative. We can see that the

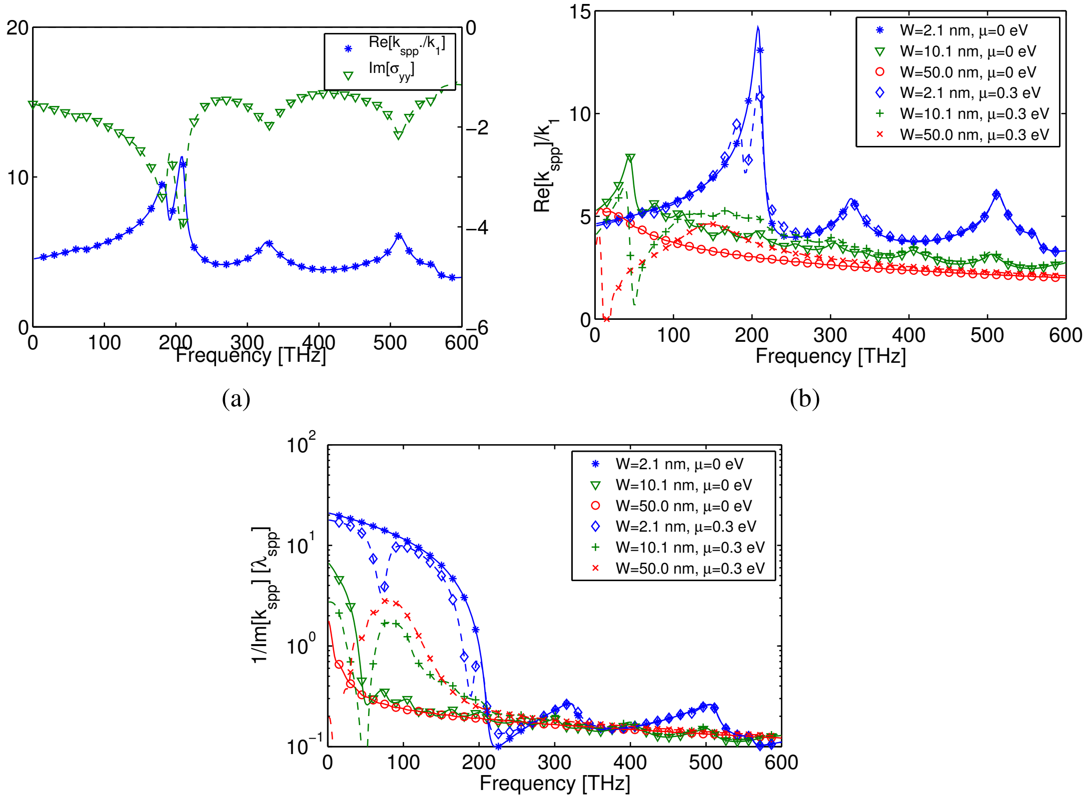

(a) (b)

(c)

Figure 15. TE Modes Analysis: (a) Real part of k_{spp}/k_1 and imaginary part of σ_{yy} for an AGNR with $W = 2.1$ nm, (b) Real part of k_{spp}/k_1 for different AGNR width W and chemical potential μ, and (c) $1/e$-amplitude decay propagation distance in terms of λ_{spp} for different AGNR width W and chemical potential μ ($T = 300$ K).

real part of k_{spp} can be more than two orders of magnitude higher than that of the wave vector in medium $n = 1$, *i.e.*, in the air.

In Figure 15(b), the real part of the SPP wave vector for TE modes propagating along the x-axis, normalized by the wave vector in the medium 1, $\text{Re}\{k_{spp}\}/k_1$, is shown as a function of the frequency for different values of W and of the chemical potential μ. TE SPP modes propagate along the x-axis mainly due to inter-band transitions. This can be clearly seen for example for $W = 2.1$ nm, in which the SPP mode compression factor, $\text{Re}\{k_{spp}\}/k_1$ can reach much higher values than for the rest of frequencies. When increasing the AGNR width, the major inter-band peaks are attenuated, and the same occurs with the SPP mode compression factor. As for the conductivity, the chemical potential does not drastically affect the propagation of TE SPP modes.

In Figure 15(c), the inverse of the imaginary part of the SPP wave vector along the x-axis, $1/\mathrm{Im}\{k_{spp}\}$, is shown as a function of the frequency for different values of W and μ. This is plotted in terms of λ_{spp} in (35) to better understand it's behavior. The $1/e$-amplitude decay distance of TE SPP waves is relatively larger in terms of λ_{spp}, but due to the much lower mode compression factor $\mathrm{Re}\{k_{spp}\}/k_1$, the actual propagation length of TE SPP waves is similar or even slightly lower than that of TM modes. Finally, the propagation of TE SPP modes along the y-axis is also possible for those cases in which $\mathrm{Im}\{\sigma_{xx}\} < 0$. However, these are only very weakly propagating modes, as given by their very low mode compression factor $\mathrm{Re}\{k_{spp}\}/k_1$. This makes them less significant for the design of plasmonic nano-antennas.

2.4.3 Antenna Frequency Response

In the same way as in Section 2.3.3, we model the graphene-based heterostructure composed of the AGNR, the dielectric material and the ground plane, as a *plasmonic resonant cavity*. This imposes a condition of the AGNR length L for the antenna to resonate. Up to this point, in Section 2.4.1 and Section 2.4.2, we have analyzed the impact of the finite width W of the AGNR on its conductivity and on the propagation of SPP waves, while considering the length L of the AGNR to tend to infinite or, at least, to be much larger than W. As llustrated in Figure 13, the conductivity of AGNRs tends to that of infinitely large graphene sheets as the width W increases. For example, for $W = 50$ nm, the impact of the lateral confinement of electrons in the y-axis on the conductivity along the x-axis is almost negligible. Therefore, the length L of the AGNR does not impact the conductivity as long as we consider it to be in the order of a few hundreds nanometers. Similarly, the dispersion of SPP modes in AGNRs given by (42) and (43) is determined by the permittivity of the surrounding media and the conductivity of the AGNR, but not by its length L. However, for the plasmonic nano-antenna to resonate, there is an additional constraint on the AGNR length, which depends on the type of SPP modes propagating along the antenna.

2.4.3.1 TM Modes

The condition on the nano-strip length L for a TM SPP wave mode to propagate along the x-axis is

$$L = m\frac{\lambda_{spp}}{2} = m\frac{\pi}{\text{Re}\{k_{spp}\}} \tag{45}$$

where $m = 1, 2, ...,$ and λ_{spp} and k_{spp} refer to the SPP wavelength and SPP wave vector, respectively. The SPP wave vector k_{spp} in (42) depends on the AGNR width W and chemical potential μ. As a result, the resonant length L of the antenna, or inversely, the resonant frequency of a fixed length L AGNR depends also on these two parameters. Note the difference with classical metallic antennas, in which the wave vector in the vacuum k_0 (or an equivalent effective wave vector k_{eff} which captures the impact of the dielectric and the ground plane) is used instead of the SPP wave vector k_{spp}. For $m = 1$, the condition imposed by (45) is the same as the condition given by (21).

In Figure 16(a), we plot the resonant antenna length L (45) for the fundamental TM SPP mode ($m = 1$) along the x-axis. As discussed in Section 2.4.2, SPP TM modes only exists at specific frequencies for which the imaginary part of the dynamic complex conductivity σ_{xx} is positive. For the frequencies that the TM mode exists, the wave compression factor $\text{Re}\{k_{spp}\}/k_1$ allows for a much shorter L than that of classical metallic antennas. For example, an antenna with $L = 1$ μm and $W = 2.1$ nm, at $\mu = 0.3$ eV and $T = 300$ K, approximately radiates at 8.5 THz (Figure 16(b)). This is 35 times shorter than the size required for a metallic antenna operating at the same frequency. These results are consistent with our preliminary model described in Section 2.3, with the simulation-based analysis that we conducted in [76] for infinitely large graphene sheets, as well as, for the experimental SPP propagation measurements reported in [61, 53].

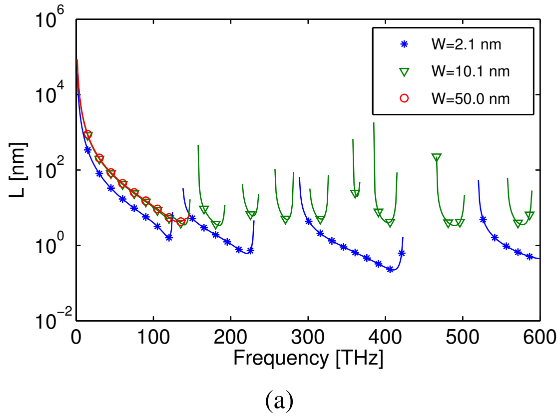

(a) (b)

Figure 16. Antenna resonant length L for (a) the fundamental TM mode ($m = 1$ in (45)), and (b) the fundamental TM mode in the Terahertz Band ($\mu = 0.3$ eV, $T = 300$ K).

2.4.3.2 TE Modes

The condition on the nano-strip length L for a TE SPP wave mode to propagate along the x-axis is

$$L = \frac{2q-1}{\sqrt{\left(\frac{2p-1}{W}\right)^2 - \left(\frac{2}{\lambda_{spp}}\right)^2}} = \frac{(2q-1)\,\pi}{\sqrt{\left(\frac{(2p-1)\pi}{W}\right)^2 - \text{Re}\{k_{spp}\}^2}} \tag{46}$$

where $p, q = 1, 2, ...$, and λ_{spp} and k_{spp} are the SPP wavelength and wave vector for TE SPP modes, respectively. The SPP wavevector k_{spp} given by (43) depends on the AGNR width W and chemical potential μ. Therefore, there is a double dependance on the width W when determining the resonant length of TE modes in nano-strip antennas. In Figure 17(a), the resonant antenna length L for TE modes is shown as a function of the frequency. However, as expected from 46, much higher frequencies are needed to actually see the impact of the length on the TE mode. Alternatively, much wider nano-strips can be considered, but in that case, rather than AGNRs, we would require the use of much larger graphene sheets.

Up to this point, we have discussed the frequency response of the antenna. However, little has been said about the efficiency of the antenna itself. Based on our numerical analysis in Section 2.4.2.2, the propagation length of the SPP modes in graphene given by $1/\text{Im}\{k_{spp}\}$ is on the order of a few SPP wavelengths λ_{spp} which seems somehow desirable for the radiation from graphene-based heterostructures. However, the radiation principle

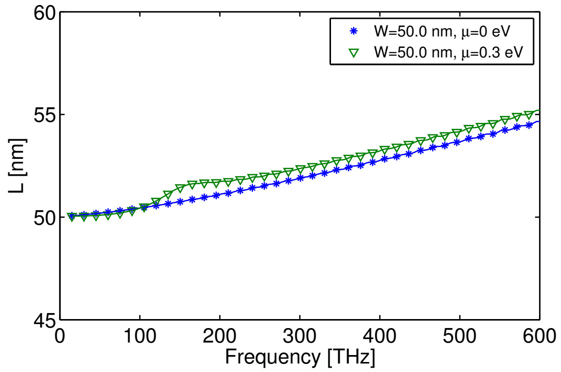

(a)

Figure 17. Antenna resonant length L for the fundamental TE mode ($p = q = 1$ in (46)) ($T = 300$ K).

itself might differ largely with the AGNR width. For example, for relatively wide nano-patches, it is common to model the antenna as four magnetic currents, one in each edge, two of them being radiative and two of them resulting in non-radiative. Our current and future work is aimed at characterizing the antenna efficiency and gain. While our study has been focused on AGNRs, a similar study can be conducted for ZGNRs, which would lead to similar results.

2.5 Conclusions

In this chapter, we have proposed, modeled and analyzed a novel graphene-based plasmonic nano-antenna for communication among nanomachines. The proposed nano-antenna is based on a thin graphene nanoribbon and reassembles a nano-strip antenna. Two different approaches have been utilized to analyze the frequency response on the nano-antenna. On the one hand, we have used the tight-binding model of GNRs to obtain their transmission line properties. From these, we have then obtained the propagation speed of SPP waves in GNRs and the antenna first resonant frequency. On the other hand, we have first analytically and numerically computed the conductivity of semi-finite size graphene nanoribbons as a function of their width and chemical potential. Then, we have extensively analyzed and discussed the propagation of SPP waves in GNRs. Finally, we have modeled our antenna as a plasmonic resonant cavity and obtained its frequency response. In both cases, the results show that, by exploiting the high wave compression mode of SPP waves in AGNRs, graphene-based nano-antennas are able to work at much lower frequencies than classical metallic antennas of the same size. For example, a one-micrometer-long ten-nanometers-wide plasmonic nano-antenna is expected to radiate in the Terahertz Band (0.1-10 THz). As we will describe in Chapter 9, we will further validate our analytical models by means of COMSOL Multi-physics in the one-to-one nano-link. This result opens the door to EM communication in nanonetworks.

CHAPTER 3

CHANNEL MODELING AND CAPACITY ANALYSIS FOR NANONETWORKS IN THE TERAHERTZ BAND

The second step towards enabling electromagnetic nanonetworks is the characterization of the frequency band at which nanomachines are expected to communicate. In this chapter, we motivate and develop a new channel model for communication in the Terahertz Band (0.1-10 THz). We revisit the concept of molecular absorption and provide formulations for the total path loss and molecular absorption noise in the Terahertz Band, by means of radiative transfer theory [41] and making intensive use of the HITRAN (high resolution transmission molecular absorption database) line catalog [117]. In addition, we propose different power allocation schemes and evaluate the performance of the Terahertz Band in terms of channel capacity.

3.1 Motivation and Related Work

As we have shown in Chapter 2, graphene-based plasmonic nano-antennas are expected to operate in the Terahertz Band (0.1-10 THz). Existing related papers in the field [26, 137, 106, 76, 81] reach similar conclusions. In addition to the antenna, graphene is also considered as the building material of novel nano-devices able to operate at Terahertz Band frequencies. Graphene-based nano-systems for Terahertz wave generation have been analytically and experimentally proved in [96, 94, 95]. Modulators for Terahertz Band signals have also been experimentally shown in [122, 70], which take advantage of the intra-band transitions in the conductivity of graphene at Terahertz Band frequencies. Similarly, filters and polarizers [160] and frequency mixers and multipliers [149, 148, 147, 74] for Terahertz Band operation have been analytically and experimentally demonstrated. Moreover, Terahertz Band signal detection with graphene devices has been demonstrated in [22].

After nanomachine design and manufacturing, the Terahertz Band channel is one of the main aspects that makes the realization of nanonetworks a challenge. This still unregulated frequency range spans the frequencies between 100 GHz and 10 THz [56]. While the frequency regions immediately below and above this band (the microwaves and the far infrared, respectively) have been extensively investigated, this is still one of the least-explored zones of the electromagnetic spectrum. Existing channel models for lower frequency bands do not capture the peculiarities of the Terahertz Band, *e.g.*, the very high molecular absorption loss, the very high reflection loss or the cross-polarization effects at Terahertz Band frequencies [35, 54, 64, 67, 108]. In addition, the few Terahertz Band channel models existing to date [107, 108, 161, 111] are aimed at characterizing the communication between devices that are several meters far. In particular, due to the very high attenuation created by molecular absorption (hundreds of dB/m), current efforts on device development, channel characterization and standardization are focused on the communication in the absorption-defined window at 300 GHz [56]. However, in light of the expectedly short transmission range of nanomachines, there is a need to understand and model the entire Terahertz Band for distances below one meter. This is the contribution of this chapter.

3.2 Total Path Loss

The path loss, A, for a traveling wave in the Terahertz Band is defined as the product of the spreading loss, A_{spread}, and the molecular absorption loss, A_{abs}:

$$A\left(f,d\right) = A_{spread}\left(f,d\right) A_{abs}\left(f,d\right), \tag{47}$$

where f stands for frequency and d is the path length.

The spreading loss accounts for the attenuation due to the expansion of the wave as it propagates through the medium, and it is defined as

$$A_{spread}\left(f,d\right) = \left(\frac{4\pi f d}{c_0}\right)^2, \tag{48}$$

where c_0 stands for the speed of light in vacuum and we consider that the electromagnetic power is spherically spread with distance.

The absorption loss accounts for the attenuation that a propagating wave suffers because of molecular absorption, *i.e.*, the process by which part of the wave energy is converted into internal kinetic energy of the excited molecules in the medium. The absorption loss A_{abs} reflects this reduction in the wave energy, and it is defined as

$$A_{abs}(f, d) = \frac{1}{\tau(f, d)}, \tag{49}$$

where f stands for frequency, d is the path length, and τ is the transmittance of the medium. This parameter measures the fraction of incident radiation that is able to pass through the medium and can be calculated using the Beer-Lambert Law as [41]

$$\tau(f, d) = e^{-k(f)d}, \tag{50}$$

where k refers to the medium absorption coefficient and is given by

$$k(f) = \sum_{i,g} k^{i,g}(f) \tag{51}$$

where $k^{i,g}$ is the individual absorption coefficient for the isotopologue[1] i of gas g. For example, a standard medium is mainly composed of nitrogen (78.1%), oxygen (20.9%) and water vapor (0.1.0-10.0%), and each gas has different isotopologues that resonate at several frequencies. The major contribution comes from water vapor molecules.

The absorption coefficient of an isotopologue i of gas g, $k^{i,g}$, in m^{-1}, for a molecular volumetric density, $Q^{i,g}$, in molecules/m^3, at pressure p and temperature T is given by

$$k^{i,g}(f) = \frac{p}{p_o}\frac{T_{STP}}{T}Q^{i,g}\sigma^{i,g}(f), \tag{52}$$

where p_0 and T_{STP} are the Standard-Pressure-Temperature values and $\sigma^{i,g}$ is the absorption cross section for the isotopologue i of gas g in m^2/molecule. The total absorption depends on the number of molecules of a given gas that are found along the path. For a given gas mixture, the total number of molecules of the isotopologue i of gas g per volume unit, $Q^{i,g}$, at pressure p and temperature T, can be obtained from the Ideal Gas Law [140] as

$$Q^{i,g} = \frac{n}{V}q^{i,g}N_A = \frac{p}{RT}q^{i,g}N_A, \tag{53}$$

---

[1] A molecule that only differs from another in its isotopic composition.

where n is the total number of moles of the gas mixture that is being considered, V stands for the volume, $q^{i,g}$ is the mixing ratio for the isotopologue i of gas g, N_A stands for the Avogadro constant and R is the gas constant.

The absorption cross section $\sigma^{i,g}$ in (52) can be further decomposed in the line intensity $S^{i,g}$ and the spectral line shape $G^{i,g}$ as

$$\sigma^{i,g}(f) = \mathrm{S}^{i,g} G^{i,g}(f). \tag{54}$$

The line intensity $S^{i,g}$ is a parameter directly obtained from the HITRAN database. To obtain the line shape, $G^{i,g}$, we first need to determine the position of the resonant frequency $f_c^{i,g}$ for an isotopologue i of gas g. This frequency increases linearly with the pressure from its zero-pressure position as

$$f_c^{i,g} = f_{c0}^{i,g} + \delta^{i,g} p/p_0, \tag{55}$$

where $f_{c0}^{i,g}$ is the zero-pressure position of the resonance, p_0 is the reference pressure and $\delta^{i,g}$ is the linear pressure shift. These parameters are directly read from the HITRAN database.

The absorption from a particular molecule is not confined to a single frequency, but is spread over a range of frequencies. For a system in which the pressure is above 0.1 atm, the spreading is mainly governed by the collisions between molecules of the same gas. The amount of broadening depends on the molecules involved in the collisions and it is usually referred as the Lorentz half-width $\alpha_L^{i,g}$ [41]. This can be obtained as a function of the air and self-broadened half-widths, α_0^{air} and $\alpha_0^{i,g}$, respectively, as

$$\alpha_L^{i,g} = \left[(1 - q^g)\,\alpha_0^{air} + q_g \alpha_0^{i,g}\right]\left(\frac{p}{p_0}\right)\left(\frac{T_0}{T}\right)^{\gamma}, \tag{56}$$

in which the temperature broadening coefficient γ as well as α_0^{air} and $\alpha_0^{i,g}$ are obtained directly from the HITRAN database.

For the Terahertz Band, an appropriate line shape to represent the molecular absorption is the Van Vleck-Weisskopf asymmetric line shape [143]:

$$F^{i,g}(f) = \frac{\alpha_L^{i,g}}{\pi}\frac{f}{f_c^{i,g}}\left[\frac{1}{\left(f - f_c^{i,g}\right)^2 + \left(\alpha_L^{i,g}\right)^2} + \frac{1}{\left(f + f_c^{i,g}\right)^2 + \left(\alpha_L^{i,g}\right)^2}\right], \tag{57}$$

An additional adjustment to the far ends of the line shape can be done to account for the continuum absorption [18]:

$$G^{i,g}(f) = \frac{f}{f_c^{i,g}} \frac{\tanh\left(\frac{hc_0 f}{2k_B T}\right)}{\tanh\left(\frac{hc_0 f_c^{i,g}}{2k_B T}\right)} F^{i,g}(f), \tag{58}$$

where h is the Planck constant, c_0 is the speed of light in vacuum, k_B stands for the Boltzmann constant and T is the system temperature.

The total molecular absorption loss can be now computed by combining (58), (54), (50) and (49). As an example, the absorption coefficient for the different isotopologues of oxygen and water vapor molecules are shown as functions of frequency in Figure 18. Oxygen or O_2 (Figure 18(a)) has more than two thousand resonances in the Terahertz Band, mainly within 100 GHz and 6 THz. However, the major contribution to the total absorption in a standard medium comes from water vapor molecules or H_2O (Figure 18(b)), with more than four thousand resonant peaks within the entire band, and an absorption coefficient six orders of magnitude above that of the oxygen resonances. Rather than the attenuation introduced by fog or raindrops in conventional RF systems in the Megahertz and Gigahertz spectral bands, in the Terahertz Band, the water vapor molecules present in a standard medium already significantly affects the channel performance.

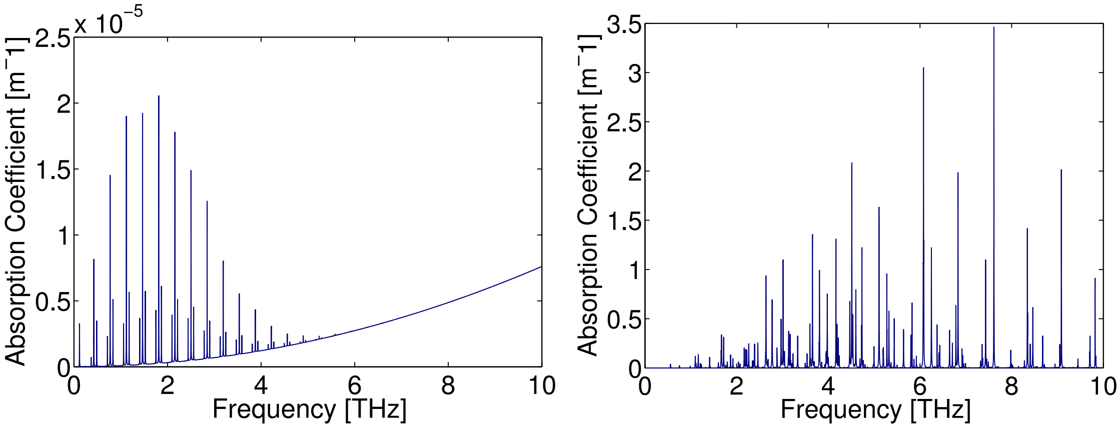

(a) O_2 (b) H_2O

Figure 18. Molecular absorption coefficient k^g in m^{-1} for oxygen and water vapor as functions of the frequency.

3.3 Molecular Absorption Noise

Up to this point, it has been considered that the molecules present in the medium only affect the properties of the channel in terms of attenuation. However, molecular absorption also introduces noise [12]. Indeed, the internal vibration of the molecules turns into the emission of electromagnetic radiation at the same frequency that the incident waves that provoked this motion. In our model, we consider this as a noise factor that affects the propagation of electromagnetic waves in the Terahertz Band and we provide a way to compute it.

The parameter that measures this phenomenon is the emissivity of the channel, ε, and it is defined as

$$\varepsilon\left(f, d\right) = 1 - \tau\left(f, d\right) \tag{59}$$

where f is the frequency of the electromagnetic wave, d stands for the total path length and τ is the transmissivity of the medium given by (50).

The equivalent noise temperature due to molecular absorption T_{mol} in Kelvin that an omnidirectional antenna detects from the medium is further obtained as:

$$T_{mol}\left(f, d\right) = T_0 \varepsilon\left(f, d\right) \tag{60}$$

where f is the frequency of the electromagnetic wave, d stands for the total path length, T_0 is the reference temperature and ε refers to the emissivity of the channel given by (59). This type of noise is only present around the frequencies in which the molecular absorption is considerably high. Water vapor molecules are again the main factor affecting the Terahertz Band channel.

Besides the molecular absorption noise, the antenna noise temperature has contributions from several sources, such as the noise created by surrounding nanomachines or the same device per se. To compute the total noise temperature of the system, T_{noise}, the noise introduced by the receiver needs to be taken into account:

$$T_{noise} = T_{sys} + T_{ant} = T_{sys} + T_{mol} + T_{other} \tag{61}$$

where T_{sys} refers to the system electronic noise temperature, T_{ant} is the total antenna noise temperature, T_{mol} is the molecular absorption noise, and T_{other} accounts for any other additional noise source. For the time being, there is no accurate noise model for graphene-based electronic devices, but the initial predictions point to very low noise factors in this nanomaterial [98]. For this, we focus only on the noise introduced by the channel, *i.e.*, the molecular absorption noise.

To compute the equivalent noise power at the receiver, it is necessary to define the transmission bandwidth, which depends on its turn on the transmission distance and the composition of the medium. For a given bandwidth, B, the molecular absorption noise power at the receiver can be calculated as:

$$P_n(f,d) = \int_B S_N(f,d)\,df = k_B \int_B T_{noise}(f,d)\,df \tag{62}$$

where f stands for frequency, d is the transmission distance, S_N refers to the noise power spectral density (p.s.d.), k_B is the Boltzmann constant and T_{noise} refers to the equivalent noise temperature. Up to this point, we have given formulations to compute the total path loss and the molecular absorption noise power. In the following section, we investigate the capacity of the Terahertz Band channel by using the developed model.

3.4 Channel Capacity

In order to quantize the potential of the Terahertz Band for communication in nanonetworks, we use the channel capacity as a performance metric. In our analysis, we look at the Terahertz Band as a single transmission window almost 10 THz wide. We believe that this is the main new opportunity for communication in nanonetworks.

Based on the proposed channel model, the Terahertz Band channel is highly frequency-selective. In this section, we consider the molecular absorption noise to be additive, colored, Gaussian and independent of the transmitted signal. A more accurate stochastic model of noise is developed in Section 4.4.1. Under these assumptions, the capacity can be obtained by dividing the total bandwidth into many narrow sub-bands and summing the individual capacities [40]. The i-th sub-band is centered around frequency f_i, $i = 1, 2, ...$ and it has width Δf. If the sub-band width is small enough, the channel appears as frequency-nonselective and the noise p.s.d. can be considered locally flat. The resulting capacity in bits/s is then given by

$$C(d) = \sum_i \Delta f \log_2 \left[1 + \frac{S(f_i) A^{-1}(f_i, d)}{S_N(f_i, d)} \right], \tag{63}$$

where d is the path length, S is the transmitted signal p.s.d., A is the channel path loss and S_N is the noise p.s.d..

The total path loss and the system noise are determined by the signal frequency, the transmission distance and the molecular composition of the channel, whereas different distributions for the transmitted signal p.s.d. can be adopted. For example, in the simplest case, this is flat,

$$S_{flat}(f) = S_0 \text{ for } f \in B, \text{ 0 elsewhere.} \tag{64}$$

Alternatively, the transmitted signal p.s.d. can be optimally defined to maximize the channel capacity, subject to the constraint that the total transmitted power is finite. For this, the signal p.s.d., S_{opt}, should satisfy the water-filling principle:

$$\begin{aligned} &S_{opt}(f) + A(f, d) S_N(f, d) = K, \text{ and} \\ &S_{opt}(f) = 0 \text{ if } K < A(f, d) S_N(f, d), \text{ both for } f \in B, \text{ 0 elsewhere,} \end{aligned} \tag{65}$$

where K is a constant whose value depends on the total transmitted power, which will remain as a design parameter in our analysis.

Despite the simplicity or the optimality of these two power-allocation schemes, their feasibility can be compromised by the limited capabilities of a single nanomachine. As we will explain in detail in Section 4.2.1, recent advancements in solid-state Terahertz Band signal generators and detectors point to the possibility of transmitting very short pulses, just one-hundred-femtosecond long. The major spectral components of these pulses are contained within the Terahertz Band. For simplicity, we model these pulses as Gaussian-shaped,

$$p(t) = \frac{a_0}{\sqrt{2\pi}\sigma} e^{-(t-\mu)^2/(2\sigma^2)}, \tag{66}$$

where a_0 is a normalizing constant to adjust the pulse total energy, σ is the standard deviation of the Gaussian pulse in seconds, and μ is the location in time for the center of the pulse in seconds. The p.s.d. of the transmitted pulse, S_p, is given by

$$S_p(f) = a_0^2 e^{-(2\pi\sigma f)^2}, \tag{67}$$

The time derivatives of a Gaussian pulse can be easily obtained by the combination of delay lines, and will be also included in the quantitative evaluation of the channel. The p.s.d. of the time derivate of a Gaussian pulse is also Gaussian-shaped, but the frequency position of its main components increases with the derivative order n:

$$S_p^{(n)}(f) = (2\pi f j)^{2n} a_0^2 e^{-(2\pi\sigma f)^2}. \tag{68}$$

Finally, we also compute the channel capacity for the case in which a transmission window at 350 GHz with a 51 GHz flat bandwidth is used. Within this sub-band, the p.s.d., S_{win} is considered flat.

3.5 Numerical Results

In order to illustrate and understand the different properties of the Terahertz Band from the communication perspective, the developed channel model is numerically investigated for different medium compositions, in terms of total path loss, molecular absorption noise and channel capacity. In our analysis, the contributions to molecular absorption from oxygen, carbon dioxide, methane, nitrogen dioxide, ozone, nitrous oxide, carbon monoxide, and water vapor are considered. Their average concentration in a dry atmosphere is used unless the contrary is stated [41].

3.5.1 Total Path Loss

The total path loss A, given by (47), depends on the electromagnetic wave frequency f, the transmission distance d and the composition of the medium that is being considerwed. In order to illustrate the interrelations between these variables, in Figure 19, the total path loss is shown in dB as a function of both the frequency (x-axis) and the distance (y-axis) for different concentrations of water vapor molecules. Due to the spreading loss given by (48), the total path loss increases with both the distance and the frequency, independently of the molecular composition of the channel, similarly to conventional communication models in the Megahertz or few Gigahertz frequency ranges. However, several peaks of attenuation can be observed due to the molecular absorption loss given by (49). As discussed in Section 3.2, the total absorption depends on the number of molecules that the propagating electromagnetic wave encounters before reaching its destination. In a homogeneous channel, this is directly proportional to the molecular cross-section given in (54) and the total path length d.

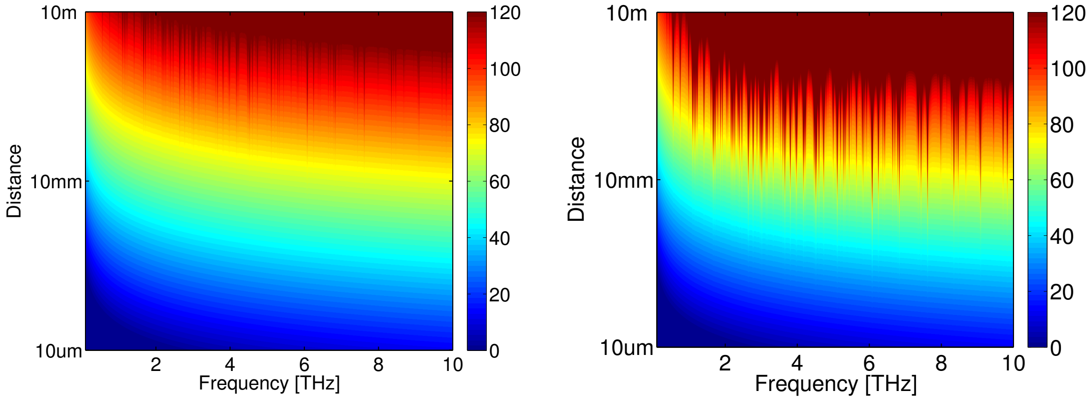

(a) 0.1% H_2O (b) 10% H_2O

Figure 19. Total path loss in dB as a function of the frequency and the distance for two different concentrations of water vapor molecules (the values for path loss have been truncated at 120 dB to avoid masking relevant transmission windows in the short-range).

The main features of the Terahertz Band from the communication perspective are summarized as follows:

- The total path loss of a propagating wave in the Terahertz Band does not only depend on the transmission distance and the system frequency, but also on the composition of the transmission medium at a molecular level. In other words, apart from the spreading loss associated to any propagating wave, the presence or absence of absorbent molecules drastically alters the channel behavior. From this, the optimal transmission frequency and its associated bandwidth for a given transmission distance can be determined.

- Within a nanonetwork, it is unlikely to consider single-hop transmission distances above several tens of millimeters. Within this range, the available bandwidth is almost the entire band, from a few hundreds of Gigahertz to almost ten Terahertz, even for high concentrations of water vapor molecules, which is the major factor affecting the channel path loss. This opens a wide range of opportunities for communications, from femtosecond-long pulse-based communication systems to multiple access methods based on frequency division techniques. However, molecular absorption still determines the frequency response of the channel, and allows, for example, the definition of optimally shaped transmission signals.
- For short-range macroscale communications, *i.e.*, up to a few meters, the channel conditions define a set of transmission windows up to several tens of Gigahertz wide each. Current research on Terahertz Band communication is mainly aimed to exploit the first available window below 350 GHz [108]. The development of graphene-based devices implicitly working in this domain can potentially enable the (simultaneous) use of all them in a cognitive fashion.

These results motivate both, the further analysis of the Terahertz Band and the identification of applications that can benefit from very large bandwidths in the ultra short range.

3.5.2 Molecular Absorption Noise

The total noise power P_n, given by (62), in a Terahertz Band communication system depends on the electronic noise temperature at the receiver, T_{sys}, and the molecular absorption noise temperature created by the channel, T_{mol} given by (60). As discussed in Section 3.3, the electronic noise temperature of the system is expectedly low due to the electron transport properties of graphene. As a result, the main source of noise in the Terahertz Band is the molecular absorption noise introduced by the channel. In the following, taking into account that the computation of the molecular absorption noise power would require the definition of the usable bandwidth B, the molecular absorption noise temperature is calculated instead.

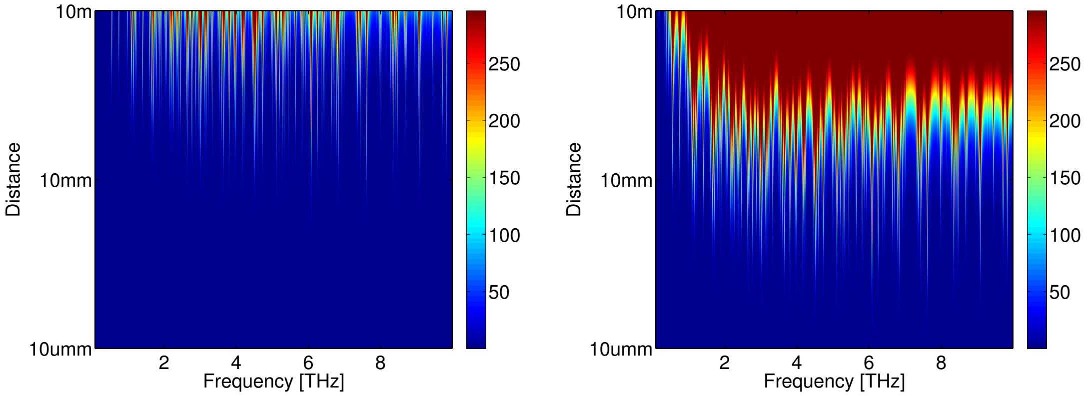

(a) 0.1% H_2O (b) 10% H_2O

Figure 20. Molecular absorption noise temperature T in Kelvin as a function of the frequency and the distance for two different concentrations of water vapor molecules.

The molecular absorption noise temperature T_{mol}, given by (60), is shown in Figure 20 as a function of the frequency (x-axis) and the distance (y-axis) for different concentrations of water vapor molecules. In the very short range, the absence of highly absorbent molecules in the medium results in very low noise temperatures. On the contrary, when the number of absorbent molecules that a propagating electromagnetic wave encounters along the channel increases, several peaks in the total noise temperature can be observed. The presence of water vapor molecules is again the main factor affecting the properties of the Terahertz Band channel.

Similarly to the system total path loss, the total system noise defines a set of usable transmission windows which change with the transmission distance between the nanomachines. For the ultra short range, up to several tens of millimeters, the molecular absorption noise power is very low when compared to other noise sources. For the short range, the wise selection of center frequency(s) and bandwidth(s) can diminish the effect of the noise on the system performance.

3.5.3 Channel Capacity

The capacity C, given by (63), of the Terahertz Band channel is determined by the channel path loss A, given by (47), the noise p.s.d. S_N, defined in (62), and the p.s.d. of the transmitted electromagnetic wave. The maximum total transmission power is set to 100 mW. In Section 4.2.1, we will analyze more realistic values for the particular case of nanonetworks.

3.5.3.1 Channel Capacity for Different Power Allocation Schemes

In Figure 21, the channel capacity is shown for the four power allocation schemes proposed in Section 3.4: the capacity-optimal p.s.d. S_{opt} (65), a uniform distribution of the power within the entire Terahertz Band S_{flat} (64), the p.s.d. corresponding to the first time derivative of a one-hundred-femtosecond-long Gaussian pulse $S_p^{(1)}$ (68), and the p.s.d for the case in which a transmission window at 350 GHz, S_{win}, is used. A standard medium with 1% of water vapor molecules is considered, unless the contrary is stated.

For a transmission distance below several tens of millimeters, the molecular absorption is almost negligible. In this case, uniformly distributing the power across the entire band tends to the optimal p.s.d.. On the contrary, by utilizing a single transmission window, even if 51 GHz wide, the capacity in this case would be up to two orders of magnitude below the optimal p.s.d. When the transmission distance is increased, the effect of the molecular absorption is intensified, and uniformly distributing the power along the band is no longer a capacity-efficient option. For a transmission distance on the order of a few meters, utilizing the first transmission window at 350 GHz turns to be the best option. From these results, we also highlight that the exchange of one-hundred-femtosecond-long pulses is a good compromise between achievable capacity and nano-transceiver architecture complexity.

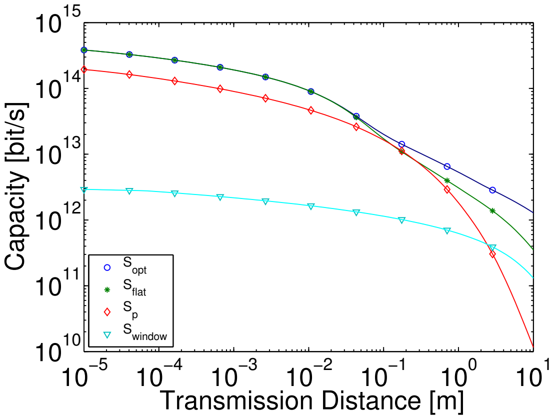

Figure 21. Capacity as a function of the distance for four different p.s.d. (1% H_2O).

3.5.3.2 Channel Capacity for Different Molecular Compositions

The channel path loss A, given by (47), and the noise p.s.d. S_N, defined in (62), are mainly determined by the channel molecular composition. Within the Terahertz Band, the main contribution comes from water vapor molecules. The channel capacity C, given by (63), as a function of the distance for different concentrations of water vapor molecules is shown in Figure 22(a) for the optimal power distribution S_{opt} (65), and the for the flat p.s.d. S_{flat} (64), and in Figure 22(b), for the p.s.d. corresponding to the first time derivative of a one-hundred-femtosecond-long Gaussian pulse $S_p^{(1)}$ (68), and for the case in which the first transmission window at 350 GHz is chosen S_{win}.

The channel capacity of the same electromagnetic nanonetwork can considerably change depending on the medium conditions. In classical communication channels, the system performance is mainly affected by severe changes in the atmospheric conditions such as fog, rain or snow. In nanonetworks, the limitation on the transmission power and the expected high-sensibility of nanomaterials, make the presence of just a few molecules a major challenge for efficient communication. This effect depends on the total number of molecules found along the channel, and, thus, either when increasing the path length or the concentration of molecules among the path, the performance degradation is similar.

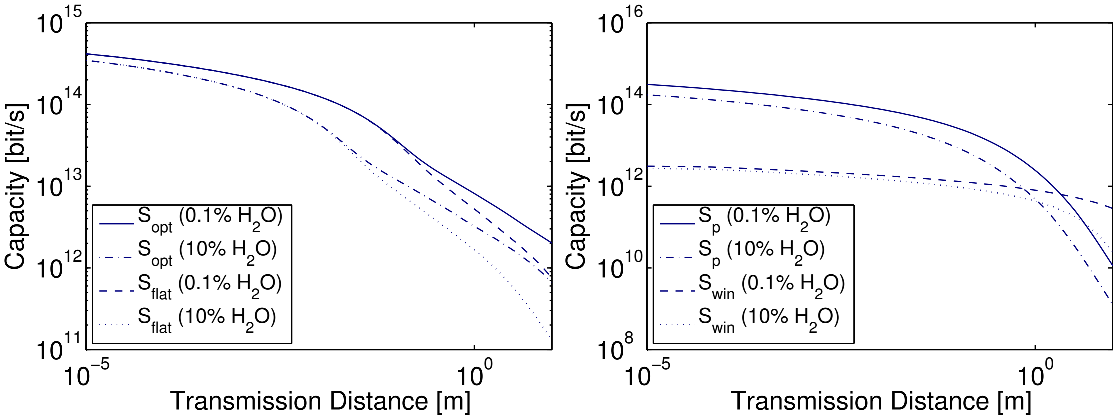

(a) S_{opt} and S_{flat} (b) S_p and S_{win}

Figure 22. Capacity as a function of the distance for different power allocation schemes with different concentrations of water vapor molecules.

3.5.3.3 Channel Capacity for Different Pulse Shapes

The possibility to generate and transmit femtosecond-long Gaussian pulses by using structures in the nanoscale, invites us to think of a potential communication scheme based on the transmission of ultra-low energy pulses. For a fixed energy, the p.s.d. of a Gaussian-shaped pulse can be modified either by changing its width or by computing its time derivative, which can be obtained by a combination of delay lines.

In Figure 23(a), the channel capacity C, given by (63), is illustrated as a function of the distance d, when the p.s.d. corresponding to the first time derivative of a Gaussian pulse $S_p^{(1)}$ (68) is used. Different pulse durations σ are considered ranging from 50 fs to 150 fs. When the pulse-width is increased, the p.s.d. becomes sharper, *i.e.*, the power is concentrated around the center of the Gaussian-shaped pulse. This effect increases the channel capacity for distances above several tens of millimeters, where it has been shown before that it is more efficient to concentrate the power in the lower part of the band. On the contrary, the capacity can be slightly increased in the very short range if shorter pulses are used. Indeed, a shorter pulse has a flatter p.s.d., and this is closer to the shape of the optimal power allocation scheme for the shorter range.

In Figure 23(b), the channel capacity C, given by (63), is illustrated as a function of the distance d, when the p.s.d. corresponding to a one-hundred-femtosecond-long Gaussian $S_p^{(n)}$ (68) is used, for different time derivative orders n. By computing the time derivative of the pulse, the corresponding p.s.d. is shifted towards the higher part of the band. Taking into account that the total path loss increases with frequency and distance, the channel capacity is reduced with the derivative order, specially for distances above several tens of millimeters. Finally, we would like to highlight that independently of the exact pulse shape, the transmission of very short pulses represents an efficient way to exploit the huge bandwidth provided by the Terahertz Band.

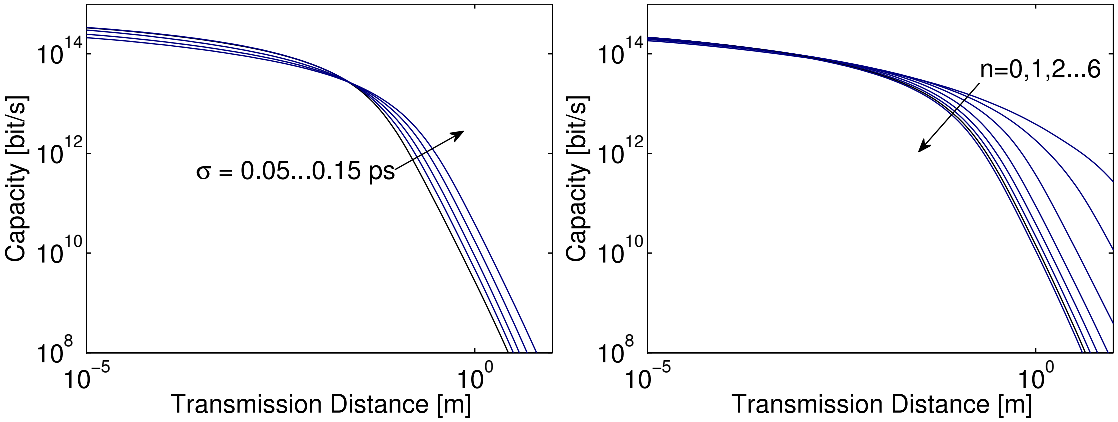

(a) Varying pulse-width σ (n = 1)　(b) Varying time derivative order n (σ = 100 fs)

Figure 23. Capacity as a function of the distance for different pulse shapes (1% H_2O).

3.6 Conclusions

In this chapter, we have developed a novel channel model based on radiative transfer theory to compute the path loss and the noise in the Terahertz Band. Then, we have proposed different power allocation schemes and, finally, we have computed the channel capacity of the Terahertz Band by using the developed channel model. Our results show that the Terahertz Band channel has a strong dependence on both the molecular composition of the medium and the transmission distance. The main factor affecting the behavior of the Terahertz Band is the absorption by water vapor molecules, which does not only attenuate the transmitted signal, but it also introduces colored noise. In the very short range, *i.e.*, for a transmission distance in the order of several tens of millimeters, the Terahertz Band can be considered as a single transmission window almost 10 THz wide. This is the main difference with existing Terahertz communications systems which are focused on utilizing a single transmission window below 350 GHz. The very high channel capacity of the Terahertz Band does not only support very high transmission bit-rates, but it also enables new information encoding and modulation techniques as well as novel networking protocols more suited for resource-limited nanomachines. Amongst others, we have suggested the use of femtosecond-long pulses for transmission of information among nanomachines, and showed how it poses an interesting paradigm for short range communication in nanonetworks. Motivated by this result, in the next chapter we propose new pulse-based modulation schemes for nanonetworks in the Terahertz Band.

CHAPTER 4

FEMTOSECOND-LONG PULSE-BASED MODULATION FOR TERAHERTZ BAND COMMUNICATION

The next step towards enabling electromagnetic nanonetworks is the development of novel modulations suited for the capabilities of nanomachines and tailored to the peculiarities of the Terahertz Band channel. In this chapter, we develop a pulse-based modulation and channel access scheme for nanonetworks in the Terahertz Band, which is based on the transmission of one-hundred-femtosecond-long pulses by following an asymmetric On-Off Keying modulation Spread in Time (TS-OOK). We motivate the feasibility of this scheme and investigate its performance in terms of maximum achievable information rate for the single-user and the multi-user cases. The computation of the achievable information rate takes into account the transmitted waveforms, the propagation effects, the noise sources, the multi-user interference and the information source statistics. In our analysis, we make use of our developed Terahertz Band channel model. Moreover, we develop new stochastic models of the noise and multi-user interference in the Terahertz Band.

4.1 Motivation and Related Work

For the time being, EM nano-transceivers cannot generate high-power carrier signals at Terahertz Band frequencies. Indeed, several compact Terahertz Band plasmonic signal generators and detectors are being developed [66, 97, 144, 145]. Contrary to classical Terahertz Band radiation sources, which would require high power bulky devices and sophisticated cooling systems [162, 99], novel solid-state Terahertz Band emitters can electronically excite SPP waves at Terahertz Band frequencies from a compact structure built on a High Electron Mobility Transistor (HEMT) based on semiconductor materials as well as graphene. However, as we will explain in Section 4.2.1, when working at room temperature, only broadband non-coherent radiation has been generated. In particular, very short pulses, just a hundred femtosecond long, can be generated, with a power of just a few μW per pulse. This might not be enough for long range Terahertz Band communication, but opens the door to communication in nanonetworks.

The lack of nano-transceivers able to generate a carrier signal at Terahertz Band frequencies results in the impossibility to utilize classical carrier-based modulations and motivates the use of pulse-based communication schemes in nanonetworks. Pulse-based modulations have been widely used in high-speed wireless communication systems such as Impulse Radio UltraWideBand (IR-UWB) and Free Space Optical (FSO) systems. In IR-UWB, one-hundred-picosecond-long pulses are transmitted over the 3.1-10.6 GHz band, while satisfying the FCC spectral mask [93]. These pulses are usually sent by following a multi-level Pulse-Position Modulation (PPM) or Pulse Amplitude Modulation (PAM) with Time Hopping (TH) orthogonal sequences and spread in time [45, 112]. PPM or PAM are preferred over OOK because, in the conventional symmetric Additive White Gaussian Noise (AWGN) channel, OOK exhibits a 3 dB inferiority to PPM or PAM in terms of required signal-to-noise ratio to achieve a specific bit error probability. OOK is only considered when the simplicity of the transceiver is the major design constraint [164, 9].

These considerations are no longer valid for pulse-based communication in nanonetworks. First, as we will describe in Section 4.2.1, nanoscale transceivers can generate pulses which are approximately one-hundred-femtosecond long, *i.e.*, three orders of magnitude shorter than in IR-UWB. This makes the detection of the pulses much more challenging, and motivates the use of very simple modulations. In addition, the phase of the transmitted pulses cannot be controlled, which makes the use of antipodal modulations unfeasible. More importantly, as we will explain in Section 4.4.1, the behavior of the molecular absorption noise is drastically different to that of the conventional AWGN channel. All these facts motivate the investigation of new pulse-based communication schemes tailored to the peculiarities of nanonetworks in the Terahertz Band.

Besides IR-UWB, pulse-based modulations are also widely used in FSO communication systems. In these systems, very short pulses, *e.g.*, usually one to ten femtoseconds long, are transmitted in bursts by following OOK, PAM or other simple binary modulations. The use of photodetectors usually results in an asymmetric noise behavior, which is conceptually similar to that of the molecular absorption noise at Terahertz Band frequencies [24, 14]. However, in FSO, pulses are not spread in time and, thus, concurrent transmission from different users result in interference, unless more advanced medium sharing techniques are used. As IR-UWB, in our proposed scheme, pulses are spread in time, mainly due to the nano-transceiver limitations (Section 4.2.1). This reduces the maximum achievable bit-rate but enables concurrent transmissions amongst different nanomachines (Section 4.3.2). Next, we describe the peculiarities of Terahertz Band pulse-based systems, which will be leveraged to proposed a new modulation and channel access scheme.

4.2 Terahertz Band Pulse-based Systems

In this section, first, we review the state of the art in nanoscale Terahertz Band signal generators and detectors. Then, we describe the main channel phenomena that affect the propagation of pulses in the Terahertz Band, which are considered in our analysis.

4.2.1 Signal Generation and Detection

Terahertz Band signal generators and detectors for communication among nanomachines must be i) compact, *i.e.*, up to several hundreds of square nanometers or a few square micrometers at most; ii) fast, *i.e.*, able to support modulation bandwidths of at least several GHz; ii) energy-efficient, and iv) preferably tunable. Several technologies are been investigated for the generation and detection of Terahertz Band radiation from compact devices.

From the signal generation perspective, Quantum Cascade Lasers (QCLs) [153, 77] and frequency up-converters [103, 78] are two of the main alternatives. On the one hand, QCLs can be used as local oscillators (LO) in heterodyne transceiver architectures. QCLs can operate at frequencies above a few THz and can generate an average power in the order of a few mW when operating at cryogenic temperatures. However, the need of an external laser for optical electron pumping, their limited performance at room temperature, and especially their size (at least several square millimeters), hamper the application of QCLs for communication among nanomachines. On the other hand, frequency up-conversion techniques, which combine GHz sources and multi-stage frequency multipliers, do not require external optical devices and can operate at room temperature. However, their size (at least a few square millimeters) and narrow modulation bandwidth (few MHz at most) limit their application in high-speed communication.

From the signal detection point of view, bolometers [130, 17] and Schottky diodes [125] have been investigated for direct detection of Terahertz Band radiation. On the one hand, bolometric detectors are able to detect very low power signals and have a high modulation bandwidth (up to a few GHz). However, their performance is usually reduced when operating at room temperature and their size poses a major constraint for the nanomachines. Similarly, detection systems based on Schottky diodes can operate at room temperature and exhibit a high modulation bandwidth (up to 10 GHz), but their size and difficulty in the integration with the rest of the nano-transceiver pose significant challenges.

More recently, compact signal generators and detectors are being developed by using a single HEMT based on III-V semiconductors (e..g., Gallium Nitride, Gallium Arsenide) as well as graphene [66, 97, 144, 145]. In particular, it has been recently shown that SPP waves at Terahertz Band frequencies can be excited in the channel of a HEMT with nanometric gate length by means of either electrical or optical pumping. The working principle of such devices in emission is as follows. When a voltage is applied between the drain and the source of the HEMT, electrons are accelerated from the source to the drain. This sudden movement of electrons results in the excitation of a SPP wave due to the energy band-structure of the building material of the HEMT. At cryogenic temperatures, the periodic excitation of the electrons can result in well-defined resonant SPP waves. At room temperature, SPP waves are overdamped, and thus, only broadband incoherent waveforms are generated, *i.e.*, very short pulse-like radiation (one-hundred-femtosecond long). In any case, the generated SPP waveforms can be then radiated by the nano-antennas proposed in Chapter 2.

Reciprocally, in reception, the injection of SPP waves in the channel of a HEMT, for example by means of a graphene-based plasmonic nano-antenna, results into electrons being pushed from the source to the drain. This effectively creates a voltage between the drain and the source. Recent works show how HEMT-based plasmonic detectors provide excellent sensitivities with the intrinsic possibility of high-speed response (in principle just limited by the read-out electronics impedance). Similarly as in transmission, at room temperature, HEMT-based detectors can only measure the amplitude of the received signals (absolute power), but not its phase.

For all these, as we have already introduced in Section 3.4, we model the transmitted signals as one-hundred-femtosecond-long Gaussian pulses. The p.s.d. of these pulses has its main frequency components in the Terahertz Band. In Figure 24, we show the first time derivative of a one-hundred-femtosecond-long Gaussian pulse, both in the time domain and in the frequency domain. Its p.s.d. is centered at 1.6 THz with a 3dB bandwidth between 0.7 THz and 2.5 THz. Pulses with a peak power of a few μW, *i.e.*, with equivalent energies of just a few aJ (10^{-18}J), have been reported in the related literature [144, 145]. An additional technology limitation is that pulses cannot be transmitted in a burst, but due to the relaxation time of SPP waves in the HEMT channel, need to be spread in time. In our analysis, we consider the pulse energy and the spreading between pulses to be two technology parameters.

4.2.2 Pulse Propagation

The propagation of the generated pulses is determined by the Terahertz Band channel behavior. In particular, to characterize the propagation of the pulses, we are interested in the channel temporal response. Starting from Section 3.2, the Terahertz Band channel impulse

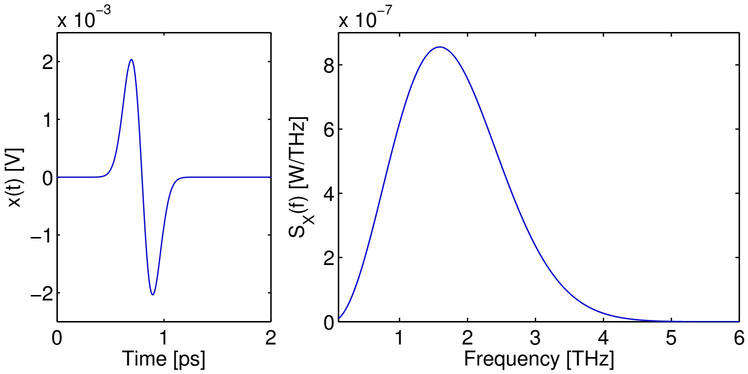

Figure 24. First time derivative of a one-hundred-femtosecond-long Gaussian pulse with a total energy of 1 aJ, both in the time domain (left) and in the frequency domain (right).

response H in the frequency domain can be written as

$$H(f,d) = H_{spread}(f,d)\, H_{abs}(f,d)\,, \tag{69}$$

where H_{spread} and H_{abs} refer to the spreading loss and the molecular absorption loss, respectively, and are given by

$$H_{spread}(f,d) = \left(\frac{c_0}{4\pi d f_0}\right) \exp\left(-\imath 2\pi f d / c_0\right), \tag{70}$$

$$H_{abs}(f,d) = \exp\left(-\frac{1}{2} k(f)\, d\right), \tag{71}$$

where f stands for frequency, d stands for distance, c_0 is the speed of light in the vacuum, f_0 is the antenna design center frequency, and k is the medium absorption coefficient. In our model, we consider that the radiated power is spherically spread with distance and detected with an isotropic broadband antenna with effective area given by $A_{eft} = \lambda_0^2/4\pi$, where $\lambda_0 = c_0/f_0$.

Finally, the channel impulse response h in the time domain t can be obtained by using the Inverse Fourier transform

$$h(t,d) = \mathcal{F}^{-1}\left\{H(f,d)\right\}. \tag{72}$$

This inverse Fourier Transform does not have an analytical expression. In our analysis, we will numerically compute the channel time response.

4.3 Time Spread On-Off Keying

In this section, we describe the proposed communication technique for nanonetworks, which serves both as a modulation scheme as well as a multiple access mechanism.

4.3.1 Modulation Definition

In light of the capabilities of nano-transceivers, we propose the use of TS-OOK for communication among nanomachines in the Terahertz Band. TS-OOK is based on the exchange of one-hundred-femtosecond-long pulses among nanomachines. The functioning of this communication scheme is as follows. Assuming that a nanomachine needs to transmit a binary bit stream,

- *A logical "1" is transmitted by using a one-hundred-femtosecond-long pulse and a logical "0" is transmitted as silence, i.e., the nanomachine remains silent when a logical zero is transmitted.* An OOK modulation is chosen because of the peculiar behavior of the noise in the Terahertz Band. As we will show in Section 4.4.1, noise in the Terahertz Band increases when molecules are irradiated; if no user is transmitting, molecular absorption noise becomes negligible. Thus, by being silent, the probability of incorrect symbol detection is lowered and, in addition, no energy is consumed in transmission. To avoid the confusion between the transmission of silence and the no transmission, initialization preambles and constant-length packets are used. After the detection of the preamble, the receiver counts the symbols in a packet. During this time, silence is considered a logical "0".

- *The time between transmissions is fixed and much longer than the pulse duration.* Due to nano-transceiver limitations exposed in Section 4.2.1, pulses or silences are not transmitted in a burst, but spread in time as in IR-UWB. By fixing the time between consecutive transmissions, after an initialization preamble, a nanomachine does not need to continuously sense the channel, but it just waits for the next transmission. This feature can be used to save energy if this is the main constraint of the network. Alternatively, during the time between transmissions a nanomachine can follow other nanomachines' bit streams or transmit its own data. This scheme does not require tight synchronization among nanomachines all the time, but only selected nanomachines will be synchronized after the detection of the initialization preamble for the duration of a packet transmission.

Under this scheme, the signal transmitted by a nanomachine u, $s_T^u(t)$ is given by:

$$s_T^u(t) = \sum_{k=1}^{K} A_k^u p\left(t - kT_s - \tau^u\right), \tag{73}$$

where K is the number of symbols per packet, A_k^u refers to the amplitude of the k-th symbol transmitted by the nanomachine u (either 0 or 1), p stands for a pulse with duration T_p, T_s refers to the time between consecutive transmissions, and τ^u is a random initial transmission delay. In general, the time between symbols is much longer than the time between pulses. Following the usual notation, we define $\beta = T_s/T_p \gg 1$.

The signal received by a nanomachine j can be written as

$$s_R^j(t) = \sum_{k=1}^{K} A_k^u p\left(t - kT_s - \tau^u\right) * h^{u,j}(t) + n_k^{u,j}(t), \tag{74}$$

where $h^{u,j}$ is the Terahertz channel impulse response between the nanomachines u and j, in (72), and $n_k^{u,j}$ stands for the molecular absorption noise created between u and j by the transmission of symbol k. $h^{u,j}$ depends on the specific medium conditions and the distance between the transmitter u and the receiver j. Similarly, the molecular absorption noise $n_k^{u,j}$ depends on the medium conditions and the transmission distance and it is correlated with the transmitted symbol k, as we will explain in Section 4.4.1.

4.3.2 Medium Sharing with TS-OOK

TS-OOK enables robust and concurrent communication among nanomachines. In the envisioned nanonetworking scenarios, nanomachines can start transmitting at any time without being synchronized or controlled by any type of network central entity. However, due to the fact that the time between transmissions T_s is much longer than the pulse duration T_p, several nanomachines can concurrently use the channel without necessarily affecting each other. In addition, the very short symbol duration T_p makes collisions between symbols highly unlikely. Moreover, not all types of collisions are *harmful*. For example, there are no collisions between silences, and collisions between pulses and silences are only harmful from the silence perspective, *i.e.*, the intended receiver for the pulse will not notice any difference if silence is received at the same time. In any case, collisions may occur, creating multi-user interference and thus limiting the achievable information rate of this communication scheme.

In the multi-user scenario, the signal received by a nanomachine j is given by

$$s_R^j(t) = \sum_{u=1}^{U} \sum_{k=1}^{K} A_k^u p\left(t - kT_s - \tau^u\right) * h^{u,j}(t) + n_k^{u,j}(t), \tag{75}$$

where $U-1$ is the number of interfering nanomachines, K is the number of symbols per packet, A_k^u refers to the amplitude of the k-th symbol transmitted by the nanomachine u (either 0 or 1), p stands for a pulse with duration T_p, T_s refers to the time between consecutive transmissions, τ^u is a random initial time, $h^{u,j}$ is the channel impulse response between u and j in (72), and $n_k^{u,j}$ stands for the molecular absorption noise created by the k-th transmission between u and j.

In Figure 25, we show an example of TS-OOK for the case in which two nanomachines are simultaneously transmitting different binary sequences to a third nanomachine. The upper plot corresponds to the sequence “1100001”, which is transmitted by the first nanomachine. A logical “1” is represented by the first derivative of a Gaussian pulse with T_p=100 fs, and a logical “0” is represented by silence. The time between symbols is T_s=5 ps, which is very small for a real case, but convenient for illustration purposes. This signal is propagated through the channel (thus, distorted and delayed) and corrupted with molecular absorption noise (only when pulses are transmitted). Similarly, the second plot shows the sequence transmitted by the second nanomachine, “1001001”. This second transmitter is farther from the receiver than the first transmitter. Thus, the signal suffers from higher attenuation, higher distortion and a longer delay. This can be seen in the third plot, which illustrates the signal at the receiver.

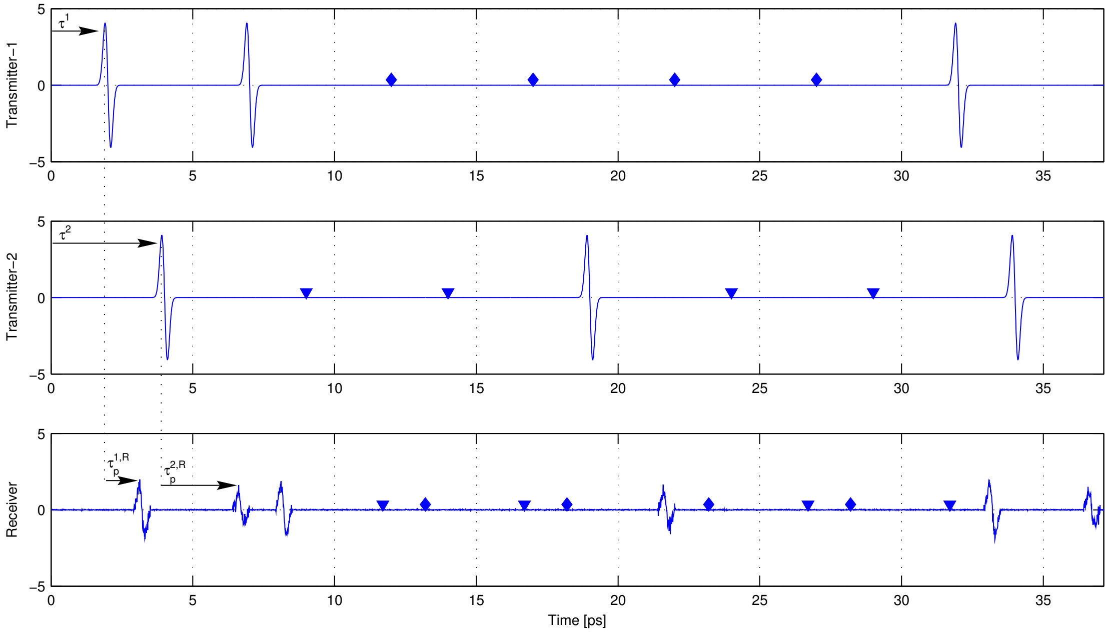

Figure 25. TS-OOK illustration: top) First nanomachine transmitting the sequence "1100001"; middle) Second nanomachine transmitting the sequence "100101"; bottom) Overlapped sequences at the receiver side.

4.4 Single-user Achievable Information Rate in TS-OOK

In this section, we develop a stochastic model of molecular absorption noise and analytically investigate the achievable information rate for TS-OOK in the single-user case.

4.4.1 Stochastic Model of Molecular Absorption Noise

To study the achievable information rate for TS-OOK in the single-user case, it is necessary to stochastically characterize the noise in the Terahertz Band. As described in Section 3.3, molecular absorption is one of the main noise sources at Terahertz Band frequencies. Excited molecules re-radiate part of the energy that they have previously absorbed out-of-phase. This is conventionally modeled as a noise factor [12].

A more detailed analysis of molecular absorption noise allows us to identify the following two main properties. On the one hand, molecular absorption noise is correlated to the transmitted signal. In particular, molecular absorption noise increases when transmitting, *i.e.*, there is only background noise unless the molecules are irradiated [41]. On the other hand, different molecules resonate at different frequencies and, moreover, their resonance is not confined to a single frequency but spread over a narrow band. As a result, the power spectral density (p.s.d.) of the noise has several peaks in frequency.

For a specific resonant frequency v, this noise can be characterized by a Gaussian probability distribution, with mean equal to zero and variance given by the noise power within the band of interest,

$$\mathcal{N}_v\left(\mu_v = 0, \sigma_v^2 = \int_B S_{N_v}(f)\, df\right), \tag{76}$$

where $S_{N_v}(f)$ refers to the p.s.d. of the molecular absorption noise created by the resonance v, and B stands for the receiver's equivalent noise bandwidth. By considering the different resonances from the same molecule as well as the resonances in different molecules to be independent, we can model the total molecular absorption noise also as additive Gaussian noise, with mean equal to zero and variance given by the addition of the noise power corresponding to each resonance, $\mathcal{N}\left(\mu = 0, \sigma^2 = \sum_v \sigma_v^2\right)$.

The variance of the molecular absorption noise can also be obtained by integrating the total noise p.s.d. over the receiver's noise equivalent bandwidth. The total molecular absorption noise p.s.d. S_{N_m} affecting the transmission of a symbol $m \in \{0, 1\}$ is contributed by the background atmospheric noise p.s.d. S_{N^B} [12] and the self-induced noise p.s.d. $S_{N_m^X}$, which are defined as

$$S_{N_m}(f, d) = S_{N^B}(f) + S_{N_m^X}(f, d), \tag{77}$$

$$S_{N^B}(f) = \lim_{d\to\infty} k_B T_0 \left(1 - \exp\left(-k(f)\, d\right)\right) \left(\frac{c_0}{\sqrt{4\pi} f_0}\right)^2, \tag{78}$$

$$S_{N_m^X}(f, d) = S_{X_m}(f) \left(1 - \exp\left(-k(f)\, d\right)\right) \left(\frac{c_0}{4\pi d f_0}\right)^2, \tag{79}$$

where f stands for the frequency, d refers to the transmission distance, k_B is the Boltzmann constant, T_0 is the room temperature, k is the molecular absorption coefficient, c_0 is the speed of light in the vacuum, f_0 is the design center frequency, and S_{X_m} is the p.s.d. of the transmitted signal. The term S_{N^B} takes into account that the background noise is i) generated from molecules that radiate just for being at a temperature above 0 K, and ii) detected by an isotropic broadband antenna with effective area given by $A_{eff} = \lambda_0^2/4\pi$. The term $S_{N_m^X}$ takes into account that the induced noise is i) generated by the transmitted signal X_m, ii) spherically spread from the transmitting antenna, and iii) detected by an isotropic broadband antenna with effective area A_{eff}.

Finally, the total noise power N_m when the symbol $m \in \{0, 1\}$ is transmitted is given by

$$N_m(d) = \int_B S_{N_m}(f, d) |H_r(f)|^2 \, df, \tag{80}$$

where B is the receiver's noise equivalent bandwidth and H_r is the receiver's impulse response. For the time being, we consider a matched-filter receiver architecture for simplicity. In Chapter 6, we will provide a more advanced symbol detection scheme tailored to the capabilities of nanomachines.

4.4.2 Analytical Study of the Single-user Information Rate

The maximum achievable information rate in bit/symbol IR_{u-sym} of a communication system is given by

$$IR_{u-sym} = \max_X \{H(X) - H(X|Y)\}, \tag{81}$$

where X refers to the source of information, Y refers to the output of the channel, $H(X)$ refers to the entropy of the source X, and $H(X|Y)$ stands for the conditional entropy of X given Y or the equivocation of the channel.

In our analysis, we consider the source of information X to be discrete, and the output signal of the transmitter s_T^u in (73), the channel response h in (72) and the molecular absorption noise n to be continuous. Under these considerations, the source X can be modeled as a discrete binary random variable. Therefore, the entropy of the source $H(X)$ is given by:

$$H(X) = -\sum_{m=0}^{1} p_X(x_m) \log_2 p_X(x_m), \tag{82}$$

where $p_X(x_m)$ refers to the probability of transmitting the symbol $m = \{0, 1\}$, *i.e.*, the probability to stay silent or to transmit a pulse, respectively.

The output Y of the channel can be modeled as a continuous random variable. In particular, the output of the transmitter is distorted by the channel h, and corrupted by the molecular absorption noise n. The only random component affecting the received signal is the molecular absorption noise.

In this case, the equivocation of the channel $H(X|Y)$ is given by:

$$H(X|Y) = \int_y f_Y(y) H(X|Y = y)\, dy = -\int_y f_Y(y) \sum_{m=0}^{1} p_X(x_m|Y = y) \log_2 (p_X(x_m|Y = y))\, dy, \tag{83}$$

where $p_X(x_m|Y = y)$ stands for the probability of having transmitted x_m given the output y. By recalling the Mixed Bayes Rule and the Total Probability Theorem [101], the equivocation $H(X|Y)$ can be written in terms of the probability of the channel output Y given the input x_m, $f_Y(Y|X = x_m)$,

$$H(X|Y) = \int_y \sum_{m=0}^{1} f_Y(y|X = x_m)\, p_X(x_m) \log_2 \left(\frac{\sum_{n=0}^{1} f_Y(y|X = x_n)\, p_X(x_n)}{f_Y(y|X = x_m)\, p_X(x_m)} \right) dy. \tag{84}$$

Based on the stochastic model of molecular absorption noise, the p.d.f. of the output of the system Y given the input $X = x_m$ can be written as:

$$f_Y(y|X = x_m) = \frac{1}{\sqrt{2\pi N_m}} e^{-\frac{1}{2}\frac{(y-a_m)^2}{N_m}}, \tag{85}$$

where N_m stands for the received noise power associated to the transmitted symbol x_m, which is given by (80), and a_m refers to the amplitude of the received symbol, which is obtained by using the Terahertz Band channel response given in Section 4.2.2.

By combining (82), (84) and (85) in (81), the achievable information rate in bit/symbol can be written as

$$\begin{aligned} IR_{u-sym} = \max_{X} \Bigg\{ & -\sum_{m=0}^{1} p_X(x_m)\log_2 p_X(x_m) - \int \sum_{m=0}^{1} \frac{1}{\sqrt{2\pi N_m}} e^{-\frac{1}{2}\frac{(y-a_m)^2}{N_m}} p_X(x_m) \\ & \cdot \log_2\left(\sum_{n=0}^{1} \frac{p_X(x_n)}{p_X(x_m)} \sqrt{\frac{N_m}{N_n}} e^{-\frac{1}{2}\frac{(y-a_n)^2}{N_n}+\frac{1}{2}\frac{(y-a_m)^2}{N_m}} \right) dy \Bigg\} \\ = -\max_{p_X(x_0)} \Bigg\{ & \int \frac{p_X(x_0)}{\sqrt{2\pi N_0}} e^{-\frac{1}{2}\frac{y^2}{N_0}} \log_2\left(p_X(x_0)\left(1+\frac{1-p_X(x_0)}{p_X(x_0)}\sqrt{\frac{N_0}{N_1}} e^{-\frac{1}{2}\frac{y^2}{N_0}+\frac{1}{2}\frac{(y-a_1)^2}{N_1}}\right)\right) \\ & + \frac{1-p_X(x_0)}{\sqrt{2\pi N_1}} e^{-\frac{1}{2}\frac{(y-a_1)^2}{N_1}} \log_2\left((1-p_X(x_0))\left(1+\frac{p_X(x_0)}{1-p_X(x_0)}\sqrt{\frac{N_1}{N_0}} e^{-\frac{1}{2}\frac{(y-a_1)^2}{N_1}+\frac{1}{2}\frac{y^2}{N_0}}\right)\right) dy \Bigg\}. \end{aligned} \tag{86}$$

Finally, the maximum achievable information rate in bit/second is obtained by multiplying the rate in bit/symbol (86) by the rate at which symbols are transmitted, $R = 1/T_s = 1/(\beta T_p)$, where T_s is the time between symbols, T_p is the pulse length, and β is the ratio between them. If we assume that the $BT_p \approx 1$, where B stands for the channel bandwidth, the rate in bit/second is given by:

$$IR_u = \frac{B}{\beta} IR_{u-sym}. \tag{87}$$

If $\beta = 1$, *i.e.*, all the symbols (pulses or silences) are transmitted in a burst, and the maximum rate per nanomachine is achieved, provided that the incoming information rate and the read-out rate to and from the nano-transceiver can match the channel rate. By increasing β, the single-user rate is reduced, but the requirements on the transceiver are greatly relaxed, as we explained in Section 4.2.1. Analytically solving the maximum information rate expression given by (86) is not feasible. Instead, we numerically investigate it in Section 4.6. Up to this point, it has been assumed that only one nanomachine is utilizing the channel. In the following section, the impact of interference in the information rate is investigated.

4.5 Multi-user Achievable Information Rate in TS-OOK

In this section, we develop a stochastic model for interference in TS-OOK and formulate the multi-user achievable information rate analytically.

4.5.1 Stochastic Model of Multi-user Interference in TS-OOK

Multi-user interference in TS-OOK occurs when symbols from different nanomachines reach the receiver at the same time and overlap. Without loss of generality, we focus on the symbols transmitted by the nanomachine number 1. Then, the interference I at the receiver j during the detection of a symbol from node number 1 is given by:

$$I = \sum_{u=2}^{U} A^{u} \left(p * h\right)^{u,j} \left(\mathcal{T}_1^u\right) + n^{u,j} \left(\mathcal{T}_1^u\right), \tag{88}$$

where U refers to the total number of nanomachines, A^u is the amplitude of the symbol transmitted by the nanomachine u (either one or zero), $(p * h)^{u,j}$ stands for the transmitted pulse convoluted with the channel impulse response between nanomachines u and j, $\mathcal{T}_1^u$ is the time difference at the receiver side between the transmissions from nanomachines 1 and u, and $n^{u,j}$ is the absorption noise created at the receiver by the transmissions from the nanomachine u.

Many stochastic models of interference have been developed to date. For example, an extensive review of the existing models can be found in [16, 7, 157]. However, these models do not capture the peculiarities of the Terahertz Band channel, such as the molecular absorption loss and the additional molecular absorption noise created by interfering nodes. In order to provide a stochastic characterization of the interference in TS-OOK, we make the following considerations:

1. Nanomachines are not controlled by a central entity, but they communicate in an uncoordinated fashion.

2. Transmissions from different nanomachines are independent and follow the same source probability X.

3. The random initial time τ in (73) is uniformly distributed.

4. Nanomachines are uniformly distributed in space, thus, the propagation delay between any pair of nanomachines is also uniformly distributed in time.

5. Collisions between silences are not harmful. Collisions between pulses and silences are only harmful from the silence perspective.

Under these considerations, the time difference at the receiver side between the transmissions from the nanomachines 1 and u, $\mathcal{T}_1^u$, can be modeled as a uniform random variable over $[0, T_s]$. In addition, we can model the overall interference I as a Gaussian random process, $\mathcal{N}_I\left(\mu_I = E\left[I\right]; \sigma_I^2 = N_I\right)$, where $E\left[I\right]$ and N_I are the mean and variance of the interference, respectively. Indeed, for a single interfering nanomachine, the amplitude of the interference depends on the propagation conditions and the distance between this user and the receiver. In addition, this interference can be constructive or destructive, depending on the reflections that pulses may suffer. Then, for a large number of users, we can invoke the Central Limit Theorem [101], and make the Gaussian assumption for I.

The mean of the interference $E\left[I\right]$ is defined as:

$$E\left[I\right] = E\left[\sum_{u=2}^{U} A^u \left(p * h\right)^{u,j} \left(\mathcal{T}_1^u\right) + n^{u,j} \left(\mathcal{T}_1^u\right)\right] = \sum_{u=2}^{U} \frac{T_p}{T_s} a^{u,j} p_X\left(x_1\right) = \sum_{u=2}^{U} \frac{a^{u,j}}{\beta} p_X\left(x_1\right), \quad (89)$$

where U refers to the total number of nanomachines, T_p is the pulse length, T_s is the time between symbols, and $a^{u,j}$ is the average amplitude of a pulse at the receiver, j, transmitted by the nanomachine u.

The variance of the interference is given by:

$$N_I = E\left[I^2\right] - E\left[I\right]^2, \quad (90)$$

where

$$\begin{aligned} E\left[I^2\right] &= E\left[\left(\sum_{u=2}^{U} A^u \left(p * h\right)^{u,j} \left(\mathcal{T}_1^u\right) + n^{u,j} \left(\mathcal{T}_1^u\right)\right)^2\right] \\ &= \sum_{u=2}^{U} \left(\frac{\left(a^{u,j}\right)^2 + N^{u,j}}{\beta}\right) p_X\left(x_1\right) + 2 \sum_{u=2<v}^{U} \left(\frac{p_X\left(x_1\right)}{\beta}\right)^2 a^{u,j} a^{v,j}, \end{aligned} \quad (91)$$

and which results in

$$N_I = \sum_{u=2}^{U} \left(\frac{\left(a^{u,j}\right)^2 + N^{u,j}}{\beta}\right) p_X\left(x_1\right) + 2 \sum_{u=2<v}^{U} \left(\frac{p_X\left(x_1\right)}{\beta}\right)^2 a^{u,j} a^{v,j} - \left(\sum_{u=2}^{U} \frac{a^{u,j}}{\beta} p_X\left(x_1\right)\right)^2, \quad (92)$$

where U is the total number of nanomachines, $a^{u,j}$ refers to the amplitude of the pulse transmitted by u at the receiver j, $N^{u,j}$ is the noise power created from the transmission from u to j, and $p_X(x_1)$ is the probability of transmitting a pulse.

4.5.2 Analytical Study of the Multi-user Information Rate

We define the multi-user achievable information rate as the maximum aggregated throughput that can be transmitted over the network, *i.e.*,

$$IR_{net} = UIR_u^I = \frac{B}{\beta} IR_{u-sym}^I, \tag{93}$$

where U refers to the number of interfering nanomachines, IR_u^I is the maximum achievable information rate in bit/second for every single nanomachine in the presence of interference, B is the channel bandwidth and β is the spreading factor, and IR_{u-sym}^I is the achievable information rate in bit/symbol. Because of multi-user interference, IR_{u-sym}^I cannot be directly computed from (81). The optimal source distribution X depends on the number of interfering nanomachines in the network, U, and, thus, obtaining the multi-user maximum achievable information rate means to jointly optimize X and U.

In order to determine the IR_{u-sym}^I as a function of the number of nanomachines U, we need to add the contribution of interference into the probability of the output Y given the input $X = x_m$. Taking into account the previously introduced model for interference, now (85) becomes

$$f_Y^I(y|X = x_m) = \frac{1}{\sqrt{2\pi (N_m + N_I)}} e^{-\frac{1}{2}\frac{(y - E[I] - a_m)^2}{N_m + N_I}}, \tag{94}$$

where N_m stands for the noise power associated to the symbol m, N_I is variance of the interference, and $E[I]$ is the mean value of the interference. Then, IR_{u-sym}^I can be obtained by combining (94), (84) and (82) in (81). Finally, the multi-user achievable information rate is given by

$$\begin{aligned} IR_{net} &= \max_{X}\left\{U\frac{B}{\beta}\left(-\sum_{m=0}^{1} p_X\left(x_m\right)\log_2 p_X\left(x_m\right) - \int\sum_{m=0}^{1}\frac{1}{\sqrt{2\pi\left(N_m+N_I\right)}}e^{-\frac{1}{2}\frac{(y-E[I]-a_m)^2}{N_m+N_I}}p_X\left(x_m\right)\right.\right. \\ &\qquad\left.\left.\cdot\log_2\left(\sum_{n=0}^{1}\frac{p_X\left(x_n\right)}{p_X\left(x_m\right)}\sqrt{\frac{N_m+N_I}{N_n+N_I}}e^{-\frac{1}{2}\frac{(y-E[I]-a_n)^2}{N_m+N_I}+\frac{1}{2}\frac{(y-E[I]-a_m)^2}{N_m+N_I}}\right)dy\right)\right\} \\ &= -\max_{p_X(x_0)}\left\{U\frac{B}{\beta}\int\frac{p_X\left(x_0\right)}{\sqrt{2\pi\left(N_0+N_I\right)}}e^{-\frac{1}{2}\frac{(y-E[I])^2}{N_0+N_I}}\cdot\right. \\ &\qquad\log_2\left(p_X\left(x_0\right)\left(1+\frac{1-p_X\left(x_0\right)}{p_X\left(x_0\right)}\sqrt{\frac{N_0+N_I}{N_1+N_I}}e^{-\frac{1}{2}\frac{(y-E[I])^2}{N_0+N_I}+\frac{1}{2}\frac{(y-a_1-E[I])^2}{N_1+N_I}}\right)\right) \\ &\qquad+\frac{1-p_X\left(x_0\right)}{\sqrt{2\pi\left(N_1+N_I\right)}}e^{-\frac{1}{2}\frac{(y-a_1-E[I])^2}{N_1+N_I}}\cdot \\ &\qquad\left.\log_2\left(\left(1-p_X\left(x_0\right)\right)\left(1+\frac{p_X\left(x_0\right)}{1-p_X\left(x_0\right)}\sqrt{\frac{N_1+N_I}{N_0+N_I}}e^{-\frac{1}{2}\frac{(y-a_1-E[I])^2}{N_1+N_I}+\frac{1}{2}\frac{(y-E[I])^2}{N_0+N_I}}\right)\right)dy\right\}. \end{aligned} \tag{95}$$

Similarly to the single-user case, analytically solving this optimization problem is not feasible. For this, we numerically investigate it next.

4.6 Numerical Analysis

4.6.1 Single-user Achievable Information Rate

First, we numerically investigate the maximum achievable information rate for TS-OOK in the single-user case.

4.6.1.1 Received Signal Power and Noise Power Ratios

First of all, it is convenient to visualize the behavior of the received pulse power and noise power with the distance. The received power P_1 when a pulse has been transmitted is shown in Figure 26(a) as a function of the transmission distance d. In the same figure, the noise powers associated with the transmission of a pulse and of silence, N_1 and N_0, respectively, are also represented as functions of the transmission distance d. In particular,

- For distances below a few millimeters, the received power P_1 is much larger than the molecular absorption noise power N_1, created by the propagating pulse.

- For longer transmission distances, the received power P_1 and the noise power N_1, but the latter does so at a lower pace. More noise is generated as the signal propagates, but this is spread over a larger volume.

- The power N_0 associated with the transmission of silence is constant with distance and usually much smaller than N_1. This asymmetry in the noise behavior is the main difference with respect to the classical AWGN channel.

In Figure 26(b), the signal to noise ratio when a pulse is transmitted $S_1N_1R = P_1/N_1$ and the pulse-noise-power to silence-noise-power ratio N_1/N_0 are shown as functions of d. These two ratios play a major role in the achievable information rate and the probability source distribution for which it is achieved, as we explain next.

4.6.1.2 Achievable Information Rate

The single-user maximum achievable information rate IR_{u-sym} in (86) in bit/symbol is shown in Figure 26(c) as a function of the transmission distance d, for different values for the transmitted pulse energy E_p. Besides the Terahertz Band asymmetric noise model described in Section 4.4.1, we evaluate the case in which the same noise power affects the transmission of pulses and silences, as in the AWGN channel. The results are as follows:

- For transmission distances below a few millimeters, the information rate is almost constant and equal to 1 bit/symbol, which is the maximum information per symbol that can be transmitted in a binary system. For example, if $\beta = 1000$ and $B = 10$ THz, the single-user information rate is approximately 10 Gigabits per second. If $\beta = 10$, information rates in the order of 1 Terabit per second are possible. Ultimately, the achievable information rate is limited but the symbol generation rate and the maximum rate at which the electronics at the receiver side can process the received signals. As discussed in Section 4.2.1, the use of graphene and other very high-electron-mobility materials, will enable the processing at speeds up to a few Terabits per second, thus, making the most out of the Terahertz Band channel.

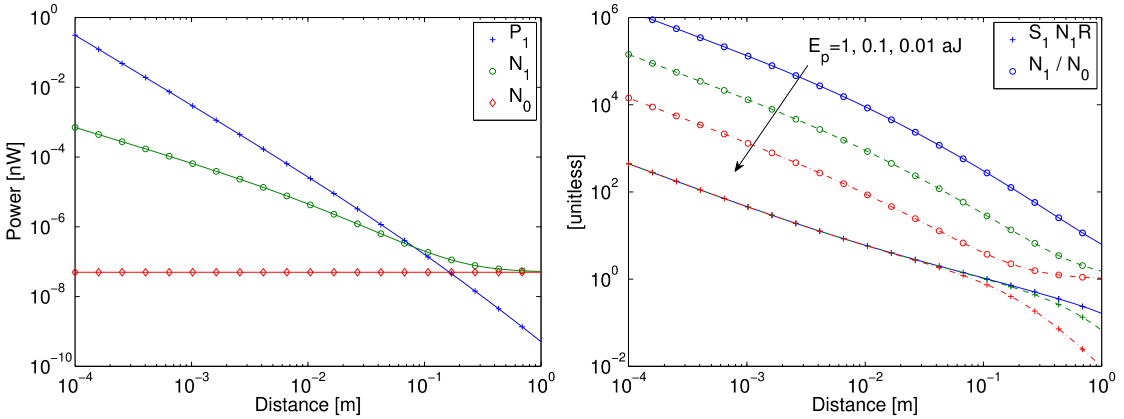

(a) Received signal power P_1, noise power when a pulse is transmitted N_1, and noise power associated with silence N_0 ($E_p = 0.01$ aJ).

(b) Signal to noise ratio when a pulse is transmitted S_1N_1R and pulse noise power to silence noise power ratio N_1/N_0.

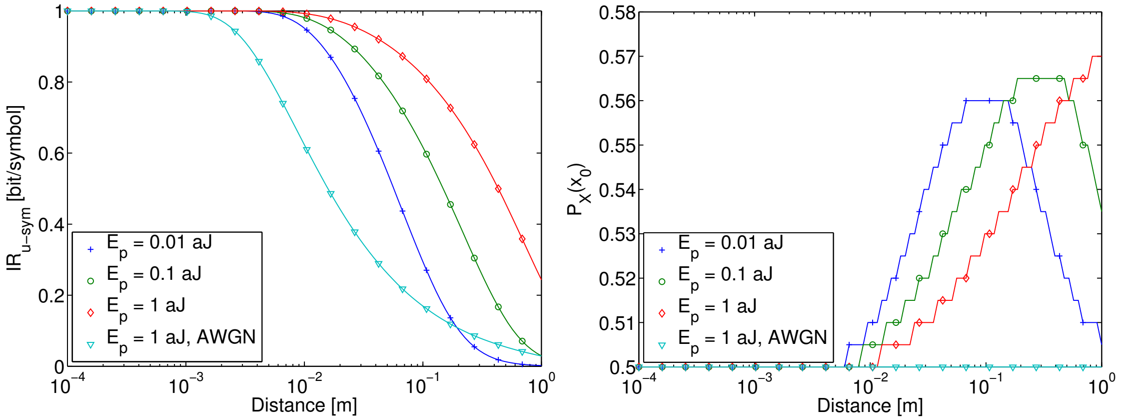

(c) Single-user information rate in bit/symbol for different noise power N_1 and N_0 ratios.

(d) Optimal probability to transmit a logical "0" for different noise power N_1 and N_0 ratios.

Figure 26. Numerical analysis of the single-user achievable information rate in TS-OOK.

- As the transmission distance increases, the achievable information rate decreases, but it does so at a lower pace than in the case of the symmetric additive Gaussian noise channel. This phenomenon can be explained as follows. When the transmission distance increases, the received signal power P_1 associated with the transmission of a pulse and the noise power N_1 created by the propagation of this pulse become comparable and, thus, the pulse to noise ratio, S_1N_1R, tends to one. However, as long as the total signal power received is higher than the background noise level N_0, the receiver can still distinguish between a transmission and a no-transmission, because the p.d.f.s of the two signals are largely different.

- When the transmission distance further increases, the noise power N_1 tends to N_0, and thus, the achievable information rate tends to zero because the symbols cannot be distinguished, as expected.

4.6.1.3 Optimal Source Probability Distribution

The asymmetric behavior of the Terahertz channel is also reflected on the optimal source probability distribution X for which the maximum achievable information rate is achieved. The optimal probability to transmit a logical "0", $p_X(X_0)$, for which the maximum rate is achieved is shown in Figure 26(d) as a function of the transmission distance d for different values of the pulse-noise-power to silence-noise-power ratio N_1/N_0. In particular,

- For transmission distances below a few millimeters, the optimal source probability distribution corresponds to the binary equiprobable distribution ($p_X(x_0) = p_X(x_1) = 0.5$), as in the symmetric AWGN channel.

- When the transmission distance increases, even if both silence and pulses can be easily detected, the optimal probability distribution is no longer the equiprobable one, but one that favors the transmission of silence rather than pulses, because the total noise or equivocation is much lower when zeros are transmitted. In particular, $p_X(x_0)$ approaches 0.55 for distances above 10 mm.

Ultimately, these results motivate the development of channel coding schemes in which more zeros than ones are used.

4.6.2 Multi-user Achievable Information Rate

In this section, we quantitatively study the effects of interference on the achievable information rate of a single user and on the aggregated throughput. The energy of a transmitted pulse is kept constant and equal to 0.01 aJ. The ratio between the time between pulses and the pulse duration is kept constant and equal to $\beta = 1000$.

4.6.2.1 Single-user Achievable Information Rate with Multi-user Interference

In Figure 27(a), the achievable information rate for every nanomachine IR^{I}_{u-sym} in bit/symbol, obtained from (81), (82) and (84) in (94), is shown as a function of the number of nanomachines U and the transmission distance d. The results show that

- For a low number of interfering nanomachines, the achievable information rate behaves with distance similarly to the single-user case studied in Section 4.6.1.
- As the number of interfering nanomachines increases, the total interference becomes the dominant term in the equivocation of the channel. As a result, the achievable information rate of every user tends to zero. Interference affects in the same way the reception of noise and the reception of pulses and, thus, once it becomes the dominant contribution to the received signal, the achievable information rate degrades quickly.

4.6.2.2 Multi-user Achievable Information Rate and Optimal Source Probability Distribution

The multi-user achievable information rate in bit/symbol, $IR_{net-sym} = IR_{net}(\beta/B)$ with IR_{net} given by (95), as a function of the number of interfering nanomachines U and the transmission distance d is shown in Figure 27(b). Different trends for the multi-user achievable information rate can be observed depending on the transmission distance and the number of nanomachines. To understand this behavior, it is important to identify which is the optimal source probability distribution X for which the multi-user achievable information rate is achieved. In Figure 27(c), the optimal probability to transmit a logical “0” $p_X(x_0)$, for which the single-user achievable information rate and the aggregated multi-user achievable information rate are achieved, is shown as a function of the number of nanomachines U and the transmission distance d.

In the multi-user scenario, *the optimal source distribution clearly prioritizes the transmission of logical “0”s or silence over logical “1”s or pulses*, i.e., $p_X(x_0) \gg p_X(x_1)$. This

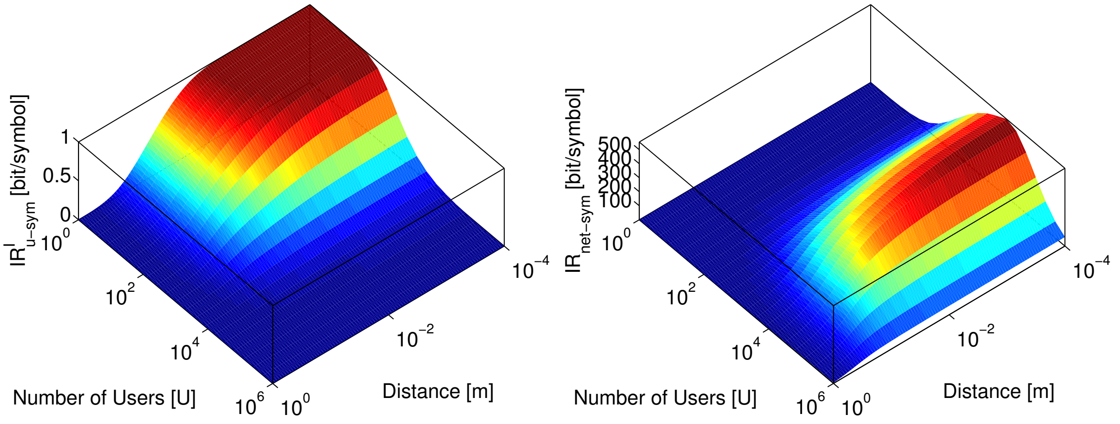

(a) Single-user achievable information rate for every single nanomachine.

(b) Aggregated multi-user achievable information rate.

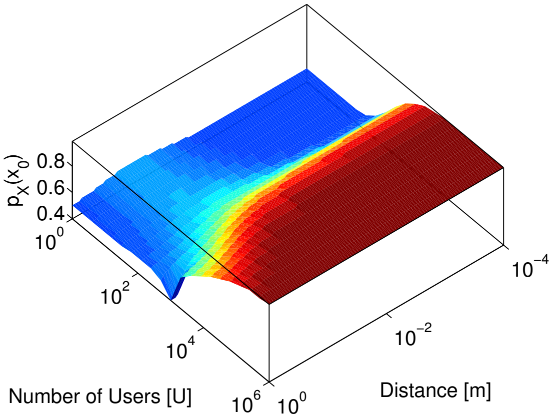

(c) Optimal probability to transmit a logical "0".

Figure 27. Numerical analysis of the multi-user achievable information rate in TS-OOK.

is due to the fact that by transmitting silence, both the molecular absorption noise and especially the interference power are drastically reduced. Indeed, this result is just numerically stating that collisions between silence are never harmful, and, thus, it is more convenient for the entire network to minimize the number of pulses that are sent. This behavior is not seen in PAM or PPM modulations, where the information is modulated in the shape or the position of the pulses, and pulses are always transmitted. In TS-OOK, *the information is ultimately placed in the presence or absence of "signal"* (in this case a pulse due to technology limitations, but could be just any signal shape or even noise). This result motivates the development of channel coding schemes suited for nanomachines and which maximize the number of logical "0"s. Note that, at the same time, by transmitting less pulses, the total energy consumption for every device is also reduced. Finally, note that for the highest node densities, the Gaussian approximation might not hold any longer, due to the fact that the probability to transmit a pulse tends to 0 and thus, the interference tends to 0. However, the utilized model is sufficient to illustrate the trends in the achievable rates.

We can now explain the behavior of the multi-user achievable information rate for the different transmission distances:

- When the transmission distance is short, below a few tens of millimeters, the multi-user achievable information rate increases with the number U of nanomachines up to a point at which it reaches a constant value. This effect appears because, even when the number of interfering nanomachines is drastically increased, provided that the individual probability to transmit silence is much higher than the probability to transmit a pulse ($p_X(x_0) \gg p_X(x_1)$), the total interference does not increase at the same pace. Thus, the received signal power is sufficiently large to be distinguishable from the reception of silence.

- When the transmission distance is increased, even by transmitting primarily silence, the power of the received signal when a pulse is transmitted diminishes very fast because of the very high path-loss of the Terahertz Band, and it is very difficult for the receiver to discern between pulses and silence. It is interesting to note that, for transmission distances above a few tens of millimeters, there is an optimal number of users for which the multi-user achievable information rate is maximum. The optimal point is again related to the relation between the transmitted and received pulse energy and the total interference power.

4.7 Conclusions

In this chapter, we have presented a new communication modulation and channel access scheme for nanomachines, which is based on the exchange of femtosecond-long pulses by following an on-off keying modulation spread in time. We have studied the performance of this new paradigm analytically and provided numerical solutions to the maximal achievable information rate for the single-user and the multi-user cases. We have developed analytical models for the path-loss, molecular absorption noise and interference in the Terahertz Band, which is the expected frequency range of operation of novel graphene-based plasmonic nano-antennas and nano-transceivers.

Our results show that nanonetworks can support a very large number of nanomachines (*i.e.*, tens of thousands of nanomachines in close vicinity) simultaneously transmitting at very high bit-rates (*i.e.*, up to several Terabits per second, each), given that asymmetric channel coding schemes are used to prioritize the transmission of silence. Indeed, both the maximum single-user and multi-user information rates are achieved when asymmetric source probability distributions are used, contrary to the classical symmetric AWGN channel. This study stimulates discussion and further research on channel coding and medium access techniques for nanonetworks in the Terahertz Band, which will be provided in Chapter 5 and Chapter 8, respectively.

CHAPTER 5

LOW-WEIGHT CHANNEL CODES FOR ERROR PREVENTION IN ELECTROMAGNETIC NANONETWORKS

An additional step towards enabling electromagnetic communication among nanomachines is the development of error control mechanisms suited for this paradigm. In this chapter, we propose the use of low-weight channel codes for error prevention in electromagnetic nanonetworks. Rather than retransmitting or trying to correct channel errors, we attempt to prevent these errors from happening in first instance. In particular, we show that, by reducing the channel coding weight, *i.e.*, the average number of logical "1"s in a codeword, both the molecular absorption noise in the Terahertz Band and the multi-user interference in TS-OOK can be mitigated. As a result, the channel equivocation and the Codeword Error Rate (CER) are reduced. This is achieved without penalizing and even increasing the achievable information rate after coding. In addition, we show that there is an optimal coding weight for which the achievable information rate is maximized, which depends on the channel and network conditions. This result motivates the development of novel link policies and Medium Access Control protocols that can dynamically adapt the coding weight to the channel and network conditions.

5.1 Motivation and Related Work

Molecular absorption noise in the Terahertz Band and multi-user interference in TS-OOK result in channel errors. Classical error control mechanisms might not directly be used in nanonetworks due to several reasons:

- *Automatic Repeat reQuest (ARQ)* mechanisms are not adequate for nanonetworks due to the very large amount of energy needed to retransmit a packet. As we will discuss in Chapter 7, nanoscale energy harvesting mechanisms are needed by nanomachines to operate. The time needed to harvest enough energy to transmit one full packet can be of up to several minutes, and thus, retransmissions drastically impact the throughput of nanonetworks.

- *Forward Error Correction (FEC)* mechanisms are generally too complex for the expected capabilities of the nanomachines. As we mentioned before, the number of nano-transistors in a nano-processor limits the complexity of the operations that it can complete. Even with current processing technologies, the time needed to encode and decode a packet can be much longer than the packet transmission time. Similarly, Hybrid ARQ systems are too complex for the capabilities of nanomachines.

These constraints motivate a different approach to error control in nanonetworks. In particular, instead of ignoring the channel error sources and retransmitting a packet several times (ARQ approach) or trying to correct the channel errors a posteriori (FEC approach), it is relevant to look at how these channel errors can be prevented from happening a priori. The peculiar nature of channel errors in nanonetworks opens the door to a different type of error control mechanisms, which reduce the number of channel errors by adapting the coding weight to the nanonetwork conditions. This is possible thanks to the peculiar nature of molecular absorption noise in the Terahertz Band and multi-user interference in TS-OOK. Modifying the coding weight is a much simpler operation than using error correction techniques and, in the simplest case, can be implemented with a look-up table.

Existing channel codes generally make use of all the possible codewords independently of their weight. However, it is sometimes desirable to limit the values that the weight of the codewords can take. In this direction, ration coding techniques were proposed in [135] to reduce the electronic noise in chip interconnects. By keeping the weight of the codewords constant, it was shown that the electronic noise can be reduced. In a similar direction, in [113], the performance of sparse Low Density Parity Check (LDPC) codes was analyzed in terms of error probability as a function of their weight. In particular, the authors showed that for the binary symmetric channel and the parallel Z channel, the block error probability of LDPC codes could be reduced by reducing the code weight.

Next, we first look at how the coding weight affects both the molecular absorption noise and multi-user interference power and, then, we analyze the performance of generic low-weight codes in nanonetworks.

5.2 Impact of Coding Weight on the Channel Error Sources

The two main sources of channel errors for nanonetworks operating under TS-OOK are molecular absorption noise and multi-user interference. The molecular absorption noise and the multi-user interference power depend on the coding weight, as we show next.

From Section 4.4.1, we know that the molecular absorption noise and the transmitted symbol are correlated. In particular, the p.d.f. $\mathcal{N}$ of the molecular absorption noise at the receiver conditioned to the transmission of symbol x_m (silence for a logical "0" and a pulse for a logical "1"), $f_{\mathcal{N}}(n|X = x_m)$, where n refers to noise, is given by,

$$f_{\mathcal{N}}(n|X = x_m) = \frac{1}{\sqrt{2\pi N_m}} e^{-\frac{1}{2}\frac{n^2}{N_m}}, \tag{96}$$

where N_m refers to the variance of the molecular absorption noise given by (80). As illustrated in Figure 26(a), the value of N_m changes drastically whether a pulse is transmitted ($m = 1$) or nothing is transmitted ($m = 0$). Moreover, the total noise power drastically changes with distance, by several orders of magnitude.

Similarly, from Section 4.5.1, we know that the interference power depends on the interfering nodes source probability distribution X. Previously, we analyzed the interference in TS-OOK by modeling it as a Gaussian process. This assumption is valid for the case in which the network is supporting a very high traffic load, and it is shown that it is a useful asset for the analysis of the multi-user achievable information rate. However, in order to be more general, we need much more general models for the interference.

To better understand the correlation between the multi-user interference power and the coding weight, we first develop a new interference model that only assumes that nanomachines are randomly deployed by following a spatial Poisson point process. In particular, we want to obtain a closed-form expression for the probability density function of the interference power I created at the receiver side, $f_I(i)$, where i refers to interference power. Without loss of generality, we position the receiver at the origin of coordinates. The interference created at the receiver side by the nanomachines contained in an area of radius a is given by

$$I_a = \sum_{d \le a} g(d), \tag{97}$$

where g refers to the power of a given signal at a distance d from its transmitter. From Section 4.2.2, g can be written as

$$g(d) = \int_B S_x(f) \left(\frac{c_0}{4\pi f d} \right)^2 e^{-k(f)d} df, \tag{98}$$

where B refers to the bandwidth of the transmitted signal, S_x is the p.s.d. of the transmitted symbol x, f stands for frequency, c_0 refers to the speed of light, and k is the molecular absorption coefficient of the medium. In Figure 28, g is illustrated as a function of the distance d. For the distances considered in our analysis, between a few hundred of micrometers and up to one meter, g can be approximated by the polynomial

$$g(d) \approx \beta (d)^{-\alpha}, \tag{99}$$

where α and β are two constants which depend on the specific channel molecular composition as well as on the power and the shape of the transmitted signal. In particular, for a standard medium composition with 10% of water vapor molecules, $\alpha \approx 2.1$ and $\beta \approx 1.39 \cdot 10^{-18}$, when using one-hundred-femtosecond-long Gaussian pulses with an energy equal to 0.1 aJ.

To compute the overall interference created by the nanomachines contained within a disc of radius a, it is necessary to know the spatial distribution of the nodes. In our analysis, we model the positions of the nanomachines as a spatial Poisson point process. Therefore, the probability of finding k nodes in a disc of radius a and area A in m^2 can be written as

$$P[k \text{ in } A(a)] = \frac{(\lambda A(a))^k}{k!} e^{-\lambda A(a)}, \tag{100}$$

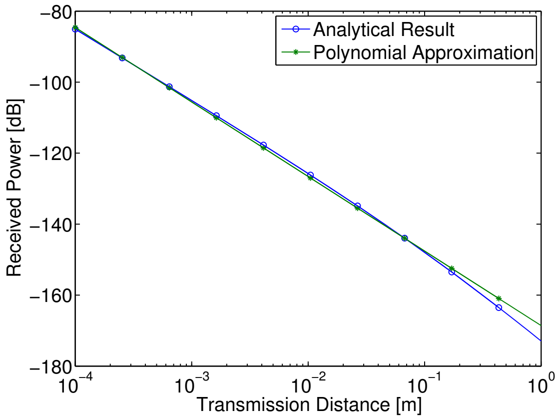

Figure 28. Received power in dBW as a function of the transmitted distance when transmitting one-hundred-femtosecond-long pulses with an energy equal to 0.1 aJ, in a medium with 10% of water vapor molecules.

where λ refers to the Poisson process parameter in nodes/m^2 and ! stands for the factorial operation.

A collision between symbols will occur when these reach the receiver at the same time. In TS-OOK, by considering also a Poisson distribution of the arrivals in time, the probability of having an arrival during T_s seconds is a uniform random probability distribution with p.d.f. equal to $1/T_s$. Thus, for a given transmission, a collision will occur with probability $2T_p/T_s$ (we assume that a correlation-based energy detector is used at the receiver). We should note that not all types of symbols *harmfully collide*, but only pulses (logical "1"s) create interference. Therefore, we can replace the Poisson parameter λ in (100) by

$$\lambda \rightarrow \lambda' = \lambda_T \left(2T_p/T_s\right) p_X \left(X = 1\right), \tag{101}$$

where λ_T refers to the density of active nodes in nodes/m^2, T_p refers to the symbol length, T_s stands for the time between symbols, and $p_X(X = 1)$ refers to the probability of a nanomachine to transmit a pulse (logical "1").

Following a similar procedure as in [131], to obtain a closed-form solution of the interference power, we first compute the characteristic function of the interference I_a created by the nodes in a disc of radius a, Φ_{I_a}, calculate its limit when the radius a goes to infinity, Φ_I, and obtain the p.d.f. of the interference power f_I as the inverse Fourier transform of Φ_I.

We define the characteristic function of the interference power I_a as

$$\Phi_{I_a}(\omega) = E\left\{exp\left(\jmath\omega I_a\right)\right\}, \tag{102}$$

which by using conditional expectation and taking into account the spatial Poisson distribution of the nodes, can be evaluated as

$$\Phi_{I_a}(\omega) = E\left\{E\left\{e^{\jmath\omega I_a}|k \text{ in } A(a)\right\}\right\} = \sum_{k=0}^{\infty}\frac{\left(\lambda'\pi a^2\right)^k}{k!}e^{-\lambda'\pi a^2}E\left\{e^{\jmath\omega I_a}|k \text{ in } A(a)\right\}, \tag{103}$$

where "k in $A(a)$" refers to the event of having k active nodes in a disk of radius a, and the expectation is over the random variable I_a. To compute this last term, we can proceed as follows. Under the Poisson assumption, when having k nodes in a disc of radius a, their locations follow independent and identically distributed uniform distributions. If R is the distance to the origin from a point that is uniformly distributed in A, then the p.d.f. of R is

$$f_R(d) = \begin{cases} (2r)/a^2 & 0 \le \mathrm{d} \le \mathrm{a} \\ 0 & \text{otherwise.} \end{cases} \tag{104}$$

Taking into account that the characteristic function of the sum of a number of independent random variables is the product of the individual characteristic functions, we can write

$$E\left\{e^{\jmath\omega I_a}|k \text{ in } A(a)\right\} = \left(\int_0^a \frac{2r}{a^2}e^{\jmath\omega g(d)}dr\right)^k. \tag{105}$$

By combining (105) in (103), summing the series, and computing the limit when $a \to \infty$, the characteristic function of the interference power becomes

$$\Phi_I(\omega) = exp\left(\jmath\lambda'\pi\omega\left(\int_0^\infty \left[1/g(t)\right]^2 e^{\jmath\omega t}dt\right)\right), \tag{106}$$

where λ' refers to spatial Poisson point process parameter as defined in (101) in nodes/m^2 and g stands for the received power at the origin for a signal transmitted at a distance t in (99).

Finally, for the specific case in which g can be approximated as a polynomial of the form $\beta t^{-\gamma}$, with $0 < \gamma = 2/\alpha < 1$, the integral in (106) may be evaluated to obtain:

$$\Phi_I(\omega) = exp\left(-\lambda'\pi\beta\Gamma(1-\gamma)\, e^{-\pi\gamma/2}\omega^{\gamma}\right), \tag{107}$$

where $\Gamma(\cdot)$ stands for the gamma function. For $0 < \gamma < 1$, the p.d.f. of I can now be obtained by taking the inverse Fourier transform, and results in

$$f_I(i) = \frac{1}{\pi i}\sum_{k=1}^{\infty}\frac{\Gamma(\gamma k+1)}{k!}\left(\frac{\pi\lambda'\beta\Gamma(1-\gamma)}{i^{\gamma}}\right)^{k}\sin k\pi(1-\gamma), \tag{108}$$

where λ' refers to the spatial Poisson point parameter given by (101), $\gamma \approx 0.95$ and $\beta \approx 1.39 \cdot 10^{-18}$.

In Figure 29(a), the p.d.f. f_I of the interference power (108) is illustrated for different values of λ'. In particular, λ' is obtained from (101), with $T_s/T_p = 1000$, $p_X(X = 1) = 0.5$ and for λ_T ranging between 0.01 nodes/mm^2 and 0.1 nodes/mm^2. For example, the interference created by a Poisson field of nanomachines with $\lambda_T = 0.1$ nodes/mm^2 which are operating under the previous conditions, has an average power of approximately -153 dBW. When the node density is decreased to $\lambda_T = 0.01$ nodes/mm^2, this value goes to -167 dBW.

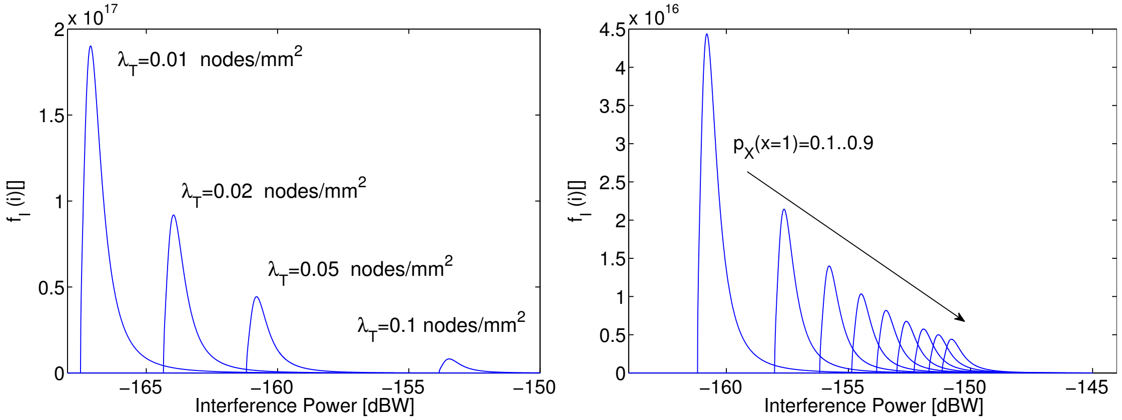

(a) Varying λ_T, $p_X(X = 1) = 0.5$ (b) Varying $p_X(X = 1)$, $\lambda_T = 0.1$ nodes/mm^2

Figure 29. Probability density function of the interference power for different transmitting node densities λ_T (left) and different probabilities to transmit a pulse $p_X(X = 1)$ (right), when $T_s/T_p = 1000$.

In Figure 29(b), the p.d.f. f_I of the interference power (108) is illustrated for different values of $p_X(X = 1)$, with $T_s/T_p = 1000$ and $\lambda_T = 0.1$ nodes/mm^2. It can be seen that the overall interference can decrease in more than 10 dB when the probability to transmit a pulse (logical "1") changes from 0.9 to 0.1. Based on these results as well as on the outcomes of the molecular absorption model, it is clear that the transmission of pulses (logical "1"s) increases both the total molecular absorption noise and the multi-user interference, which potentially results in a higher number of channel errors. New error control mechanisms can be developed by exploiting this unique behavior, as we present next.

5.3 Low Weight Coding for Channel Error Prevention

In existing communication systems, channel codes are used to allow the receiver of a message to detect and correct transmission errors. We propose to use channel codes to reduce the chances of having these errors in first instance. Our aim is not to develop new types of error correcting codes, but to analytically and numerically show how by controlling the coding weight, *i.e.*, the average number of bits equal to "1" in a codeword, of any type of codes, the molecular absorption noise power and the interference power can be reduced without compromising the information rate or even improving it.

In light of our discussion in Section 5.2, it is clear from (80), (101) and (108) that the probability of transmitting a pulse (logical "1") is directly related with the molecular absorption noise and the interference behaviors. By controlling the weight of the transmitted codewords, the probability distribution of "1"s and "0"s can be modified. Ultimately, by using *constant low-weight channel codes*, we can reduce the molecular absorption noise and the interference of the system. This reduction comes with the price of longer codewords, as usually in order to uniquely code a message with a lower weight, it will be necessary to use a larger number of bits.

To illustrate this effect, we proceed as follows. In our analysis, the length of an unencoded message is constant and equal to n bits. For a given n, the total number of possible n-bit words is given by 2^n. The length of an encoded message is $m \geq n$ bits, and its weight, which is defined as the number of bits equal to "1", is denoted by u. For a given m, the total number of possible codewords with weight exactly equal to u is given by:

$$\mathcal{W}(m, u) = \frac{m!}{(m-u)!u!}. \tag{109}$$

Therefore, in order to be able to encode all the possible n-bit source messages into *fixed weight u* codewords, the following condition must be satisfied:

$$\mathcal{W}(m,u) \geq 2^n, \tag{110}$$

where m refers to the size of the encoded words. For example, for $n = 32$ bits, a total of $m = 35$ bits are needed to generate 2^{32} codewords with exact weight equal to $u = 17$.

Then, for a constant weight code, the probability $p_X(X=1)$ of transmitting a logical "1" or pulse, and the probability $p_X(X=0)$ of transmitting a logical "0", *i.e.*, being silent, are:

$$p_X(X=1) = \frac{u}{m}; \quad p_X(X=0) = \frac{m-u}{m}, \tag{111}$$

where m stands for the number of bits in the encoded message, u stands for its weight and both m and u must satisfy (110). In Figure 30, the necessary codeword length in bits and the codeword weight necessary to achieve a specific probability of transmitting a pulse when encoding 32-bit messages is shown. For example, in order to achieve a probability of pulse transmission $p_X(X=1) = 0.3$, the encoded message size is $m = 42$ bit with weight $u = 12$.

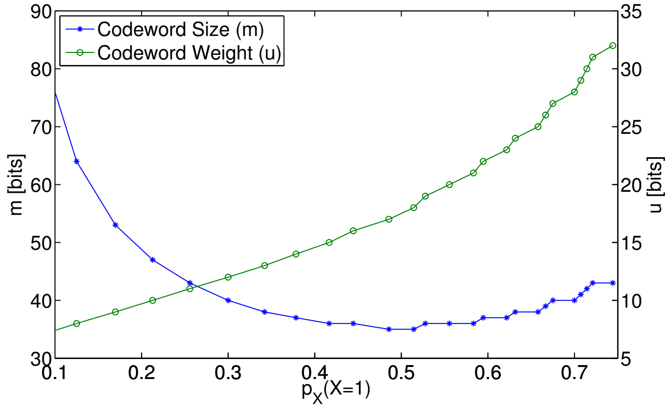

Figure 30. Codeword size m and constant code weight w as a function of the target probability of transmitting a logical "1".

Note that, up to this point, we are not advocating for any specific type of coding scheme. We are mainly estimating the additional number of bits which are necessary to obtain a constant low-weight set of codewords. Ideally, low-weight error correction codes can be built in one step. Alternatively, these can be obtained in a two cascade coding design. In any case, by reducing the weight of the code, we can reduce the molecular absorption noise and interference in the network. However, due to the fact that additional bits are being transmitted to reduce the coding weight, it is intuitive to think that the amount of useful information that can be transmitted per unit of time is reduced. This compromise is analyzed next.

5.4 Performance Analysis

In this section, we analytically study the impact of low weight channel codes on the information rate after coding and the Codeword Error Rate (CER). In addition, we show the existence of an optimal coding weight that maximizes the information rate after coding.

5.4.1 Information Rate After Coding

In Section 4.5, we have computed the achievable information rate with TS-OOK over the asymmetric Terahertz Band channel in the absence of coding. Next, we compute the achievable information rate after coding of TS-OOK with constant low-weight channel codes. In particular, the information rate after coding $IR_{u-coded}$ in bits/second for TS-OOK is given by

$$IR_{u-coded} = \frac{B}{\beta} IR_{u-sym-coded} = \frac{B}{\beta}\frac{n}{m}\left(H\left(X\right) - H^{I}\left(X|Y\right)\right), \tag{112}$$

where n and m are the unencoded and encoded message lengths respectively, B stands for the bandwidth, β is the ratio between the symbol duration and the pulse length, X refers to the source, Y refers to the output of the channel, $H\left(X\right)$ refers to the entropy of the source X, and $H^{I}\left(X|Y\right)$ stands for the equivocation of the channel in the presence of interference.

As before, we model the source of information X as a discrete binary random variable. The output of the transmitter is attenuated by the channel and corrupted by molecular absorption noise and interference. We consider the channel behavior to be deterministic. Thus, the only random components affecting the received signal are the noise and the interference. For the receiver, we consider both a soft receiver architecture, which provide us with a continuous output, and a hard receiver architecture, whose output is discrete.

5.4.1.1 Information Rate with a Soft Receiver

When using a soft receiver architecture, the output Y is continuous. In this case, the channel equivocation $H^I(X|Y)$ in (112) is given by (84). The p.d.f. $f_Y(y|X = x)$ of the channel output Y conditioned to the transmission of the symbol $X = x$ in (84) is now given by,

$$f_Y^{I'}(y|X = x) = \delta(y - a_m) * f_N(n = y|X = x) * \left(2y f_I\left(i = y^2\right)\right) \tag{113}$$

where δ stands for the Dirac delta function, a_m stands for the amplitude of the received symbol, f_N is the p.d.f. of the noise given by (96), f_I stands for the p.d.f. of the interference power given by (108), and $*$ denotes convolution. This equation considers the overall interference power I to be independent of the current symbol transmission $X = x$.

The maximum achievable information rate in this case can be obtained by combining (82), (84) and (113) in (112). Analytically solving the resulting equation is not feasible. Instead of this, we numerically investigate the achievable information rate after coding with a soft receiver in Section 5.5.

5.4.1.2 Information Rate with a Hard Receiver

A soft receiver with a continuous output infers the maximum achievable information rate at the cost of complexity. In practice, due to the limitation on the internal data size in nanomachines, quantization is unavoidable. For this, in our analysis, we also consider a 1-bit hard receiver architecture tailored to the asymmetric Terahertz Band channel. With a 1-bit hard receiver, the channel becomes a Binary Asymmetric Channel (BAC) and Y is now a discrete random variable. This channel is fully characterized by the four transition probabilities:

$$\begin{aligned}
p_Y(Y=0|X=0) &= \int_{th_1}^{th_2} f_Y(y|X=0)\,dy,\\
p_Y(Y=1|X=0) &= 1-p_Y(Y=0|X=0),\\
p_Y(Y=0|X=1) &= \int_{th_1}^{th_2} f_Y(y|X=1)\,dy,\\
p_Y(Y=1|X=1) &= 1-p_Y(Y=0|X=1),
\end{aligned} \tag{114}$$

where $f_Y(y|X=x)$ is the probability of the channel output Y conditioned to the transmission of the symbol $X=x$ in (85) and th_1 and th_2 are two threshold values. Contrary to the classical symmetric additive Gaussian noise channel, in the asymmetric channel, there are two points at which $f_Y(y|X=0)$ and $f_Y(y|X=1)$ intersect. We consider these thresholds to be defined for the case without interference. Thus, th_1 and th_2 can be analytically computed from the intersection between two Gaussian distributions $\mathcal{N}(0,N_0)$ and $\mathcal{N}(a_1,N_1)$ respectively, which results in

$$th_{1,2}=\frac{a_1N_0}{N_0-N_1}\pm\frac{\sqrt{2N_0N_1^2\log(N_1/N_0)-2N_0^2N_1\log(N_1/N_0)+a_1^2N_0N_1}}{N_0-N_1}, \tag{115}$$

where a_1 is the amplitude of the received signal given that a pulse has been transmitted and N_0 and N_1 stand for the distance dependent noise powers given by (80).

The equivocation of the channel $H^I_{BAC}(X|Y)$ for the BAC can be written as

$$H^I_{BAC}(X|Y)=\sum_{y=0}^{1}\sum_{x=0}^{1}p_Y(Y=y|X=x)\,p_X(X=x)\log_2\left(\frac{\sum_{q=0}^{1}p_Y(Y=y|X=q)\,p_X(X=q)}{p_Y(Y=y|X=x)\,p_X(X=x)}\right), \tag{116}$$

where $p_Y(Y=y|X=x)$ refers to the probability of receiving symbol $Y=y$ conditioned to the transmission of symbol $X=x$ and is given in (114). Finally, the information rate can be obtained by combining (112), (114) and (116). In Section 5.5, we numerically analyze the information rate of low-weight codes with a hard receiver with double threshold.

5.4.1.3 Optimal Coding Weight

From the information rate $IR_{u-coded}$ given by (112), we can make the following statements:

- For a fixed message size n, the encoded message size m increases exponentially when reducing the coding weight u, according to (110) and (109), as shown in Figure 30.
- The source entropy $H(X)$ given by (82) is maximized when $p_X(X = 1) = p_X(X = 0) = 0.5$. The coding weight u that maximizes the source entropy is given by $n/2$.
- The channel equivocation $H(X|Y)$ both for a soft receiver (84) and for a discrete output hard receiver (116) decreases when the coding weight u is reduced.

As a result, we can state that there is an optimal coding weight for which the information rate is maximized. The optimal coding weight depends on the channel conditions, *i.e.*, the molecular absorption noise (96), and the network conditions, *i.e.*, the multi-user interference (108). Analytically finding the optimal coding weight is not feasible. Alternatively, we numerically investigate the optimal coding weight that maximizes the information rate in Section 5.5.

5.4.2 Codeword Error Rate

In addition to the information rate, an additional relevant metric is the CER. The use of low-weight channel codes prevents the generation of channel errors due to molecular absorption noise and multi-user interference. This turns into a reduced symbol error rate (SER). The SER is given by

$$SER = p_Y(Y = 1|X = 0)\, p_X(X = 0) + p_Y(Y = 0|X = 1)\, p_X(X = 1), \tag{117}$$

where $p_Y(Y = y|X = x)$ is the probability of receiving symbol $Y = y$ given that symbol $X = x$ has been transmitted, which is given by (114), and $p_X(X = x)$ is the probability to transmit symbol $X = x$, which depends on the coding weight u and it is given by (111). The CER can be then computed as

$$CER = 1 - (1 - SER)^m, \tag{118}$$

where m is the encoded message length. We numerically investigate the CER in Section 5.5.

5.5 Numerical Results

In this section, we numerically investigate the performance of constant low-weight channel codes in terms of information rate after coding as well as CER. In our analysis, the unencoded message size n is equal to 32 bit. The coding weight u and the resulting probabilities to transmit a pulse or silence, $p_X(X = 1)$ and $p_X(X = 0)$, respectively, are computed accordingly by using (109) and (111). For the computation of the channel path-loss and the molecular absorption noise, the models developed in Chapter 3 are used. We consider a standard medium composition with a 10% of water vapor molecules. In an attempt to keep these numbers realistic and significant, the energy of the transmitted one-hundred-femtosecond-long Gaussian pulses is limited to 0.1 aJ. The stochastic models for the molecular absorption noise and the interference power given by (96) and (108) are used.

5.5.1 Information Rate After Coding

5.5.1.1 Information Rate with a Soft Receiver

The information rate $IR_{u-coded}$ with a soft receiver architecture, obtained by combining (82), (84) and (113) in (112), is shown in Figure 31 as a function of the transmission distance d, for different node densities λ_T in nodes/mm^2 and for different probabilities to transmit a logical "0", $p_X(X = 0)$ (111).

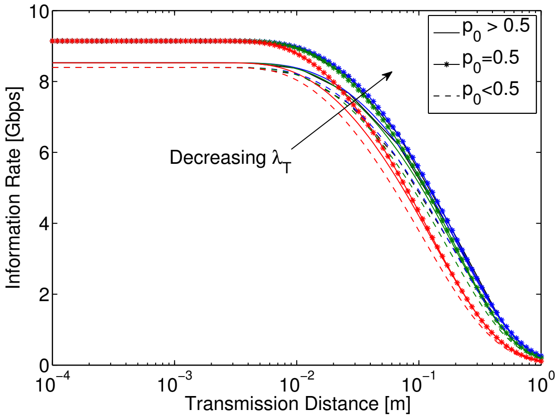

Figure 31. Information rate with a soft receiver architecture as a function of the transmission distance for different node densities and different probabilities of pulse transmission ($\beta = 1000$, $\lambda_T = 0.01, 0.1, 1$ nodes/mm^2).

For very short transmission distances $d < 10$ mm, the received signal power when a pulse is transmitted, *i.e.*, a_1, is much higher than the molecular absorption noise N_1, N_0 and the multi-user interference I, and the information rate reaches its maximum value. For this region, the maximum information rate is obtained when the coding weight is 0.5, as in the classical symmetric channel. As the transmission distance is increased, the received signal power when a pulse is transmitted a_1 tends to 0, but the noise power N_1 remains larger than the noise power N_0. Because the interference affects in the same way the transmission of "0"s and "1"s, a soft receiver will still be able to distinguish between symbols, and its equivocation can be minimized by choosing a lower coding weight. As the transmission distance is further increased, the noise power N_1 tends to N_0, and thus, symbols cannot be distinguished anymore. These results are in accordance to what we described in Section 4.6.2. The behavior of the information rate follows the same pattern for different node densities.

5.5.1.2 *Information Rate with a Hard Receiver*

The information rate $IR_{u-coded}$ with a hard receiver architecture, obtained by combining (82) and (116) in (112), is shown in Figure 32 as a function of the transmission distance d, for different node densities λ_T in nodes/mm^2 and for different probabilities to transmit a logical "0", $p_X(X = 0)$ (111).

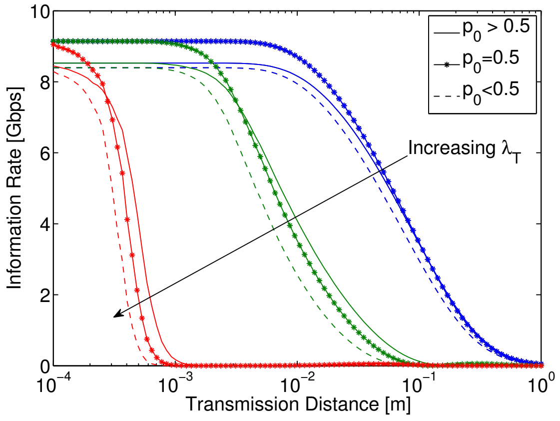

Figure 32. Information rate with a hard receiver architecture as a function of the transmission distance for different node densities and different probabilities of pulse transmission (β = 1000, $\lambda_T = 0.01, 0.1, 1$ nodes/mm^2).

For a specific node density, we can also distinguish three main regions in the behavior of the information rate after coding. In this case, the impact of the coding weight is more noticeable because the multi-user interference I (108) drastically impacts the performance of the hard receiver. In particular, interference shifts the received signal and makes a fixed-threshold th_1, th_2 in (115) detection scheme not optimal (contrary to the far more complex soft receiver architecture). In this case, the reduction of the coding weight, *i.e.*, the increase of $p_X(X = 0)$, turns into an improvement in the achievable information rate after coding. This result validates our original hypothesis and justifies this work. This effect can clearly be seen by analyzing the behavior of the codeword error rate (Section 5.5.2).

5.5.1.3 Optimal Coding Weight

In Figure 33, the optimal probability to transmit a logical "0", $p_X(X = 0)$, that maximizes the information rate is shown for both a soft receiver architecture and a hard receiver architecture, as a function of the transmission distance d.

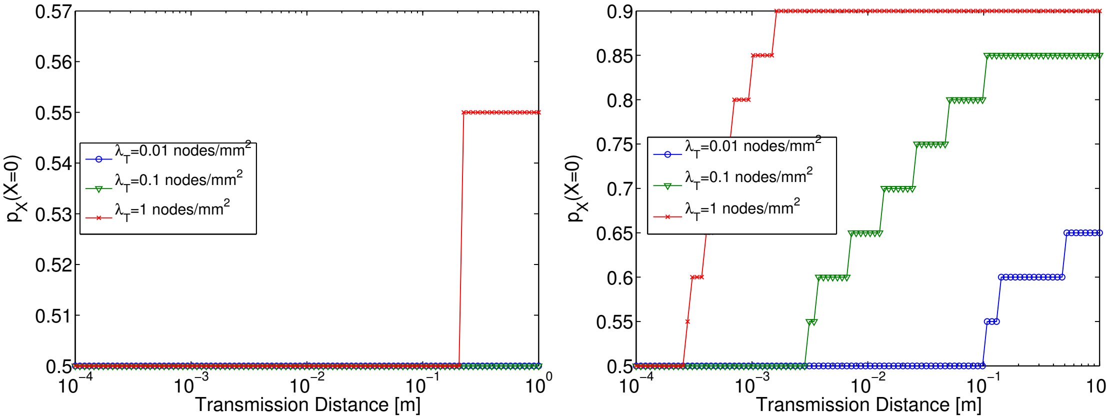

Figure 33. Optimal probability to transmit a logical "0", $p_X(X = 0)$**, that maximizes the information rate is shown for both a soft receiver architecture (left) and a hard receiver architecture (right)** ($T_s/T_p = 1000$, $\lambda_T = 0.01, 0.1, 1$ **nodes/mm**^{2}**).**

Following the same discussion as for the information rate after coding, we can also distinguish three main regions. For very short transmission distances, $d < 1$ mm, the optimal coding weight corresponds to the equiprobable source distribution $p_X(X = 0) = p_X(X = 1) = 0.5$. As the transmission distance is increased, the optimal coding weight increases the transmission of logical “0”s, *i.e.*, silence, and $p_X(X = 0) > 0.5$. This is specially visible for the hard-receiver architecture.

5.5.2 Codeword Error Rate

In Figure 34, the CER (118) is shown as a function of the transmission distance d, for different node densities λ_T in nodes/mm^2 and for different probabilities to transmit a logical “0”, $p_X(X = 0)$ (111). For a specific node density, the reduction of the coding weight turns into reduced error rates. This is specially valid for high interference scenarios, *i.e.*, high node densities in our analysis. For distances in the order of a few millimeters, which is expectedly the transmission range of nanomachines, the use of low-weight channel codes can clearly improve the CER. In particular, for very high node-densities, the improvement can be up to 150%.

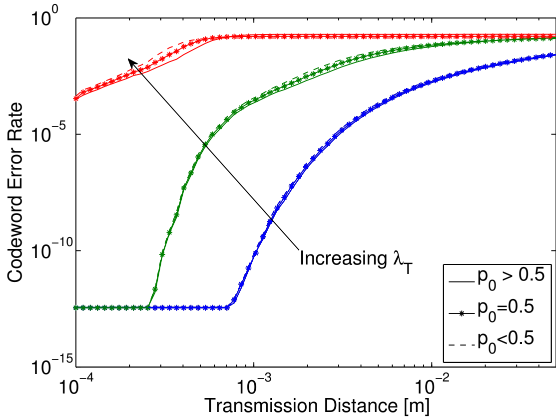

Figure 34. CER as a function of the transmission distance for different node densities and different probabilities of pulse transmission ($T_s/T_p = 1000$, $\lambda_T = 0.01, 0.1, 1$ nodes/mm^2).

The control of coding weight is a simple process that turns into energy savings, by i) transmitting less pulses (logical “1”s), ii) avoiding retransmissions, and iii) reducing the energy in computation and signal processing. Moreover, as discussed above, this is done without penalizing the information rate or even improving it.

5.6 Conclusions

In this chapter, we have proposed the utilization of low-weight channel codes to prevent channel errors in pulse-based electromagnetic nanonetworks in the Terahertz Band. For this, we have first investigated the impact of the coding weight on the two main error sources in electromagnetic nanonetworks, namely, the molecular absorption noise and the multi-user interference. Then, we have proposed the control of the coding weight as a mechanism to reduce the noise and interference power. Finally, we have investigated the performance of low-weight codes in terms of information rate and codeword error rate.

The results show how, by using low-weight channel codes, the overall noise and interference can be reduced while keeping constant or even increasing the achievable information rate. Moreover, we have shown that there is an optimal coding weight, which depends on the channel and network conditions, for which the information rate is maximized. Ultimately, these results motivate the development of novel link transmission policies as well as novel Medium Access Control protocols that can dynamically adapt the coding weight to the channel and network conditions, which we investigate in Chapter 8.

CHAPTER 6

RECEIVER SYMBOL DETECTION SCHEME FOR PULSE-BASED COMMUNICATION IN NANONETWORKS

In this chapter, we present a new receiver symbol detection scheme to support pulse-based modulations in the Terahertz Band, such as the scheme proposed in Chapter 4. The symbol detection is based on a Continuous-time Moving Average (CTMA) architecture, which is implemented with a single low-pass filter. This scheme bases its decision in the received signal power maximum peak after the CTMA. Afterwards, to decode the symbol, this maximum is compared with a previously defined threshold. This scheme is first analyzed in an interference-free environment, and its performance is compared to that of existing symbol detectors for pulse-based communication systems at lower frequency bands. In addition, in order to evaluate the impact of multi-user interference, the revised interference model for TS-OOK, which we developed in Chapter 5, is considered to analyze the performance degradation as a function of the density of active nanomachines.

6.1 Motivation and Related Work

As we discussed in Chapter 4, state-of-the-art Terahertz Band nano-transceivers are able to generate and detect very short pulses, which are usually just one-hundred-femtosecond long. The very low power of such pulses, *i.e.*, peak power of up to a few μW, and the very high path-loss of the Terahertz Band channel (Chapter 3), makes the detection of such pulses very challenging.

Existing receiver architectures cannot directly be used for the detection of femtosecond-long pulses, when transmitted at several Gigabits or even Terabits per second [39, 69, 83, 166]. Amongst others, as we discussed in Chapter 4, the assumptions on the shape, energy, duration and emission rate of the pulses as well as on the channel effects are different for nanonetworks in the Terahertz Band. In addition, multi-user interference that originates from uncoordinated transmission among nanomachines may further challenge the proper detection cause a major obstacle for communication in nanonetworks.

In the following section, we describe our proposed symbol detection scheme and compare it to existing symbol detection schemes.

6.2 Symbol Detection

The symbol detector consists of a low pass filter which approximates a CTMA, a peak detector, a decision maker implemented in the decoder and the sampling provided by the synchronization block. The symbol detection block diagram is shown in Figure 35 within a suggested receiver architecture based on power detection. As shown, the symbol detector is located after a Terahertz Band front-end, which amplifies and conditions the input signal, and a power detector. The power detection has been well explored in other non-coherent impulse-based communication schemes, and it is shown that it can achieve up to 10 times power consumption savings [155].

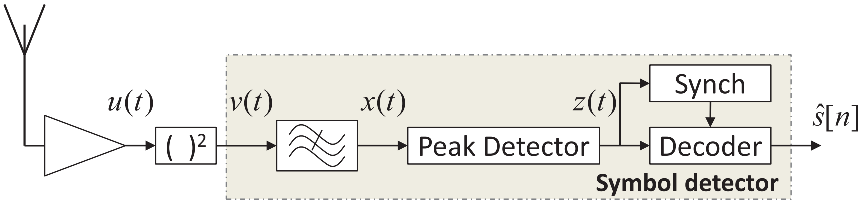

Figure 35. Receiver block diagram architecture.

Usual symbol detectors sample the output of a switched integrator in a single instant of time. In particular, in optical schemes [55], the symbol reception is phase-synchronized using Phase Locked Loop (PLL), so the output can be sampled at the optimal point. In carrier-less communications, such as IR-UWB [39], phase synchronization is highly discouraged, so the received signal power is integrated over a time window wider than the pulse time. Afterwards, the output value is sampled at the end of the integration time. Both cases need high synchronization between devices before the transmission starts. To relax the synchronization constraints in the expected time interval of arrival in IR-UWB, the integration time window is increased in the order of 10 to 100 times the pulse time T_p, so the pulse can fit into the integration window [69, 166]. This significantly lowers the performance of the receiver due to the fact that the *useful* signal power is averaged with respect to the extra noise power (See Figure 36).

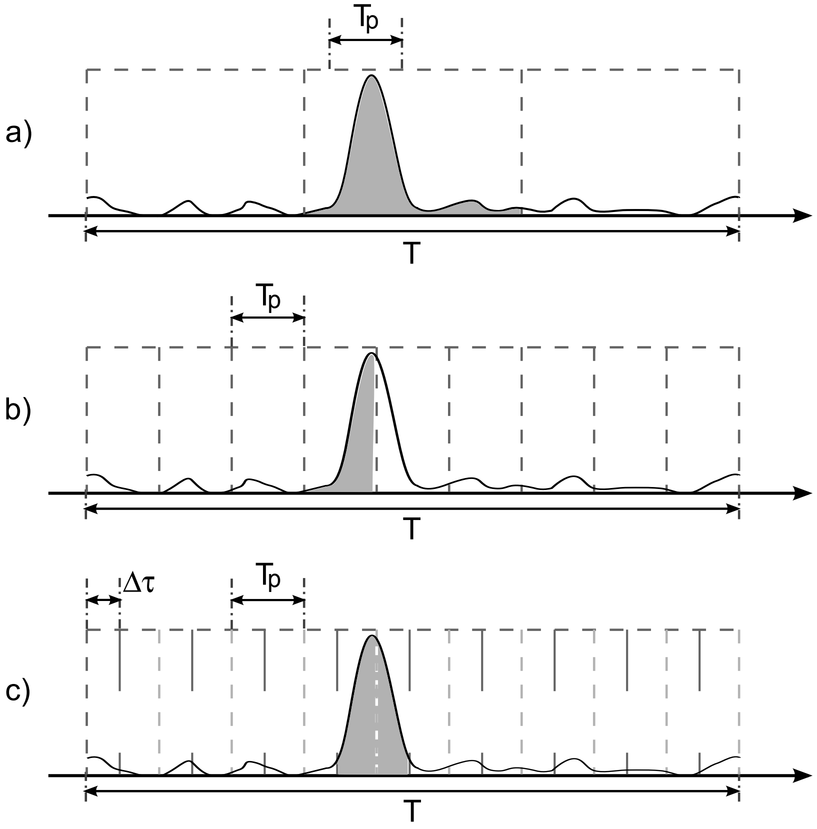

Figure 36. CTMA symbol detection. a) The integration time window is greater than the pulse time so additional noise is also integrated. b) The integration time window is reduced to the pulse time, the pulse does not fit into the time window. c) Thanks to CTMA, there are infinite T_p integration time windows over the time T so the pulse fits into only one of these time windows.

6.2.1 Continuous-time Moving Average

When the receiver integrates the pulse over a time window which is greater than the pulse time, the noise contribution proportionally increases with this time window, as shown in Figure 36. This effect drops the performance of the receiver in terms of SER by reducing the SNR ratio. There is a compromise between simplicity and minimum energy per bit.

To mitigate this noise effect, we need to reduce the integration time up to the pulse time length, T_p. However, since the expected time interval, T, is still kept in the order of 10 to 100 times the pulse time, we need to implement a total of T/T_p integrators in parallel and decide after the pulse reception which one has integrated the pulse energy. This makes this implementation impractical for low complexity devices.

As shown in Figure 36, there is a probability that the pulse does not perfectly fit in the integration time window. To make this happen we either must delay the integrators by a $\Delta\tau$ time (see Figure 36) or we must increase the number of integrators. By overlapping them we make sure that the pulse can fit in one of them. However, by increasing the number of integrators, the receiver complexity is also increased.

Since we can consider that, due to the asynchronous nature of impulse-based communication, the delay $\Delta\tau$ is unknown, we need to overlap infinite T_p time windows delayed a $\Delta\tau$ tending to zero. Under this assumptions, we define the Continuous-Time Moving Average as the linear time-invariant (LTI) system with input to output relation defined as:

$$x_{CTMA}(t) = \int_{t-T_p}^{t} v(t)dt \tag{119}$$

where x_{CTMA} stands for its output, t refers to time, T_p is the pulse time and v refers to the input of the LTI system.

This LTI system implements for each time t_i the integration over a pulse time T_p of the input power during the time interval $(t_i - T_p, t_i)$. Thus, this LTI system implements the infinite number of integrators needed to fit the upcoming pulse into one of the integrators over T. We refer as t_j the time that makes the upcoming pulse to perfectly fit into the integration window and $x(t_j)$ the result of this integration.

However, the limited time resolution is fixed to the whole expected time interval T, so the possibility of trying to detect the time t_j and its value $x(t_j)$ is discarded. Notice that, in a noise-free situation, the maximum value of the signal $x(t)$ is given when the pulse perfectly fits into the time window, thus we have that $\max\ x(t) = x(t_j)$ while when silence is transmitted, the maximum is still kept as zero. Thus, we use the $\max\ x(t)$, which provides a good estimator of $x(t_j)$, to decode the received symbol.

An ideal CTMA symbol detection scheme is not implementable. We next describe how we approximate this system using a low pass filter and how the pulse detection is performed. We aim at simplicity in order to guarantee the future integration of this symbol detector into nanomachines.

6.2.2 Low-Pass Filter-based CTMA

Lumped elements are usually proposed to approximate rectangular impulse responses by means of reactance networks [36]. Due to simplicity constraints, we approximate this CTMA symbol detection scheme by using a second order low-pass filter. This filter could be easily implemented with a chain of two RC filters in cascade with orders of magnitude of R ~ kΩ and C ~ fF, or even solutions implemented with graphene transistors, since their model implicitly provides a low-pass behavior [116].

To determine the cutoff frequency or, equivalently, the time width of the low-pass filter, we propose a square error minimization between both impulse responses as a function of the a parameter, defined in the low-pass filter impulse response h_{lpf}, and the pulse time T_p, defined in the impulse response h_{CTMA} of the CTMA. These impulse responses are given by:

$$h_{CTMA}(t) = \begin{cases} \frac{1}{T_p} & \text{If } 0 < t < T_p \\ 0 & \text{Otherwise} \end{cases} \quad , \quad h_{lpf}(t) = a^2 t e^{-at} \tag{120}$$

where h_{CTMA} is the impulse response of an ideal integrator with T_p time of integration and h_{lpf} refers to the impulse response of a second order low-pass filter with two real poles with parameter a. In order to find the closer low-pass filter to the ideal integrator, we have minimized the square error between both impulse responses as function of the parameter a. This minimization is given for $a = 1.4615/T_p$.

6.2.3 Peak Detection and Decoding

To accordingly decode the received symbol, we introduce a peak detector and a decoder. These two blocks, which are aided by the synchronization block, decode the symbol according to:

$$\hat{s}[n] = \begin{cases} 1 & \text{if } \max\limits_{t \in (0,T)} x(t) > V_{th} \\ 0 & \text{otherwise} \end{cases} \tag{121}$$

where t refers to time, T is the expected time interval where we expect that the pulse will arrive, and V_{th} stands for the voltage threshold.

The proposed peak detector is based in a continuous-time comparison. This is composed of by a comparator and a latch circuit such that, whenever the input is higher than the predefined threshold, the output of the circuit is fixed to "1" until an external control circuit resets the output to "0". This comparator starts operating anytime the expected time interval starts. This timing is provided by the synchronization block.

Once the expected time interval has reached the end, the decoder aided by the synchronization block checks the output of the peak detector and decodes the symbol. Additionally, since the symbol detector is not integrating the signal during all the expected time interval T, but only during a time T_p, the decoder can oversample its input a few times over the expected time interval to decide whether the pulse has already arrived. This possibility can open up very interesting but simple symbol time estimation schemes for symbol detection.

Notice that, although no maximum function is carried out in the real reception, if at a time t_j, $x(t_j)$ is above the threshold, the maximum value $x(t_i)$ must be also above this threshold. The analysis of the symbol decision criterion is performed in the following section.

6.3 Analytical Model for the Symbol Detection

In this section we provide an analytical model for the CTMA-based symbol detector in a multi-user interference-free environment, *i.e.*, only the effect of background noise is considered. With this, we are able to obtain the probability density functions of the received symbols and to provide a lower bound in the SER.

The symbol decision criterium is based on the output signal of the Low-pass filter, x, which can be written for a single pulse arriving at a random time τ as:

$$x(t) = \left(s[i]w(t - iT_s - \tau) * h_c(t) + n(t)\right)^2 * h_{lpf}(t) \tag{122}$$

where $*$ denotes convolution, $s[i]$ stands for the transmitted symbol which can be either "0" or "1", w refers to the one-hundred-femtosecond-long pulse, T_s is the symbol period, h_c stands for the transfer function provided by the channel, n refers to the noise of bandwidth W and h_{lpf} is the impulse response of the low-pass filter.

Then $\hat{s}$ is decoded according to (121). To model $\max x(t)$, we consider that the SER tends to the ideal energy detector receiver when the time of observation tends to zero. The low-pass filter provides a high correlation between consecutive instants of time that enables the discretization of the continuous-time function x into N independent random variables.

Then, $\max x(t)$ can be expressed as function of the vector $\boldsymbol{X} = \{X_1, X_2, \cdots, X_N\}$ which refers to the discretized function x with:

$$\max_{t\in(0,T)} x(t) = \max_N \boldsymbol{X} = \max_N \{x(t_1), x(t_2), \cdots, x(t_N)\} \tag{123}$$

where T refers to the time of observation, N stands for the number of independent discretized variables, and $x(t_1), \cdots, x(t_N)$ is the value of the input signal x at the $t_1, \cdots, t_N$ instants.

6.3.1 Detection of Logical "0"

In impulse-based On-Off keying modulation schemes, such as TS-OOK, a logical "0" is transmitted as silence. When silence is transmitted, just noise is detected in the receiver.

For this we can consider $\boldsymbol{X}$ as a vector with identically N random variables, with probability density function f_n. The probability density function of $\max \boldsymbol{X}$ can be expressed as a function of f_n by:

$$f_{max,n}(y, N) = NF_n(y)^{N-1} f_n(y) \tag{124}$$

where N is the number of discrete random variables, f_n refers to the probability density function of a single x_i variable and f_n stands for its cumulative distribution function. Each X_i corresponds to the square value of the noise signal over the bandwidth provided by the low-pass filter. This is commonly modeled in the literature as a chi-square distribution with $v = 2T_pW$ degrees of freedom random variable [87], with T_p the pulse time and W its bandwidth. This probability density function is expressed in terms of the normalized random variable $Y = 2X/N_{00}$, for a two sided power spectral noise density $N_{00}/2$ and is given by:

$$f_n(y) = \frac{1}{2^{v/2}\Gamma(\frac{v}{2})} y^{(v-2)/2} e^{-y/2}, \quad y \geq 0 \tag{125}$$

where Γ is the gamma function, v refers the degrees of freedom and y the normalized random variable.

In particular, if TS-OOK and ultra-short impulse-based modulations uses $T_pW = 1$, we obtain for $f_{max,n}(y, N)$:

$$f_{max,n}(y, N) = \frac{1}{2} N \left(1 - e^{-y/2}\right)^{N-1} e^{-y/2}. \tag{126}$$

however, only if the pulse is strictly one-hundred-femtosecond long, this condition is valid. Since the n-th time derivative of a Gaussian pulse is considered for the pulse generation, and also the low-pass filter is an approximation of an ideal integrator, values of T_pW are expected to be higher. In particular, for a second time derivative Gaussian pulse we have $T_pW = 3.5$. For this, there is no closed-form expression of $f_{max,n}(y, N)$ so that the function must be numerically evaluated.

6.3.2 Detection of Logical “1”

A logical “1” is transmitted by using a one-hundred-femtosecond-long pulse. The signal x received is noise plus signal during a very short time and noise during most of the time. This fact leads to consider two different types of random variables, namely N_n independent noise random variables with f_n distribution and N_s random variables with f_{sn} distribution. Then, in this case we can express the maximum as:

$$\max_N \boldsymbol{X}_{sn} = \max_N\{\boldsymbol{X}_{n,N_n}, \boldsymbol{X}_{s,N_S}\} \tag{127}$$

where $\boldsymbol{X}_{sn}$ refers to the vector containing the random variables that model a pulse in reception, $\boldsymbol{X}_{s,N_s}$ stands for the vector of N_s random variables that model x when a pulse is being received. $\boldsymbol{X}_{n,N_n}$ is the vector containing noise with N_n identically distributed independent random variables. The total number of random variables of noise and signal must be kept equal to $N = N_n + N_s$ since N is function of the time interval. Then, its probability density function can be written as:

$$f_{max,sn}(y, N_s, N_n) = F_{max,s}(y, N_s)f_{max,n}(y, N_n) + f_{max,s}(y, N_s)F_{max,n}(y, N_n) \tag{128}$$

where $f_{max,sn}(y, N_s, N_n)$ is the probability density function of $\max x(t)$ when transmitting a pulse in terms of the normalized random variable $Y = 2X/N_{01}$, with N_s and N_n random variables, $f_{max,s}(y, N_s)$ stands for the probability density function of the maximum of $\boldsymbol{X}_{s,N_s}$, with $F_{max,s}(y)$ its cumulative distribution function, $f_{max,n}(y, N_n)$ the probability density function of $\max \boldsymbol{X}_{n,N_n}$ and $F_{max,n}(y, N_n)$ its cumulative distribution function. Each component of $\boldsymbol{X}_{s,N_s}$ is characterized by the probability density function $f_s(y)$. Similar to f_n, $f_s(y)$ is usually modeled in the literature as a normalized non-central chi-squared distribution with $v = 2T_pW$ degrees of freedom with the normalized random variable $Y = 2X/N_{01}$ for a two sided power spectral noise density $N_{01}/2$ [87]. This is given by:

$$f_s(y) = \frac{1}{2}\Big(\frac{y}{\lambda}\Big)^{(v-2)/4} e^{-(y+\lambda)/2} I_{(v-2)/2}(\sqrt{(y\lambda)}) \tag{129}$$

where $\lambda = 2E/N_{01}$ refers to the non-centrality parameter and $I_n(z)$ stands for the nth order modified Bessel Function of the first kind. $f_{max,s}(y)$ can be expressed by using (124).

However, provided that the noise level must be kept lower than the signal level to guarantee a certain SER, $\max_N \boldsymbol{X}_{sn} = \max_N\{\boldsymbol{X}_{n,N_n}, \boldsymbol{X}_s\} \approx \max_{N_s}\{\boldsymbol{X}_s\}$, and then:

$$f_{max,sn}(y, N_s) = f_{max,s}(y, N_s). \tag{130}$$

In any case, since $f_{max,s}(y, N_s)$ is not solvable, $f_{max,sn}(y, N_s, N_n)$ cannot lead to a closed-form expression.

6.3.3 Threshold and SER

The performance of the symbol detector can be expressed in terms of the error detection probability of every symbol, and averaging them by their symbol probability. The error detection probabilities for both symbols are defined as:

$$\begin{aligned} P_{\epsilon|s=0} &= \int_{2V_T/N_{00}}^{\infty} f_{max,n}(y, N)dy \ , \\ P_{\epsilon|s=1} &= \int_{0}^{2V_T/N_{01}} f_{max,sn}(y, N)dy \end{aligned} \tag{131}$$

where V_T stands for the threshold, N_{00} and N_{01} refer to the noise level for the symbols “0” and “1” respectively and $f_{max,n}(y, N)$ and $f_{max,sn}(y, N)$ are the probability density functions for the symbols “0” and “1”.

Finally, we seek to obtain the probability of symbol error. This SER varies as function of the detection threshold and can be expressed as:

$$SER = p_{s=0} \cdot P_{\epsilon|s=0} + p_{s=1} \cdot P_{\epsilon|s=1} \tag{132}$$

where $P_{\epsilon|s=0}$ and $P_{\epsilon|s=1}$ refers to the detection probabilities in (131) and $p_{s=0}$ and $p_{s=1}$ the symbol probability. The detection threshold, V_T, is set such that the SER is minimized according to the MAP criterion, *i.e.*,:

$$f_{max,n}\left(\frac{2V_T}{N_{00}}, N\right) p_{s=0} = f_{max,sn}\left(\frac{2V_T}{N_{01}}, N\right) p_{s=1}. \tag{133}$$

This optimization is not analytically solvable so in the following section, this is numerically evaluated.

6.4 Performance Evaluation in an Interference-free Environment

In this section, we validate the expressions for the probability density functions of both symbols, “0” and “1”, throughout simulation in a multi-user interference-free environment. We analyze the performance of the receiver and the symbol detector in terms of SER as a function of the channel attenuation and noise.

6.4.1 System Model

The following assumptions are considered in our analysis:

- The path-loss and noise in the Terahertz Band are computed by using the models introduced in Chapter 3. A standard medium with 10% of water vapor is considered.
- Although the channel is asymmetric, we suppose the worst case scenario where the noise level for both symbols is considered the same, and we refer this noise level as $N_0 = N_{00} = N_{01}$. This is due to the fact that a pulse from another transmitting nanosystem can excite the channel just before the symbol “0” is transmitted.
- Only the channel noise has been taken into account in the numerical and simulation results, since no specific technology has been considered to implement the transceiver and, thus, a receiver noise model is not available.
- The transmitter encodes logical “1”s by using one-hundred-femtosecond-long Gaussian pulses with an energy equal to 1 picoJoule. The second time-derivative of the Gaussian pulse is supposed to be detected in the receiver. The logical “0” is transmitted as silence.
- The symbol probabilities are considered equal for the logical “1”s and “0”s. $p_{s=0} = p_{s=1} = 0.5$.
- No interfering nodes are considered.

6.4.2 Model Validation

In order to validate the symbol detection probability model, we compare the numerical results of the analytical model given by (126) and (129) with the simulation results given by the emulation of the receiver block diagram from Figure 35 when receiving the symbols "0" and "1". In this simulation, the second time-derivative of a one-hundred-femtosecond-long Gaussian pulse has been implemented. The values of the energy per bit and the noise level chosen belong to a distance between devices of 66 mm. Using this pulse, the pulse time-bandwidth product is $T_p W = 3.5$. The normalized results of the simulations are shown superimposed over the numerical results in Figure 37. The simulation results provide the random variable $\max x(t)$. To match results, we have appropriately normalized this variable to $Y = 2X/N_{00}$ when a logical "0" is received or to $Y = 2X/N_{01}$ when the pulse received is a logical "1".

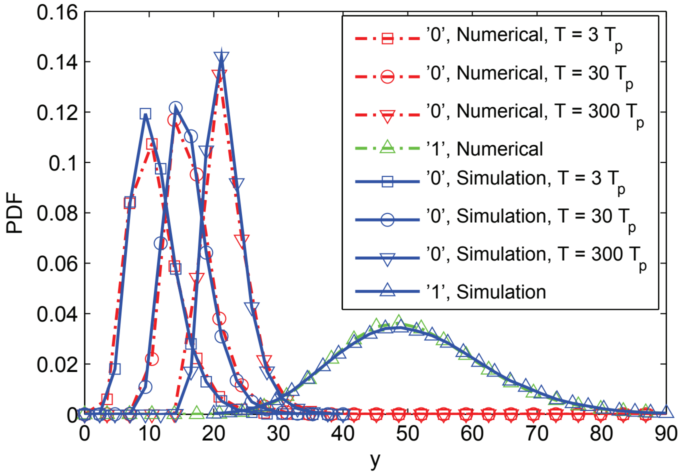

Figure 37. Probability density function of $\max\{x\}$ **when receiving logical "0"s and "1"s for a distance of 66 mm in the Terahertz channel.**

6.4.2.1 Logical "0"

In Figure 37, the probability density function for the detection of a logical "0" is represented for three different time intervals $T = \{3, 30, 300\}\ T_p$. These three time intervals can be discretized by a number $N = \{2, 15, 110\}$ of random variables. As shown, the average value presents logarithmic growth with this time interval.

6.4.2.2 Logical "1"

The probability density function for the detection of a logical "1" is represented in Figure 37. The time for the detection of this symbol can be discretized by a number $N_s = 2$ of random signal variables. The fact that this probability density function does not present any variation with the time interval length validates the approximation proposed in (130). To observe the effect of the time interval in the variation of the logical "1" requires very large time intervals or very low E/N_0 ratio, which leads to very bad values of SER. This last particular case is out of our study because a SER in the order of 10^{-3} to 10^{-4} is the usual target in communications.

6.4.3 SER Estimation

Figure 38 shows the SER estimation as a function of the distance. In the figure, three curves, referred as *Max*, show the proposed architecture estimated SER for the values of $n = T/T_p = \{3, 30, 300\}$. Equivalently, three curves for the same values of n are shown for classic receiver architectures based on integration over the time interval T. These curves are referred as *Int*. In order to make fair this comparison, we compare the proposed receiver architecture with the classic one [], both architectures are with the same level of detail, thus considering the same sources of noise and communicating in the Terahertz Band. As the figure shows, decreasing the integration time to T_p by using the CTMA mitigates the impact of noise. As a result, the proposed receiver outperforms existing receivers by increasing up to a 50% the maximum distance for a relation $n = T/T_p = 300$, in order to guarantee a SER of 10^{-4}. Moreover, from the figure, we observe the strong impact that the molecular absorption has over the attenuation and noise in terms of the distance. A distance increase of around a 10% worsens the SER in several orders of magnitude.

Alternatively, we also show the dependence of the SER with the relation $n = T/T_p$. This dependence is shown in Figure 39 for a fixed distance of 66 mm. As shown, when the time interval T is similar to T_p, we obtain similar performance with both receivers. However, as this relation increases, the proposed receiver outperforms the previous architecture.

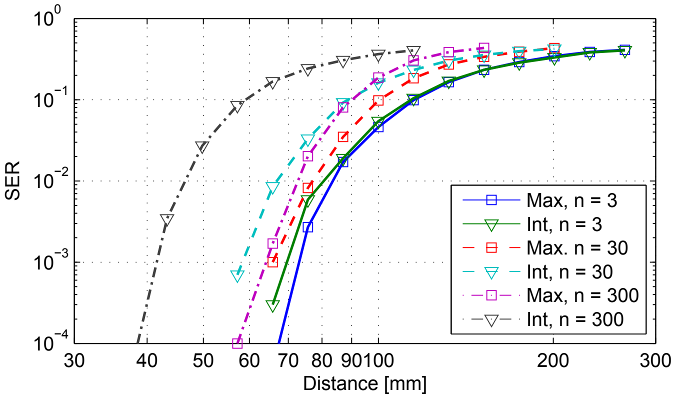

Figure 38. Comparison between the SER provided by the proposed receiver and the state-of-the-art receiver architecture for different time intervals in the Terahertz channel.

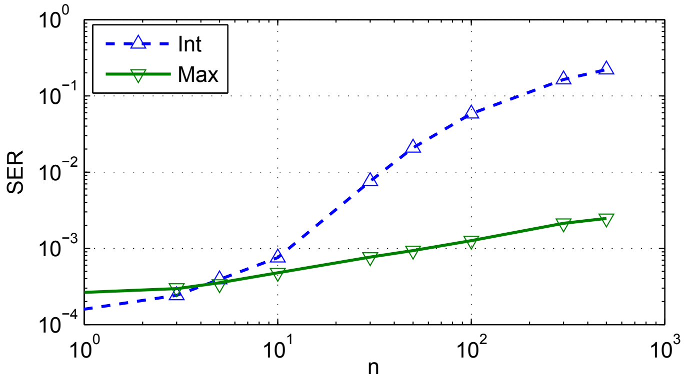

Figure 39. Comparison between the SER provided by the proposed receiver and current receiver in terms of $n = T/T_p$.

For nanosystems, where simplicity and consumption must be kept as the main constraints, increasing the time interval means significantly relaxing the design conditions.

6.4.4 Regression Model for the SER Estimation

The expressions for the probability density function of the max $\boldsymbol{X}|s = 0$ and max $\boldsymbol{X}|s = 1$ functions are composed by the maximum of a large number of chi-square distributions. This fact makes the SER estimation to be difficult to calculate. For this, we derive a regression model for the SER estimation, based on the observed dependency with the n relation.

Figure 39 shows that there is a log-log behavior in the SER versus the relation $n = T/T_p$. Moreover, this log-log behavior is approximately constant for any ratio of E/N_0, and even for different noises for “1”s and “0”s, N_{01} and N_{00}. This log-log relation provides a relation between the SER at two different ratios n_1 and n_2 given by:

$$SER_{n_2} = r^{0.45} SER_{n_1} \tag{134}$$

where $r = T_2/T_1 = n_2/n_1$ is the relation between time intervals.

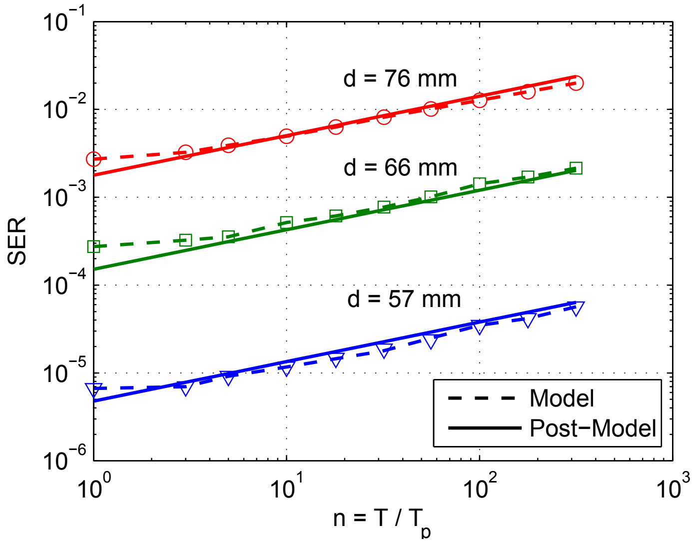

Figure 40. Comparison of the model with the regression model for the SER estimation. The results are shown for different distances between devices.

Then, computing the Engler model [31] to calculate the SER for $n = 1$ with parameter $TW = 3.5$ and by using (134), we can obtain the SER for any distance and n ratio. Figure 40 shows a comparison between the original model and its regression model. As shown, this regression model matches with the expected value for any of the three distances.

6.4.5 Maximum Bitrate

Impulse-based modulation schemes, such as TS-OOK, spread one-hundred-femtosecond-long pulses in time. This time-spread is characterized by the parameter $\beta = T_s/T_p$ and it is usually in the order of $\beta \sim 1000$. For this, in the previous sections, different symbols are considered independent. Although this architecture is proposed mainly to support time-spread impulse-based modulations, this receiver can also support bitrates of up to a few Terabits per second. When the bitrate increases and it gets close to $\beta \sim 1$, the non-idealities of using a low-pass filter to approximate a CTMA plus the pulse overlapping produced by using the second time derivative of a Gaussian pulse affect the system by providing an intersymbol interference (ISI). For this, we have performed a simulation of the Terahertz channel and the receiver architecture considering this overlapping effects between symbols. Figure 41 shows the achievable SER in terms of bitrate for two different distances between nanosystems. As shown, until approximately $R = 2$ Tbps the SER is mainly limited by noise, so the SER is kept constant at $SER \approx 2 \cdot 10^{-4}$ for a distance $d = 66$ mm. Then, as soon as the bitrate increases, the receiver is highly affected by the ISI, dropping the SER to $SER = 0.5$ when $R = 5$ Tbps. Concerning the distance $d = 50$ mm, the ratio E/N_0 is high enough to neglect the SER when the system is limited by noise. However, as shown in the figure, when the ISI is affecting the receiver, the SER tends to the same values, presenting a $SER = 0.5$ when $R = 5$ Tbps.

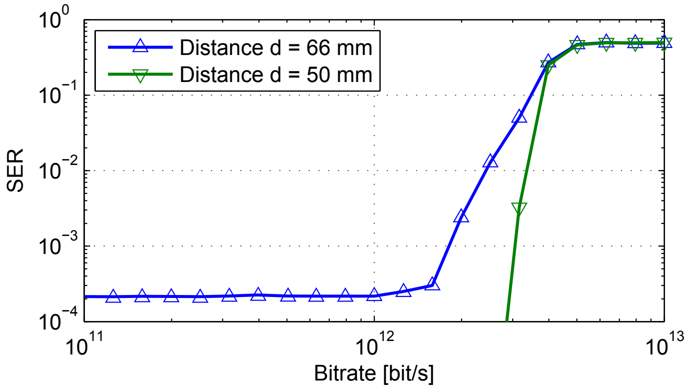

Figure 41. SER in terms of bitrate.

6.5 Performance Analysis in an Interference-limited Environment

In this section, we explore the effect that neighboring nodes have over the communication in terms of multi-user interference. For this, we make use of the revised interference model that we developed in Chapter 5. Starting from this, the impact on the symbol probabilities are analyzed and the performance of the receiver under multi-user interference is shown in terms of SER as a function of the channel distance and node density.

6.5.1 Symbol Detection Model

As shown in Section 6.3, the symbol decision is a function of the variable $\max x(t)$ which is modeled as a random variable which takes the maximum value at the output of the Low-pass filter during an observation time T. Similar to the interference-free environment, $\max x(t)$ can be expressed as a function of the discretized vector $\mathbf{X} = \{X_1, \cdots, X_N\}$ of N independent random variables. The number N of independent random variables depends on the time of observation, T, and bandwidth of the low-pass filter.

In order to model $\max \mathbf{X}$, we fist consider the random variables X_i for both cases, the transmission of a logical "0" and a logical "1". As it follows, the probability density functions f_i and f_{is}, which model a single variable X_i in both cases, are obtained. Afterwards, similar methodology as in Section 6.3 is applied to obtain the probability density function of $\max \mathbf{X}$, for both cases. In particular, f_i is appropriately combined with (124) in case of transmitting a logical "0" and both f_i and f_{is} are combined with (130) otherwise.

In both cases, a closed-form expression cannot be obtained. However, both cases can be approximated when the noise is located far below the interference level.

6.5.1.1 X_i Model when Silence

In the case of the multi-user interference environment, the received power at the receiver can be approximated by the joint contribution of noise plus interference. Its probability distribution can be given by:

$$f_i(x) \approx f_n(x) * f_{int}(x) \tag{135}$$

where $f_n(x)$ refers to the noise contribution and it is modeled as a denormalized chi-square distribution from (7). $f_{int}(x)$ stands for the interference power contribution.

After low-pass filtering for providing x, this pdf is given by estimating the pdf of the resulting signal after convoluting power profile at $v(t)$ and the impulse response of the low-pass filter, $h_{lpf}(t)$. Although this result does not lead to a closed-form expression, the term f_{int} can be well approximated by adding a correcting ξ factor within the expression of $f_I(i)$.

Therefore:

$$f_{int}(i) = \frac{1}{\pi i}\sum_{k=1}^{\infty}\frac{\Gamma(\gamma k+1)}{k!}\left(\frac{\pi\lambda'\xi\beta\Gamma(1-\gamma)}{i^{\gamma}}\right)^{k}\sin(k\pi(1-\gamma)). \tag{136}$$

This correcting factor is a function of the product between the bandwidth at $v(t)$ and the length of the impulse response of $h_{lpf}(t)$. This has been numerically solved being $\xi = 1.2$.

6.5.1.2 X_i Model when Signal

Similar to the model when transmitting silence, the received power when transmitting signal can be approximated by the joint contribution of noise plus signal plus interference. Therefore, its pdf can be given by:

$$f_{is}(x) \approx f_s(x) * f_{int}(x) \tag{137}$$

where $f_s(x)$ refers to the noise plus signal contribution, and it is modeled as a denormalized non-central chi-squared distribution as in (11) and $f_{int}(x)$ stands for the interference power contribution (136).

6.5.2 Model Validation

In order to validate the receiver performance under multi-user interference and to observe its degradation in terms of SER, the same assumptions as in Section 6.4 have been considered in the analysis. The input power level pdf model is validated under the assumption of a noiseless channel in Figure 42. This is given by combining (136) with (126) and it is compared to the simulation results given by the emulation of the receiver block diagram from Figure 35.

Additionally, Figure 43 shows the pdf of receiving logical "0"s and "1"s at a distance of 66 mm. Since the pdf of X_i cannot be numerically estimated, the estimation of this probability density function has been done through simulation. As shown, when the interfering power increases due to an increase in the node density, both logical values shift to higher power values.

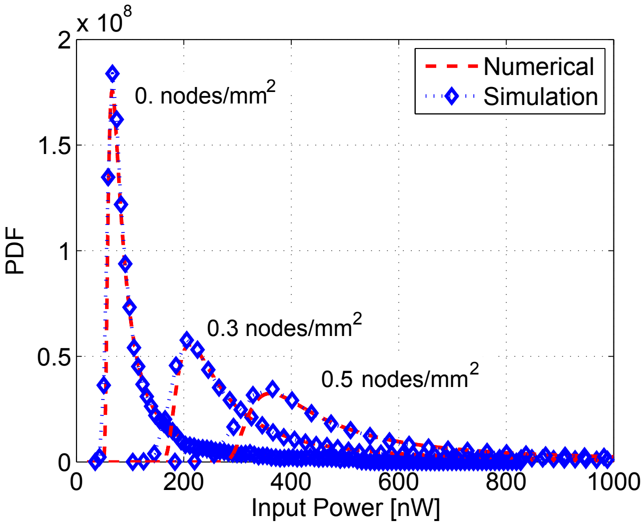

Figure 42. Input power level pdf in a multi-user interference noiseless environment. Comparison between the model and the simulated results.

6.5.3 SER Estimation

Figure 44 shows the SER estimation as a function of the distance. The figure compares the effect of the interference produced by the neighboring nodes over the performance of the receiver for three different node densities. In the figure, an observation time of $T = 3T_p$ has been chosen. In order to enable the comparison with the receiver performance in an interference-free environment, a lower bound in the SER is given by the interference-free situation. As shown, the effect of multi-user interference reduces the maximum distance transmission in the sense that to achieve a target SER, the distance between nodes must be reduced. As an example, in case of fixing $SER = 10^{-4}$ the distance is degraded in a 55% and 85% for node densities of 0.3 and 0.5 nodes/mm^2 respectively, while the distance at 0.1 nodes/mm^2 is not significantly reduced in order to achieve the targeted SER.

Additionally, to better show the impact of the node density over the SER performance, the dependence of the SER in terms of the node density for three different observation times, $T = \{3, 30, 300\}$, is shown in Figure 45.

As shown in both figures, the receiver is able to successfully operate without being significantly limited by interferences up to a node density of about 0.1 nodes/mm^2. In case of

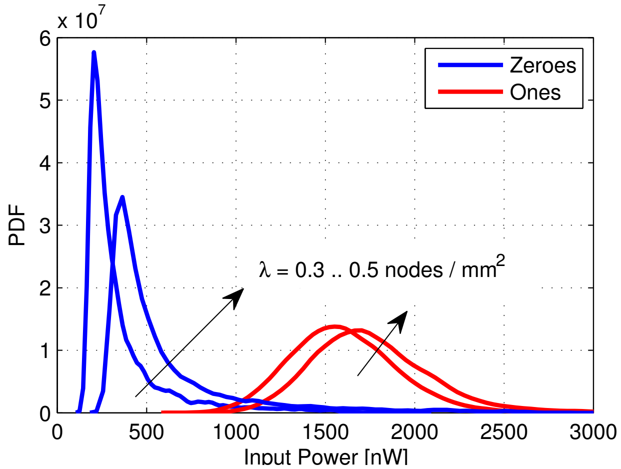

Figure 43. Probability density function of max $x(t)$ **when receiving logical "0"s and "1" for a distance of 66 mm for a multi-user interference environment in the Terahertz channel.**

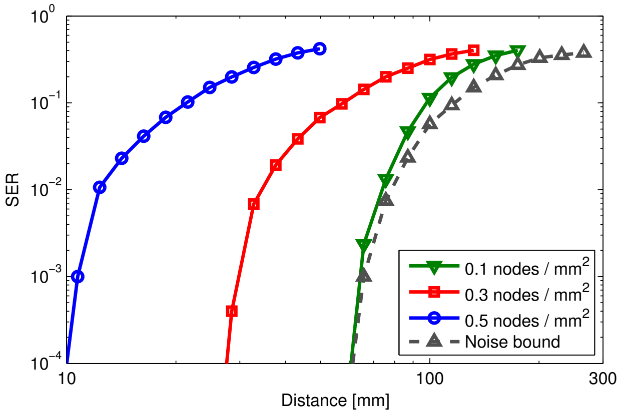

Figure 44. Impact of multi-user interference produced by uncoordinated neibhoring nodes in the SER provided by the proposed receiver in terms of the distance.

greater node densities, the interference has a severe impact over the receiver performance. This opens the door for the development of novel interference-aware MAC protocols built on top of this receiver topology in order to mitigate the degradation in performance due to interference, as we will investigate in Chapter 8.

6.6 Conclusions

In this chapter, we have proposed a novel symbol detection scheme at the receiver for impulse-based Terahertz Band communication. The proposed receiver design is based on a Continuous-Time Moving Average symbol detection scheme, which can be implemented

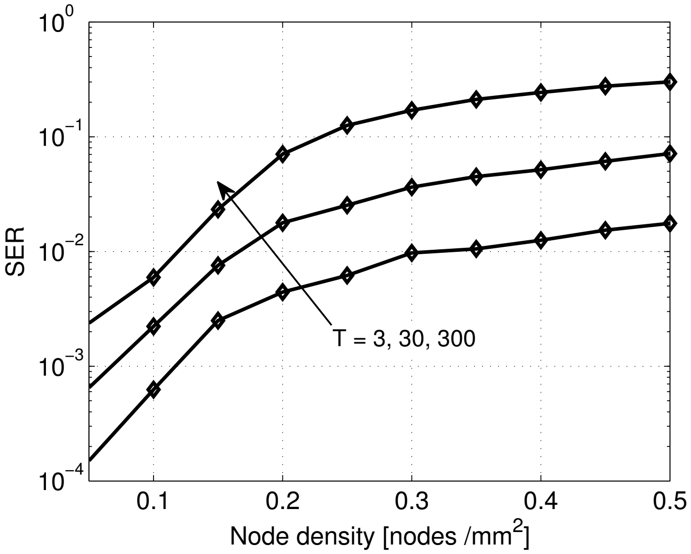

Figure 45. Impact of the node density over the SER performance for a fixed distance of 66 mm.

with a single low-pass filter. This symbol detection scheme simplifies the receiver architecture and relaxes the synchronization requirements.

To evaluate the performance of the proposed receiver, we have obtained closed-form mathematical expressions for the probability density functions of the received symbols and we have validated the developed symbol detection model through simulation in a interference-free environment. Moreover, we have computed the symbol error rate for the proposed receiver as a function of different system parameters and we explore the effects of the inter-symbol interference when the bit-rate is increased up to tens of Terabits per second. We have also analyzed the effect of interfering nodes on the receiver performance.

The results show that this novel symbol detection scheme outperforms existing pulse-radio based detectors when used in the Terahertz Band, by reducing the symbol error rate and increasing the achievable transmission distance for a target SER. These results open novel research challenges in synchronization schemes for impulse-based Terahertz communications in nanonetworks. Moreover, the severe impact that multi-user interference in largely deployed nanonetworks has over the receiver performance motivates the development of novel ways to mitigate the interference.

CHAPTER 7

JOINT ENERGY HARVESTING AND COMMUNICATION ANALYSIS FOR PERPETUAL NANONETWORKS IN THE TERAHERTZ BAND

One of the major bottlenecks in nanonetworks is posed by the very limited energy that can be stored in a nanomachine in contrast to the energy that is required by the device to operate and, specially, to communicate. Recently, novel energy harvesting mechanisms have been proposed to replenish the energy stored in nanomachines. With these mechanisms, nanonetworks can overcome their energy bottleneck and even have infinite lifetime, provided that the energy harvesting and consumption processes are jointly designed. In this chapter, an energy model for self-powered nanomachines is developed which successfully captures the correlation between the energy harvesting and the energy consumption processes. The energy harvesting process is realized by means of a piezoelectric nanogenerator, for which a new circuital model is developed which can accurately reproduce existing experimental data. The energy consumption process is due to the communication in the Terahertz Band (0.1-10 THz). The proposed energy model captures the dynamic network behavior by means of a probabilistic analysis of the total network traffic and the multi-user interference. A mathematical framework is developed to obtain the probability distribution of the nanomachine energy and to investigate the end-to-end packet delivery probability, the end-to-end packet delay, and the throughput of perpetual nanonetworks.

7.1 Motivation and Related Work

A major challenge in nanonetworks is posed by the very limited energy that can be stored in nano-batteries, which requires the use of energy-harvesting systems. Conventional energy-harvesting mechanisms, *e.g.*, solar energy, wind power, or underwater turbulences [134], cannot be utilized in nanonetworks mainly due to technology limitations. Alternatively, piezoelectric nano-generators have been recently proposed [152, 158]. For example, a piezoelectric nano-generator is experimentally demonstrated in [158]. In particular, an array of Zinc Oxide (ZnO) nanowires is used to power a laser diode (LD). The waiting time to power the LD just for a few milliseconds is in the order of ten minutes with a 50 Hz vibration. This number illustrates the major energy limitations of nanomachines.

The lifetime of energy harvesting networks can tend to infinity provided that the energy harvesting and the energy consumption processes are jointly designed [42, 80]. In contrast to the classical battery-powered devices, the energy of the self-powered devices does not just decrease until the battery is empty, but it has both positive and negative fluctuations. These variations are not captured in classical energy models [124, 151]. Even in several recent models for energy harvesting networks [71, 75, 82, 123], the correlation between the energy harvesting and the energy consumption processes are not fully captured. In particular, existing models usually assume constant energy harvesting and transmission rates. However, it is reasonable to consider that if a nanomachine fully deplenishes its battery and cannot respond to a communication request, the transmitting nano-device will attempt to retransmit. This increases the overall network traffic, the multi-user interference and it ultimately has an impact in the energy of the transmitting nanomachine and its neighbors.

In the following Section, we propose an energy model for self-powered nanomachines. This model considers both the energy harvesting process by means of a piezoelectric nano-generator and the energy consumption process due to communication with TS-OOK. This model allows us to compute the probability distribution of the nanomachine energy and to investigate its variations as function of several system and network parameters.

7.2 Energy Harvesting With Piezoelectric Nano-Generators

Conventional energy harvesting mechanisms, *e.g.*, solar energy, wind power, or underwater turbulences [91, 134], cannot be utilized in nanonetworks. For example, the efficiency of photovoltaic nano-cells for solar energy harvesting is extremely low even if novel nano-components such as CNTs are used to improve their sensitivity [62]. In addition, in many of the applications of nanonetworks, sunlight is not available. Moreover, classical mechanisms to harvest kinetic energy from wind or underwater turbulences are not feasible in the nanoscale due to the technology limitations [2].

A pioneering mechanism to power nanomachines is to harvest vibrational energy by exploiting the piezoelectric effect of Zinc Oxide (ZnO) nanowires [152]. A piezoelectric nano-generator, shown in Figure 46, consists of i) an array of ZnO nanowires, ii) a rectifying circuit, and iii) a nano-ultra-capacitor. When the nanowires are bent or compressed, an electric current is generated between the ends of the nanowires. This current is used to charge a capacitor. When the nanowires are released, an electric current in the opposite direction is generated and used to charge the capacitor after proper rectification. The compress-release cycles of the nanowires are created by an external energy source, *e.g.*, ambient vibrations or artificially generated ultrasonic waves [152].

Piezoelectric nano-generators have been prototyped in [158, 159]. In [158], a very dense array of vertically-aligned ZnO nanowires is used to power a LD for the transmission of a very short pulse. In [159], both the vertical and lateral integration of a large number of ZnO nanowires in an array is demonstrated and used to power a nanowire pH sensor and a nanowire UV sensor. However, there is no analytical model for the energy capacity and the harvesting rate of these nano-generators. Only the fundamental limits of a single nanowire were analytically explored in [37], but a system-level model which captures the effect of the rectifying circuit and the capacitor is missing.

In this section, we develop the an analytical model for piezoelectric nano-generators which captures the fundamental principles, capabilities and limitations of the energy harvesting process. We compare our results with the experimental measurements in [158] and we determine realistic values for the energy capacity and the energy harvesting rate.

7.2.1 General Model

As shown in Figure 46, we model a piezoelectric nano-generator as a non-ideal current source composed by an ideal voltage source V_g in series with a resistor R_g. The generator voltage V_g corresponds to the electrostatic potential of a bent nanowire minus the voltage dropped in the rectifying circuit. The value of the resistor is $R_g = V_g/I_g$, where I_g stands for the generator current. This is defined as $I_g = \Delta Q/t_{cycle}$, where ΔQ is the amount of electric charge, or harvested charge, obtained from a single compress-release cycle of the nanowire array and t_{cycle} is the cycle length.

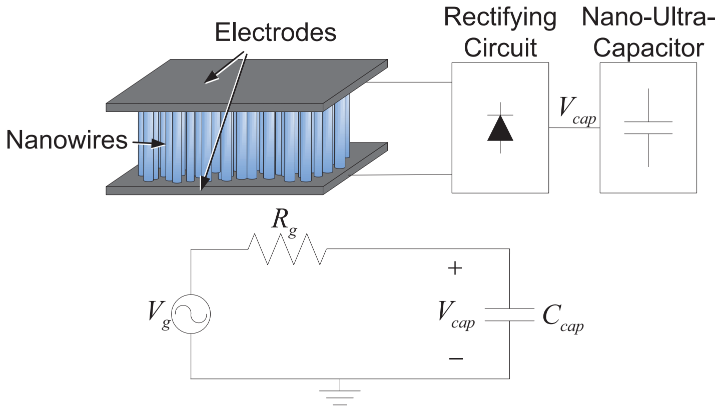

Figure 46. Piezoelectric nano-generator (top) and its equivalent model (bottom).

The voltage V_{cap} of the charging capacitor can be computed as a function of the number of cycles n_{cycle}:

$$V_{cap}\left(n_{cycle}\right) = V_g\left(1 - e^{\left(-\frac{n_{cycle}t_{cycle}}{R_g C_{cap}}\right)}\right) = V_g\left(1 - e^{\left(-\frac{n_{cycle}\Delta Q}{V_g C_{cap}}\right)}\right), \tag{138}$$

where t_{cycle} is the cycle length, R_g is the resistor of the non-ideal source and C_{cap} is the capacitance of the ultra-nano-capacitor. V_g is the generator voltage and ΔQ is the harvested charge per cycle, which are determined by the nanowire array. In this computation we do not take into account the leakage in the nano-capacitor [165] due to the fact that these values have yet not been quantified and are expectedly very low [104].

The energy stored in the capacitor E_{cap} can be computed as a function of the number of cycles n_{cycle}:

$$E_{cap}\left(n_{cycle}\right) = \frac{1}{2}C_{cap}\left(V_{cap}\left(n_{cycle}\right)\right)^2, \tag{139}$$

where C_{cap} is the capacitance of the ultra-nano-capacitor and V_{cap} is computed from (138).

The energy capacity $E_{cap-max}$, which is defined as the maximum energy stored in the ultra-nano-capacitor, corresponds to

$$E_{cap-max} = \max\{E_{cap}\left(n_{cycle}\right)\} = \frac{1}{2}C_{cap}V_g^2, \tag{140}$$

where C_{cap} is the capacitance of the ultra-nano-capacitor and V_g is the generator voltage.

The number of cycles n_{cycle} needed to charge the ultra-nano-capacitor up to an energy value E is then

$$n_{cycles}(E) = \left\lceil -\frac{V_g C_{cap}}{\Delta Q} \ln\left(1 - \sqrt{\frac{2E}{C_{cap}V_g^2}}\right)\right\rceil, \tag{141}$$

where V_g is the generator voltage, C_{cap} refers to the ultra-nano-capacitor capacitance, ΔQ is the harvested charge per cycle and V_g is generator voltage. The operator $\lceil\cdot\rceil$ returns the lowest integer number which is higher than the operand.

Finally, the energy harvesting rate λ_e in Joule/second at which the ultra-nano-capacitor is charged can be computed as a function of the current energy in the nano-ultra-capacitor E_{cap} (139) and the increase in the energy of the capacitor ΔE:

$$\lambda_e\left(E_{cap}, \Delta E\right) = \left(\frac{n_{cycle}}{t_{cycle}}\right)\frac{\Delta E}{n_{cycle}\left(E_{cap} + \Delta E\right) - n_{cycle}\left(E_{cap}\right)}, \tag{142}$$

where n_{cycle} is the number of cycles given by (141) and t_{cycle} refers to the time between consecutive cycles.

If the compress-release cycles are created by an artificially generated ultrasonic wave, t_{cycle} is constant and corresponds to the inverse of the frequency of the ultrasonic wave. If the compress-release cycles are created by an ambient vibration, the time t_{cycle} is the time between arrivals of a random process. For common vibration sources such as the vents of the air conditioning system of an office or the foot steps on a wooden deck, these arrivals follow a Poisson distribution [118].

The numerical results obtained with this analytical solution accurately match the measurements reported in [158]. In that experimental setup, a total charge per cycle ΔQ= 3.63 nC is measured. This is used to charge an array of eight micro-capacitors with capacitance C_{cap}=166 μF at a voltage V_g= 0.42 V. In Figure 47, the voltage in the capacitor V_{cap} as a function of the number of cycles n_{cycle} reported in [158] is compared to the numerical results for V_{cap} given by our analytical model in (138). The proposed model for the voltage of the capacitor V_{cap} accurately matches the measurements.

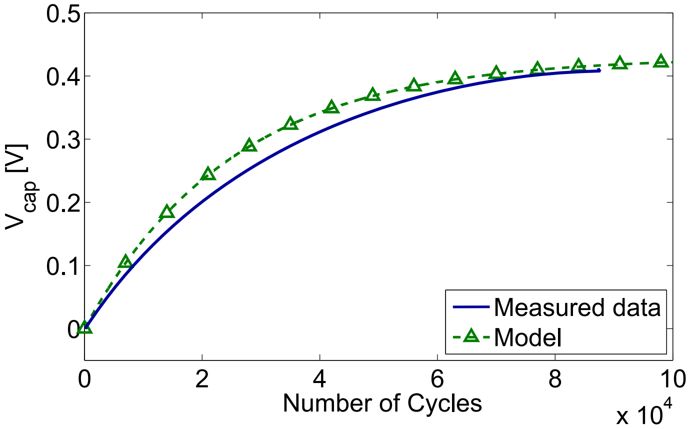

Figure 47. Comparison between the measured voltage in the capacitor V_{cap} as a function of the number of cycles n_{cycle} and the numerical results for V_{cap} given by our analytical model in (138).

7.2.2 Tailored Model for Nanomachines

The size of the piezoelectric nano-generators that are prototyped in [158, 159] is in the order of 10 mm^2. However, the target size of a nanomachine is in between 10 μm^2 and 1000 μm^2. Therefore, we need to determine realistic values for the amount of electric charge harvested per cycle ΔQ and the capacitance of the ultra-nano-capacitor C_{cap}, in order to compute the energy capacity $E_{cap-max}$ in (140) and the energy harvesting rate λ_e in (142).

The electric charge harvested per cycle ΔQ depends on the size of the nanowire array and the efficiency of the harvesting process. Based on the results in [159], a ΔQ= 6 pC is conceivable for a 1000 μm^2 array of nanowires when these are infiltrated by insulating polymers. The capacitance of an ultra-nano-capacitor C_{cap} depends on the capacitor technology that is used and the capacitor size. Amongst others, a capacitance of C_{cap}= 9 nF is conceivable for electrostatic ultra-nano-capacitors based on Onion-Like-Carbon (OLC) electrodes with the target size of nanomachines [104].

For these values, the energy capacity $E_{cap-max}$ in (140) is approximately 800 pJ when the capacitor C_{cap} is charged at V_g= 0.42 V. Then, the number n_{cycle} of cycles (141) which are needed to charge the capacitor C_{cap} up to 95% of its energy capacity $E_{cap-max}$ in (140) is approximately 2500 cycles. For example, for a constant vibration generated by the vents of the air conditioning system of an office (vibration frequency $1/t_{cycle}$= 50 Hz), the time needed to fully charge the capacitor C_{cap} up to its capacity $E_{cap-max}$ is approximately $n_{cycle}t_{cycle}$= 50 seconds. For the human heart beat ($1/t_{cycle}$ = 1 Hz), the recharging time is 42 minutes.

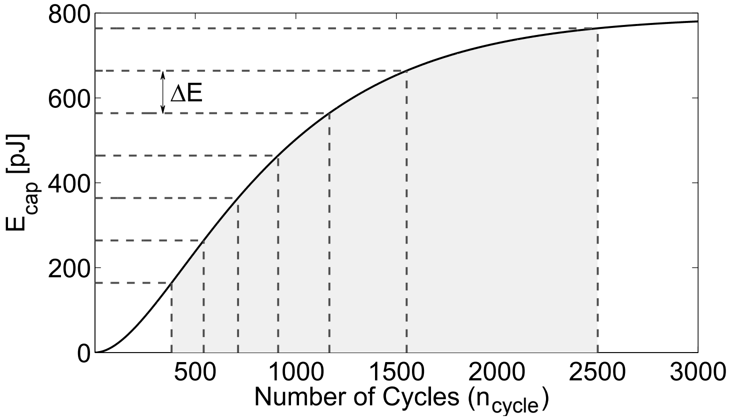

Figure 48. Energy stored in the ultra-nano-capacitor as a function of the number of cycles.

Finally, the energy stored in the capacitor E_{cap} is shown in Figure 48 as a function of the number of cycles. For example, to increase the energy stored in the capacitor E_{cap} by a fixed amount ΔE= 100 pJ from an initial value of 164 pJ, the number n_{cycle} of needed cycles is approximately 160 cycles. To increase the stored energy in the capacitor E_{cap} by the same amount ΔQ=100 pJ but for the case in which this is already charged at E_{cap}= 564 pJ, 384 cycles are needed. However, note that there is *no need to wait for the ultra-nano-capacitor to be fully recharged* to consume its energy.

These values are meaningful only when jointly analyzed with the energy consumption characteristics of nanomachines. Several processes affect the energy consumption of nanomachines (*e.g.*, sensing, computing, data storing and communication). Due to the fact that nanomachines are envisioned to operate at very high frequencies [2, 3, 5], communication is considered as the most energy demanding process. For this, we describe next the energy consumption due to communication in nanonetworks.

7.3 Energy Consumption in Terahertz Band Communication

We are interested in quantifying the energy consumed in the transmission and in the reception of a packet, $E_{packet-tx}$ and $E_{packet-rx}$, respectively, when using TS-OOK with low-weight channel codes. We consider that a packet consists of N_{bits} bits, from which N_{header} bits correspond to the header and N_{data} corresponds to the payload of the packet. Then, the energy consumed when transmitting or receiving a packet is given by

$$\begin{aligned} E_{packet-tx} &= N_{bits} W E_{pul-tx} \\ E_{packet-rx} &= N_{bits} E_{pul-rx}, \end{aligned} \tag{143}$$

where E_{pul-tx} and E_{pul-rx} are the energy consumed in the transmission and in the reception of a pulse, respectively, and W refers to the coding weigh. Note that by being silent, the transmitter can reduce its energy consumption, but not the receiver.

We need to determine the values for E_{pul-tx} and E_{pul-rx}. We fix the energy per pulse to E_{pul-tx}= 1 pJ and target transmission distances in the order of 10 mm. We also consider that the energy consumed in the reception of a pulse E_{pul-rx} is 10 times lower than E_{pul-tx}. With these numbers, the energy consumption $E_{packet-tx}$ for the transmission of, for example, a 200 bit-long packet is 200 pJ. Thus, given an energy capacity $E_{cap-max}$ in (140) of 800 pJ, only 4 packets can be transmitted with a fully charged ultra-nano-capacitor. It is clear that the energy-harvesting process and the energy consumption process are not balanced.

7.4 Joint Energy Model for Nanomachines

Classical energy models cannot be used for nanomachines mainly because they are focused on analyzing and minimizing the energy consumption of wireless devices whose total energy decreases until their batteries are depleted [124, 151]. Recently, a few models for energy harvesting sensors have been proposed in [71, 75, 82, 123]. However, these models cannot be directly used in nanonetworks because they do not capture the peculiarities of the energy harvesting and the energy consumption in nanomachines. In particular, the analysis in [75] is optimized for solar energy harvesting sensor networks, in which the energy harvesting rate changes over time by following a realistic sunlight profile. It is also assumed that the battery of the sensors can store enough energy to operate for several hours. In nanonetworks, sunlight may not be available in the envisioned applications and, in addition, the energy capacity of the battery is expectedly very small. In [71, 82, 123], the energy harvesting rate is considered constant, which is not a valid assumption for nanonetworks as we discussed in Section 7.2. Moreover, the impact of the energy fluctuations on the network traffic and behavior is not analyzed. Experimental results are given in [42, 80, 165], but no analytical solution is provided. As we mentioned before, nanomachines have not been built yet, and developing an analytical energy model is necessary to first identify and understand the capabilities and limitations of nanonetworks and ultimately aid in the design of future nanonetwork protocols and network architectures.

In this section, we develop an energy model for nanomachines based on the energy harvesting process described in Section 7.2 and the communication energy consumption process described in Section 7.3. This proposed model successfully captures the overall network behavior by taking into account the changes over time in the total network traffic and the multi-user interference. From the steady state analysis of the model, a framework is set to further investigate the impact on the network performance of different communication parameters. The major outcome of this model is the energy probability distribution of a nanomachine as a function of the energy harvesting and the communication parameters.

7.4.1 Model Definition

We model the nanomachine energy by means of a Non-Stationary Continuous-Time Markov Process, $\mathcal{E}(t)$, which describes the evolution in time t of the energy states of a nanomachine. As described in Section 7.2, the energy harvesting process follows a Poisson distribution when ambient vibrations are considered. For the communication process, we consider that nanomachines generate new information also by following a Poisson distribution. Due to the fact that packets might not be always successfully transmitted or received, retransmissions are allowed. By limiting the number of retransmissions per packet and by exponentially randomizing the time between transmissions, the network traffic can be characterized by a time-varying Poisson distribution.

The process $\mathcal{E}(t)$ is represented by the Markov chain in Figure 49 and it is fully characterized by its transition rate matrix $\boldsymbol{Q}(t)$:

$$\boldsymbol{Q} = \begin{array}{ccccccccc}
0 & 1 & 2 & \cdots\ N_{RT}-1 & & N_{RT} & N_{RT}+1 & \cdots & N_R \\
-\lambda_e^0 & \lambda_e^0 & 0 & \cdots & 0 & 0 & 0 & \cdots & 0 \\
\lambda_{rx}(t) & -\left(\lambda_e^1 + \lambda_{rx}(t)\right) & \lambda_e^1 & \cdots & 0 & 0 & 0 & \cdots & 0 \\
0 & \lambda_{rx}(t) & -\left(\lambda_e^2 + \lambda_{rx}(t)\right) & \cdots & 0 & 0 & 0 & \cdots & 0 \\
\vdots & \vdots & \vdots & \ddots & \vdots & \vdots & \vdots & \ddots & \vdots \\
\lambda_{tx}(t) & 0 & 0 & \cdots & \lambda_{rx}(t) & -\left(\lambda_e^{N_{RT}} + \lambda_{rx}(t) + \lambda_{tx}(t)\right) & \lambda_e^{N_{RT}} & \cdots & 0 \\
\vdots & \vdots & \vdots & \ddots & \vdots & \vdots & \vdots & \ddots & \vdots \\
0 & 0 & 0 & \cdots & 0 & 0 & 0 & \cdots & -\left(\lambda_{rx}(t) + \lambda_{tx}(t)\right)
\end{array} \tag{144}$$

Each element in the matrix, $q^{ij}(t)$, refers to the rate at which the transitions from state i to state j occur. We define the state probability vector as $\boldsymbol{\pi}(t) = \left\{\pi^0(t), \pi^1(t), ...\right\}$, where $\pi^n(t)$ refers to the probability of finding the process $\mathcal{E}(t)$ in state n at time t. Next, we describe the model in detail.

7.4.1.1 Energy States

Each state in the Markov chain in Figure 49 corresponds to an energy state of the nanomachine. In the state $n = 0$, the nanomachine only has a minimal energy E_{min} necessary to

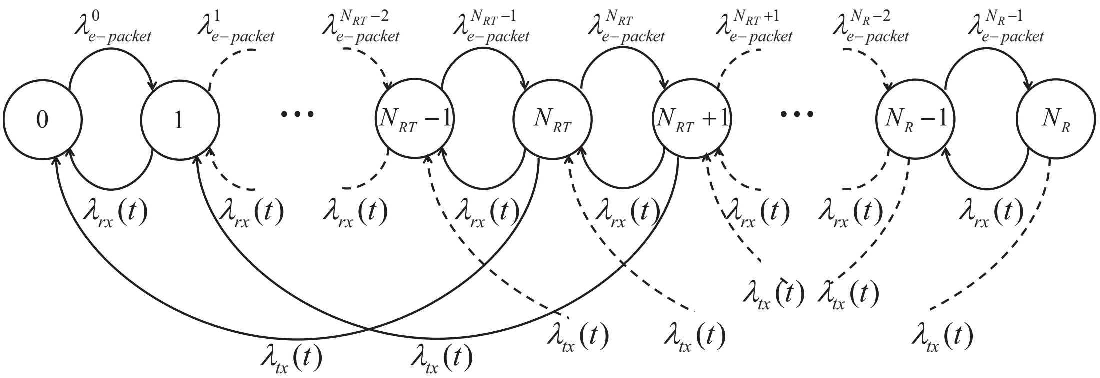

Figure 49. Markov chain representation of the proposed model for the temporal energy variations in nanomachines.

operate. In the state $n = 1$, the nanomachine has energy $E_{packet-rx}$ to receive one packet, as defined in (143). In general, the energy E^n of the state n is

$$E^n = E_{min} + nE_{packet-rx}. \tag{145}$$

In the maximum energy state, which is given by $n = N_R$, the capacitor is full, which corresponds to having enough energy either to transmit N_T information packets or to receive N_R packets. The values of N_T and N_R are given by

$$\begin{aligned} N_T &= \left\lfloor \frac{E_{cap-max} - E_{min}}{E_{packet-tx}} \right\rfloor, \\ N_R &= \left\lfloor \frac{E_{cap-max} - E_{min}}{E_{packet-rx}} \right\rfloor, \end{aligned} \tag{146}$$

where $E_{cap-max}$ refers to the energy capacity of the harvesting system given by (140), and $E_{packet-tx}$ and $E_{packet-rx}$ are the energy consumed in the transmission and in the reception of a N_{bits} long packet, respectively, defined in (143). The operator $\lfloor\cdot\rfloor$ returns the highest integer number which is lower than the operand. For this model, $N_R > N_T$, and the total number of states corresponds to $N_R + 1$. For convenience, we define $N_{RT} = N_R/N_T$ as the number of packets received with the energy required for the transmission of a packet.

7.4.1.2 Packet-energy-harvesting Rate

As shown in Figure 49, the transition from an energy state n to a state $n + 1$ happens according to the packet-energy-harvesting rate $\lambda_{e-packet}^{n}$. As described in Section 7.2, due to the non-linearities in the energy-harvesting process, the energy-harvesting rate λ_e in (142) depends on the current energy state n. As a result, the transitions between states are not homogenous, but differ for every state.

The packet-energy-harvesting rate $\lambda^n_{e-packet}$ in energy-packet/second, between an energy state n and an energy state $n+1$, can be written as a function of the energy in the current state E^n and the energy required to receive a packet $E_{packet-rx}$:

$$\lambda^n_{e-packet} = \lambda_e \left(E^n, E_{packet-rx} \right) / E_{packet-rx}, \tag{147}$$

where λ_e is the energy-harvesting rate in Joule/second in (142).

7.4.1.3 Packet Transmission and Reception Rates

As shown in Figure 49, the transition from a higher energy state to a lower energy state is governed by the packet transmission rate $\lambda_{tx}(t)$ and the packet reception rate $\lambda_{rx}(t)$. The transmission of a packet results in a transition between a state n and a state $n - N_{RT}$. The reception of a packet results in a transition between a state n and the state $n-1$. $\lambda_{tx}(t)$ and $\lambda_{rx}(t)$ depend on the packet generation rate λ_{packet} of a nanomachine, which we consider constant, the relayed traffic λ_{neigh} and the energy states of all the nanomachines involved in the communication process (transmitter, receiver and interfering nodes). The overall network traffic and the energy in the nanomachines are correlated and their relation needs to be captured by the energy model.

To determine $\lambda_{tx}(t)$ and $\lambda_{rx}(t)$ we can proceed as follows. First, in order to successfully transmit a packet, the following conditions need to be satisfied:

- A packet cannot be transmitted if the energy level of the transmitting nanomachine, modeled by the process $\mathcal{E}_{tx}(t)$, at transmission time t_0 is lower than N_{RT}, *i.e.*, $\mathcal{E}_{tx}(t_0) \in \{0, 1, ..., N_{RT}-1\}$. This probability can be written as

  $$p_{drop-tx}(t) = \sum_{i=0}^{N_{RT}-1} \pi^i_{tx}(t), \tag{148}$$

  where $\pi^i_{tx}(t)$ is an element of the vector $\boldsymbol{\pi_{tx}}(t) = \left\{ \pi^0_{tx}(t), \pi^1_{tx}(t), ... \right\}$, which is the state probability vector of the process $\mathcal{E}_{tx}(t)$.

- A packet will not be received if the energy state of the receiving nanomachine, modeled by the process $\mathcal{E}_{rx}(t)$, at time $t_0 + T_{prop}$ is $n = 0$, where T_{prop} refers to the propagation delay between transmitter and receiver. This probability is given by

$$p_{drop-rx}(t) = \pi_{rx}^{0}(t), \tag{149}$$

where $\pi_{rx}^{0}(t)$ is an element of the vector $\boldsymbol{\pi_{rx}}(t) = \left\{\pi_{rx}^{0}(t), \pi_{rx}^{1}(t), ...\right\}$, which is the state probability vector of the process $\mathcal{E}_{rx}(t)$.

- A packet will not be properly received if the channel introduces transmission errors. This probability is

$$p_{error} = 1 - (1 - BER)^{N_{bits}}, \tag{150}$$

where BER refers to the bit error rate and N_{bits} is the packet length in bits, defined as in Section 7.3. The BER depends on the transmission power, the transceiver architecture, the distance between the communicating nanomachines and the channel and noise behavior. For the time being, we do not consider any error correcting scheme.

- A packet will not be properly received if it collides with other nanomachines' transmissions. This probability can be written as

$$p_{coll}(t) = 1 - e^{-\lambda_{net}(t) W T_p N_{bits}}, \tag{151}$$

where $\lambda_{net}(t)$ refers to the network traffic, W is the coding weight, T_p is the pulse duration, and N_{bits} is the packet length. This probability is in general much lower than $p_{drop-tx}(t)$ and $p_{drop-rx}(t)$ due to the fact that the transmission of the information with very short pulses minimizes the chances of having a collision. Note that, as described in Section 7.3, the packets only collide if their symbols exactly overlap in time and silences (logical "0"s) do not create collisions.

We now define the probability $p_{success}(t)$ of successful transmission at time t as

$$p_{success}(t) = \left(1 - p_{drop-tx}(t)\right)\left(1 - p_{drop-rx}(t)\right)(1 - p_{error})(1 - p_{coll}(t)). \tag{152}$$

The total traffic rate $\lambda_{net}(t)$ between neighboring nanomachines in (151) is given by

$$\begin{aligned} \lambda_{net}(t) &= \sum_{i=0}^{K} \left(\lambda_{packet} + \lambda_{neigh}\right)\left(1 - p_{drop-tx}(t)\right)(1 - p_{success}(t))^{i} = \\ &= (M+1)\,\lambda_{packet}\left(1 - p_{drop-tx}(t)\right)\frac{1 - (1 - p_{success}(t))^{K+1}}{p_{success}(t)}, \end{aligned} \tag{153}$$

where K is the maximum number of retransmissions, λ_{packet} refers to the packet generation rate and λ_{neigh} refers to the rate of the traffic coming from the neighbors, which we consider to be equal to $M\lambda_{packet}$, where M is the number of neighbors. In this definition, we take into account that only if the transmitter has enough energy, an attempt to transmit will result in a packet in the channel.

Then, the reception rate $\lambda_{rx}(t)$ is given by

$$\lambda_{rx}(t) = \lambda_{net}\left(1 - p_{drop-rx}(t)\right), \tag{154}$$

where it is taken into account that only packets that are not dropped in reception are counted by the receiver. Note that even if the packet is not properly received due to channel errors or collisions, the energy is consumed.

Finally, the transmission rate $\lambda_{tx}(t)$ is given by

$$\lambda_{tx}(t) = \lambda_{packet}\frac{1 - (1 - p_{success}(t))^{K+1}}{p_{success}(t)}, \tag{155}$$

where we are taking into account that a nanomachine attempts to transmit the packets that it generates and all the packets that it has received without errors and which have not collided.

Up to this point, we have defined all the terms in the model for the available energy of nanomachines.

7.4.2 Steady-state Analysis

In classical sensor networks, a usual metric to measure the energy efficiency of a communication solution is the network lifetime, *i.e.*, the time between the moment at which the network starts functioning until the time at which the first sensor depletes its battery. In self-powered networks, the network lifetime tends to infinite, given that even if at some point a nanomachine runs out of energy, it will eventually recharge itself.

We are interested in determining the behavior of the system in the steady state. We assume that the network reaches an equilibrium when time tends to infinity. This is correct if we consider the energy harvesting rate λ_e and the packet generation rate λ_{packet} to be stationary. Then, in the steady state, the state probability vector $\boldsymbol{\pi}$, the transition rate matrix $\boldsymbol{Q}$ given by (144), and the equations (148), (149), (151), (152), (153), (154) and (155) lose their temporal dependence. In addition, if we consider the source of vibration and the traffic in the network to be homogenous, the steady state is the same for all the nanomachines and, thus, the state probability vectors $\boldsymbol{\pi_{tx}}$ in (148) and $\boldsymbol{\pi_{rx}}$ in (149) can be replaced by $\boldsymbol{\pi}$.

In this case, the probability mass function (p.m.f.) of the nanomachine energy can be written as a function of the steady state probability vector $\boldsymbol{\pi}$:

$$p_{\mathcal{E}}\left(E^i\right) = \pi^i, \tag{156}$$

i.e., the probability of having an energy exactly equal to $E^i = E_{min} + iE_{packet-rx}$ is π^i. Similarly, the cumulative distribution function (c.d.f.) of the nanomachine energy is

$$F_{\mathcal{E}}(E) = \sum_i \left\{\pi^i | E_i \leq E\right\} \tag{157}$$

and the probability of a nanomachine to have at least E energy is given by $1 - F_{\mathcal{E}}(E)$.

To determine the steady state probabilities in (156) and (157), we need to solve the system of $N_R + 1$ equations given by $\boldsymbol{\pi Q} = \mathbf{0}$ with the additional equation given by the normalization condition for the steady state probability vector, $\sum_i \pi^i = 1$. Note the transition rate matrix $\boldsymbol{Q}$ in (144) depends on the packet transmission rate λ_{tx} from (155) and the packet reception rate λ_{rx} from (154), which depend on the total traffic λ_{net} in (153). This depends on the probabilities of dropping a packet in transmission or in reception, $p_{drop-tx}$ in (148) and $p_{drop-rx}$ in (149), respectively, the probability of having channel errors, p_{error} in (150), and the probability of having a collision p_{coll} in (151). On their turn, these probabilities depend on the steady state probabilities of the system $\boldsymbol{\pi}$. Therefore, (155), (154), (153), (148), (149), (150) and (151) need to be jointly solved with the steady state conditions for $\boldsymbol{\pi}$ and $\boldsymbol{Q}$. These form a system of $N_R + 10$ equations from which finding a closed-form expression of $\boldsymbol{\pi}$ is not feasible. However, these equations define a mathematical framework that allows us to numerically investigate the effect of different system parameters on the network performance, as we do in the next section.

7.5 Numerical Results

In this section, first, we validate the analytical energy model introduced in Section 7.4 by means of simulation. Then, we use this model to investigate the impact of energy on three different common metrics in nanonetworks.

7.5.1 Energy Model Validation

We use MATLAB to simulate a nanonetwork composed by 100 nanomachines which are uniformly distributed over a 1 cm^2 surface and which transmit information in a multi-hop fashion. Each nanomachine harvests vibrational energy by means of a piezoelectric nanogenerator with the following parameters. The energy capacity $E_{cap-max}$ in (140) is 800 pJ, which corresponds to the energy in a capacitor with C_{cap}= 9 nF charged at V_g= 0.42 V. For the computation of the energy-harvesting rate λ_e in (142), an ambient vibration with an average time between vibrations t_{cycle} = 1/50 s is considered. The amount of charge ΔQ harvested per cycle is 6 pC. The battery is fully discharged at the beginning of a simulation.

Each nanomachine generates new packets by following a Poisson distribution with parameter $\lambda_{packet} = \lambda_{info}/N_{bits}$, where λ_{info} accounts for both new data and forwarded traffic, and N_{bits} is the packet length. A packet is composed by N_{header}= 32 bits of header and N_{data}= 96 bits for the payload. Packets are broadcasted to the neighboring nodes by means of TS-OOK. The transmitted pulses are one-hundred-femtosecond long. The separation between symbols three orders of magnitude larger than the pulse length. The energy consumption for the transmission of a pulse $E_{pulse-tx}$ and for the reception of a pulse $E_{pulse-rx}$ are 1 pJ and 0.1 pJ, respectively (this provides the system with a BER of 10^{-4} at 10 mm).

The energy consumption in the transmission and in the reception of a packet, $E_{packet-tx}$ and $E_{packet-rx}$, respectively, are computed from (143) (coding weight $W = 0.5$).

To validate our model, we compare the normalized histogram of the nanomachines energy evolution over time in the simulations with the p.m.f. of the nanomachine energy, $p_{\mathcal{E}}$ in (156), obtained from the proposed analytical model. A total of twenty 10000-second long simulations are used to compute the histogram. The initial samples of each run are discarded to account only for the steady state of the network. This is shown in Figure 50 for different packet generation rates, λ_{info}. The simulation results and the numerical results from the steady-state analysis of the energy model match accurately. From the figures, it is clear that for low packet generation rates, *e.g.*, 3 bit/second, the p.m.f. is centered around the highest energy levels, *i.e.*, the device has enough energy for the majority of the cases. As the information-generation rate is increased, the p.m.f. of the nanomachine energy shifts towards the lower energy levels. In light of these results, we next analyze the performance of energy harvesting nanonetwork by means of our analytical model.

7.5.2 End-to-End Successful Packet Delivery Probability

The first nanonetwork performance metric that we investigate is the end-to-end successful packet delivery probability. This is defined as

$$p_{success-e2e} = \left(1 - (1 - p_{success})^{K+1}\right)^{N_{hop}} \tag{158}$$

where N_{hop} is the total number of hops, K is the total number of retransmissions and $p_{success}$ refers to the probability of successful transmission in (152). In our analysis we consider that the average distance between two nanomachines is constant and, thus, the average number of hops N_{hop} for a packet is fixed for a given end-to-end transmission distance. In our analysis, we consider an average of 5 hops per packet.

In Figure 51, the end-to-end successful packet delivery probability $p_{success-e2e}$ is shown as a function of the packet size N_{bits} and the number of retransmissions K. From this representation, it is clear that there is an optimal packet size and number of retransmissions that

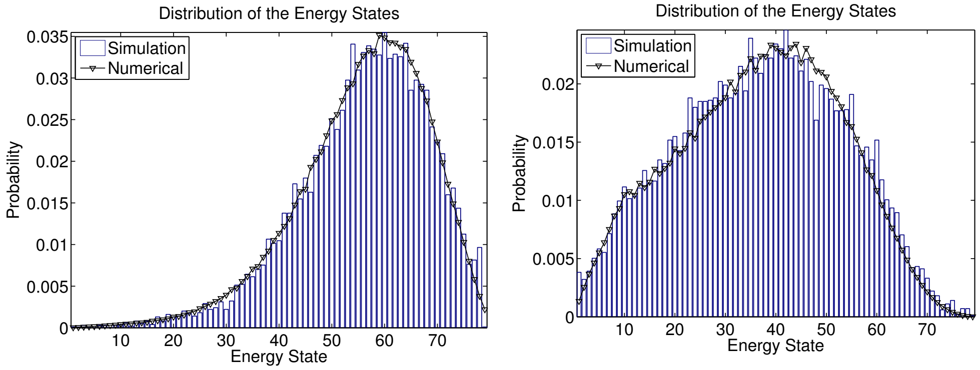

(a) λ_{info} = 3 bit/second

(b) λ_{info} = 5 bit/second

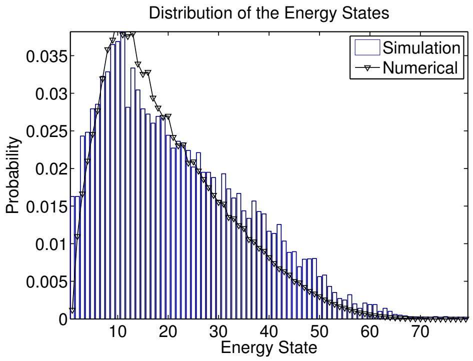

(c) λ_{info} = 7 bit/second

Figure 50. Probability mass function of the nanomachine energy as a function of the energy state for different information generation rates.

maximize the $p_{success-e2e}$. On the one hand, the transmission of shorter packets increases the number of energy states N_R from (146) in which a nanomachine can be. This increases the number of packets that can be processed in a single energy charge. In addition, the packet energy harvesting rate λ_e^n in (147) increases by decreasing the packet size. Moreover, due to the non-linearities in the energy harvesting process, the rate at which the energy is harvested is higher when the nano-device is approaching its lower energy states (see Figure 48). Therefore, the time needed to recover from the lower energy level is shorter. On the other hand, for a constant information generation rate λ_{info}, a higher number of packets $\lambda_{packet} = \lambda_{info}/N_{data}$ needs to be transmitted to convey the same amount of information. This can have a major impact in the network traffic λ_{net} in (153) as well as in the energy of a relaying node. In addition, each packet has a fixed header with N_{header} bits. In this case, the optimal scheme corresponds to transmit 48 bit packets with up to 1 retransmissions.

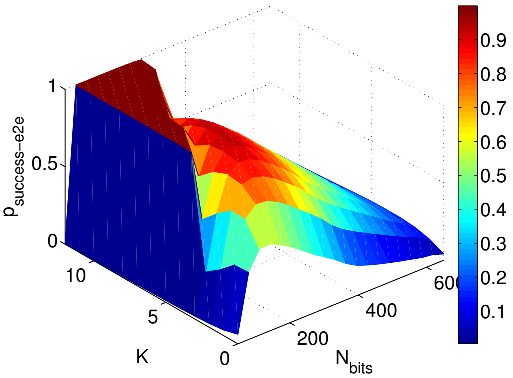

Figure 51. End-to-end successful packet delivery probability as a function of N_{bits} and K.

7.5.3 End-to-End Packet Delay

The second metric in our analysis is the end-to-end packet delay, T_{e2e}, which is given by

$$T_{e2e} = N_{hop} \sum_{i=0}^{K} \left(T_{prop} + T_{data} + iT_{t/o} \right) \tag{159}$$

where N_{hop} is the total number of hops and K is the total number of retransmissions. T_{prop} is the propagation time, T_{data} is the packet transmission time, and $T_{t/o}$ is a time-out time, which we define as follows:

$$\begin{aligned} T_{t/o} = p_{drop-tx} T_{RT} + \left(1 - p_{drop-tx}\right) \Big(& p_{drop-rx} T_R \\ & + \left(1 - p_{drop-rx}\right) (1 - p_{error} p_{coll})\, T_o \Big) \end{aligned} \tag{160}$$

where $p_{drop-tx}$ stands for the probability of having enough energy to transmit the packet (148), $p_{drop-rx}$ refers to the probability of having enough energy to receive a packet (149). p_{error} and p_{coll} are the probabilities of having channel errors or suffering collisions, respectively, and are given by (150) and (151), respectively. T_{RT} refers to the average time needed to harvest enough energy to transmit a packet, and it is given by:

$$T_{RT} = \sum_{i=0}^{N_{RT}-1} \pi_{tx}^{i} / q_{tx}^{i} \tag{161}$$

where N_{RT} is the number of packets that can be received with the energy required for the transmission of a packet, π_{tx}^{i} refers to the probability of finding the process $\mathcal{E}_{tx}$ in state i, and q_{tx}^{i} is the i-th element in the diagonal of the transition rate matrix $\boldsymbol{Q_{tx}}$. T_R stands for the average time needed to harvest enough energy to receive a packet, and it is given by:

$$T_R = 1/q_{rx}^0 \tag{162}$$

where q_{rx}^0 refers to the first element of the transition rate matrix $\boldsymbol{Q_{rx}}$ of the receiver. We consider in our analysis that a nanomachine will attempt to retransmit the packet after waiting a back-off time proportional to T_R. Finally, T_o is a random back-off time before retransmitting when channel errors or collisions are the reason for non proper reception.

The end-to-end packet delay is shown in Figure 52 as a function of the packet size N_{bits} and the number of retransmissions K. From this representation, it is clear that there is an optimal packet size and number of retransmissions that minimize the T_{e2e}. In addition to the previous reasoning regarding the packet length, note that the number of retransmissions has also a major impact on the network performance. By increasing the number of retransmissions K, the probability of successful transmission $p_{success}$ and the end-to-end delay are reduced. However, if the reason to retransmit is the lack of energy either at the transmitter or the receiver side, the necessary waiting time $T_{t/o}$ to recharge the energy system up to a minimal level will determine the end-to-end delay T_{e2e} from (160). Intuitively, a packet that can be transmitted without having to wait in any nanomachine can reach the destination at speeds that approach the capacity of the channel (tens of Gigabits per second for the transmission power in this scenario). On the contrary, if the packet needs to wait several times for a nanomachine to recharge, the end-to-end delay will approach the energy harvesting rate, which is several orders of magnitude lower than the information rate. In this case, the optimal strategy would be to transmit 48-bit long packets without retransmissions.

7.5.4 Throughput

The third metric that we consider is the nanonetwork throughput, th_{put}, which is defined as

$$th_{put} = \frac{N_{data} p_{success-e2e}}{T_{e2e}} \tag{163}$$

where N_{data} refers to the number of data bits per packet, $p_{success-e2e}$ refers to the end-to-end successful packet delivery probability in (158) and T_{e2e} is the end-to-end packet delay

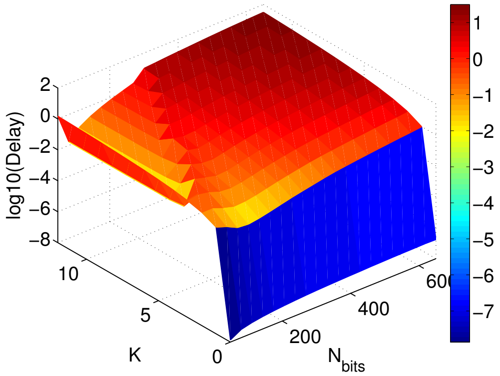

Figure 52. End-to-end packet delay as a function of N_{bits} and K.

from (160). The throughput is shown in Figure 53 as a function of the packet size N_{bits} and the number of retransmissions K. Similarly than before, there is an optimal packet size that maximizes the network throughput. The optimal parameters for this network are N_{bits}=175 bits without retransmissions. Ultimately, these results illustrate the fact that even if the Terahertz Band enables nanomachines to communicate at very high bit-rates, their energy limitations can drastically reduce their throughput.

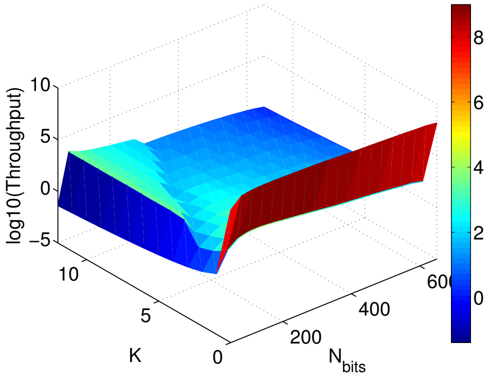

Figure 53. Throughput as a function of N_{bits} and K.

7.6 Conclusions

In this chapter, we have proposed the first energy model for self-powered nanomachines with the final goal of jointly analyzing the energy harvesting and the energy consumption processes. For this, we have developed an analytical model for the energy harvesting process of a nanomachine powered by a piezoelectric nano-generator, we have reviewed the energy consumption process due to communication among nanosensors in the Terahertz Band, and we have jointly modeled the temporal variations in the nanosensor energy and their correlation with the overall network traffic. From this model, we have developed a mathematical framework to investigate the impact of the packet size and the retransmission policy on the end-to-end successful packet delivery probability, the end-to-end packet delay, and the throughput of nanonetworks. Integrated nanomachines have not been built yet and, thus, the development of an analytical energy model is a fundamental step towards the design of nanonetworking architectures and protocols.

CHAPTER 8

PHLAME: A PHYSICAL LAYER AWARE MAC PROTOCOL FOR NANONETWORKS IN THE TERAHERTZ BAND

Due to the expectedly very high density of nanomachines in nanonetworks, novel Medium Access Control (MAC) protocols are needed to regulate the access to the channel and to coordinate concurrent transmissions among nanomachines. In this chapter, a new PHysical Layer Aware MAC protocol for Electromagnetic nanonetworks in the Terahertz Band (PHLAME) is presented. This protocol is built on top of TS-OOK and exploits the benefits of novel low-weight channel coding schemes. In PHLAME, the transmitting and receiving nanomachines jointly select the optimal communication scheme and channel coding parameters which maximize the probability of successfully decoding the received information while minimizing the generated multi-user interference. The performance of the protocol is analyzed in terms of energy consumption, delay and achievable throughput, by taking also into account the energy limitations of nanomachines. The results show that PHLAME, by exploiting the properties of the Terahertz Band and being aware of the nanomachines limitations, is able to support very densely populated nanonetworks with nanomachines transmitting at tens of Gigabits per second.

8.1 Motivation and Related Work

Classical MAC protocols cannot directly be used in nanonetworks because they do not capture either the limitations of nanomachines or the peculiarities of the Terahertz Band:

- First, the majority of existing MAC protocols for wireless networks have been designed for band-limited channels. This is not the case of nanonetworks because, as shown in Chapter 3, the Terahertz Band channel provides nanomachines with an almost 10 THz wide window. This is the main difference between graphene-enabled wireless communication for nanonetworks in the Terahertz Band and the classical wireless paradigms.

- Second, classical MAC protocols which are based on carrier-sensing techniques cannot be used in pulse-based communication systems. Only some solutions proposed for Impulse Radio Ultra Wide Band (IR-UWB) networks [57] could be considered, but their complexity limits their usefulness in the nanonetwork scenario. For example, it does not seem feasible to generate and distribute orthogonal time hopping sequences among nanomachines as in IR-UWB.
- Third, the main limitation for nanomachines results from the very limited energy that can be stored in nano-batteries, which requires the use of novel energy-harvesting systems, as we have analyzed in Chapter 7. As a result, the energy of nanomachines has both positive and negative temporal fluctuations which change the availability of the nanomachine to communicate over time.

In this chapter, we present the PHLAME, a PHysical Layer Aware MAC protocol for Electromagnetic nanonetworks in the Terahertz Band. This protocol is built on top of the Rate Division Time-Spread On Off Keying (RD TS-OOK), which is a revised version of our proposed pulse-based communication scheme for nanomachines, *i.e.*, TS-OOK, and it exploits the benefits of novel low-weight channel coding schemes. PHLAME is based on the joint selection by the transmitter and the receiver of the optimal communication scheme and channel coding parameters which minimize the interference in the nanonetwork and maximize the probability of successfully decoding the received information. Moreover, the fluctuations in the energy of the nanomachines are taken into account. To the best of our knowledge, this is the first MAC protocol for EM nanonetworks that captures the peculiarities of the Terahertz Band as well as the expected capabilities of graphene-based nanomachines.

8.2 Rate Division Time Spread On-Off Keying

The Rate Division Time Spread On-Off Keying (RD TS-OOK) is a modulation and channel access mechanism for nanomachines based on the asynchronous exchange of femtosecond-long pulses, which are transmitted following an on-off keying modulation spread in time. It is the natural evolution and multi-user extension of our proposed TS-OOK in Chapter 4.

The functioning of this communication scheme is very similar to that of TS-OOK. The main difference remains in the fact that the time between symbols T_s and the symbol rate $\beta = T_s/T_p$ are different for different nanomachines and for different types of packets. This is done to minimize the probability of multiple sequential symbol collisions in a packet. If all the nanomachines are transmitting at the same symbol rate, a collision in one symbol entails a collision in every symbol until the end of the first packet. These type of collisions are usually referred to as catastrophic collisions. In other pulse-based schemes such as in IR-UWB, orthogonal time hopping sequences are used to avoid this condition [57]. Due to the complexity of generating, distributing and updating these sequences among nanomachines, we advocate for the variation of the transmission symbol rate β [154].

RD TS-OOK provides almost orthogonal channels to nanomachines in close vicinity. First, as in TS-OOK, symbol collisions are very unlikely due to the very short length of the transmitted symbols T_p and due to the fact that the time between symbols T_s is much longer than the symbol duration T_p. Second, even if a symbol collision occurs, not all types of collisions are *harmful*. For example, there are no collisions between silences, and collisions between pulses and silences are only harmful from the silence perspective, *i.e.*, the intended receiver for the pulse will not notice any difference if silence is received at the same time. Moreover, by allowing different nanomachines to transmit at different symbol rates, a collision in a given symbol does not lead to multiple consecutive collisions in the same packet.

Figure 54 illustrates an example of RD TS-OOK for the case in which two nanomachines start transmitting to a third common receiver, with different initial transmission

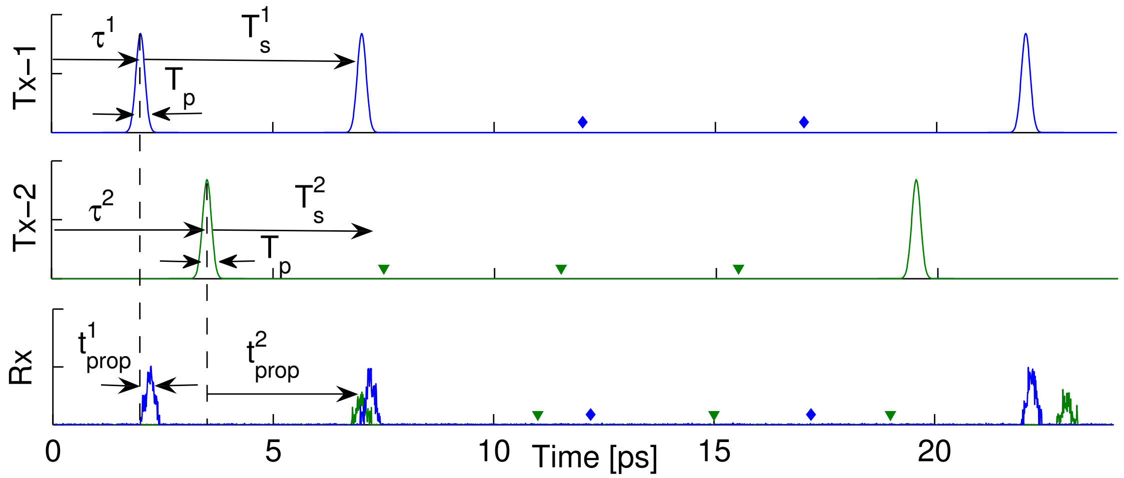

Figure 54. RD TS-OOK illustration: top) First nanomachine transmitting the sequence “11001”; middle) Second nanomachine transmitting the sequence “10001”; bottom) Overlapped sequences at the receiver side.

times τ^1 and τ^2. The upper plot corresponds to the sequence “11001”, which is transmitted by the first nanomachine. A logical “1” is represented by a short pulse and a logical “0” is represented by silence. The time between symbols T_s^1 is much larger than the symbol duration T_p. This transmitted signal is propagated through the channel and corrupted with molecular absorption noise by the time it reaches the receiver. Similarly, the second plot shows the sequence transmitted by the second nanomachine, “10001”, with a different symbol rate T_s^2. In this example, the second nanomachine is farther from the receiver than the first nanomachine. As a result, the signal at the receiver suffers from higher attenuation, longer delay, and more noise. The signal at the receiver side is shown in the third plot. In this specific case, the delay introduced by the channel to each signal, t^1_{prop} and t^2_{prop}, is such that the first symbol of the second nanomachine overlaps with the second symbol of the first nanomachine. As a result of using different symbol rates, consecutive symbols in both nanomachines do not overlap.

8.3 Protocol Description

PHLAME is a novel MAC protocol tailored to the peculiarities of the Terahertz Band and which takes into account the limitations of electronic nanomachines. The protocol is built on top of RD TS-OOK, and it is split in two stages, namely, the handshaking process and the data transmission process, which we describe next.

8.3.1 Handshaking Process

The aim of the handshaking process is twofold. First, it allows a receiver to coordinate multiple simultaneous transmissions. Second, it facilitates the joint selection of i) the transmission symbol rate and ii) the channel coding scheme which make the data transmission more reliable. The handshaking process is divided in two substages,

- The *handshaking request* is triggered by any nanomachine that has information to be transmitted and which has enough energy to complete the process. A transmitter generates a `Transmission Request(TR)` packet, which contains the Synchronization Trailer, the Transmitter ID, the Receiver ID, the Packet ID, the transmitting Data Symbol Rate (DSR) and the Error Detecting Code (EDC).

  The DSR field specifies the symbol rate β^i that will be used to transmit the data packet. The strength of RD TS-OOK against collisions increases when different nanomachines transmit at different rates. In PHLAME, every transmitting node randomly selects a symbol rate from a set of coprime rates, which have been shown to minimize the probability of having catastrophic collisions [154]. The EDC field is a conventional checksum field to detect transmission errors.

  The TR packet is transmitted using a Common Coding Scheme (CCS), which specifies a predefined symbol rate β^0 and channel coding scheme. When using the same symbol rate β^0, catastrophic collisions might occur among TR packets. However, the TR packets are very short and the EDC field should suffice to detect simple errors in the majority of the cases. Finally, the transmitter waits for a timeout before trying to retransmit the TR packet, if necessary.

- The *handshaking acknowledgment* is triggered by the receiver of the TR packet, which uses the CCS to decode the received bitstreams when listening to the channel. If a TR packet is successfully decoded, the receiver will check whether it can handle an additional incoming bitstream. In our scenario, we consider that due to the energy limitations of nanomachines, after the transmission or the active reception of a packet, a device needs to wait for a certain *recovery time* in order to restore its energy by means of energy harvesting systems, as we modeled in Chapter 7. This time is much longer than the packet transmission delay and this poses a major constraint.

If the handshake is accepted, the receiver replies to the transmitter with a `Transmission Confirmation(TC)` packet, which is encoded by using the CCS. The TC packet contains the Synchronization Trailer, the Transmitter ID, the Receiver ID, the Packet ID, the transmitting Data Coding Scheme (DCS) and the Error Detecting Code. The DCS is selected by the receiver in order to guarantee a target Packet Error Rate (PER). This depends on the perceived channel quality, which can be estimated from the received pulse shape and intensity, or the measured noise.

To achieve the target PER, we consider that nanomachines make use of low-weight channel codes concatenated with simple repetition codes. For this, first, the DCS field specifies the channel code weight, *i.e.*, the average number of logical “1”s in the encoded data. By reducing the code weight, *i.e.*, by encoding the information using more logical “0”s than logical “1”s, both molecular absorption noise and interference can be mitigated without affecting the achievable information rate, as we showed in Chapter 5. Second, the DCS specifies the order of the repetition code that will be used to protect the information. Since RD TS-OOK reduces possible transmissions errors by avoiding catastrophic symbol collisions, a simple repetition code is enough to decode the information in the majority of the cases.

8.3.2 Data Transmission Process

At this point, a `Data Packet(DP)` is transmitted at the symbol rate β^i specified by the transmitter in the DSR field, and encoded with the weight and repetition order specified by the receiver in the DCS field. The DP contains a Synchronization Trailer, the Transmitter ID, the Receiver ID, and the useful Data. The Error Detecting Code has been removed from the packet since, by using different symbol rates, catastrophic collisions are highly unlikely, and randomly positioned errors can be fixed by means of the chosen channel coding scheme. If the DP is not detected at the receiver before a time-out the receiver assumes that the handshaking process failed.

8.4 Performance Analysis

In this section, we analyze the performance of PHLAME in terms of energy consumption, packet latency and normalized throughput.

8.4.1 System Model

We make the following considerations in our analysis:

- The path-loss and noise in the Terahertz Band are computed by using the models introduced in Chapter 3. A standard medium with 10% of water vapor is considered.
- The interference is modeled as in Chapter 5, by assuming a Poisson field of interferers. The density of active nodes is a parameter value in our analysis.
- The transmitter encodes logical "1"s by using the first time-derivative of 100 femtosecond long Gaussian pulses. The energy of a pulse is limited to 100 pJ.
- A non-coherent receiver architecture is considered, with an integration time T_i equal to ten times the symbol duration T_p [40].
- The recovery time for a nanomachine after transmission or active reception of a DP is three orders of magnitude longer than the data packet duration [152].

- The receiver can simultaneously track a fixed number of incoming packets, K. We model this as a finite length queueing system with K servers and without waiting lane (a packet that cannot be served is discarded) [65].

- The RD TS-OOK symbol rates are randomly chosen by each node from a pool of pairwise coprime rate codes in the order of 1000 (*e.g.*, 1009, 1013, 1019).

- The TR and TC packets in PHLAME are 16 Bytes. DPs are 125 Kbytes. The packet length is arbitrarily chosen, but it seems appropriate to use relatively large DPs because RD TS-OOK does not cannibalize the channel and transmission errors are expectedly sparse.

- The target Packet Error Rate is equal to 10^{-3}. The possible bit coding schemes are limited to a non repetition code with weight equal to 0.5 (the number of logical "1"s and "0"s is the same), a 3-repetition code with weight equal to 0.4 (only 40% of the bits are logical "1"s), a 5-repetition code with weight equal to 0.3, a 7-repetition code with weight equal to 0.2 and a 9-repetition code with weight equal to 0.1. We consider that a n-repetition code is a coding scheme that replicates n times each symbol, either pulses or silences.

8.4.2 Energy Consumption

The energy consumption is contributed by the consumption at the transmitter and at the receiver.

8.4.2.1 Transmitter Energy Consumption

This is mainly governed by the number of handshaking attempts and the length and code weight used for the transmission of the DP. Three possible cases can happen when starting a new packet transmission:

1. The handshaking process fails because:
    (a) The TR packet collides with other packets

   (b) The receiver cannot allocate one more transmission due to memory constraints.
   (c) The receiver is in the energy recovery stage.

2. The handshaking process fails because the TC packet collides at the transmitter.
3. The handshaking process succeeds, and the nodes go into the Data Transmission phase.

To estimate the energy consumption at the transmitter, we consider the energy involved in the transmission, E_{TX}, reception, E_{RX}, and time-out, $E_{t/o}$, for each one of the aforementioned cases. These partial energies are given by:

$$\begin{aligned} E_1 &= E_{TX}^{TR} + E_{t/o}^{H} \\ E_2 &= E_{TX}^{TR} + E_{RX}^{TC} \\ E_3 &= E_{TX}^{TR} + E_{RX}^{TC} + E_{TX}^{DP}. \end{aligned} \tag{164}$$

Each type of packet used by PHLAME (TR, TC and DP) has a different number of bits and it is encoded using different channel coding schemes. Moreover, the data packets' structure depends on the selected DSR and DCS. When more robust codes are needed, the repetition code order is increased and its weight is reduced. This makes packets longer but not necessarily much more energy consuming, because only the transmission of pulses consumes energy, and this decreases with the code weight. At the same time, transmitting with lower weight codes can also reduce the overall interference and ultimately the number of retransmissions, as we discussed in Chapter 5.

Each case for the energy consumption described above occurs with a certain probability, which can be calculated as:

$$\begin{aligned} p_1 &= 1 - p_a^{Rx} p_s^{TR} \\ p_2 &= p_a^{Rx} p_s^{TR} \left(1 - p_s^{TC}\right) \\ p_3 &= p_a^{Rx} p_s^{TR} p_s^{TC} \end{aligned} \tag{165}$$

where p_a^{Rx} refers to the probability of acceptance at the receiver, and p_s^{TR} and p_s^{TC} refer to the probability of successful reception of the TR and the TC packets, respectively. p_a^{Rx} is computed by taking into account the maximum number K of simultaneous incoming packets that the receiver can handle and its energy status. p_s^{TR} and p_s^{TC} are computed from the symbol error probability with the type of pulses that are considered, and by taking into account the error correcting capabilities of the used channel codes.

The consumed energy in the transmitter depends on the number of retransmissions required to complete the handshaking. Since the probability of successful handshaking is exactly p_3, the energy consumed at the transmitter is:

$$E_{transmitter} = \frac{1}{p_3} \left(p_1 E_1 + p_2 E_2 + p_3 E_3 \right). \tag{166}$$

By combining (164) and (165) into (166), we reach the following closed-form expression:

$$\begin{aligned} E_{transmitter} =& \frac{1}{p_a^{Rx} p_s^{TR} p_s^{TC}} \Big(\left(1 - p_a^{Rx} p_s^{TR}\right) \left(E_{TX}^{TR} + E_{t/o}^{H}\right) \\ &+ p_a^{Rx} p_s^{TR} \left(1 - p_s^{TC}\right) \left(E_{TX}^{TR} + E_{RX}^{TC}\right) \Big) \\ &+ E_{TX}^{TR} + E_{RX}^{TC} + E_{TX}^{DP}. \end{aligned} \tag{167}$$

8.4.2.2 Receiver Energy Consumption

The energy at the receiver is governed by the number of handshaking attempts as well as the DP transmission. The handshaking fails when the receiving node is unable to decode the TR packet, when it cannot handle another transmission or when the TC packet collides. Similarly as before, by expressing the energies and the probabilities for each case, the energy consumption at the receiving node can be written as:

$$\begin{aligned} E_{receiver} =& \frac{1}{p_a^{Rx} p_s^{TR} p_s^{TC}} \Big(\left(1 - p_a^{Rx} p_s^{TR}\right) E_{RX}^{TR} \\ &+ p_a^{Rx} p_s^{TR} \left(1 - p_s^{TC}\right) \left(E_{RX}^{TR} + E_{TX}^{TC} + E_{t/o}^{DP}\right) \Big) \\ &+ E_{RX}^{TR} + E_{TX}^{TC} + E_{RX}^{DP}. \end{aligned} \tag{168}$$

Finally, the total energy consumption per useful bit of information is obtained by adding (167) and (168) and dividing it by the length of the DP.

8.4.3 Packet Latency

To study the packet latency we should take into account that the different types of packets in PHLAME have different lengths and are encoded using different parameters. In particular, we consider that packets have the following average durations:

$$\begin{aligned} T^{TR} &= B^{TR}\beta_{min}T_i \\ T^{TC} &= B^{TC}\beta_{min}T_i \\ T^{DP} &= B^{DP}N_r\frac{\beta_{max}-\beta_{min}}{2}T_i \end{aligned} \tag{169}$$

where T^{TR}, T^{TC} and T^{DP} stand for the packet duration of TR, TC and DP packets, respectively; B^{TR}, B^{TC} and B^{DP} are the number of bits in the TR, TC and DP packets, respectively; β_{min} and β_{max} stand for the minimum and maximum symbol rates that the nanomachines can select, T_i refers to the integration time and N_r is the required number of symbols per bit to achieve the target PER.

Following a similar procedure as before, we can write the closed-form expression for the average packet delay as:

$$\begin{aligned} T_{PCK} = &\frac{1}{p_a^{Rx}p_s^{TR}p_s^{TC}}\left(\left(1-p_a^{Rx}p_s^{TR}\right)\left(T^{TR}+T_{t/o}^{H}\right)\right. \\ &\left.+\,p_a^{Rx}p_s^{TR}\left(1-p_s^{TC}\right)\left(T^{TR}+T_{t/o}^{DP}\right)\right) \\ &+T^{TR}+T^{TC}+T^{DP}. \end{aligned} \tag{170}$$

8.4.4 Normalized Throughput

We define the normalized throughput as the maximum information rate that the MAC layer can support divided by the maximum data rate that a node can transmit in a single nanomachine scenario. For this, we divide the nanomachine bit-rate that PHLAME can provide by the maximum achievable bit-rate imposed by RD TS-OOK. This is given by:

$$Tput = \frac{R_b^{PHLAME}\ [bps]}{R_b^{max}\ [bps]} = \frac{\dfrac{L_D}{T_{PCK}}}{\dfrac{1}{N_r \dfrac{\beta_{max}-\beta_{min}}{2} T_i}} \tag{171}$$

where L_D stands for the payload length in the data packet, T_{PCK} is the packet latency found in (170), N_r refers to the coding rate used, T_i is the observation time and β_{max}, β_{min} are the maximum and minimum symbol data rate, respectively.

8.5 Numerical Results

In this section we provide numerical results on the performance of PHLAME in terms of energy consumption, packet latency and normalized throughput.

8.5.1 Energy Consumption

In Figure 55 (left), the total energy consumption per bit as a function of the node density is shown for different maximum number of simultaneously handled packets at the receiver, k. When the node density is increased, the interference in the network increases, and this has a twofold impact on the energy consumption. First, a higher interference turns into an increased number of handshaking attempts. Second, once the handshake has been completed, the DP is transmitted using higher order repetition codes which are necessary to guarantee the target PER. The steps in the energy curves correspond to the transitions in the coding scheme from a non repetition code to a 3-repetition code, a 5-repetition code, and so on. At the same time, by allowing the receiver to handle more than one packet simultaneously, the energy decreases.

In Figure 56 (left), we show the energy consumption per useful bit of information in a nanonetwork operating under RD TS-OOK, but in which rather than using PHLAME, the DPs are directly transmitted without any type of handshaking. There are almost three

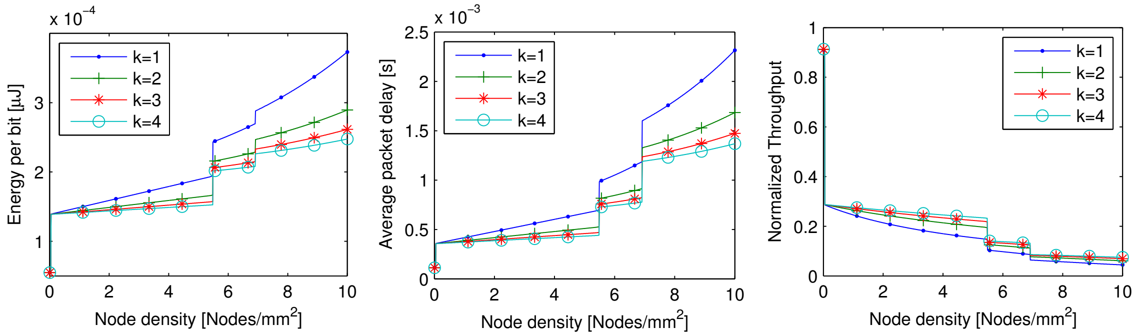

Figure 55. Energy per bit consumption, average packet delay and normalized throughput as functions of the node density for different maximum number of simultaneous packets that can be handled by the receiver.

orders of magnitude difference between PHLAME and the protocol without handshake. This result depends on the packet length and the offered load parameters. For a very dense network, as the one we are considering, a handshake avoids having to retransmit the entire DP several times. We acknowledge that a more complete analysis on the impact of the packet size in the system has to be conducted.

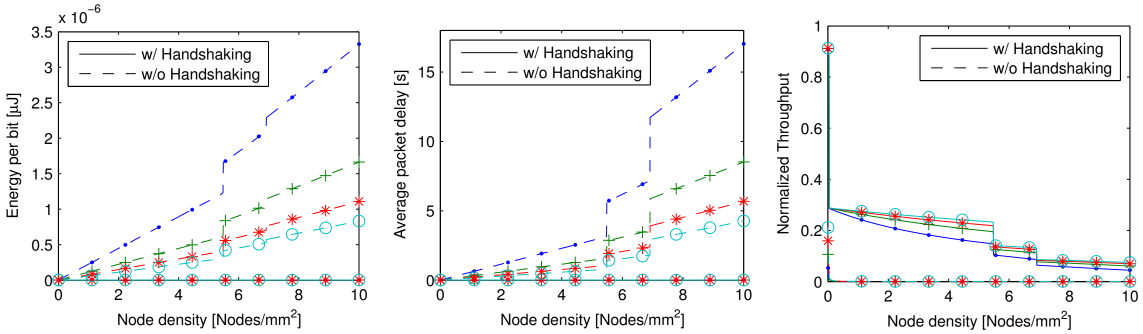

Figure 56. Comparison between PHLAME and similar protocol without handshaking stage in terms of the energy per bit consumption, average packet delay and normalized throughput as functions of the node density for different maximum number of simultaneous packets that can be handled by the receiver.

Finally, we would like to emphasize the energy reduction achieved by using low-weight coding schemes. In Figure 57, the energy consumption per bit of PHLAME is compared to that of the case in which only the repetition code order is variable and the code weight remains at 0.5. The results show that especially for very dense networks, lowering the code weight can reduce the overall energy consumption by more than half. This is due to the fact that the interference is mitigated when using lower weight codes, and this minimizes both the number of handshake attempts and the probability of symbol errors and energy consumed in the DP.

8.5.2 Packet Latency

In Figure 55 (center), the average packet delay given by (170) is shown as a function of the node density. The impact of the capabilities of the receiving node in terms of maximum number of packets that a nanomachine can handle is illustrated. When the node density is increased, the interference is increased, and consequently the number of handshaking attempts increases. This turns into longer packet transmission delays. However, the major increase comes from the change in the repetition code order that is necessary to achieve the target PER. Similarly as before, by allowing the receiver to handle more than one packet simultaneously, the overall delay is clearly reduced. Finally, note that a simple handshaking process can reduce the time delay by almost three orders of magnitude, as shown in Figure 56 (center), where the delay in PHLAME is compared to that of RD TS-OOK without handshaking process.

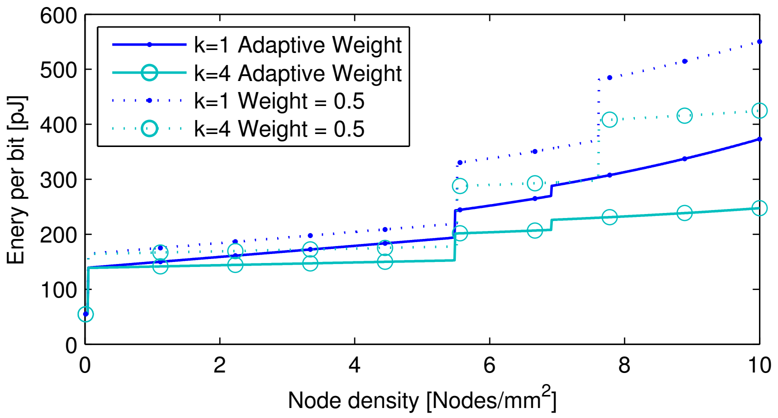

Figure 57. Energy per bit consumption as a function of the node density for different code weights.

8.5.3 Throughput

The normalized throughput is shown in Figure 55 as a function of the node density. Similarly as before, the changes in the coding scheme as the interference increases, create the steps in the throughput curves. As expected, the normalized throughput of PHLAME is much larger than that of a similar protocol without the handshaking stage (Figure 56). The main reason for this result comes from the fact that the handshake does not only inform the receiver about a new incoming transmission, but first, it asks for its permission based on its status, and, second, it determines the best communication parameters and coding scheme.

8.6 Conclusions

In this chapter, we have presented a PHysical Layer Aware MAC protocol for Electromagnetic nanonetworks (PHLAME). This protocol is tailored to a novel communication scheme based on the exchange of femtosecond-long pulses spread in time. Our solution allows the transmitter and the receiver to jointly select in an adaptive fashion several communication parameters such as the symbol rate or the encoding scheme and the channel code weight, by means of a handshaking process.

We have analyzed the performance of the proposed protocol in terms of energy consumption per useful bit of information, average packet delay and normalized achievable throughput. The results show that, despite its simplicity, PHLAME is able to support densely populated nanonetworks by exploiting the peculiarities of the Terahertz Band, the expected capabilities of nanomachines, and the benefits of low weight coding schemes.

CHAPTER 9

EMULATION OF A ONE-TO-ONE NANO-LINK

For the time being, to the best of our knowledge, functional nanomachines have not been build. As a result, advanced simulation platforms are needed to validate the developed analytical models and communication solutions. In this chapter, we describe the simulation framework that we have developed to emulate a one-to-one nano-link between two nanomachines. The developed framework combines two commercially available tools, namely, COMSOL Multi-physics [19] and Matlab. In particular, the proposed graphene-based plasmonic nano-antenna (Chapter 2) and the Terahertz Band channel (Chapter 3) are emulated in COMSOL. The signals radiated by a first nano-antenna in transmission are generated in Matlab by following the proposed femtosecond-long pulse-based modulation (Chapter 4) and the low-weight coding technique (Chapter 5). The signals detected by a second nano-antenna in reception are demodulated and decoded in Matlab accordingly. Despite the very high computational complexity, the developed platform shows to be a robust tool for the validation of the developed models.

9.1 Simulation Framework Overview

The conceptual block diagram for the developed simulation framework is shown in Figure 58. In particular,

- First, the graphene-based plasmonic nano-antenna (Chapter 2) is simulated with COMSOL Multi-physics. The starting point for the simulation is the inclusion of graphene in COMSOL as a new material with anisotropic conductivity given by our model. The details on the nano-antenna implementation are given in Section 9.2.

- Second, the Terahertz Band channel (Chapter 3) is also simulated with COMSOL. To isolate the channel effects from the antenna effects, the channel between an ideal

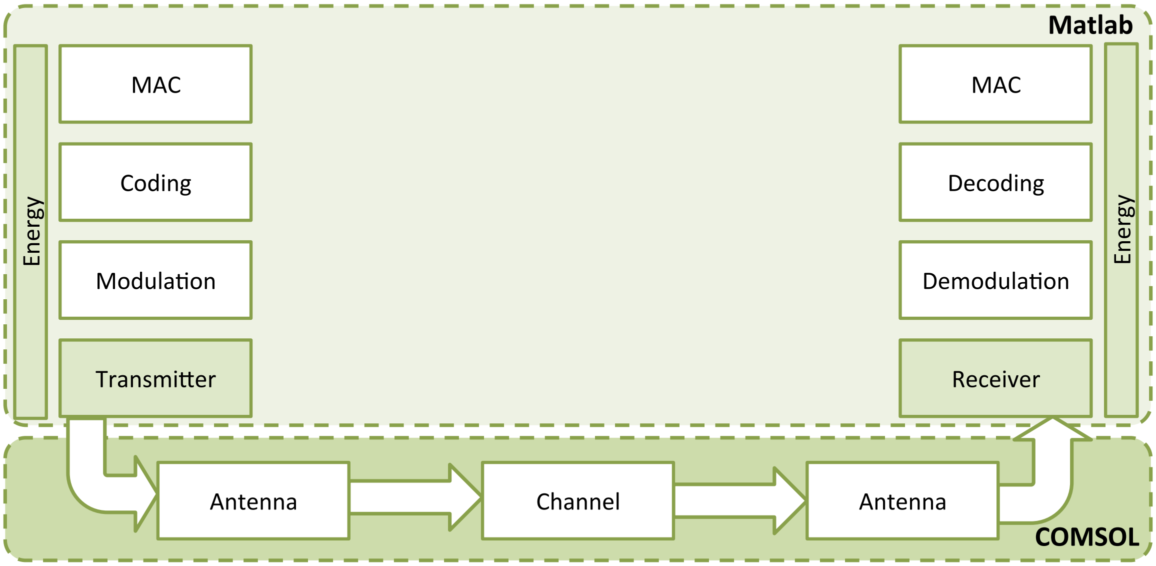

Figure 58. Block diagram of the one-to-one nano-link emulation platform.

point source and an ideal point detector is simulated. The details on the channel definition in COMSOL are explained in Section 9.3.

- Third, a one-to-one nano-link is simulated in COMSOL by utilizing two nano-antennas in the same simulation model, *i.e.*, a nano-antenna in transmission and a nano-antenna in reception. The details on the one-to-one model definition in COMSOL are explained in Section 9.4.

- Fourth, the COMSOL simulation is linked to Matlab by means of LiveLink. This enables a much simpler control of the simulation and, more importantly, the integration with the rest of the developed solutions. The details on the linkage of the two simulation environments are given in Section 9.5.

- Finally, the complete end-to-end nano-link can be established. In particular,
  - The signals that are transmitted through the nano-antenna are generated in Matlab. A binary sequence is encoded by means of our proposed low-weight channel codes (Chapter 5) and modulated with TS-OOK (Chapter 4). The transmitter acts as an ideal Gaussian-pulse generator for the time being, but could

be replaced by more accurate transmitter models in COMSOL. The generated signal is input to COMSOL with LiveLink.

  - Similarly, the signals at the output of the receiving nano-antenna are sent from COMSOL to Matlab by means of LiveLink. The proposed receiver architecture (Chapter 6) is used to detect and demodulate the received symbols. The decoded bitstream is then compared to the transmitted binary sequence.

9.2 Graphene-based Plasmonic Nano-antenna Simulation with COMSOL Multi-physics

The starting point of the one-to-one nano-link emulation is the simulation of the proposed graphene-based plasmonic nano-antenna. Next, we explain the implementation of such antenna in COMSOL. This section provides enough details to reproduce our simulation results. For the non-familiar reader, COMSOL provides a large collection of tutorial and example models [19], which can serve as the starting point.

9.2.1 Definition of the Nano-antenna

The first step is to define the geometry of the antenna. Our proposed nano-antenna is composed of a GNR, which is placed over the ground plane with a dielectric material layer in between. For this, we define the following geometry:

- The ground plane and the dielectric substrate are defined as a `block`, with width `W_sub` and length `L_sub`. The ground plane must be much larger than the antenna active element, *i.e.*, the GNR.

- The GNR is not defined as a geometric entity, but will be set as the upper boundary of the dielectric layer.

- The nano-antenna is fed by a stub. This is a common technique to feed patch antennas. The stub is defined as a `block`, with width `W_stub` and length `L_stub`. A good example on how to design the stub can be found in the COMSOL simulation example titled `Inset Microstrip Patch Antenna`.

- The simulation space is defined by a `sphere` with radius `Radius`.
- To guarantee the accuracy of the simulation and to minimize the number of unrealistic reflections from the simulation space boundaries, a `Perfectly Matched Layer` or PML, which surrounds the entire nano-structure, is defined. The PML width is `Radius_PML`.

In order to ease a parametrized analysis and the control of the model from Matlab, we define a set of global parameters to determine the geometry of the nano-antenna. In Figure 59, a set of working parameters and the resulting nano-structure are shown.

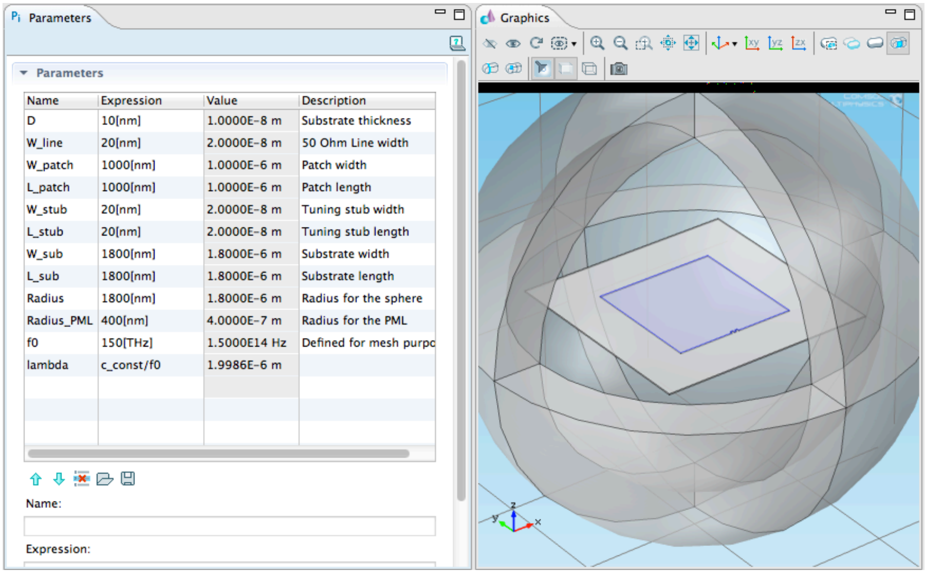

Parameters

Name	Expression	Value	Description
D	10[nm]	1.0000E-8 m	Substrate thickness
W_line	20[nm]	2.0000E-8 m	50 Ohm Line width
W_patch	1000[nm]	1.0000E-6 m	Patch width
L_patch	1000[nm]	1.0000E-6 m	Patch length
W_stub	20[nm]	2.0000E-8 m	Tuning stub width
L_stub	20[nm]	2.0000E-8 m	Tuning stub length
W_sub	1800[nm]	1.8000E-6 m	Substrate width
L_sub	1800[nm]	1.8000E-6 m	Substrate length
Radius	1800[nm]	1.8000E-6 m	Radius for the sphere
Radius_PML	400[nm]	4.0000E-7 m	Radius for the PML
f0	150[THz]	1.5000E14 Hz	Defined for mesh purpo
lambda	c_const/f0	1.9986E-6 m	

Name:

Expression:

Figure 59. Graphene-based nano-antenna simulation example parameter set and resulting geometry.

The next step consists in assigning the corresponding material to each layer. The ground plane is modeled as a PEC layer, which in COMSOL does not correspond to a material but to a boundary condition, as we will define afterwards. The dielectric layer is mainly determined by the permittivity or dielectric constant ε_r. As in Chapter 2, we consider Silicon with $\varepsilon_r = 4$ in our frequency range of interest. As we mentioned before, the definition of graphene is not done through an entity and a given material, but as a boundary condition.

To analyze the frequency response of the antenna, we proceed as follows. First, we define a new `Electromagnetic Waves, Frequency Domain` study in COMSOL. We use the frequency form of the wave equation to be solved by the simulator. The ground plane behaves as a PEC layer. For this, we select the corresponding boundary and create a new `Perfect Electric Conductor` condition in COMSOL.

For the definition of graphene, we proceed as follows. First, we define a new `Transition Boundary Condition` or TBC in COMSOL. A TBC is used to model a layer which is physically very thin (one-atom-thick in for GNRs) but electrically not thin. The following properties for the TBC are defined. Graphene is an anisotropic material, *i.e.*, its electromagnetic response is different for different dimensions. COMSOL allows us to capture this peculiarity by means of the relative dielectric permittivity matrix of the material $\boldsymbol{\varepsilon_r}$ (see Figure 60). This parameter can be obtained from the conductivity model developed in Section 2.4.1.2, as follows:

$$\boldsymbol{\varepsilon_r}(f) = \varepsilon_{r1}\boldsymbol{I_{2D}} + \mathrm{i}\frac{\boldsymbol{\sigma_{2D}}(f)}{2\pi f}, \tag{172}$$

where f stands for frequency, ε_{r1} refers to the real relative dielectric constant of the material on which the GNR stands (*i.e.*, 4 in our simulations), $\boldsymbol{I_{2D}}$ refers to the two dimensional identity matrix, and $\boldsymbol{\sigma_{2D}}$ refers to the two dimensional conductivity matrix, which can be written as

$$\boldsymbol{\sigma_{2D}}(f) = \begin{pmatrix} \sigma_{xx}(f) & \sigma_{xy}(f) \\ \sigma_{yx}(f) & \sigma_{yy}(f) \end{pmatrix}, \tag{173}$$

where σ_{xx} and σ_{yy} are given by (27), and we will consider the diagonal conductivity to be zero for this analysis. The values for σ_{xx} and σ_{yy} are loaded into COMSOL as interpolated functions. For different antenna widths, `W_patch` we use different values of the conductivity, as we described in Section 2.4. When the conductivity is incorporated as a component of the complex permittivity, no separate conductivity value needs to be input in COMSOL.

The next element needed is the excitation of the antenna. In our simulation, we incorporate a `Lumped Port` (see Figure 61). The port is assigned to the input boundary of the

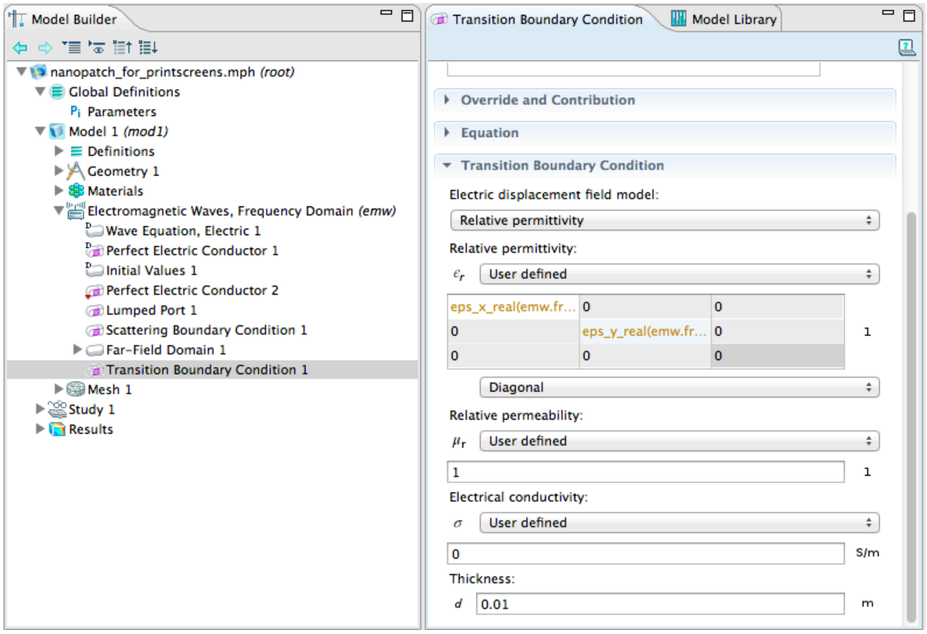

Electric displacement field model:

Relative permittivity

Relative permittivity:

ϵ_r User defined

eps_x_real(emw.fr…	0	0	
0	eps_y_real(emw.fr…	0	1
0	0	0	

Diagonal

Relative permeability:

μ_r User defined

1 — 1

Electrical conductivity:

σ User defined

0 — S/m

Thickness:

d 0.01 — m

Figure 60. Transient boundary condition and design parameters utilized to simulate graphene.

stub. We define a uniform port, with z-polarized current, and with an input impedance that matches the antenna impedance at the resonant frequency. This value is given by the parameter `z-port` in COMSOL. To be able to measure the radiation diagram of the antenna, we incorporate a `Far Field Domain`. This assigned to the outer boundaries of the PML.

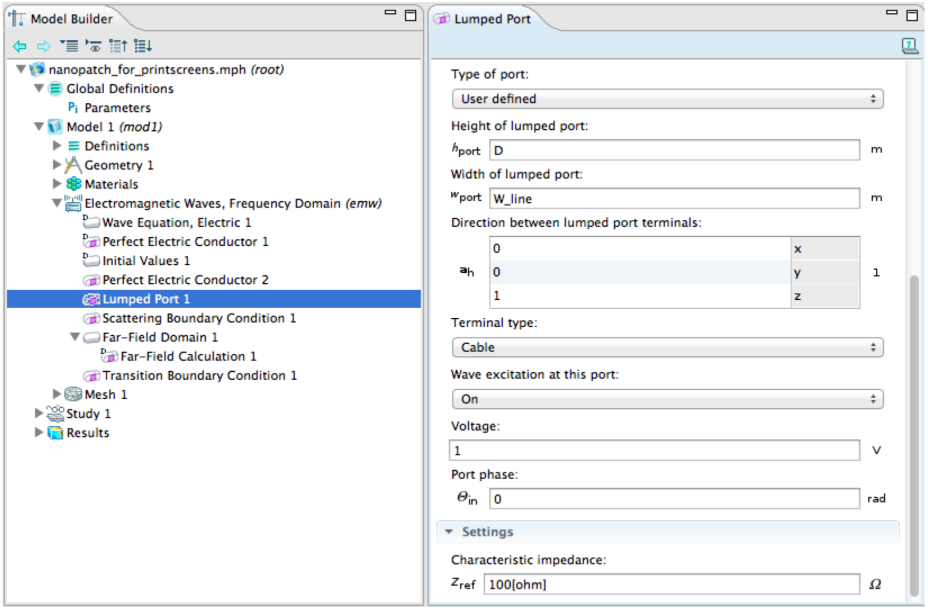

Type of port:

User defined

Height of lumped port:

h_{port} D — m

Width of lumped port:

w_{port} W_line — m

Direction between lumped port terminals:

	0	x	
a_h	0	y	1
	1	z	

Terminal type:

Cable

Wave excitation at this port:

On

Voltage:

1 — V

Port phase:

θ_{in} 0 — rad

Characteristic impedance:

Z_{ref} 100[ohm] — Ω

Figure 61. Lumped port and design parameters utilized to simulate the feeding point of the nanoantenna.

The final step before running the simulation is to define the mesh structure. To guarantee the accuracy of the results, it is recommended to define the maximum element length to be approximately $\lambda/5$, where λ refers to the wavelength at the frequency under study. In general, this condition should be satisfied for the highest frequency in the analysis (the smallest wavelength). In addition, the confinement factor, *i.e.*, the shrinkage in the wavelength, should be captured. For the particularly narrow sections of the geometry, such as the stub, a separate much finer mesh is defined, with maximum element size equal to `W_line/3`. For, the PML we use a swept mesh (see Figure 62).

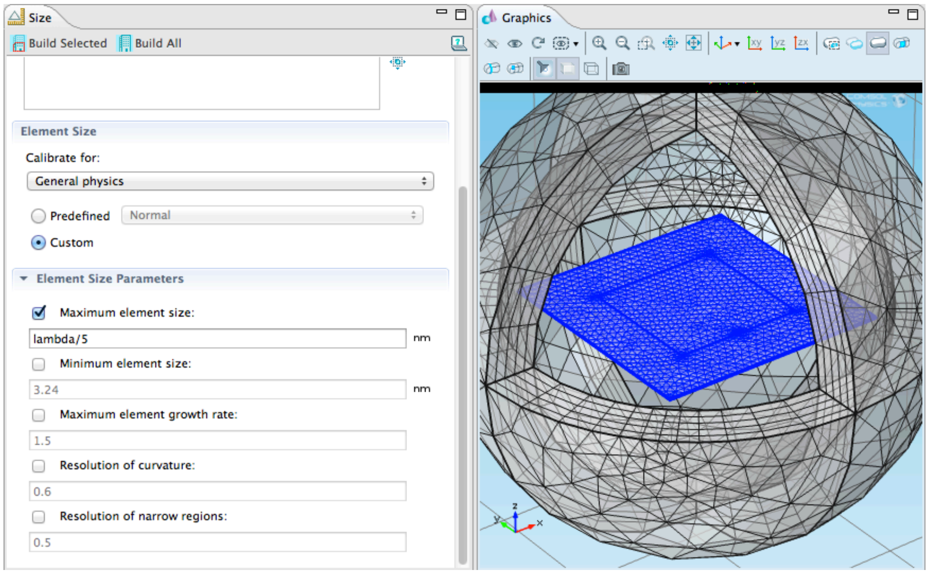

Calibrate for: General physics

○ Predefined Normal

● Custom

☑ Maximum element size: lambda/5 nm

☐ Minimum element size: 3.24 nm

☐ Maximum element growth rate: 1.5

☐ Resolution of curvature: 0.6

☐ Resolution of narrow regions: 0.5

Figure 62. Mesh setup parameters and resulting meshed geometry.

9.2.2 Simulation Results

First, we are interested in observing the propagation of SPP waves and, more importantly, to identify their resonances. In Figure 63, we illustrate the electric field in the resonant plasmonic cavity for three different propagation modes. A square nano-patch antenna with side-length equal to one thousand nanometers is used. In Figure 63(a), a non-resonating mode is shown. In Figure 63(b), the fundamental TM SPP wave mode is illustrated. In Figure 63(c), a TEM mode of order 2 is illustrated.

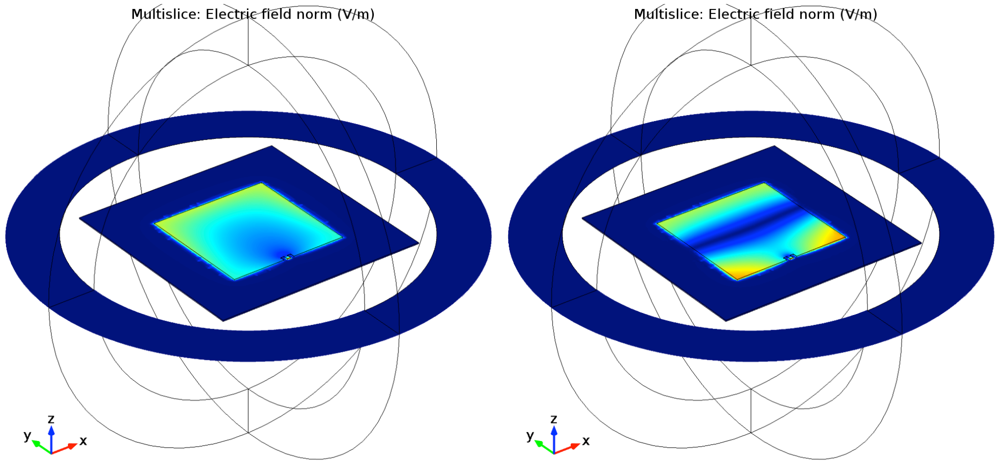

(a) Non-resonating mode, $f = 1.38$ THz (b) Fundamental TM mode, $f = 3.72$ THz

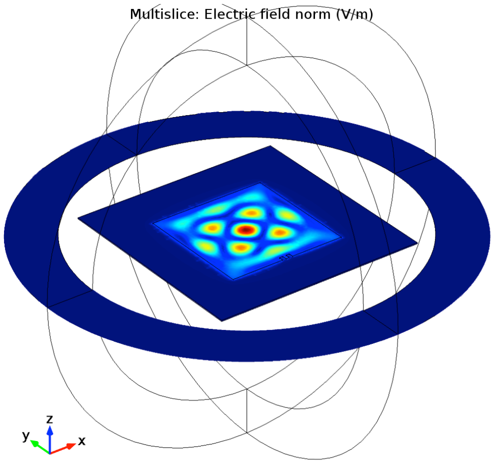

(c) Higher order TEM mode, $f = 7.59$ THz

Figure 63. Electric field at the GNR for three different SPP wave modes at three different frequencies.

We focus on the analysis of the TM SPP wave mode, which, as we mentioned in Section 2.4.3, is the best radiating mode for a resonant cavity. In Figure 64, we illustrate the electric field corresponding to the TM mode for two different antenna designs. In particular, in Figure 64(a), a square nano-patch antenna with side-length equal to one thousand nanometers is simulated at a frequency equal to 3.72 THz. As explained in Section 2.4.3, a patch antenna radiates from its edges. For the fundamental resonant frequency of the TM mode, the expected resonant frequency is given by (45), with $m = 1$. The discrepancy between the simulation result and the expected result remains mainly in the selection of the antenna feeding system as well as the dielectric thickness. In Figure 64(b), the normalized radiation diagram is shown. As expected from a patch antenna, the antenna radiates almost isotropically. In Figure 64(c), we show the electric field for a one-hundred-nanometer-wide one-micrometer-long nano-antenna. Similarly, the normalized radiation diagram is shown in Figure 64(d), which is, as expected, isotropic. Optimal nano-antenna designs have not been investigated in this work. In any case, the possibility to develop a nano-antenna that can radiate in the Terahertz Band rather than in the far infrared or at optical frequencies validates our initial hypothesis. Efficient antenna designs should be investigated and our analytical models and this simulation platform can be used for that purpose.

In addition, we also characterize the `S11` parameter, which measures how much power can be effectively injected into the antenna. We look at this parameter to prevent a high impedance-mismatch from shadowing the results. In our analytical study in Chapter 2, we did not investigate the feeding mechanism for the antenna. By means of simulation, we tune the stub size and adapt the lumped port input impedance conveniently. For example, the input impedance for the antenna in Figure 64(a) is approximately -11 dB when the input port impedance is 100 Ω. For the the nano-antenna in Figure 64(c), the input impedance is in the order of -8 dB. Ultimately, the efficiency of the nano-antenna depends also on the input impedance and its matching with the lumped port. Alternative ways to excite the SPP waves in the nano-antenna should be investigated. As we will explain in Chapter 10, the development of a plasmonic nano-transceiver, able to generate SPP waves and inject them in the nano-antenna, is part of our future work. Till this point, we have explained how to utilize COMSOL to design graphene-based plasmonic nano-antennas. These results validate our initial hypothesis and motivate the further investigation of different nano-antenna designs as well as feeding mechanisms.

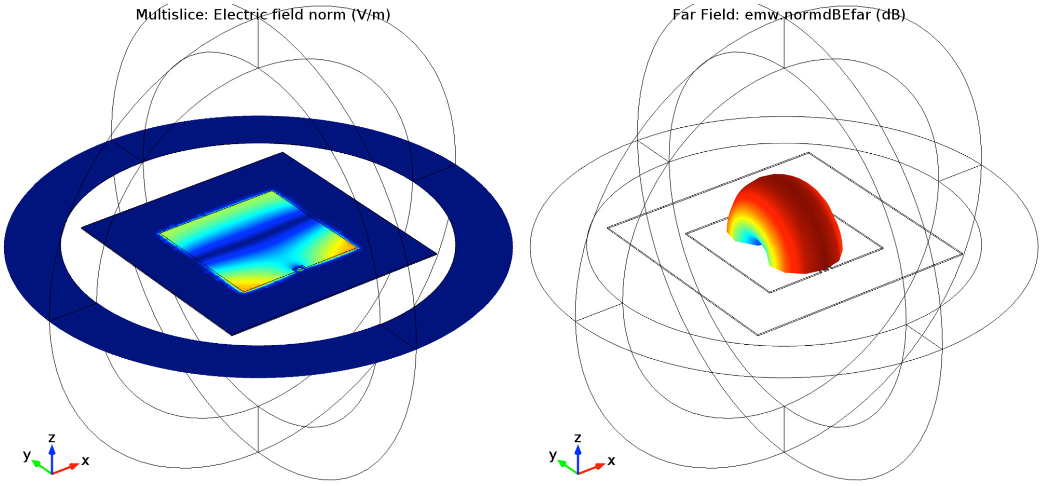
Multislice: Electric field norm (V/m)

Far Field: emw.normdBEfar (dB)

(a) E-field, W = 1000 nm, f = 3.72 THz

(b) Radiation diagram, W = 1000 nm, f = 3.72 THz

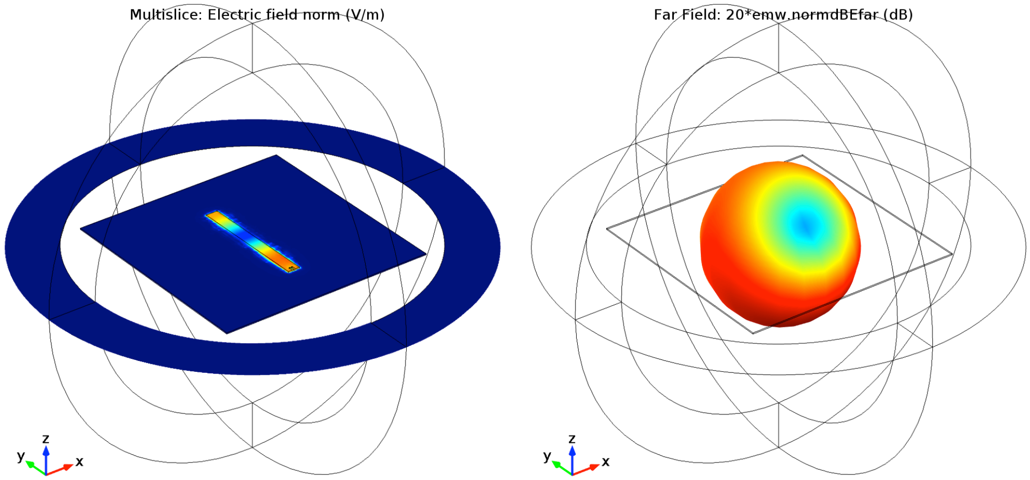
Multislice: Electric field norm (V/m)

Far Field: 20*emw.normdBEfar (dB)

(c) E-field, W = 100 nm, f = 3.72 THz

(d) Radiation diagram, W = 100 nm, f = 3.73 THz

Figure 64. Electric field at the GNR for two different nano-antenna widths.

9.3 Terahertz Band Channel Simulation with COMSOL Multi-physics

The next step is the simulation of the Terahertz Band channel and the validation of the channel model developed in Chapter 3. In this section, we describe how to simulate the Terahertz Band channel in COMSOL and provide several simulation results both in the frequency domain and in the time domain.

9.3.1 Definition of the Channel

We consider the following scenario to analyze the Terahertz Band channel:

- To isolate the channel response from the nano-antenna response, we use an ideal `Point Dipole` as the source of electromagnetic radiation. For this, we define a `point` in the geometry that will be assigned to be the source.
- Similarly, we use an ideal `Domain Point Probe` as the detector of electromagnetic radiation, instead of a nano-antenna, to investigate only the channel effects. Therefore, we define several `points` in the geometry at different distances from the source point.
- To reduce the complexity of the simulation and reduce the simulation time, the simulation space is defined by a `circle` with radius `Radius`.
- To guarantee the accuracy of the simulation and to minimize the number of unrealistic reflections from the simulation space boundaries, a `Perfectly Matched Layer`, which surrounds the source and the detector, is defined. The PML width is `Radius_PML`.

In order to ease a parametrized analysis and the control of the model from Matlab, we define a set of global parameters to determine the geometry of the scenario. In Figure 65, a set of working parameters and the resulting scenario are shown.

The next step consists of assigning the corresponding material to the medium. The definition of air in COMSOL does not include the information about molecular absorption in the HITRAN database [117]. For this, besides assigning the material `air` to the geometry in our scenario, we should also specify the peculiar behavior of the medium when setting the electromagnetic analysis.

To analyze the channel frequency response, we proceed as follows. First, we define a new `Electromagnetic Waves, Frequency Domain` study in COMSOL. We use

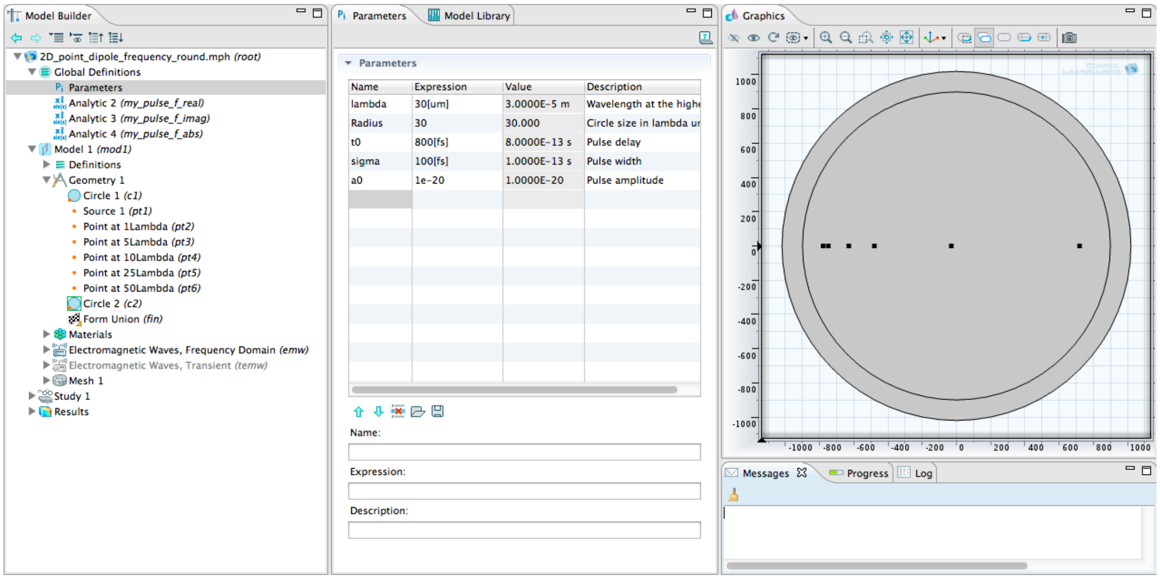

Name	Expression	Value	Description
lambda	30[um]	3.0000E-5 m	Wavelength at the highe
Radius	30	30.000	Circle size in lambda ur
t0	800[fs]	8.0000E-13 s	Pulse delay
sigma	100[fs]	1.0000E-13 s	Pulse width
a0	1e-20	1.0000E-20	Pulse amplitude

Figure 65. Channel simulation scenario parameter set and example geometry.

the frequency form of the wave equation to be solved by the simulator. In the `Wave Equation, Electric` configuration window (see Figure 66), we specify that the material type is non-solid. In addition, we should also specify that we will be using the relative permittivity of the medium to determine the electric displacement field. The complex relative permittivity of air ε_{r-air} at Terahertz Band frequencies can be obtained from the molecular absorption coefficient as

$$\varepsilon_{r-air}(f) = \varepsilon'_{r-air}(f) - \mathrm{i}\varepsilon''_{r-air}(f), \tag{174}$$

$$\varepsilon'_{r-air}(f) = n^2_{air}(f) - k^2_{air}(f), \tag{175}$$

$$\varepsilon''_{r-air}(f) = 2n_{air}(f)\,k_{air}(f), \tag{176}$$

where f stands for frequency, and n_{air} and k_{air} refer to real and imaginary part of the refractive index of air, respectively. In our case, these are given by

$$n_{air}(f) = 1, \tag{177}$$

$$k_{air}(f) = \frac{4\pi c_0 \tau(f)}{f}, \tag{178}$$

where c_0 is the speed of light in vacuum and τ refers to molecular absorption coefficient given by (50) in Chapter 3.

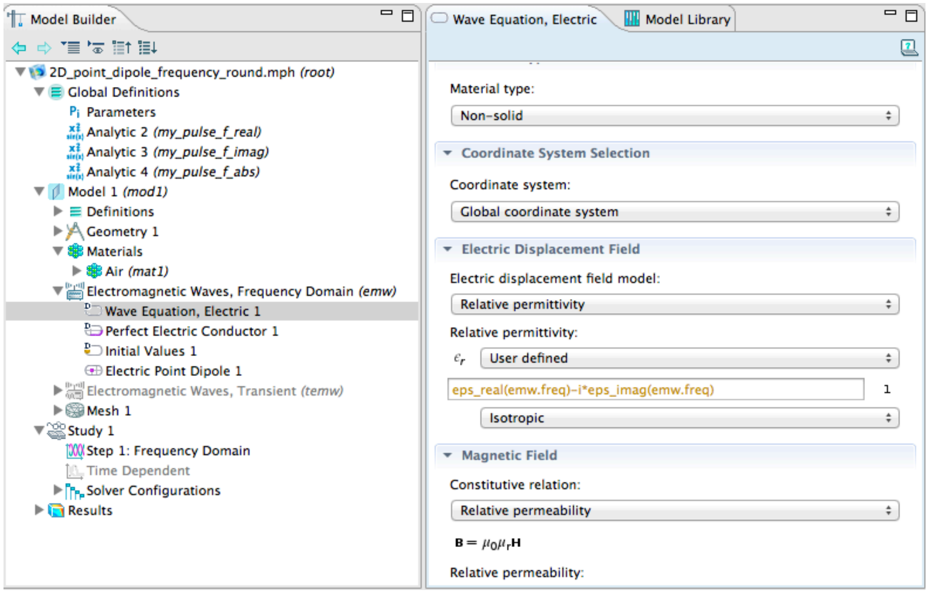

Material type: Non-solid

Coordinate System Selection

Coordinate system: Global coordinate system

Electric Displacement Field

Electric displacement field model: Relative permittivity

Relative permittivity:

ϵ_r User defined

eps_real(emw.freq)-i*eps_imag(emw.freq) 1

Isotropic

Magnetic Field

Constitutive relation: Relative permeability

$\mathbf{B} = \mu_0 \mu_r \mathbf{H}$

Relative permeability:

Figure 66. Implementation of the molecular absorption coefficient in COMSOL by means of the relative dielectric constant.

As mentioned before, the source of electromagnetic radiation in this particular case is represented by an `Electric Point Dipole`, with vertical polarization (y-axis). The magnitude of the dipole moment electric current is first left constant and equal to 1 mA. The final step before running the simulation is to define the mesh structure. As for the nano-antenna, to guarantee the accuracy of the results, it is recommended to define the maximum element length to be approximately $\lambda/5$, where λ refers to the wavelength at the frequency under study, *i.e.*, 10 THz in this analysis.

9.3.2 Simulation Results

9.3.2.1 Frequency Domain

First, we investigate the Terahertz Band channel frequency response. In Figure 67, the electric field in the geometry under study is shown at different frequencies. As we mentioned before, the dipole is vertically polarized (y-axis) and, thus, the maximum direction of radiation is along the x-axis. The radiation diagram of an ideal dipole is well-known and matches the simulation results.

Second, in order to investigate the impact of molecular absorption, we look at the full frequency response at two `Domain Point Probes` located at $d = 0.75$ mm and

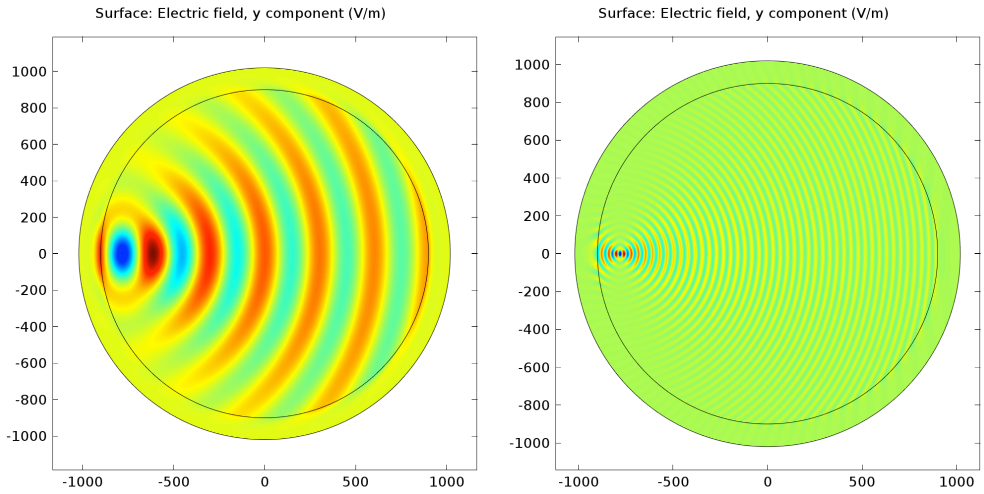

(a) $f = 0.1$ THz (b) $f = 1$ THz

Figure 67. Vertical component of the electric field amplitude E_y across the simulation scenario at different frequencies.

$d = 1.5$ mm. We acknowledge that these are very short distances, but are in line of the expected transmission range of nanomachines. The only reason for which we cannot at this point show the channel response at longer distances comes from the computational complexity introduced by meshing a larger geometry with a maximum mesh element size of 6 μm, which corresponds $\lambda/5$ at the highest frequency under analysis.

In Figure 68, we show the channel frequency response for the two aforementioned points. We compare the results obtained by simulation with the results obtained with (47) from our analytical model developed in Chapter 3. First of all, we make the following observations. As we mentioned before, in order to simplify the computational complexity, we simulate a 2D geometry instead of a 3D scenario. Correspondingly, the electromagnetic wave does not spread in the space spherically, but cylindrically. Therefore, we should replace the spherical spreading factor in (48) by the corresponding cylindrical spreading factor. In addition, due to the way in which the `electric point dipole` is implemented in COMSOL, the frequency dependency in the spreading factor, which comes from the ideal effective area of an isotropic antenna, should be replaced by the peculiar model used in COMSOL. The resulting path loss can be then written as:

$$A\left(f,d\right)=\frac{c_0^2}{4\pi f_0}\frac{1}{\pi d^2}e^{-k(f)d}, \tag{179}$$

where f stands for frequency, d refers to distance, c_0 is the speed of light in vacuum and f_0 is the point dipole design frequency.

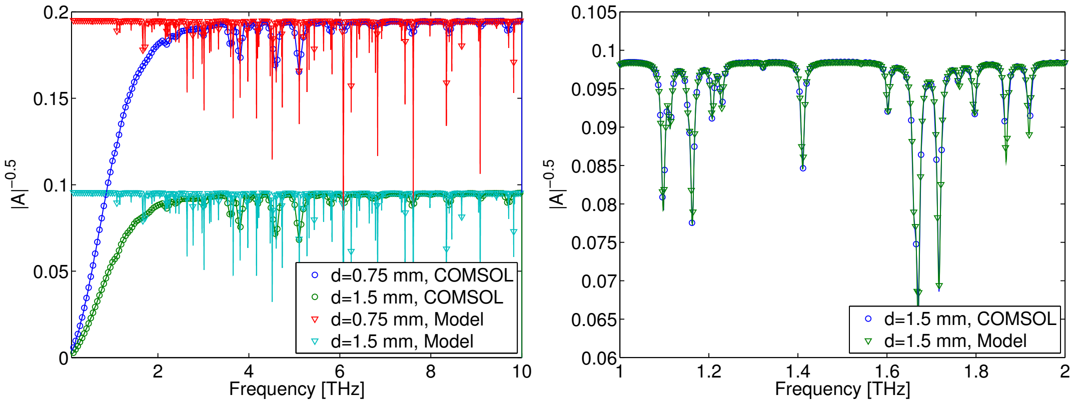

(a) f = 0.1 – 10 THz (b) f = 1 – 2 THz

Figure 68. Terahertz Band channel frequency response.

In Figure 68(a), the channel frequency response over the entire Terahertz Band is shown. We can observe the following. First of all, at low frequencies, we can see a mismatch between our refined analytical model and the simulation results. This is a consequence of the way in which COMSOL models the electric point dipole frequency response. For higher frequencies, the simulation results accurately match our analytical model. Once again, the computational complexity limits the accuracy of the results. To better show this fact, in Figure 68(b), we show the channel frequency response between 1 THz and 2 THz only, with a higher accuracy. These results validate our model in the frequency domain.

9.3.2.2 Time Domain

In addition to the frequency domain analysis, we want to validate the channel impulse response in the time domain. This is specially useful for the validation of the propagation of the one-hundred-femtosecond-long pulses introduced in Chapter 4. All the elements in our geometry are defined as described in Section 9.3.1. However, this time we set a

`Electromagnetic Waves, Time Transient` analysis. In addition, because we are interested in characterizing the propagation of very short pulses (Chapter 4), we define the input current at the electric point dipole to be the first time derivative of a delayed Gaussian pulse with variance equal to 100 fs.

In Figure 69, we show the y component of the electric field in our scenario at two different time instants. The pulse is radiated at $t_0 = 800$ fs. The radiation diagram of the electric point dipole shapes the direction of propagation of the pulse. As it advances, its amplitude is lower as its power is spread over a large area. As before, the simulation of a 2D geometry results into a cylindrical spreading instead of a spherical spreading.

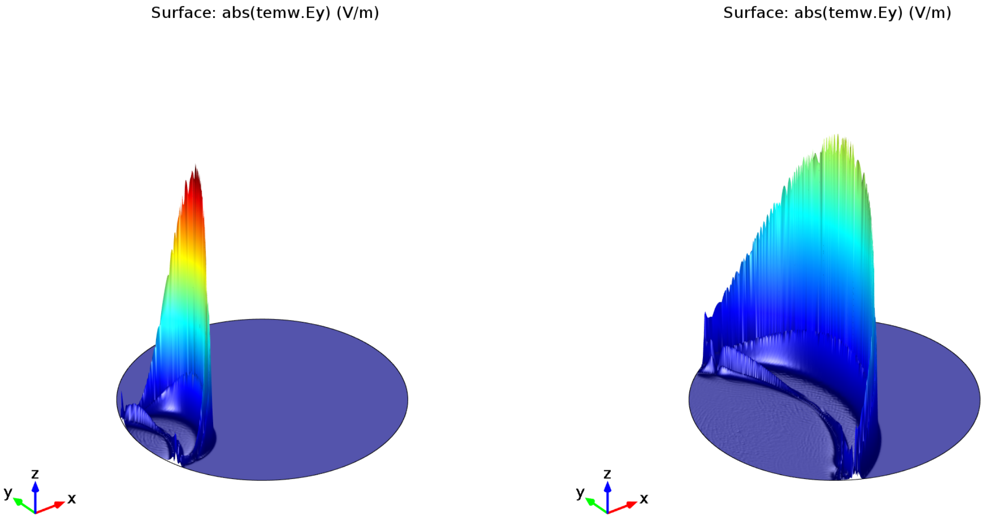

(a) $t = 0.4$ ps (b) $t = 10$ ps

Figure 69. Vertical component of the electric field amplitude E_y across the simulation scenario at different time instants.

In Figure 70(a), the received signal at a distance $d = 1$ mm is illustrated. The received signal analytical model developed in Chapter 4 can accurately reproduce the results obtained in the COMSOL simulations. The delay in the maximum of the received signal perfectly matches in the two cases. The shape of the received pulses is also very similar. Once again, the differences originate in the specific response of the point dipole model used by COMSOL. This can be observed by comparing the p.s.d. of the received signal y, which is illustrated in Figure 70(b). Finally, the distance dependence of the channel impulse response is also validated, by analyzing the received signal at different distances. In Figure 70(c), the received signal y at distances equal to 500 μm, 1 mm, 2.5 mm and 5 mm are shown, which further validates our analytical model. In the rest of the section, we use the channel model to analyze the performance of TS-OOK.

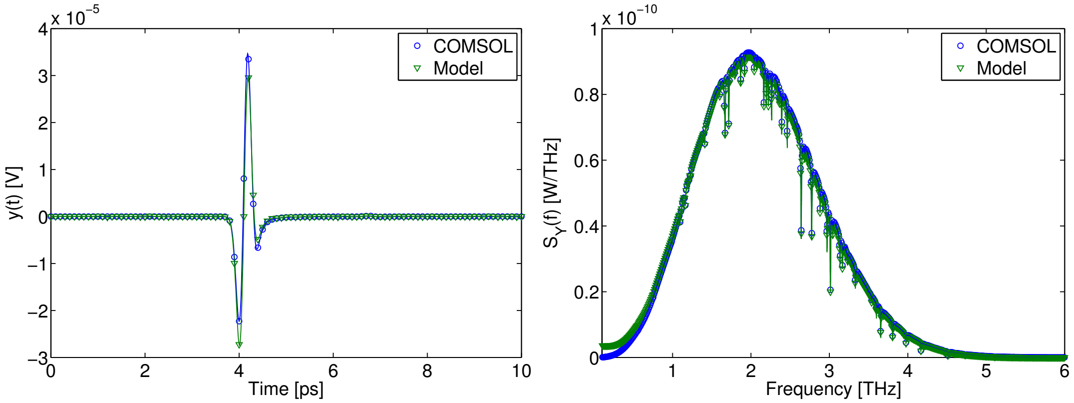

(a) Received signal at d = 1 mm (b) P.s.d. of the received signal at d = 1 mm

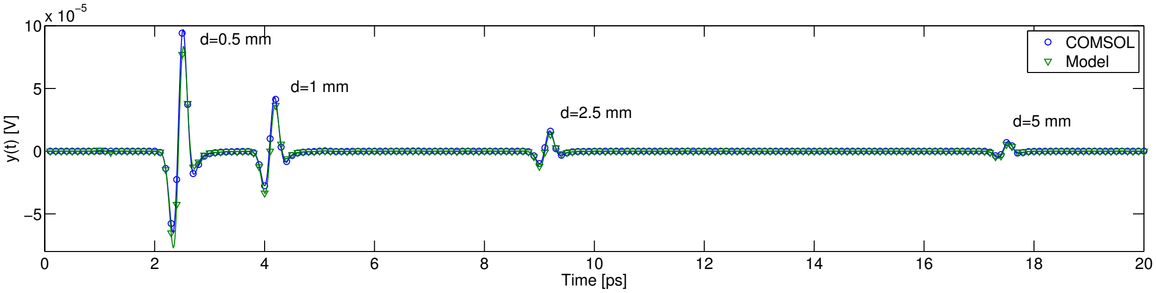

(c) Received signal at difference distances d.

Figure 70. Time domain simulation of the propagation of femtosecond-long pulses.

Up to this point, we have individually validated the graphene-based nano-antenna response and the Terahertz Band channel behavior, which, for the time being, are the only components implemented in COMSOL.

9.4 One-to-one Nano-link with COMSOL Multi-physics

After separately analyzing the response of the proposed graphene-based nano-antennas and the Terahertz Band channel, we simulate a complete one-to-one nano-link with COMSOL, which is composed of a transmitting nano-antenna and a receiving nano-antenna, with air in between. In this Section, we first describe how the geometry is defined and we then show some simulation results.

9.4.1 Definition of the One-to-One Nano-link Geometry

The one-to-one nano-link can be easily defined by starting from the graphene-based nano-antenna geometry. In particular, after the definition of the nano-antenna (Section 9.2), we need to create a copy of the nano-structure. This can be easily done in COMSOL as follows:

- Right click on the `Geometry` section of the `Model Builder` window, and choose `Transformation` and `Copy`.
- Select the elements that need to be copied, In our case, the main substrate block (whose bottom layer behaves as the ground plane), the patch and stub.
- Specify the direction and distance at which the elements should be copied. In our case, we choose to move the copied elements at a distance `d_tr` along the z-axis (see Figure 71).
- In order to have the two antenna facing each other, we need to then rotate the copied elements. For this, we choose `Geoemetry`, `Transformation`, `Rotate`. In this first example, we want the two antennas to be perfectly aligned. For this, we specify the rotation center to be defined as $\{0, 0, d_{tr}\}$ and the angle to rotate to be 180°.

In Figure 71, we illustrate the resulting geometry. The sphere that defined the volume of simulation has been re-centered and its radius has been increased in order to be able to englobe the totality of the two antennas. The materials in the geometry do not need to be modified. As long as the copied nano-antenna was defined by following the instructions in Section 9.2, the materials have already been assigned and, thus, there is no need for further modifications.

The next step is to set the electromagnetic study parameters. In particular,

- For the nano-antenna, we follow the same procedure as in Section 9.2:

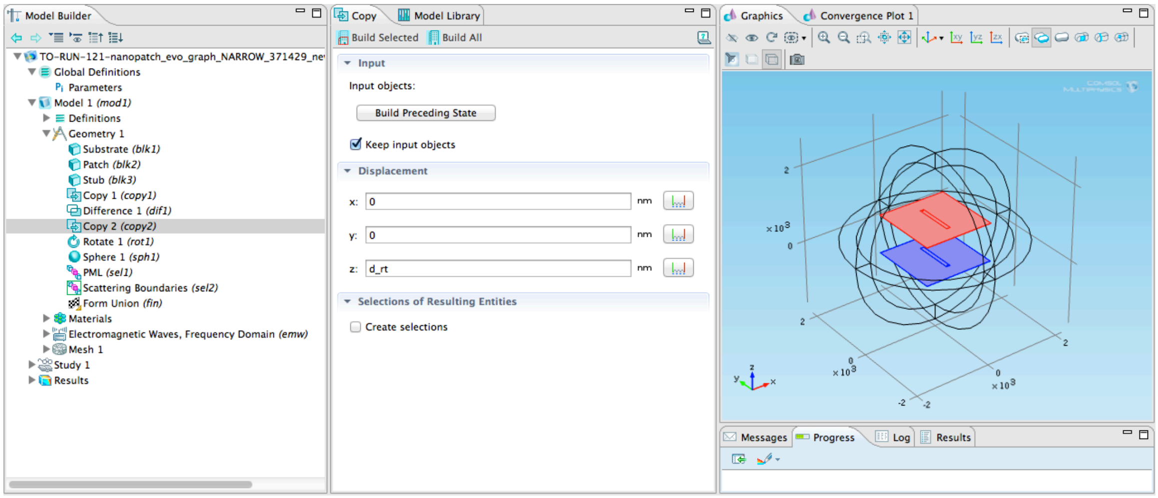

Input

Input objects:

Build Preceding State

☑ Keep input objects

Displacement

x: 0 nm

y: 0 nm

z: d_rt nm

Selections of Resulting Entities

☐ Create selections

Figure 71. One-to-one nano-link example simulation geometry.

  - The two ground planes should be defined as a `Perfect Electric Conductor`.
  - The two GNRs should be defined as a `Transition Boundary Condition`, with the relative permittivity given by (172).
  - The transmitting nano-antenna has an active `Lumped Port` attached to the stub with a constant input current.
  - The receiving nano-antenna has a passive `Lumped Port` attached to the stub.

- For the channel, we only need to take into account that the space between antennas in filled with a medium whose relative permittivity is given by (176).

The entire geometry should be meshed as described in Section 9.2. The plasmonic effects in the nano-antenna impose the use of a rather small element size, which can compromise the feasibility of the analysis due to the resulting computational complexity.

9.4.2 Simulation Results

In this section we analyze by simulation the joint frequency response of the two nano-antennas and the channel. We are interested in the S_{21} parameter, *i.e.*, the relation between the output at receiving nano-antenna and the input at the transmitting nano-antenna. In Figure 72, the joint frequency response of the two nano-antennas with the channel in between is shown at two different distances as a function of frequency. Due to the high computational complexity involved in simulating a large geometry with the aforementioned maximum element size, we limit our current results to a few micrometers at most. In any case, the methodology introduced in this section is valid and can be easily extended to larger geometries if computationally feasible. For the same reason, we have reduced the patch and the substrate width, to 100 nm and 800 nm, respectively. The antenna length is kept constant and equal to 1000 nm. The S_{21} in dB is shown in Figure 72(a) as a function of the frequency. We can clearly identify the impact of the antenna resonances on the joint one-to-one nano-link. The first resonance appears at approximately 2.2 THz. This center frequency can be tuned by adjusting the width of the patch and the thickness of the dielectric substrate. The 3 dB bandwidth at this frequency is approximately 1 THz, which is convenient for the radiation of one-hundred-femtosecond-long pulses. For completeness, we also show in Figure 72(b) the S_{11} parameter as a function of frequency. A 100 Ω port impedance is used in this set of results.

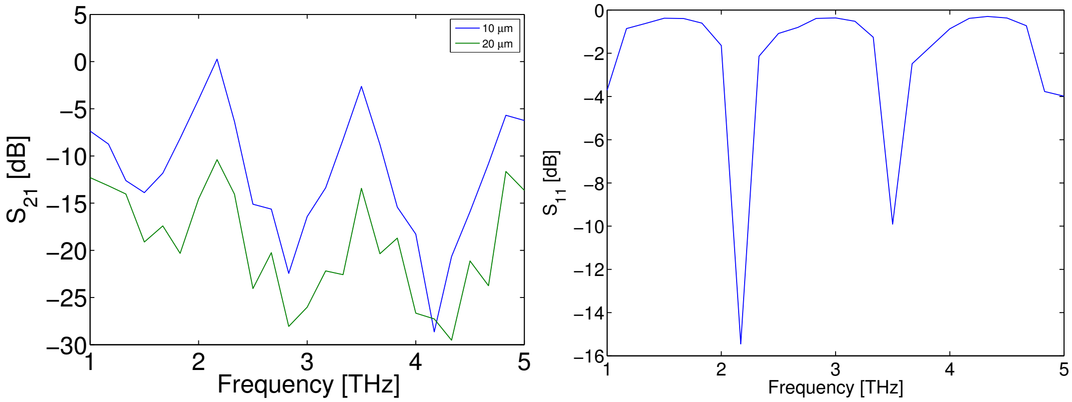

(a) S_{21} (b) S_{11}

Figure 72. One-to-one nano-link frequency response.

Unfortunately, the `Transition Boundary Condition` used to implement graphene in COMSOL is not supported when performing a time-domain transient analysis. As a result, when using the graphen-based plasmonic nano-antenna as the signal emitter and detector, only frequency-domain simulations can be conducted. To obtain time domain results, the resulting frequency response can be converted into a time response by means of the inverse Fourier transform, as described in Section 4.2.2.

9.5 Linkage of COMSOL Multi-physics and Matlab

The validation of all the developed solutions requires us to combine analytical models in Matlab with the simulation models developed in COMSOL. For this, it is necessary to link the two platforms. Fortunately, COMSOL supports tight integration with Matlab by means of LiveLink. The possibility to parametrically setup and control the simulations in COMSOL from Matlab allows us to hide the complexity behind accurate electromagnetic simulation tools and makes it easier for a greater part of the engineering community to comfortably run simulations.

Provided that Matlab is already present in the system, the regular installation of COMSOL already creates a link between the two platforms. Therefore, the command `COMSOL with Matlab` can be directly executed. The power of LiveLink remains in the fact that for every single action that can be done in COMSOL with a graphic user interface, there is the corresponding Matlab command. More importantly, besides creating simulation models from scratch, COMSOL models can be directly saved as M-files. Therefore, we can easily link our COMSOL models developed in Section 9.2 and Section 9.3 with Matlab.

9.5.1 Definition of the One-to-one Geometry in Matlab

Our starting point is the the M-file generated when saving the COMSOL model described in Section 9.4. The M-file contains a chronological description of our actions realized in COMSOL. To prevent a redundant Matlab script, it is advisable that the `Reset History` command in COMSOL is run before saving the file model as a M-file. After this, we can easily identify the following Sections in the M-File:

- *Parameters Definition:* This part of the code contains the parameters and constants that we have used for the definition of the model geometry. We can easily replace the values from the COMSOL model by Matlab variables. This drastically simplifies the execution of parametrize analysis.

```
model.param.set('D', '10[nm]', 'Substrate thickness');
model.param.set('W_patch', [num2str(W), '[nm]'], 'Patch width');
model.param.set('L_patch', [num2str(L), '[nm]'], 'Patch length');
...
```

- *Geometry and Material Definition:* This part of the code contains a set of commands to define the geometrical entities in the model as well as their materials:

```
model.geom('geom1').feature.create('blk1', 'Block');
model.geom('geom1').feature('blk1').name('Substrate');
model.geom('geom1').feature('blk1').set('base', 'center');
model.geom('geom1').feature('blk1').set('size', {'W_sub' 'L_sub' 'D'});
...
```

- *Study Definition:* This part of the code contains the commands required to define the specific study that will be used with this model.

```
model.physics.create('emw', 'ElectromagneticWaves', 'geom1');
model.physics('emw').feature.create('pec2', 'PerfectElectricCond...
model.physics('emw').feature('pec2').selection.set([15 20 21]);
...
```

- *Mesh Definition:* This part of the code contains the commands required to create the mesh.

```
model.mesh.create('mesh1', 'geom1');
model.mesh('mesh1').feature.create('ftet1', 'FreeTet');
...
```

- *Solution and Results:* This final part contains the code to set up the variables under study, obtain the solution, and setup the output results.

```
model.sol('sol1').attach('std1');
model.sol('sol1').feature('st1').name('Compile Equations: Frequency...
model.sol('sol1').feature('st1').set('studystep', 'freq');
...
```

Finally, the simulation is run and the results are obtained by using the command

```
model.sol('sol1').runAll;
```

Until here, we have explained how the nano-antennas and the channel COMSOL simulation models can be utilized from Matlab. Next, we specify how our modulation, coding and receiver solutions can be incorporated in this software platform.

9.5.2 Coding, Modulation and Receiver Solutions in the One-to-one Nano-Link

At this point, it is straightforward to incorporate the rest of our solutions to the one-to-one model. The key point is that we can replace the input current or voltage of the `Port` at the transmitting nano-antenna by any frequency-dependent or time-dependent signal, which we can generate in Matlab. This can be done by the following command-line:

```
model.physics('emw').feature('lport1').set('V0', 'input_signal(emw.freq)');
```

Therefore, as we did in Chapter 4 and Chapter 5, we can generate the signals to transmit according to the targeted coding weight and by using the one-hundred-femtosecond-long pulses, but, instead of convoluting them with the analytical channel response, we use them as the port excitation in COMSOL. After the simulation is completed, the received signal can be obtained from the output of the `Port` at the receiving nano-antenna, which can be read with the following command line:

```
model.result.numerical('gev1').getReal();
```

provided that it has been included in as a `Global Evaluation` value in the model results:

```
model.result.numerical.create('gev1', 'EvalGlobal');
model.result.numerical('gev1').set('probetag', 'none');
```

```
model.result.numerical('gev1').set('table', 'tbl1');
model.result.numerical('gev1').set('expr', 'emw.S21dB');
model.result.numerical('gev1').set('unit', 'dB');
model.result.numerical('gev1').set('descr', 'S-parameter, dB');
model.result.numerical('gev1').setResult;
```

The received signal is then processed in Matlab with our symbol detection scheme as we did in Chapter 6. The current results provided in Chapter 4, Chapter 5 and Chapter 6 have already been obtained by starting from the validated channel models.

9.6 Conclusions and Future Extensions

In this chapter, we have developed a software platform to emulate a one-to-one nano-link between two nanomachines. First, we have explained in detail how the proposed graphene-based plasmonic nano-antenna can be implemented in COMSOL and we have provided several simulation results. Second, we have described the steps required to properly simulate the Terahertz Band channel, by incorporating the information from the HITRAN database. We have also provided several simulation results in the frequency domain and in the time domain which prove the validity of our analytical Terahertz Band channel model. Then, we have jointly modeled two nano-antennas and the channel and obtained the joint response in COMSOL. Finally, we have showed how COMSOL and Matlab can be linked and how the resulting platform can be used to validate any solution developed in Matlab.

The developed platform can provide very accurate results at the cost of computational complexity. Our results in this chapter have been focused on a single one-to-one nano-link. However, in any case, it is straightforward to extend these results in order to simulate a network of nanomachines. For example, one first additional extension would be the simulation of several transmitting nano-antennas and the characterization of the resulting interference on a receiving nano-antenna. Many interference models existing to date, including the interference model developed in Chapter 4 and Chapter 5, make several assumptions on the distribution of the active nodes, their density and the propagation effects altering the received signals. With the developed platform, we can actually validate or revise the interference model. However, as pointed out before, this would increase the computational complexity of the system. Ultimately, in any case, this tool provides a complete platform to validate our solutions and to explore new challenges for nanonetworks, before nanomachines become available.

CHAPTER 10

CONCLUSIONS

Nanonetworks will enable a plethora of long-awaited applications in many fields of our society, ranging from healthcare to homeland security, industrial development and environmental protection. Enabling the communication among nanomachines is still a major challenge. We acknowledge that there is still a long way to go before having a fully functional nanomachine, but we believe that hardware-oriented research and communication-focused investigations will benefit from being conducted in parallel from an early stage.

In this thesis, we aimed at defining the first steps towards enabling electromagnetic communication among nanomachines in the Terahertz Band (0.1-10 THz). Our starting point has been the development of novel graphene-based plasmonic nano-antennas, which efficiently operate in the Terahertz Band. We have developed a novel Terahertz Band channel model and investigated the potential of this frequency band by means of a channel capacity analysis. In light of the channel peculiarities and the nanomachine capabilities, we have proposed a set of communication mechanisms for nanonetworks, which include femtosecond-long pulse-based modulations, low-weight channel coding schemes, a new symbol detection scheme at the receiver, and a new medium access control protocol for nanonetworks. In addition, we have analyzed the performance of perpetual nanonetworks by developing a joint energy harvesting and energy consumption model for self-powered nanomachines. Finally, we have developed an emulation platform to simulate a one-to-one nano-link between nanomachines and validate the developed models.

The contributions in each chapter are summarized as follows:

- In Chapter 2, we proposed, modeled and analyzed a graphene-based plasmonic nano-antenna, which exploits the behavior of SPP in GNRs to radiate in the Terahertz Band. In particular,
    - First, we developed a transmission line model of GNRs by starting from the

tight-binding model. We then obtained the total line impedance and the SPP wave propagation speed. In addition, we modeled the nano-antenna as a resonant plasmonic cavity and obtained its fundamental resonant frequency.

  - Second, in a much more complete analysis, we studied the dynamic conductivity of GNRs by using the Kubo formalism. We then modeled the propagation of different SPP wave propagation modes and determined their complex propagation constant. In addition, we obtained the nano-antenna frequency response for different excitation modes.
  - Our results show that graphene-based plasmonic nano-antennas, which are just a few tens of nanometers wide and up to a few micrometers long at most, can radiate in the Terahertz Band, *i.e.*, two orders of magnitude below the resonant frequency of a classical metallic antenna with the same size. This results opens the door to electromagnetic communication in nanonetworks

- In Chapter 3, we developed a Terahertz Band channel model and quantized the potential of the Terahertz Band for communication by means of a channel capacity analysis. In particular,
  - We used radiative transfer theory and the information in the HITRAN database to obtain formulations for the total path-loss and molecular absorption noise in the Terahertz Band.
  - We analyzed the channel capacity of the Terahertz Band by using the developed channel model and for four different power allocation schemes.
  - Our results show that Terahertz Band channel response drastically depends on the medium composition and the transmission distance. The major impact comes from the presence of water vapor molecules. For distances below one meter, the Terahertz Band behaves as a single transmission window, almost 10 THz wide, which can support transmissions at very high speeds, up to a few

  Tbps. For longer distances, the Terahertz Band has several transmission windows, which are a few GHz-wide each, and can support transmissions at a few Gbps or more by combining several windows simultaneously.

- In Chapter 4, we developed a pulse-based modulation and channel access scheme for nanonetworks in the Terahertz Band. In particular,
  - We proposed a novel modulation scheme based on the asynchronous exchange of one-hundred-femtosecond-long pulses among nanomachines, by following an asymmetric on-off keying modulation spread in time (TS-OOK).
  - We analyzed the performance of the proposed modulation in terms of achievable information rate both in the single-user case and in the multi-user case. For this, we developed novel stochastic models of molecular absorption noise in the Terahertz Band as well as multi-user interference in TS-OOK.
  - Our results show that, when using TS-OOK, nanonetworks can support a very high number of nanomachines (up to thousands of nanomachines in close vicinity) which can transmit at very high bit-rates (up to a few Tbps).
- In Chapter 5, we proposed the use of low-weight channel codes to prevent channel errors in nanonetworks. In particular,
  - We analyzed the impact of the coding weight on the molecular absorption noise and the multi-user interference power. We revised our stochastic interference model to better understand the impact of the coding weight on its power.
  - We analyzed the performance of low-weight coding codes in terms of achievable information rate after coding and codeword error probability. We considered the developed channel, noise and interference model and two different receiver decision architectures.

    - Our results show that the number of channel errors in nanonetworks can be reduced by lowering the coding weight. This can be achieved without penalizing or even increasing the achievable information rate after coding, especially in interference-limited scenarios. Moreover, there is an optimal coding weight that depends on the network conditions. These results motivate the development of link layer control mechanisms which can dynamically adapt the coding weight to the network conditions.

- In Chapter 6, we developed a receiver symbol detection scheme to support pulse-based modulations in the Terahertz Band . In particular,
    - We proposed a new symbol detector based on a Continuous-Time Moving Average block, which can be implemented with a low-pass filter, to support the use of impulse-based communication.
    - We analytically and numerically investigated the performance of the symbol detector and compared it to that of classical symbol detection schemes in terms of symbol error rate in interference-free and interference-limited scenarios.
    - Our results show that this novel symbol detection scheme outperforms existing impulse-radio based detectors when used in the Terahertz Band, by reducing the symbol error rate and increasing the achievable transmission distance for a target SER.

- In Chapter 7, we developed a novel energy model for self-powered nanomachines that make use of novel piezoelectric nano-generators to harvest energy and communicate over the Terahertz Band. In particular,
    - We developed an analytical model for piezoelectric nano-generators based on Zinc Oxide nanowires, which can successfully reproduce existing experimental data. We also analytically modeled the energy consumption due to pulse-based

communications in the Terahertz Band.

  - We developed a joint energy harvesting and energy consumption model for perpetual nanonetworks, which captures the correlation between the energy harvesting process and the energy consumption process. In addition, we analyzed the impact of several harvesting and communication parameters on the end-to-end delay, packet delivery probability and throughput of nanonetworks in the steady state.
  - Our results show that nanonetworks can achieve perpetual operation as long as the energy harvesting process and the energy consumption process are jointly optimized. Otherwise, energy limitations can reduce the achievable throughput of nanonetworks by several orders of magnitude. The temporal energy fluctuations in nanomachines require the development of energy-aware protocols for nanonetworks.

- In Chapter 8, we developed a Medium Access Control protocol tailored the peculiarities of electromagnetic nanonetworks. In particular,
  - We proposed the PHLAME, a physical-layer aware MAC protocol for nanonetworks. This is built on top of a variation of TS-OOK, which is modified allow different nanomachines to transmit by following different time spreading factors, and makes use of low-weight channel codes. In addition, it takes into account the energy fluctuations in nanomachines.
  - We analyzed the performance of PHLAME in terms of end-to-end energy per bit consumption, end-to-end delay and throughput, by making use of our developed channel, noise and interference models.
  - Our results show that, despite its simplicity, PHLAME is able to support densely populated nanonetworks by exploiting the peculiarities of the Terahertz Band, the expected capabilities of nanomachines, and the benefits of low weight codes.

- In Chapter 9, we developed a simulation framework to emulate a one-to-one nano-link between two nanomachines and to ultimately validate the developed models. In particular,
  - We used COMSOL Multi-physics to simulate the proposed graphene-based plasmonic nano-antenna. After the validation of a single antenna, we analyzed the channel between two nano-antennas operating in the Terahertz Band and validated our proposed model.
  - We linked the COMSOL simulation models to Matlab by means of LiveLink. We then used Matlab to generate the signals that are radiated by the nano-antennas, according to the developed modulation and coding techniques.
  - The developed simulation platform can be effectively used to validate and improve the developed analytical models. Moreover, it provides a great asset for the development of future communication and networking solutions for nano-networks, which cannot be easily validated otherwise due to the absence of functional nanomachines at this time.

Our future research directions are summarized as follows:

- First and foremost, it is necessary to develop experimental prototypes of the proposed graphene-based plasmonic nano-antennas. For the time being, the conductivity of GNRs and the propagation of SPP waves in GNRs have been experimentally characterized. However, to the best of our knowledge, a graphene-based plasmonic nano-antenna has not been built yet. Besides the manufacturing of the proposed graphene-based heterostructure, a major challenge is posed by the limitations in the nano-antenna feeding and nano-antenna radiation measurement techniques. Commercial Terahertz Band sources and detectors, even at larger scales, pose several limitations in terms of frequency range and sensitivity. As a possible way to overcome this limitation, the measurement of the larger nano-antenna arrays will be considered.

In addition, the possibility to tune the antennas for either lower or higher frequency operation, where more commercial tools exist, will be investigated.

- Inline with the previous challenge, one of our next steps will be the analytical and experimental characterization of a novel graphene-based plasmonic nano-transceiver. As we just mentioned, one of the major challenges comes from the lack of suitable sources and detectors to be used with the nano-antenna. Contrary to classical antenna systems, in which an electric current is used to excite the antenna, a nano-transmitter should be able to generate a SPP wave that will then be injected into the antenna. Similarly, the nano-receiver should be able to convert the SPP wave coming from the nano-antenna into an electric signal suited for signal processing. Our starting point will be a high-electron-mobility transistor design based on graphene and a III-V semiconductor. The use of the same nanomaterial as in the nano-antenna should also minimize the interconnection losses. We will first follow the same methodology as for the antenna to analytically model its performance. Then, we will incorporate our model to the simulation platform. Ultimately, we aim at the experimental characterization of the proposed device.

- Another major research direction is the development of higher layer networking protocols for electromagnetic nanonetworks in the Terahertz Band. In this thesis, we have stopped at the link layer and developed a MAC protocol. However, many challenges arise from the peculiarities of nanonetworks when trying to create efficient networking solutions at higher layers. For example, new addressing mechanisms tailored to the very high density of nanonetworks need to be developed. In many applications of nanonetworks, a unique address for each single nanomachine is not needed. In those cases, we can explore new content-aware addressing schemes, which depend mainly on the type of device or information that a nanomachine processes. In other applications, such as in the Internet of Nano-Things, unique addresses for nanomachines might be needed. Address compression schemes will be explored. Similarly, routing in nanonetworks and reliable end-to-end transport solutions for multi-hop communication among nanomachines will be explored, by starting from the peculiarities of the physical layer, the capabilities of nanomachines and the applications of nanonetworks.

PUBLICATIONS

Journal Papers

1. I. F. Akyildiz and J. M. Jornet, “Electromagnetic Wireless NanoSensor Networks,” Nano Communication Networks (Elsevier) Journal, vol. 1, no. 1, pp. 3-19, Mar. 2010.

2. I. F. Akyildiz and J. M. Jornet, “The Internet of Nano-Things,” (invited paper) IEEE Wireless Communication Magazine, vol. 17, no. 6, pp. 58-63, Dec. 2010.

3. J. M. Jornet and I. F. Akyildiz, “Channel Modeling and Capacity Analysis for Electromagnetic Wireless Nanonetworks in the Terahertz Band,” IEEE Transactions on Wireless Communications, vol. 10, no. 10, pp. 3211-3221, Oct. 2011.

4. I. F. Akyildiz, J. M. Jornet, and M. Pierobon, “Nanonetworks: A New Frontier in Communications,” Communications of the ACM, vol. 54, no. 11, pp. 84-89, Nov. 2011.

5. J. M. Jornet, J. Capdevila-Pujol, and J. Sol-Pareta, “PHLAME: A Physical Layer Aware MAC Protocol for Electromagnetic Nanonetworks in the Terahertz Band,” Nano Communication Networks (Elsevier) Journal, vol. 3, no. 1, pp. 74-81, Mar. 2012.

6. J. M. Jornet and I. F. Akyildiz, “Joint Energy Harvesting and Communication Analysis for Perpetual Wireless Nanosensor Networks in the Terahertz Band,” IEEE Transactions on Nanotechnology, vol. 11, no. 3, pp. 570-580, May 2012.

7. I. Llatser, C. Kremers, A. Cabellos-Aparicio, J. M. Jornet, E. Alarcon, and D. N. Chigrin, “Graphene-based Nano-patch Antenna for Terahertz Radiation,” Photonics and Nanostructures (Elsevier) Journal, vol. 10, no. 4, pp. 353-358, Oct. 2012.

8. J. M. Jornet and I. F. Akyildiz, "The Internet of Multimedia Nano-Things," Nano Communication Networks (Elsevier) Journal, vol. 3, no. 4, pp. 242-251, Dec. 2012.

9. I. Llatser, C. Kremers, D. N. Chigrin, J. M. Jornet, M. Lemme, A. Cabellos-Aparicio, and E. Alarcn, "Radiation Characteristics of Tunable Graphennas in the Terahertz Band," Radioengineering Journal, Dec. 2012.

10. J. M. Jornet and I. F. Akyildiz, "Graphene-based Plasmonic Nano-antenna for Terahertz Band Communication in Nanonetworks," to appear in IEEE Journal on Selected Areas in Communications (JSAC), Special Issue on Emerging Technologies in Communications, 2013.

11. J. M. Jornet and I. F. Akyildiz, "Femtosecond-long Pulse-based Modulation for Terahertz Band Communication in Nanonetworks," submitted for journal publication, May 2013.

12. R. Gomez Cid-Fuentes, J. M. Jornet, I. F. Akyildiz, and E. Alarcon, "Receiver Signal Detection Scheme for Short-range Impulse-Radio Communication in Nanonetworks," submitted for journal publication, Dec. 2012, revised, July 2013.

13. J. M. Jornet and I. F. Akyildiz, "Low-weight Channel Codes for Error Prevention in Electromagnetic Nanonetworks in the Terahertz Band," submitted for journal publication, July 2013.

Conference Papers

1. J. M. Jornet and I. F. Akyildiz, "Graphene-based Nano-antennas for Electromagnetic Nanocommunications in the Terahertz Band," in Proc. of the 4th European Conference on Antennas and Propagation, EUCAP, Barcelona, Spain, Apr. 2010.

2. I. F. Akyildiz, J. M. Jornet and M. Pierobon, "Propagation Models for Nanocommunication Networks," (invited paper) in Proc. of the 4th European Conference on

Antennas and Propagation. EUCAP, Barcelona, Spain, Apr. 2010.

3. J. M. Jornet and I. F. Akyildiz, “Channel Capacity of Electromagnetic Nanonetworks in the Terahertz Band,” in Proc. of the IEEE International Conference on Communications, ICC, Cape Town, South Africa, May 2010.
4. J. Capdevila-Pujol, J. M. Jornet, and J. Sole-Pareta, “PHLAME: A Physical Layer Aware MAC Protocol for Electromagnetic Nanonetworks,” in Proc. of the 1st IEEE International Workshop on Molecular and Nano Scale Communication (MoNaCom), INFOCOM, Shanghai, China, Apr. 2011.
5. S. Abadal, J. M. Jornet, I. Llatser, A. Cabellos-Aparicio, E. Alarcon and I. F. Akyildiz, “Wireless NanoSensor Networks using Graphene-based Nano-Antennas,” in GRAPHENE 2011, Bilbao, Spain, Apr. 2011.
6. J. M. Jornet and I. F. Akyildiz, “Low-Weight Channel Coding for Interference Mitigation in Electromagnetic Nanonetworks in the Terahertz Band,” in Proc. of the IEEE International Conference on Communications, ICC, Kyoto, Japan, June 2011.
7. J. M. Jornet and I. F. Akyildiz, “Information Capacity of Pulse-based Wireless Nanosensor Networks,” in Proc. of the 8th Annual IEEE Communications Society Conference on Sensor, Mesh and Ad Hoc Communications and Networks, SECON, Salt Lake City, Utah, USA, June 2011.
8. I. Llatser, C. Kremers, A. Cabellos-Aparicio, J. M. Jornet, E. Alarcon, and D. N. Chigrin, “Scattering of Terahertz Radiation on a Graphene-based Nano-antenna,” in Proc. of the 4th International Workshop on Theoretical and Computational Nano-Photonics, TaCoNa-Photonics, Bad Honnef, Germany, Oct. 2011.
9. I. Llatser, C. Kremers, D. N. Chigrin, J. M. Jornet, M. Lemme, A. Cabellos-Aparicio, and E. Alarcon, “Characterization of Graphene-based Nano-antennas in the Terahertz

Band," (invited paper) in Proc. of the 6th European Conference on Antenna and Propagation, EUCAP, Prague, Czech Republic, Mar. 2012.

10. I. Llatser, S. Abadal, R. Gomez Cid-Fuentes, J. M. Jornet, A. Cabellos-Aparicio, E. Alarcon, J. Sole-Pareta, and I. F. Akyildiz, "Prospects of Graphene-enabled Wireless Communications," in GRAPHENE 2012, Brussels, Belgium, Apr. 2012.

11. J. M. Jornet, and I. F. Akyildiz, "The Internet of Multimedia Nano-Things in the Terahertz Band," (invited paper) in Proc. of the 18th European Wireless Conference, EW, Poznan, Poland, Apr. 2012.

12. R. Gomez Cid-Fuentes, J. M. Jornet, I. F. Akyildiz, and E. Alarcon, "A Receiver Architecture for Pulse-based Electromagnetic Nanonetworks in the Terahertz Band," in Proc. of the IEEE International Conference on Communications, ICC, Ottawa, Canada, June 2012.

13. J. M. Jornet, "A Joint Energy Harvesting and Consumption Model for Self-Powered Nano-Devices in Nanonetworks," in Proc. of the 2nd IEEE International Workshop on Molecular and Nano Scale Communication (MoNaCom), ICC, Ottawa, Canada, June 2012.

Patents

1. I. F. Akyildiz and J. M. Jornet, "Graphene-based Plasmonic Nano-antenna for Terahertz Band Communication," Provisional Patent Application, April 17, 2013.

2. I. F. Akyildiz and J. M. Jornet, "Graphene-based Plasmonic Nano-transceiver for Wireless Communication in the Terahertz Band," Patent Application, in preparation, 2013.

REFERENCES

[1] I. F. Akyildiz, F. Brunetti, and C. Blazquez, “Nanonetworks: a new communication paradigm,” *Computer Networks (Elsevier) Journal*, vol. 52, no. 12, pp. 2260–2279, Aug. 2008.

[2] I. F. Akyildiz and J. M. Jornet, “Electromagnetic wireless nanosensor networks,” *Nano Communication Networks (Elsevier) Journal*, vol. 1, no. 1, pp. 3–19, Mar. 2010.

[3] ——, “The internet of nano-things,” *IEEE Wireless Communications Magazine*, vol. 17, no. 6, pp. 58–63, Dec. 2010.

[4] I. F. Akyildiz, W. Su, Y. Sankarasubramaniam, and E. Cayirci, “Wireless sensor networks: a survey,” *Computer Networks (Elsevier) Journal*, vol. 38, no. 4, pp. 393–422, Mar. 2002.

[5] I. F. Akyildiz, J. M. Jornet, and M. Pierobon, “Nanonetworks: a new frontier in communications,” *Communications of the ACM*, vol. 54, no. 11, pp. 84–89, Nov. 2011.

[6] T. Ando, Y. Zheng, and H. Suzuura, “Dynamical conductivity and zero-mode anomaly in honeycomb lattices,” *Journal of the Physical Society of Japan*, vol. 71, no. 5, pp. 1318–1324, 2002.

[7] J. Andrews, R. Ganti, M. Haenggi, N. Jindal, and S. Weber, “A primer on spatial modeling and analysis in wireless networks,” *Communications Magazine, IEEE*, vol. 48, no. 11, pp. 156 –163, Nov. 2010.

[8] C. A. Balanis, *Antenna theory: analysis and design*. John Wiley & Sons, 2005.

[9] A. Barbieri, F. Pancaldi, and G. Vitetta, “A novel ultrawideband system for multiuser data communications,” *IEEE Transactions on Wireless Communications*, vol. 10, no. 12, pp. 4324–4333, 2011.

[10] R. Bennewitz, J. N. Crain, A. Kirakosian, J.-L. Lin, J. L. McChesney, D. Y. Petrovykh, and F. J. Himpsel, “Atomic scale memory at a silicon surface,” *Nanotechnology*, vol. 13, no. 4, pp. 499–502, 2002.

[11] M. W. Bockrath, “Carbon nanotubes: electrons in one dimensions,” Ph.D. dissertation, Univ. California, Berkeley, CA, 1999.

[12] F. Box, “Utilization of atmospheric transmission losses for interference-resistant communications,” *IEEE Transactions on Communications*, vol. 34, no. 10, pp. 1009–1015, Oct. 1986.

[13] L. Brey and H. A. Fertig, "Electronic states of graphene nanoribbons studied with the Dirac equation," *Physical Review B (Condensed Matter and Materials Physics)*, vol. 73, no. 23, p. 235411, 2006.

[14] W. Brown, B. Wallin, D. Lesniewski, D. Gooding, and J. Martin, "The experimental determination of on-off keying laser communications probability models and a comparison with theory," *Proc*, pp. 61 050U–61 050U–8, 2006.

[15] P. Burke, S. Li, and Z. Yu, "Quantitative theory of nanowire and nanotube antenna performance," *IEEE Transactions on Nanotechnology*, vol. 5, no. 4, pp. 314–334, Jul. 2006.

[16] P. Cardieri, "Modeling interference in wireless ad hoc networks," *IEEE Communications Surveys and Tutorials*, vol. 12, no. 4, pp. 551–572, 2010.

[17] J. K. Choi, V. Mitin, R. Ramaswamy, V. Pogrebnyak, M. Pakmehr, A. Muravjov, M. Shur, J. Gill, I. Mehdi, B. Karasik, and A. Sergeev, "Thz hot-electron microbolometer based on low-mobility 2-DEG in GaN heterostructure," *IEEE Sensors Journal*, vol. 13, no. 1, pp. 80–88, 2013.

[18] S. Clough, F. Kneizys, and R. Davies, "Line shape and the water vapor continuum," *Atmos. Res.*, vol. 23, no. 3-4, pp. 229–241, Oct. 1989.

[19] COMSOL Multiphysics Simulation Software. COMSOL. [Online]. Available: http://www.comsol.com/products/multiphysics/

[20] S. Datta, *Electronic transport in mesoscopic systems*. Cambridge University Press, 1997.

[21] ——, *Quantum Transport: Atom to Transistor*. Cambridge University Press, 2005.

[22] G. Deligeorgis, F. Coccetti, G. Konstantinidis, and R. Plana, "Radio frequency signal detection by ballistic transport in y-shaped graphene nanoribbons," *Applied Physics Letters*, vol. 101, no. 1, p. 013502, 2012.

[23] G. Deligeorgis, M. Dragoman, D. Neculoiu, D. Dragoman, G. Konstantinidis, A. Cismaru, and R. Plana, "Microwave propagation in graphene," *Applied Physics Letters*, vol. 95, no. 7, p. 073107, 2009.

[24] S. Dolinar, D. Divsalar, J. Hamkins, and F. Pollara, "Capacity of ppm on gaussian and webb channels," in *Information Theory, 2000. Proceedings. IEEE International Symposium on*, 2000, p. 410.

[25] J. Dorfmuller, R. Vogelgesang, W. Khunsin, C. Rockstuhl, C. Etrich, and K. Kern, "Plasmonic nanowire antennas: Experiment, simulation, and theory," *Nano Letters*, vol. 10, no. 9, pp. 3596–3603, 2010.

[26] M. Dragoman, A. A. Muller, D. Dragoman, F. Coccetti, and R. Plana, "Terahertz antenna based on graphene," *Journal of Applied Physics*, vol. 107, pp. 104 313–3, 2010.

[27] X. Du, I. Skachko, A. Barker, and E. Y. Andrei, “Approaching ballistic transport in suspended graphene,” *Nature Nanotechnology*, vol. 3, no. 8, pp. 491–495, Aug. 2008.

[28] J. M. Dubach, D. I. Harjes, and H. A. Clark, “Fluorescent ion-selective nanosensors for intracellular analysis with improved lifetime and size,” *Nano Letters*, vol. 7, no. 6, pp. 1827–2831, 2007.

[29] A. A. Dubinov, V. Y. Aleshkin, V. Mitin, T. Otsuji, and V. Ryzhii, “Terahertz surface plasmons in optically pumped graphene structures,” *Journal of Physics: Condensed Matter*, vol. 23, no. 14, p. 145302, 2011.

[30] T. W. Ebbesen, H. J. Lezec, H. Hiura, J. W. Bennett, H. F. Ghaemi, and T. Thio, “Electrical conductivity of individual carbon nanotubes,” *Nature*, vol. 382, no. 6582, pp. 54–56, Jul. 1996.

[31] H. F. Engler and D. H. Howard, “A compendium of analytic models for coherent and non-coherent receivers.” AFWAL-TR-85-1118, Air Force Wright Aeronautical Laboratory,, Tech. Rep., September 1985.

[32] R. Esteban, T. V. Teperik, and J. J. Greffet, “Optical patch antennas for single photon emission using surface plasmon resonances,” *Physical Review Letters*, vol. 104, p. 026802, Jan. 2010.

[33] L. Falkovsky and S. Pershoguba, “Optical far-infrared properties of a graphene monolayer and multilayer,” *Physical Review B*, vol. 76, pp. 1–4, 2007.

[34] L. Falkovsky and A. A. Varlamov, “Space-time dispersion of graphene conductivity,” *The European Physical Journal B*, vol. 56, pp. 281–284, 2007.

[35] J. Federici and L. Moeller, “Review of terahertz and subterahertz wireless communications,” *Journal of Applied Physics*, vol. 107, no. 11, p. 111101, 2010.

[36] I. Filanovsky and P. Matkhanov, “Synthesis of reactance networks shaping a quasi-rectangular pulse,” *IEEE Transactions on Circuits and Systems II: Express Briefs*, vol. 52, no. 5, pp. 242 – 245, may 2005.

[37] Y. Gao and Z. L. Wang, “Electrostatic potential in a bent piezoelectric nanowire. the fundamental theory of nanogenerator and nanopiezotronics,” *Nano Letters*, vol. 7, no. 8, pp. 2499–2505, 2007.

[38] A. K. Geim and K. S. Novoselov, “The rise of graphene,” *Nature Materials*, vol. 6, no. 3, pp. 183–191, Mar. 2007.

[39] A. Gerosa, S. Solda, A. Bevilacqua, D. Vogrig, and A. Neviani, “An energy-detector for noncoherent impulse-radio UWB receivers,” *IEEE Transactions on Circuits and Systems I: Regular Papers*, vol. 56, no. 5, pp. 1030 –1040, May 2009.

[40] A. Goldsmith, *Wireless Communications*. New York, NY, USA: Cambridge University Press, 2005.

[41] R. M. Goody and Y. L. Yung, *Atmospheric Radiation: Theoretical basis*, 2nd ed. Oxford University Press, 1989.

[42] J. Gummeson, S. S. Clark, K. Fu, and D. Ganesan, “On the limits of effective hybrid micro-energy harvesting on mobile CRFID sensors,” in *Proc. of the 8th ACM international conference on Mobile systems, applications, and services, MobiSys*, 2010.

[43] V. P. Gusynin and S. G. Sharapov, “Transport of dirac quasiparticles in graphene: hall and optical conductivities,” *Physical Review B*, vol. 73, p. 245411, Jun. 2006.

[44] V. P. Gusynin, S. G. Sharapov, and J. P. Carbotte, “AC conductivity of graphene: from tight-binding model to 2+1-dimensional quantum electrodynamics,” *International Journal of Modern Physics B*, vol. 21, p. 4611, 2007.

[45] I. Guvenc and H. Arslan, “On the modulation options for uwb systems,” in *IEEE Military Communications Conference (MILCOM)*, vol. 2, 2003, pp. 892–897 Vol.2.

[46] G. W. Hanson, “Fundamental transmitting properties of carbon nanotube antennas,” *IEEE Transactions on Antennas and Propagation*, vol. 53, no. 11, pp. 3426–3435, Nov. 2005.

[47] ——, “Dyadic Green’s functions and guided surface waves for a surface conductivity model of graphene,” *Journal of Applied Physics*, vol. 103, no. 6, p. 064302, 2008.

[48] ——, “Dyadic Green’s functions for an anisotropic, non-local model of biased graphene,” *IEEE Transactions on Antennas and Propagation*, vol. 56, no. 3, pp. 747–757, Mar. 2008.

[49] m. Heil and J. C. Silva Bueno, “Within-plant signaling by volatiles leads to induction and priming of an indirect plant defense in nature,” *Proceedings of the National Academy of Sciences*, vol. 104, no. 13, pp. 5467–5472, 2007.

[50] M. Heil and J. Ton, “Long-distance signalling in plant defence,” *Trends in Plant Science*, vol. 13, no. 6, pp. 264–272, 2008.

[51] C. Hierold, A. Jungen, C. Stampfer, and T. Helbling, “Nano electromechanical sensors based on carbon nanotubes,” *Sensors and Actuators A: Physical*, vol. 136, no. 1, pp. 51–61, 2007.

[52] F. Hipolito, A. J. Chaves, R. M. Ribeiro, M. I. Vasilevskiy, V. M. Pereira, and N. M. R. Peres, “Enhanced optical dichroism of graphene nanoribbons,” *Phys. Rev. B*, vol. 86, p. 115430, Sep. 2012.

[53] J. Horng, C.-F. Chen, B. Geng, C. Girit, Y. Zhang, Z. Hao, H. A. Bechtel, M. martin, A. Zettl, M. F. Crommie, Y. R. Shen, and F. Wang, “Drude conductivity of dirac fermions in graphene,” *Physical Review B*, vol. 83, p. 165113, Apr. 2011.

[54] K.-C. Huang and Z. Wang, “Terahertz terabit wireless communication,” *IEEE Microwave Magazine*, vol. 12, no. 4, pp. 108–116, Jun. 2011.

[55] P. Humblet and M. Azizoglu, “On the bit error rate of lightwave systems with optical amplifiers,” *Journal of Lightwave Technology*, vol. 9, no. 11, pp. 1576 –1582, Nov. 1991.

[56] IEEE 802.15 Wireless Personal Area Networks-Terahertz Interest Group (IGthz). [Online]. Available: http://www.ieee802.org/15/pub/IGthz.html

[57] *IEEE 802.15.4a: Wireless Medium Access Control (MAC) and Physical Layer (PHY) Specifications for Low-Rate Wireless Personal Area Networks (WPANs). Amendment 1: add Alternate Physical*, IEEE Standard for Information Technology, Telecommunications and Information Exchange between Systems Std.

[58] M. Jablan, H. Buljan, and M. Soljačić, “Plasmonics in graphene at infrared frequencies,” *Physical Review B*, vol. 80, p. 245435, Dec. 2009.

[59] L. Ji, Z. Tan, T. Kuykendall, E. J. An, Y. Fu, V. Battaglia, and Y. Zhang, “Multilayer nanoassembly of sn-nanopillar arrays sandwiched between graphene layers for high-capacity lithium storage,” *Energy Environ. Sci.*, vol. 4, pp. –, 2011.

[60] J. M. Jornet and I. F. Akyildiz, “The internet of multimedia nano-things,” *Nano Communication Networks (Elsevier) Journal*, vol. 3, no. 4, pp. 242–251, Dec. 2012.

[61] L. Ju, B. Geng, J. Horng, C. Girit, M. martin, Z. Hao, H. Bechtel, X. Liang, A. Zettl, Y. R. Shen, and F. Wang, “Graphene plasmonics for tunable terahertz metamaterials,” *Nature Nanotechnology*, vol. 6, pp. 630–634, Sep. 2011.

[62] P. V. Kamat, “Harvesting photons with carbon nanotubes,” *Nano Today*, vol. 1, no. 4, pp. 20–27, 2006.

[63] R. J. Kershner, L. D. Bozano, C. M. Micheel, A. M. Hung, A. R. Fornof, J. N. Cha, C. T. Rettner, M. Bersani, j. Frommer, P. W. K. Rothemund, and G. M. Wallraff, “Placement and orientation of individual DNA shapes on lithographically patterned surfaces,” *Nature Nanotechnology*, vol. 4, no. 9, pp. 557–561, Aug. 2009.

[64] T. Kleine-Ostmann and T. Nagatsuma, “A review on terahertz communications research,” *Journal of Infrared, Millimeter and Terahertz Waves*, vol. 32, pp. 143–171, 2011.

[65] L. Kleinrock, *Queueing Systems. Volume 1: Theory.* Wiley-Interscience, 1975.

[66] W. Knap, F. Teppe, N. Dyakonova, D. Coquillat, and J. Lusakowski, “Plasma wave oscillations in nanometer field effect transistors for terahertz detection and emission,” *Journal of Physics: Condensed Matter*, vol. 20, no. 38, p. 384205, 2008.

[67] M. Koch, “Terahertz communications: A 2020 vision,” in *Terahertz Frequency Detection and Identification of Materials and Objects*, ser. NATO Security through Science Series, R. Miles, X.-C. Zhang, H. Eisele, and A. Krotkus, Eds. Springer, 2007, vol. 19, pp. 325–338.

[68] F. H. L. Koppens, D. E. Chang, and F. J. Garcia de Abajo, “Graphene plasmonics: a platform for strong light matter interactions,” *Nano Letters*, vol. 11, no. 8, pp. 3370–3377, Aug. 2011.

[69] F. Lee and A. Chandrakasan, “A 2.5 nJ/bit 0.65 V pulsed UWB receiver in 90 nm CMOS,” *IEEE Journal of Solid-State Circuits*, vol. 42, no. 12, pp. 2851–2859, Dec. 2007.

[70] S. Lee, M. Choi, T. Kim, S. Lee, M. Liu, X. Yin, H. Choi, S. Lee, C. Choi, S. Choi, X. Zhang, and B. Min, “Switching terahertz waves with gate-controlled active graphene metamaterials.” *Nat Mater*, 2012.

[71] J. Lei, R. Yates, and L. Greenstein, “A generic model for optimizing single-hop transmission policy of replenishable sensors,” *IEEE Transactions on Wireless Communications*, vol. 8, no. 2, pp. 547–551, 2009.

[72] J. Li, T. Peng, and Y. Peng, “A cholesterol biosensor based on entrapment of cholesterol oxidase in a silicic sol-gel matrix at a prussian blue modified electrode,” *Electroanalysis*, vol. 15, no. 12, pp. 1031–1037, 2003.

[73] J. Lim, C. Kim, J. jang, H. Lee, Y. jung, J. Kim, S. Park, B. Lee, and M. Lee, “Design of a subwavelength patch antenna using metamaterials,” in *38th European Microwave Conference, EuMC*, Oct. 2008, pp. 1246 –1249.

[74] Y.-M. Lin, A. Valdes-Garcia, S.-J. Han, D. B. Farmer, I. Meric, Y. Sun, Y. Wu, C. Dimitrakopoulos, A. Grill, P. Avouris, and K. A. Jenkins, “Wafer-scale graphene integrated circuit,” *Science*, vol. 332, no. 6035, pp. 1294–1297, 2011.

[75] R.-S. Liu, K.-W. Fan, Z. Zheng, and P. Sinha, “Perpetual and fair data collection for environmental energy harvesting sensor networks,” *IEEE/ACM Transactions on Networking*, vol. 19, no. 4, pp. 947–960, Aug. 2011.

[76] I. Llatser, C. Kremers, A. Cabellos-Aparicio, J. M. Jornet, E. Alarcon, and D. N. Chigrin, “Graphene-based nano-patch antenna for terahertz radiation,” *Photonics and Nanostructures - Fundamentals and Applications*, vol. 10, no. 4, pp. 353–358, Oct. 2012.

[77] Q. Y. Lu, N. Bandyopadhyay, S. Slivken, Y. Bai, and M. Razeghi, “Widely tuned room temperature terahertz quantum cascade laser sources based on difference-frequency generation,” *Applied Physics Letters*, vol. 101, no. 25, p. 251121, 2012.

[78] A. Maestrini, I. Mehdi, J. Siles, J. Ward, R. Lin, B. Thomas, C. Lee, J. Gill, G. Chattopadhyay, E. Schlecht, J. Pearson, and P. Siegel, “Design and characterization of

a room temperature all-solid-state electronic source tunable from 2.48 to 2.75 thz," *IEEE Transactions on Terahertz Science and Technology*, vol. 2, no. 2, pp. 177–185, 2012.

[79] C. Manolatou and F. Rana, "Subwavelength nanopatch cavities for semiconductor plasmon lasers," *IEEE Journal of Quantum Electronics*, vol. 44, no. 5, pp. 435–447, May 2008.

[80] A. W. maria Gorlatova and G. Zussman, "Networking low-power energy harvesting devices: Measurements and algorithms," in *Proc. of the International Conference on Computer Communication, INFOCOM*, Shanghai, China, Apr. 2011.

[81] I. L. Marti, C. Kremers, A. Cabellos-Aparicio, J. M. Jornet, E. Alarcon, and D. N. Chigrin, "Scattering of terahertz radiation on a graphene-based nano-antenna," *AIP Conference Proceedings of The Fourth International Workshop on Theoretical and Computational Nanophotonics, TaCoNa*, vol. 1398, no. 1, pp. 144–146, 2011.

[82] B. Medepally, N. Mehta, and C. Murthy, "Implications of energy profile and storage on energy harvesting sensor link performance," in *Proc. of IEEE Global Telecommunications Conference, GLOBECOM*, 2009.

[83] P. Mercier, M. Bhardwaj, D. Daly, and A. Chandrakasan, "A low-voltage energy-sampling ir-uwb digital baseband employing quadratic correlation," *IEEE Journal of Solid-State Circuits*, vol. 45, no. 6, pp. 1209 –1219, Jun. 2010.

[84] S. A. Mikhailov, "Theory of the giant plasmon-enhanced second-harmonic generation in graphene and semiconductor two-dimensional electron systems," *Physical Review B*, vol. 84, p. 045432, Jul. 2011.

[85] S. A. Mikhailov and K. Ziegler, "New electromagnetic mode in graphene," *Physical Review Letters*, vol. 99, pp. 1–4, 2007.

[86] ——, "Nonlinear electromagnetic response of graphene: frequency multiplication and the self-consistent-field effects," *Journal of Physics: Condensed Matter*, vol. 20, p. 384204, 2008.

[87] R. Mills and G. Prescott, "A comparison of various radiometer detection models," *IEEE Transactions on Aerospace and Electronic Systems*, vol. 32, no. 1, pp. 467 –473, jan. 1996.

[88] P. Mukherjee and B. Gupta, "Terahertz (THz) Frequency Sources and Antennas-A Brief Review," *International Journal of Infrared and Millimeter Waves*, vol. 29, no. 12, pp. 1091–1102, Dec. 2008.

[89] D. L. Nelson and M. M. Cox, *Lehninger Principles of Biochemistry*. W. H. Freeman Company, May 2008.

[90] A. Y. Nikitin, F. Guinea, F. J. Garcia-Vidal, and L. martin Moreno, “Edge and waveguide terahertz surface plasmon modes in graphene microribbons,” *Physical Review B*, vol. 84, p. 161407, Oct. 2011.

[91] D. Niyato, E. Hossain, M. Rashid, and V. Bhargava, “Wireless sensor networks with energy harvesting technologies: a game-theoretic approach to optimal energy management,” *IEEE Wireless Communications*, vol. 14, no. 4, pp. 90 –96, Aug. 2007.

[92] K. S. Novoselov, A. K. Geim, S. V. Morozov, D. Jiang, Y. Zhang, S. V. Dubonos, I. V. Grigorieva, and A. A. Firsov, “Electric Field Effect in Atomically Thin Carbon Films,” *Science*, vol. 306, no. 5696, pp. 666–669, 2004.

[93] I. Oppermann, M. Hmlinen, and J. Linatti, Eds., *UWB: Theory and Applications*. Wiley, 2004.

[94] T. Otsuji, S. Boubanga Tombet, A. Satou, M. Ryzhii, and V. Ryzhii, “Terahertz-wave generation using graphene - toward new types of terahertz lasers,” *IEEE Journal of Selected Topics in Quantum Electronics*, vol. 19, no. 1, p. 8400209, 2013.

[95] T. Otsuji, S. A. B. Tombet, A. Satou, H. Fukidome, M. Suemitsu, E. Sano, V. Popov, M. Ryzhii, and V. Ryzhii, “Graphene-based devices in terahertz science and technology,” *Journal of Physics D: Applied Physics*, vol. 45, no. 30, p. 303001, 2012.

[96] T. Otsuji, H. Karasawa, T. Watanabe, T. Suemitsu, M. Suemitsu, E. Sano, W. Knap, and V. Ryzhii, “Emission of terahertz radiation from two-dimensional electron systems in semiconductor nano-heterostructures,” *Comptes Rendus Physique*, vol. 11, no. 7-8, pp. 421–432, Aug. 2010.

[97] T. Otsuji, T. Komori, T. Watanabe, T. Suemitsu, D. Coquillat, and W. Knap, “Plasmon-resonant microchip emitters and detectors for terahertz sensing and spectroscopic applications,” in *Proc. of SPIE*, 2010, pp. 767 102–767 102–12.

[98] A. N. Pal and A. Ghosh, “Ultralow noise field-effect transistor from multilayer graphene,” *Applied Physics Letters*, vol. 95, no. 8, 2009.

[99] L. Palfalvi, J. A. Fulop, G. Almasi, and J. Hebling, “novel setups for extremely high power single-cycle terahertz pulse generation by optical rectification,” *Applied Physics Letters*, vol. 92, no. 17, p. 171107, 2008.

[100] M. Pantoja, D. Werner, P. Werner, and A. Bretones, “TDIE modeling of carbon nanotube dipoles at microwave and terahertz bands,” *IEEE Antennas and Wireless Propagation Letters*, vol. 9, pp. 32–35, 2010.

[101] A. Papoulis and S. U. Pillai, *Probability, Random Variables and Stochastic Processes*. McGraw-Hill, 2002.

[102] S. S. P. Parkin, M. Hayashi, and L. Thomas, “Magnetic domain-wall racetrack memory,” *Science*, vol. 320, no. 5873, pp. 190–194, 2008.

[103] J. C. Pearson, B. J. Drouin, A. Maestrini, I. Mehdi, J. Ward, R. H. Lin, S. Yu, J. J. Gill, B. Thomas, C. Lee, G. Chattopadhyay, E. Schlecht, F. W. Maiwald, P. F. Goldsmith, and P. Siegel, "Demonstration of a room temperature 2.48–2.75 thz coherent spectroscopy source," *Review of Scientific Instruments*, vol. 82, no. 9, p. 093105, 2011.

[104] D. Pech, M. Brunet, H. Durou, P. Huang, V. Mochalin, Y. Gogotsi, P. Taberna, and P. Simon, "Ultrahigh-power micrometre-sized supercapacitors based on onion-like carbon," *Nature nanotechnology*, vol. 5, no. 9, pp. 651–655, Sep. 2010.

[105] N. Peres, A. Castro Neto, , and F. Guinea, "Conductance quantization in mesoscopic graphene," *Physical Review B*, vol. 73, no. 19, p. 195411, May 2006.

[106] J. Perruisseau-Carrier, "Graphene for antenna applications: Opportunities and challenges from microwaves to thz," *submitted for journal publication*, 2012.

[107] R. Piesiewicz, T. Kleine-Ostmann, N. Krumbholz, D. Mittleman, M. Koch, and T. Kurner, "Terahertz characterisation of building materials," *Electronics Letters*, vol. 41, no. 18, pp. 1002–1004, Sep. 2005.

[108] R. Piesiewicz, T. Kleine-Ostmann, N. Krumbholz, D. Mittleman, m. Koch, J. Schoebel, and T. Kurner, "Short-range ultra-broadband terahertz communications: concepts and perspectives," *IEEE Antennas and Propagation Magazine*, vol. 49, no. 6, pp. 24–39, Dec. 2007.

[109] C. M. Pieterse and marcel Dicke, "Plant interactions with microbes and insects: from molecular mechanisms to ecology," *Trends in Plant Science*, vol. 12, no. 12, pp. 564–569, 2007.

[110] L. A. Ponomarenko, F. Schedin, M. I. Katsnelson, R. Yang, E. W. Hill, K. S. Novoselov, and A. K. Geim, "Chaotic Dirac billiard in graphene quantum dots," *Science*, vol. 320, no. 5874, pp. 356–358, Apr. 2008.

[111] S. Priebe, C. Jastrow, M. Jacob, T. Kleine-Ostmann, T. Schrader, and T. Kurner, "Channel and propagation measurements at 300 GHz," *IEEE Transactions on Antennas and Propagation*, vol. 59, no. 5, pp. 1688 –1698, May 2011.

[112] R. Qiu, H. Liu, and X. Shen, "Ultra-wideband for multiple access communications," *IEEE Communications Magazine*, vol. 43, no. 2, pp. 80–87, 2005.

[113] E. Ratzer and D. MacKay, "Sparse low-density parity-check codes for channels with cross-talk," in *Proc. of IEEE Information Theory Workshop*, Mar. 2003, pp. 127–130.

[114] J. Riu, A. Maroto, and F. X. Rius, "Nanosensors in environmental analysis," *Talanta*, vol. 69, no. 2, pp. 288–301, 2006.

[115] J. Rogers, "Materials and mechanics for stretchable electronics-from electronic eye cameras to conformal brain monitors," in *International Solid-State Sensors, Actuators and Microsystems Conference*, Jun. 2009, pp. 1602–1603.

[116] F. T. Roman Sordan and V. Russo, “Logic gates with a single graphene transistor,” *Applied Physics Letters*, vol. 94, p. 073305, 2009.

[117] L. Rothman, I. Gordon, A. Barbe, D. C. Benner, P. Bernath, M.Birk, V. Boudon, L. Brown, and A.Campargue, “The HITRAN 2008 molecular spectroscopic database,” *Journal of Quantitative Spectroscopy and Radiative Transfer*, vol. 110, no. 9-10, pp. 533–572, Jun. 2009.

[118] S. Roundy, P. K. Wright, and j. M. Rabaey, *Energy Scavenging for Wireless Sensor Networks: With Special Focus on Vibrations*. Norwell, MA, USA: Kluwer Academic Publishers, 2004.

[119] K.-I. Sasaki, K. Kato, Y. Tokura, K. Oguri, and T. Sogawa, “Theory of optical transitions in graphene nanoribbons,” *Physical Review B*, vol. 84, p. 085458, Aug. 2011.

[120] K.-I. Sasaki, K. Kato, Y. Tokura, S. Suzuki, and T. Sogawa, “Pseudospin for raman *d* band in armchair graphene nanoribbons,” *Physical Review B*, vol. 85, p. 075437, Feb. 2012.

[121] K.-I. Sasaki, K. Wakabayashi, and T. Enoki, “Electron wave function in armchair graphene nanoribbons,” *Journal of the Physical Society of Japan*, vol. 80, no. 4, p. 044710, 2011.

[122] B. Sensale-Rodriguez, R. Yan, M. M. Kelly, T. Fang, K. Tahy, W. S. Hwang, D. Jena, L. Liu, and H. G. Xing, “Broadband graphene terahertz modulators enabled by intraband transitions,” *Nature Communications*, vol. 3, pp. 780+, Apr. 2012.

[123] V. Sharma, U. Mukherji, V. Joseph, and S. Gupta, “Optimal energy management policies for energy harvesting sensor nodes,” *IEEE Transactions on Wireless Communications*, vol. 9, no. 4, pp. 1326–1336, 2010.

[124] E. Shih, S.-H. Cho, N. Ickes, R. Min, A. Sinha, A. Wang, and A. Chandrakasan, “Physical layer driven protocol and algorithm design for energy-efficient wireless sensor networks,” in *Proc. of the ACM International Conference on Mobile Computing and Networking, MOBICOM*, 2001, pp. 272–287.

[125] F. Sizov and A. Rogalski, “THz detectors,” *Progress in Quantum Electronics*, vol. 34, no. 5, pp. 278 – 347, 2010.

[126] G. Y. Slepyan, S. A. Maksimenko, A. Lakhtakia, O. Yevtushenko, and A. V. Gusakov, “Electrodynamics of carbon nanotubes: Dynamic conductivity, impedance boundary conditions, and surface wave propagation,” *Phys. Rev. B*, vol. 60, pp. 17 136–17 149, Dec. 1999.

[127] G. Slepyan, M. Shuba, A. Nemilentsau, and S. Maksimenko, “Electromagnetic theory of nanodimensional antennas for terahertz, infrared and optical regimes,” in *12th International Conference on Mathematical Methods in Electromagnetic Theory, MMET*, Jul. 2008, pp. 118–123.

[128] S. Smaili, V. Singal, and Y. Massoud, “On the effect of width of metallic armchair graphene nanoribbons in plasmonic waveguide applications,” in *7th IEEE International Conference on Nano/Micro Engineered and Molecular Systems (NEMS)*, Mar. 2012, pp. 623 –626.

[129] T. Sondergaard, J. Beermann, A. Boltasseva, and S. I. Bozhevolnyi, “Slow-plasmon resonant-nanostrip antennas: Analysis and demonstration,” *Physical Review B*, vol. 77, p. 115420, Mar. 2008.

[130] J. W. Song, G. R. Aizin, J. Mikalopas, Y. Kawano, K. Ishibashi, N. Aoki, J. L. Reno, Y. Ochiai, and J. P. Bird, “Bolometric terahertz detection in pinched-off quantum point contacts,” *Applied Physics Letters*, vol. 97, no. 8, p. 083109, 2010.

[131] E. Sousa, “Performance of a spread spectrum packet radio network link in a poisson field of interferers,” *IEEE Transactions on Information Theory*, vol. 38, no. 6, pp. 1743 –1754, Nov. 1992.

[132] T. Stauber, N. M. R. Peres, and A. K. Geim, “Optical conductivity of graphene in the visible region of the spectrum,” *Physical Review B*, vol. 78, p. 085432, Aug. 2008.

[133] M. D. Stoller, S. Park, Y. Zhu, J. An, and R. S. Ruoff, “Graphene-based ultracapacitors,” *Nano Letters*, vol. 8, no. 10, pp. 3498–3502, Oct. 2008.

[134] S. Sudevalayam and P. Kulkarni, “Energy harvesting sensor nodes: survey and implications,” *IEEE Communications Surveys Tutorials*, vol. 13, no. 3, pp. 443 – 461, 2011.

[135] J. Tabor, “Noise reduction using low weight and constant weight coding techniques,” MIT, Cambridge, MA, USA, Tech. Rep., 1990.

[136] P. Tallury, A. Malhotra, L. M. Byrne, and S. Santra, “Nanobioimaging and sensing of infectious diseases,” *Advanced Drug Delivery Reviews*, vol. 62, no. 4-5, pp. 424–437, Mar. 2010.

[137] M. Tamagnone, J. S. Gomez-Diaz, J. R. Mosig, and J. Perruisseau-Carrier, “Reconfigurable terahertz plasmonic antenna concept using a graphene stack,” *Applied Physics Letters*, vol. 101, no. 21, p. 214102, 2012.

[138] D. Tessier, I. Radu, and M. Filteau, “Antimicrobial fabrics coated with nano-sized silver salt crystals,” *NSTI Nanotech*, vol. 1, pp. 762–764, 2005.

[139] I. E. Tothill, “Biosensors for cancer markers diagnosis,” *Seminars in Cell & Developmental Biology*, vol. 20, no. 1, pp. 55–62, 2009.

[140] N. J. Tro, *Principles of chemistry: a molecular approach*. Prentice-Hall, Inc., 2009.

[141] W.-K. Tse, E. H. Hwang, and S. D. Sarma, “Ballistic hot electron transport in graphene,” *Applied Physics Letters*, vol. 93, no. 2, p. 023128, 2008.

[142] A. Vakil and N. Engheta, “Transformation optics using graphene,” *Science*, vol. 332, no. 6035, pp. 1291–1294, Jun. 2011.

[143] J. H. Van Vleck and V. F. Weisskopf, “On the shape of collision-broadened lines,” *Review Mod. Physical*, vol. 17, no. 2-3, pp. 227–236, Apr. 1945.

[144] L. Vicarelli, M. S. Vitiello, D. Coquillat, A. Lombardo, A. C. Ferrari, W. Knap, M. Polini, V. Pellegrini, and A. Tredicucci, “Graphene field-effect transistors as room-temperature terahertz detectors,” *Nature Materials*, vol. 11, pp. 865–871, Oct. 2012.

[145] M. S. Vitiello, D. Coquillat, L. Viti, D. Ercolani, F. Teppe, A. Pitanti, F. Beltram, L. Sorba, W. Knap, and A. Tredicucci, “Room-temperature terahertz detectors based on semiconductor nanowire field-effect transistors,” *Nano Letters*, vol. 12, no. 1, pp. 96–101, 2012.

[146] K. Wakabayashi, K. Sasaki, T. Nakanishi, and T. Enoki, “Electronic states of graphene nanoribbons and analytical solutions,” *Science and Technology of Advanced Materials*, vol. 11, no. 5, p. 054504, 2010.

[147] H. Wang, A. Hsu, K. K. Kim, J. Kong, and T. Palacios, “Gigahertz ambipolar frequency multiplier based on cvd graphene,” in *Proc. of IEDM10*, 2010, pp. 572–575.

[148] H. Wang, A. Hsu, J. Wu, J. Kong, and T. Palacios, “Graphene-based ambipolar rf mixers,” *IEEE Electron Device Letters*, vol. 31, p. 906908, 2010.

[149] H. Wang, D. Nezich, J. Kong, and T. Palacios, “Graphene frequency multipliers,” *IEEE Electron Device Letters*, vol. 30, no. 5, pp. 547 –549, May 2009.

[150] I. Wang and Y. ping Du, “Optical input impedance of nanostrip antennas,” *Optical Engineering*, vol. 51, no. 5, p. 054002, 2012.

[151] Y. Wang, M. Vuran, and S. Goddard, “Stochastic analysis of energy consumption in wireless sensor networks,” in *Proc. of the 7th Annual IEEE Communications Society Conference on Sensor Mesh and Ad Hoc Communications and Networks, SECON*, Jun. 2010, pp. 1–9.

[152] Z. L. Wang, “Towards self-powered nanosystems: from nanogenerators to nanopiezotronics,” *Advanced Functional Materials*, vol. 18, no. 22, pp. 3553–3567, 2008.

[153] M. C. Wanke, M. Lee, C. D. Nordquist, M. J. Cich, M. Cavaliere, A. M. Rowen, J. R. Gillen, C. L. Arrington, A. D. Grine, C. T. Fuller, and J. L. Reno, “Integrated chip-scale thz technology,” *Proc. of SPIE*, pp. 80 310E–80 310E–10, 2011.

[154] M. Weisenhorn and W. Hirt, “Uncoordinated rate-division multiple-access scheme for pulsed uwb signals,” *IEEE Transactions on Vehicular Technology*, vol. 54, no. 5, pp. 1646–1662, Sep. 2005.

[155] D. Wentzloff, F. Lee, D. Daly, M. Bhardwaj, P. Mercier, and A. Chandrakasan, "Energy efficient pulsed-UWB CMOS circuits and systems," in *Proc. of IEEE International Conference on Ultra-Wideband*, Sep. 2007, pp. 282 –287.

[156] P. West, S. Ishii, G. Naik, N. Emani, V. Shalaev, and A. Boltasseva, "Searching for better plasmonic materials," *Laser & Photonics Reviews*, vol. 4, no. 6, pp. 795–808, 2010.

[157] M. Win, P. Pinto, and L. Shepp, "A mathematical theory of network interference and its applications," *Proceedings of the IEEE*, vol. 97, no. 2, pp. 205 –230, Feb. 2009.

[158] S. Xu, B. J. Hansen, and Z. L. Wang, "Piezoelectric-nanowire-enabled power source for driving wireless microelectronics," *Nature Communications*, vol. 1, no. 7, pp. 1–5, Oct. 2010.

[159] S. Xu, Y. Qin, C. Xu, Y. Wei, R. Yang, and Z. L. Wang, "Self-powered nanowire devices," *Nature Nanotechnology*, vol. 5, pp. 366–373, 2010.

[160] H. Yan, X. Li, B. Chandra, G. Tulevski, Y. Wu, M. Freitag, W. Zhu, P. Avouris, and F. Xia, "Tunable infrared plasmonic devices using graphene/insulator stacks." *Nature Nanotechnology*, vol. 7, no. 5, pp. 330–4, 2012.

[161] K. Yasuko and S. Takamasa, "Terahertz-wave propagation model," *Journal of the National Institute of Information and Communications Technology*, vol. 55, no. 1, pp. 73–77, 2008.

[162] K.-L. Yeh, M. C. Hoffmann, J. Hebling, and K. A. Nelson, "Generation of 10 mu j ultrashort terahertz pulses by optical rectification," *Applied Physics Letters*, vol. 90, no. 17, p. 171121, 2007.

[163] C. R. Yonzon, D. A. Stuart, X. Zhang, A. D. McFarland, C. L. Haynes, and R. P. V. Duyne, "Towards advanced chemical and biological nanosensors-an overview," *Talanta*, vol. 67, no. 3, pp. 438–448, 2005.

[164] X. Zhou, I. Oka, and C. Fujiwara, "Network performance of time spread ppm/cdma systems," in *Proc of 'Communications on the Move': Singapore ICCS/ISITA*, 1992, pp. 929–933.

[165] T. Zhu, Z. Zhong, Y. Gu, T. He, and Z.-L. Zhang, "Leakage-aware energy synchronization for wireless sensor networks," in *Proc. of the 7th ACM international conference on Mobile systems, applications, and services, MobiSys*, 2009, pp. 319–332.

[166] Z. Zou, D. S. Mendoza, P. Wang, Q. Zhou, J. Mao, F. Jonsson, H. Tenhunen, and L.-R. Zheng, "A low-power and flexible energy detection IR-UWB receiver for RFID and wireless sensor networks," *IEEE Transactions on Circuits and Systems I: Regular Papers*, vol. 58, pp. 1470–1482, 2011.

VITA

Josep Miquel Jornet Montana received the Engineering Degree in Telecommunications Engineering and the Master of Science in Information and Communication Technologies from the Universitat Politècnica de Catalunya, Barcelona, Spain, in 2008. He received the Ph.D. degree in Electrical and Computer Engineering from the Georgia Institute of Technology, Atlanta, GA, in August 2013, under the supervision of Prof. Ian F. Akyildiz and with a fellowship from "la Caixa" (2009-2010) and Fundación Caja Madrid (2011-2012). He is currently an Assistant Professor with the Department of Electrical Engineering at the University at Buffalo, The State University of New York. From September 2007 to December 2008, he was a visiting researcher at the Massachusetts Institute of Technology (MIT), Cambridge, MA, under the MIT Sea Grant program. He was the recipient of the Oscar P. Cleaver Award for outstanding graduate students in the School of Electrical and Computer Engineering, at the Georgia Institute of Technology in 2009. He also received the Broadband Wireless Networking Lab Researcher of the Year Award at the Georgia Institute of Technology in 2010. He is a member of the IEEE and the ACM. His current research interests are in electromagnetic nanonetworks, graphene-enabled wireless communication, Terahertz Band communication networks and the Internet of Nano-Things.